Universidade do Minho
Escola de Engenharia

Nuno Miguel Faria Araújo

HIGH-SPEED TRAINS ON BALLASTED RAILWAY TRACK
Dynamic stress field analysis

July 2010

Universidade do Minho
Escola de Engenharia

Nuno Miguel Faria Araújo

HIGH-SPEED TRAINS ON BALLASTED RAILWAY TRACK
Dynamic stress field analysis

Doctoral thesis in Civil Engineering
Area of knowledge in Geotechnics

Work performed under the supervision of
Professor António Gomes Correia

and co-supervision of
Professor Arézou Modaressi
Professor Didier Clouteau

July 2010

DECLARATION

Name: Nuno Miguel Faria Araújo

E-mail: nuno@civil.uminho.pt

Phone number: (+351) 253 510 200

Passport number: 11657830

Doctoral thesis title: HIGH-SPEED TRAINS ON BALLASTED RAILWAY TRACK

Dynamic stress field analysis

Supervisor: Professor António Gomes Correia

Co-supervisors: Professor Arézou Modaressi

Professor Didier Clouteau

Year of conclusion: 2010

Area of knowledge: Civil Engineering / Geotechnics

THE INTEGRAL REPRODUCTION OF THIS DISSERTATION IS ONLY AUTHORIZED FOR RESEARCH EFFECTS, AFTER WRITTEN DECLARATION OF THE INTERESTED PARTY, TO WHICH IT PLEDGES TO COMPLY.

University of Minho, July 2010

Nuno Araújo

Recomeça...
Se puderes,
sem angústia e sem pressa.
E os passos que deres,
nesse caminho duro,
dá-os em liberdade.
Enquanto não alcances,
não descanses.
De nenhum fruto queiras só metade.

Diário XIII
Miguel Torga

This page was intentionally left blank.

Acknowledgment

The author would like to thank all institutions and persons who made this project possible, namely:

- Foundation for Science and Technology, through POCI/ECM/1114/2004 project;

- 'Gabinete de Relações Internacionais da Ciência e do Ensino Superior', through project GRICES/CNRS - 'Sécurité des infrastructures routières et ferroviaires vis-à-vis des chargements climatiques';

- University of Minho through the Territory, Environment and Construction Centre (C-TAC) and the Department of Civil Engineering (DEC), for the logistical and human conditions;

- 'Ecole Centrale Paris' and the 'Laboratoire de Mécanique des Sols, Structures et Matériaux, through its director, Prof. Jean-Marie Fleureau;

- Prof. António Gomes Correia (University of Minho), for his supervision along this entire research project;

- Prof. Arézou Modaressi ('Ecole Centrale Paris'), for her supervision along the numerical simulation with GEFDYN software;

- Prof. Didier Clouteau ('Ecole Centrale Paris'), for his supervision along the numerical simulation with MISS software;

- Prof. Jaime Fonseca (University of Minho), for the technical support provided during the development of the hardware and software required for the laboratory work;

- Prof. Lino Costa (University of Minho), for allowing the use of his minimization algorithm (an evolutionary strategy algorithm) to improve user calibration of Hujeux constitutive law;

- all the technicians in the Civil Engineering Laboratory at University of Minho for their constant help during the laboratory work, in particular to Mr. Carlos Palha;

- Dr. João Campos and Prof. Cristiana Ferreira for their kind support in revising the text;

- finally, my greatest gratitude goes to my parents and friends for their constant support, belief and encouragement.

Abstract

The analysis of ballasted railway structures still demands many improvements towards preceding an accurate estimate of its global behavior, i.e, towards reproducing the real performance of the materials and the structure. Furthermore, in the design process, ultimate/serviceability limit states and life cycle costs should be attended. As a result, a wide range of research works are being introduced. This work contributes to the improvement of these processes throughout laboratory and numerical experiments aiming to investigate (with particular emphasis) on the dynamic stress field analysis, particularly the characteristic stress paths followed by granular elements below a typical track structure under the passage of a High-Speed Train (HST). The experimental laboratory work allowed, by means of a high-precision cyclic triaxial stress-path apparatus, the definition of the elastic domain of a foundation soil. The numerical experiments were carried out using an elastic frequency domain model and an elastoplastic time domain model, validated with *in situ* data obtained by vibration measurements in a HST railway line. These numerical models were used to analyze the influence of stiffness of the foundation (elastic domain) and structural layers of railway granular materials (elastic or elastoplastic domains) in the stress field, clearly showing that the stress response is a function of the selected constitutive law. Furthermore, the linear elastic assumption for the foundation soil was found to be questionable, suggesting that further investigation is required.

Keywords: High-Speed Train, railway structure, characteristic stress field, multimechanism elastoplastic law, elastic domain, evolutionary strategies.

This page was intentionally left blank.

Sumário

A análise de estruturas ferroviárias balastradas exige melhorias que a tornem capaz de reproduzir o comportamento global, i.e., que seja possível a reprodução do desempenho real dos materiais e da estrutura. Além disso, no processo de dimensionamento, os estados limite de utilização/últimos e os custos de manutenção devem ser considerados. Como resultado, uma ampla gama de trabalhos de investigação está actualmente em curso. Este estudo contribui para a melhoria destes processos, através de experiências laboratoriais e numéricas que focam com particular ênfase o campo dinâmico de tensões induzido nas camadas granulares das estruturas ferroviárias, quando submetidas à passagem de um comboio de alta velocidade. O trabalho experimental laboratorial permitiu, por meio de um sistema triaxial cíclico de precisão capaz de aplicar qualquer trajectória de tensões, a definição do domínio elástico de um solo de fundação. Os trabalhos experimentais numéricos foram realizados utilizando um modelo elástico no domínio da frequência e um modelo elasto-plástico no domínio do tempo, validados com medições *in situ* de vibrações numa linha ferroviária de alta velocidade. Estes modelos numéricos foram usados para analisar a influência da rigidez da fundação (domínio elástico) e das camadas granulares estruturais da via ferroviária (domínios elástico ou elasto-plástico) no campo de tensões, mostrando claramente que a resposta é função da lei constitutiva seleccionada. Além disso, a assumpção de comportamento elástico linear para o solo de fundação é questionável, requerendo-se investigação adicional.

Palavras-chave: Comboio de alta velocidade, estrutura ferroviária, campo característico de tensões, lei elasto-plástica multi-mecanismos, domínio elástico, estratégia evolutiva.

This page was intentionally left blank.

Contents

Acknowledgment **v**

Abstract **vii**

Sumário **ix**

Table of contents **xiii**

List of figures **xvii**

List of tables **xix**

Glossary **xxiii**

Introduction **xxv**

Track technology **1**
1.1. Railway transportation 1
1.2. Railway track system 1
1.3. System components 2
1.3.1. Rails 3
1.3.2. Pads 5
1.3.3. Fastening systems 5
1.3.4. Sleepers 6
1.3.5. Ballast 7
1.3.6. Subballast 9
1.3.7. Geosynthetics 11
1.3.8. Capping layer 13
1.3.9. Foundation 13
1.4. Railway design behavior 14
1.4.1. Vertical reversible deflection 14
1.4.2. Vertical cumulative deflection 14
1.4.3. Horizontal reversible deflection 15
1.5. Dynamic concepts of the moving load 15
1.5.1. Energy wave 15
1.5.2. Energy dissipation 16
1.5.3. Particular speeds of the moving load 18
1.6. Testing 19
1.7. Modeling 20

1.7.1. Simplifications . . . 20
1.7.2. Techniques . . . 22
1.7.3. Domains of analysis . . . 24
1.8. Noise and vibration . . . 24
1.9. Maintenance . . . 26
1.10. Summary . . . 29

Elastic domain of soils **31**
2.1. Introduction . . . 31
2.2. Elastic domain . . . 31
2.3. Instrumentation technique . . . 35
2.3.1. Technique selection . . . 35
2.3.2. LDTs . . . 36
2.3.3. Radial instrumentation . . . 37
2.3.4. Axial instrumentation . . . 39
2.4. Acquisition and control system . . . 40
2.4.1. Acquisition . . . 40
2.4.2. Control system . . . 41
2.5. Study soil . . . 44
2.6. Sample construction and instrumentation . . . 45
2.7. Testing program . . . 46
2.8. Analysis of the results . . . 47
2.9. Summary . . . 51

Stress-path evaluation: elastic behavior **55**
3.1. Introduction . . . 55
3.2. Mathematical formulation . . . 56
3.3. Site . . . 56
3.3.1. Thalys train . . . 57
3.3.2. Track . . . 58
3.3.3. Foundation . . . 58
3.3.4. Site geometry . . . 58
3.4. Model construction . . . 59
3.5. Model validation . . . 64
3.5.1. Measurements filtering . . . 64
3.5.2. Simulation efficiency . . . 65
3.6. Model parametric studies . . . 69
3.7. Stress-path evaluation . . . 73
3.8. Summary . . . 77

Cyclic plastic modeling **79**
4.1. Introduction . . . 79
4.2. Fundamental concepts . . . 79
4.2.1. Elastic domain . . . 82
4.2.2. Failure surface . . . 82
4.2.3. Yield surface . . . 83
4.2.4. Flow rule . . . 84
4.3. Multimechanism elastoplastic model . . . 84
4.4. Hujeux law parameters . . . 88
4.5. Parameters influence and calibration . . . 89

4.5.1. Yield surface shape . . . 89
4.5.2. Deviatoric soil domains . . . 89
4.5.3. Isotropic soil domain . . . 91
4.5.4. Dilatancy behavior . . . 91
4.5.5. Initial and critical state definition . . . 91
4.6. Laboratory data . . . 93
4.7. Manual calibration process . . . 107
4.8. Optimization technique study . . . 119
4.9. Summary . . . 124

Stress-path evaluation: elastoplastic behavior **127**
5.1. Introduction . . . 127
5.2. Mesh . . . 128
5.2.1. Published cases . . . 128
5.2.2. New mesh . . . 130
5.3. Models validation . . . 133
5.4. Characteristic stress-path . . . 139
5.5. Summary . . . 147

Main summary **151**
R.1. Conclusions . . . 151
R.2. Prospective work . . . 153

Bibliography **155**

Appendix **165**
A.1. Frequency domain model . . . 165
A.1.1. Floquet transform . . . 165
A.1.2. Floquet relation with Fourier . . . 166
A.1.3. Periodic problem . . . 166
A.1.4. Soil-track interaction . . . 167
A.1.5. Moving load . . . 168
A.2. Stress-path software . . . 171
A.2.1. Purpose . . . 171
A.2.2. Software front panel . . . 171
A.2.3. Software block diagram . . . 176
A.2.4. Channels and data file . . . 178
A.2.5. Recommended test procedure . . . 180
A.3. Hujeux law calibration software . . . 181
A.3.1. Purpose . . . 181
A.3.2. Software description . . . 181
A.3.3. Example of an evolutionary.nn file . . . 188

This page was intentionally left blank.

List of Figures

1.1 Railway components 2
1.2 Rail section (UIC60) 3
1.3 General buckling effect 4
1.4 Rubber pad 5
1.5 Rail fastening systems 6
1.6 Concrete sleepers 6
1.7 Static bearing capacity of the ballast 8
1.8 Slab-track 9
1.9 Optimum grain size curves 10
1.10 Seasonal fluctuation of the bearing capacity 11
1.11 Settlement reduction induced by geogrid inclusion 12
1.12 Stress-strain behavior induced by viscous damping 17
1.13 Model for vehicle/rail interaction 21
1.14 Noise and vibration produced by High-Speed Trains 25
1.15 Total annual expenditure for maintenance and renewal 28
1.16 Four-point system for lining process and MDZ train 29

2.1 Settlement of El-Infiernillo dam 32
2.2 Domain surfaces and secant modulus degradation curve 33
2.3 Modulus and instrumentation influence in triaxial testing 34
2.4 Strain/stress relations in soils 34
2.5 Scheme of a full bridge LDT 36
2.6 Components of the belt radial system 38
2.7 Scheme of the belt radial system 39
2.8 Direct radial measurement system 39
2.9 Stress-path chamber 41
2.10 Components used to automatize mechanical pneumatic-valves . . 42
2.11 Proportional close-loop valve 43
2.12 Tested stress-paths 43
2.13 Grain-size distribution studies 44
2.14 Sample mold and creation of the pseudo-articulation points . . . 45
2.15 Radial measurement systems 46
2.16 Applied stress-path 48
2.17 Elastic domain evaluation 49
2.18 Poisson ratio evaluation 50
2.19 Elastic domain increments 51
2.20 Normalized elastic domain surface 52
2.21 Mathematical elastic domain radius of Perafita sand 53

3.1 Thalys geometry 57
3.2 Track geometry (section) 59
3.3 Track geometry (plan) 59
3.4 Model geometry (section) 61
3.5 Model geometry (plan) 62
3.6 Reference periodic mesh 62
3.7 Periodic modes 63
3.8 Static modes 63
3.9 Influence of signal filtering 65
3.10 Acceleration comparison in frequency domain 66
3.11 Acceleration comparison in time domain 66
3.12 Velocity comparison in frequency domain 67
3.13 Velocity comparison in time domain 67
3.14 Velocity filtering 69
3.15 Sleeper acceleration (first 5 axles) 70
3.16 Sleeper velocity 71
3.17 Sleeper velocity (first 5 axles) 71
3.18 Sleeper displacement 72
3.19 Ballast stress 74
3.20 Subballast stress 74
3.21 Capping layer stress (top) 75
3.22 Capping layer stress (middle) 75
3.23 Capping layer stress (bottom) 76

4.1 Tresca and Von-Mises failure surfaces 83
4.2 Influence of b parameter on the yield surface 90
4.3 Calibration of c by means of an undrained triaxial test 92
4.4 Calibration of c by means of an isotropic triaxial test 92
4.5 Method for ψ evaluation 93
4.6 Definition of model parameters by means of the CSL 94
4.7 Triaxial tests over the ballast in $q\,p^{-1} : 3^{-1}(\epsilon_{\mathrm{a}} - \epsilon_{\mathrm{r}})$ space (1) . . 95
4.8 Triaxial tests over the ballast in $\epsilon_{\mathrm{v}} : 3^{-1}(\epsilon_{\mathrm{a}} - \epsilon_{\mathrm{r}})$ space 96
4.9 Cyclic triaxial tests over the ballast in $3^{-1}(\epsilon_{\mathrm{a}} - \epsilon_{\mathrm{r}}) : N_{\mathrm{c}}$ space . . 96
4.10 Cyclic triaxial tests over the ballast in $\epsilon_{\mathrm{v}} : N_{\mathrm{c}}$ space 97
4.11 Triaxial tests over the ballast in $q\,p^{-1} : 3^{-1}(\epsilon_{\mathrm{a}} - \epsilon_{\mathrm{r}})$ space (2) . . 97
4.12 Grain size curve of the 'Maraicheres' gravel 98
4.13 Triaxial tests over the 'Maraicheres' gravel in $q : \epsilon_{\mathrm{a}}$ space 99
4.14 Triaxial tests over the 'Maraicheres' gravel in $\epsilon_v : \epsilon_{\mathrm{a}}$ space 100
4.15 Triaxial tests over the 'Maraicheres' gravel in $e : \ln(p)$ space . . . 100
4.16 Quantification of ϕ and ψ for the 'Maraicheres' gravel 101
4.17 Cyclic conditioning over the 'Maraicheres' gravel 102
4.18 Conditioning detail over the 'Maraicheres' gravel 103
4.19 Variation of ϵ_{v} over the 'Maraicheres' gravel during conditioning 103
4.20 Cyclic drained triaxial test over the 'Maraicheres' gravel 104
4.21 Oedometric test over 'Évora' sand 105
4.22 Triaxial tests over 'Évora' sand in $q : \epsilon_{\mathrm{a}}$ space 106
4.23 Triaxial tests over 'Évora' sand in $e : p$ space 106
4.24 Triaxial tests over 'Évora' sand in $\epsilon_{\mathrm{v}} : \epsilon_{\mathrm{a}}$ space 107
4.25 Hujeux response for the ballast material 110
4.26 Hujeux response for the 'Maraicheres' gravel (part 1) 114

4.27 Hujeux response for the 'Maraicheres' gravel (part 2) 115
4.28 Hujeux response for the 'Maraicheres' gravel (in $e : \ln(p)$ space) . 115
4.29 Hujeux response for 'Évora' sand 117
4.30 Hujeux response for 'Évora' sand (in $q : \epsilon_{\mathrm{a}}$ space) 118
4.31 Evaluation stages of the $(\mu/\rho + \lambda)$-ES 121
4.32 Evolution of the adjustment error 124
4.33 'Évora' sand manual and optimized solution 125

5.1 FEM mesh 131
5.2 Loading scheme 132
5.3 Initial vertical stress 134
5.4 Study points (in function of depth) 134
5.5 Validation of the elastic law model (unloaded case) 135
5.6 Validation of the elastic law model (loaded case) 136
5.7 Validation of the Mohr-Coulomb law model (loaded case) 137
5.8 Validation of the Hujeux law model (loaded case) 138
5.9 Stresses of the elastic law model (unloaded case) 140
5.10 Stresses of the elastic law model (loaded case) 141
5.11 Stresses of the Mohr-Coulomb law model (loaded case) 142
5.12 Stresses of the Hujeux law model (loaded case) 143
5.13 Stress-path obtained with the elastic law model (unloaded case) . 145
5.14 Stress-path obtained with the elastic law model (loaded case) . . 146
5.15 Stress-path obtained with the Mohr-Coulomb law 147
5.16 Stress-path obtained with the Hujeux law 148

A.1 Periodic domain selection 167
A.2 Generic cell decomposition 168
A.3 LabVIEW® front panel 172
A.4 LabVIEW® block diagram 177
A.5 Developed MATLAB® interface for Hujeux law calibration . . . 182

This page was intentionally left blank.

List of Tables

1.1 Mitigation methods advantages and disadvantages 27

2.1 State conditions of the third phase 50

3.1 Thalys characteristics 57
3.2 Track characteristics 60
3.3 Foundation characteristics 61

4.1 Hujeux law parameters 87
4.2 Grain size distribution of ballast material 94
4.3 Static triaxial tests performed over ballast material 95
4.4 Stress-path applied over 'Maraicheres' gravel 101
4.5 Grain size distribution of 'Évora' sand 104
4.6 Ballast material data used for manual calibration 109
4.7 'Maraicheres' gravel data used for manual calibration 112
4.8 'Évora' sand data used for manual calibration 116
4.9 Manual calibration parameters 118
4.10 Optimization process studies 122
4.11 Results of the optimization process studies 123

5.1 Parameters X and Y for load distribution 130

A.1 Available variables and channel reference 178
A.2 Parameters name relation 184
A.3 Results available on RES.mat 184

This page was intentionally left blank.

Glossary

C	Speed
C_{C}	Curvature coefficient
C_{cr}	Critical train speed
C_{p}	Compression wave speed
C_{s}	Shear wave speed
E	Deformability modulus
E_0	Maximum deformability modulus
E_{a}	Adjustment error
E_{eq}	Deformability equivalent modulus
E_{sc}	Deformability secant modulus
E_{tg}	Deformability tangent modulus
F	Failure surface
F_{s}	Yield surface
G	Shear modulus
G_{s}	Specific density
I	Inertia
K	Bulk modulus
K_0	Maximum bulk modulus
M_0	Natural state line slope in $q : p$ space
M_{cs}	Limit state line slope in $q : p$ space
N	Hujeux law auxiliary variable for cyclic behavior
N_{a}	Triaxial test axial force
N_{c}	Number of cycles
R	Resolution
Sr	Degree of saturation
T	Period
U_{C}	Uniformity coefficient
U_{e}	Elastic deflection along xx direction
U_{m}	Percentage of pass material
V_{e}	Elastic deflection along yy direction
W	Displacement along zz direction
W_{e}	Elastic deflection along zz direction
W_{pd}	Cumulative differential deflection along zz direction
W_{p}	Cumulative deflection along zz direction
Ω	Peak energy stored in one cycle
Ψ	Energy dissipated per cycle
ϵ_{a}	Axial strain
ϵ_{r}	Radial strain

ϵ_{v}	Volumetric strain
γ	Shear strain
γ_{dmax}	Maximum dry unit mass
γ_{e}	Elastic shear strain
γ_{n}	Apparent unit weight
ν	Poisson ratio
ω	Circular speed
ω_{n}	Natural water content
ω_{p}	Optimum water content
ϕ	Friction angle
ρ	Mass density
σ_3	Minimum principal stress
τ	Shear stress
ξ	Damping ratio
c	Damping
c_{c}	Critical damping
d	Layer thickness
e	Void ratio
f	Frequency
h	Height
k_0	Natural impulse coefficient
k_{s}	Soil stiffness
l	Length
m	Mass
n	Wheel out-of-roundness
p	Average effective stress
p	Average stress
p	Mean stress
p	mean stress
q	Deviatoric stress
q_{u}	Bearing capacity
r	Elastic domain radius
t	Time
u	Interstitial pressure
x	First cartesian coordinate
y	Second cartesian coordinate
z	Thirst cartesian coordinate
ASTM	American Society for Testing of Materials
BEM	Boundary Element Method
CPU	Central Processing Unit
CSL	Critical State Line
DEM	Discrete Element Method
ECP	Ecole Centrale Paris
ESs	Evolution Strategies
FEM	Finite Element Method
FFT	Fast Fourier Transform
GAs	Genetic Algorithms
GEFDYN	Géomecanique Eléments Finis DYNamique
HST	High-Speed Train

IFFT	Inverse Fast Fourier Transform
KUL	Katholieke Universiteit Leuven
LabVIEW®	Laboratory Virtual Instrumentation Engineering Workbench
LDT	Local Deformation Transducer
LVDT	Linear Variable Displacement Transducer
MATLAB®	MATrix LABoratory
MISS	Modélisation des Interfaces Sol-Structure
NCL	Normal Consolidation Line
NSL	Natural State Line
OCR	Over Consolidation Ratio
SASW	Spectral Analysis of Surface Waves
SDTools	Structural Dynamics Toolbox
UM	University of Minho

This page was intentionally left blank.

Introduction

The main goal of this research work was to quantify induced stresses in railway structures due to High-Speed Trains (HST), which was supported by the undergoing construction of a large cyclic triaxial apparatus at UM facilities. Since the construction of the national high-speed railway network is expected in the near future years, the Geotechnical group initiated numerical studies in the field of railway engineering as well as the construction of a large cyclic triaxial apparatus to support those studies.

The characterization of the stress field induced by HST, a well known topic in road infrastructure but not so in railway engineering, can highly improve laboratory efficiency since it will allow the application of trajectories identical to the ones applied in real conditions. As a result, long-term irreversible behavior and mitigation techniques can be better analyzed at laboratory level.

This thesis intends to evaluate the characteristic induced stresses and for that it is divided in seven Chapters and one Appendix. In this Section the main goal of each Chapter is described in detail.

- **Introduction** describes the initial considerations and motivation of the thesis. It also presents the description of the performed work on each Chapter.

- Chapter 1, entitled **Track technology**, presents a global overview of railway technology. The functional characteristics of each component of a railway track system are described in detail. It also points out desirable design behavior and dynamic concepts, fundamental to correctly simulate high-speed railway lines. Other topics such as laboratory testing, consequences of simulation simplification and computational techniques, the production of noise and vibration and maintenance problematic are discussed. In summary, this chapter presents descriptions of several performed studies in order to gather its inherent know-how, which feeds the research developed under this work.

- Chapter 2, entitled **Geomaterials elastic domain**, describes the first performed study, which consisted of a laboratory campaign that required the development of a precise triaxial stress-path apparatus, in terms of hardware and software. It starts with a short bibliographic review on the elastic domain of soils since it was intended from the beginning to assume (in all numerical simulations) that the foundation would remain elastic.

To confirm this assumption, and attending to the fact that insufficient information was available regarding the *in situ* railway track foundation, a foundation soil (Perafita sand) was used, already object of previous studies in a bilateral cooperative project between France and Portugal, in a first phase through Technical University of Lisbon and in a second phase through UM, with 'Ecole Centrale Paris' (ECP - MSSMat) (Fleureau *et al.*, 2002; Hadiwardoyo, 2002; Reis Ferreira, 2003). For testing purposes, the design and construction of local strain instrumentation, the selection of hardware for automatic control and software code development was performed and is exposed in detail. Then, the study soil was characterized and the sample construction and testing program are described. It ends with the definitions of the elastic domain for Perafita soil, presenting future improvements on the automated system.

- Chapter 3, entitled **Stress-path evaluation: elastic behavior**, starts by addressing the importance of the definition of the characteristic stress-path, followed by the mathematical assumptions of a 3D frequency domain project developed during an European Project (SUPERTRACK) at ECP - MSSMat. This model was then validated through a case study near Brussels - Belgium (Degrande, 2000) were field data was available. After validation, studies regarding the evaluation of the stress field were performed by means of the introduction of a bedrock and/or distinct foundations stiffness, allowing the identification of evolution trends of the stress paths.

- Chapter 4, entitled **Cyclic plastic modeling**, describes the principal basis of modern plasticity models. Since limitations due to the elastic assumption became a challenge for this work, it was decided to use a multimechanism elastoplastic constitutive law (Hujeux law), which is able to integrate volumetric and irreversible behavior (Aubry *et al.*, 1982; Hujeux, 1985). The mathematical formulation of the model is presented and its calibration was performed with laboratory data obtained in several institutions. This calibration process was performed manually and complemented with the use of minimization algorithms by means of an evolutionary strategy algorithm in order to define future guidelines.

- Chapter 5, entitled **Stress-path evaluation: elastoplastic behavior**, describes the work executed with a FEM software (GEFDYN) to perform time domain analyzes. It starts with a short bibliographic review performed to improve the quality of the numerical model, mainly regarding the length of the mesh and elements. For validation purposes, field data from the case study near Brussels - Belgium was used, allowing the model to evaluate induced stress-paths. Three distinct constitutive laws were used (linear elastic, Mohr-Coulomb and Hujeux) so that results could be compared with those of Chapter 3, as well as to study the influence of the linear elastic behavior assumption.

- **Main summary** summarizes this entire document and presents the characteristics stress-path induced by HST. As prospective laboratorial work, improvements are proposed to the developed stress-path triaxial system and to the implementation of the quantified stress-path in a large cyclic triaxial apparatus able to quantify irreversible behavior of railway characteristic materials. As prospective numerical work, suggestions are made

on new approaches to improve the calibration of Hujeux law and the numerical simulation of the railway structure.

- **Appendix** is presented in this document to provide the mathematical formulation of the frequency domain model used in Chapter 3 and to describe the use of two software programs developed during this thesis, namely:
  - A LabVIEW® software for acquisition and control of proportional servo-valves and step motors. The software allows variable acquisition rate during testing and simultaneous control of two proportional servo-vales. Hardware configuration is not rigid and can be modified to distinct systems. The code is partially developed in MATLAB® (e.g. for variable acquisition rate) and it is required that the user is capable of modifying it.
  - A MATLAB® graphical user interface to assist user during Hujeux calibration and also to allow the use of a minimization algorithm. Users are not required to have any MATLAB® knowledge. It should be pointed out that the minimization theory belongs to Prof. Lino Costa and proper authorization is required before use.

As a final remark, it is important to refer that throughout this entire work, tables and graphics were defined according to Thompson and Taylor (2008) recommendations with respect to the use of the International System of Units (SI). These authors referred that the value of a quantity is its magnitude expressed as the product of a number and an unit, and the number multiplying the unit is the numerical value of the quantity expressed in that unit. More formally, the value of quantity A can be written as $A = \{A\}[\mathrm{A}]$, where $\{A\}$ is the numerical value of A when the value of A is expressed in the unit [A]. The numerical value can therefore be written as $\{A\} = A/[\mathrm{A}]$, which is a convenient form for use in figures and tables. Thus, to eliminate the possibility of misunderstanding, an axis of a graph or the heading of a column of a table was labeled, for example, as $t/\,^{\circ}\mathrm{C}$ instead of $t\,(^{\circ}\mathrm{C})$ or Temperature $(^{\circ}\mathrm{C})$.

This page was intentionally left blank.

Track technology

1.1. Railway transportation

Railways have become one of the most advanced and fast growing means of transport and are still being developed (Banister and Hall, 1994). High-Speed Trains (HST) are pointed out to be the new form of traveling for medium distances (i.e., distances below 1000 km) for the new millennium since air travels induce nowadays severe congestion in skies all over the world (Heelis *et al.*, 1999b). Krylov *et al.* (2000) pointed out that trains have a low pollution rate (per passenger) when compared with road vehicles and achieve considerable speeds.

The circulation by means of HST requires high-efficiency railway track systems. According to Burrow and Ghataora (2004) and McElvaney and Snaith (2002), a railway track combines materials (such as the rail, rail pads, sleepers, ballast and subballast) in a structural system designed to resist the combined effects of traffic and climate; and, for a pre-establish period, to provide a subgrade protection and low operational costs, safety and comfort for passengers.

Railway track systems were initially designed by engineers relying on common practice and previous experience. However, since trains are becoming faster and heavier, coupled with the need to minimize costs, a better understanding of the behavior of theses systems and its influence on the subgrade behavior is desirable. Consequently, modern railway design requires a rational approach which combines robust geotechnical knowledge and economic principles. Geotechnical principles are required to ensure that the traffic induces limited stresses, strains and deflections, while the analysis of life-cycle costs and benefits are necessary to assure a cost-effective design (Burrow and Ghataora, 2004).

In order to contribute for a better design methodology, the distinct components of the system should be well understood in terms of its functionability and required properties. This knowledge allows the refinement of future systems, towards becoming more efficient, economic and safe.

1.2. Railway track system

According to Selig and Waters (1994), a railway system (Fig. 1.1) can be divided into groups of components according to their functional purpose, namely: rails (1), pads (2), fastening systems (3), sleepers (4), ballast (5), subballast (6), geosynthetics (7), capping layer (8) and foundation(9). Geosynthetic group may

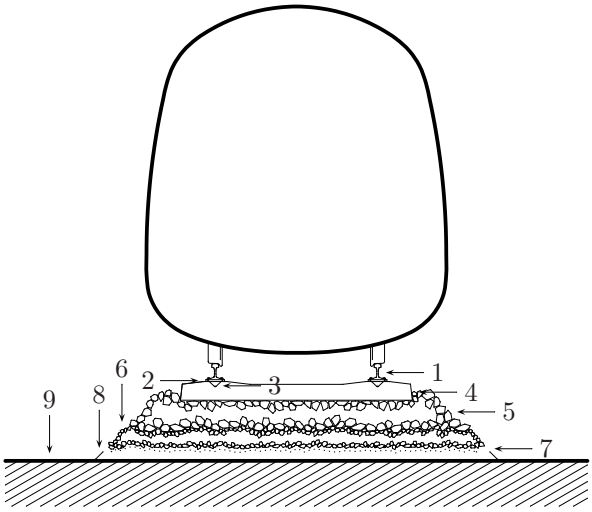

Figure 1.1: Railway components (adapt from Selig and Waters (1994))

exist on other position or not exist at all. These elements are usually regrouped as superstructure (composed of rail, pads, fastening system and sleeper) and substructure (composed of ballast, subballast, capping layer and foundation). The reference to capping layer and foundation as subgrade is also common in the literature. Nevertheless, as pointed out by Brandl (2004), the railway line should be considered as an engineering unit composed of a system of multi-layers comprising all elements from the natural soil up to the rail (or even up to the rail/wheel interaction). The design of this multi-layered HST railway line involves a gradual increase in stiffness from bottom to top. The stiffness of the subsequent layers depends not only on material properties, thickness, and compaction degree but also on the stiffness of the underlying layer. Consequently, the adverse effect of a soft foundation cannot be compensated by a higher compaction of the next layer. The entire system should exhibit an overall stiffness that allows minimum rail displacement (to allow load distribution into several sleepers) but that also limits maximum rail displacement. Ballast, subballast and capping layers should be intensively and uniformly compacted, but without local over-compaction. Conventional spot checking of the compaction degree may be sufficient for maintenance works and for secondary railway lines but it is definitely insufficient for high-speed railway lines. In such cases, the roller-integrated continuous compaction control should become mandatory as it has already been in some countries for several years (Brandl, 2004).

1.3. System components

As mentioned before, the track system is composed of a series of individual elements that, together, produce the load distribution so that low stress levels are applied in the subgrade. In order to allow the track to achieve maximum efficiency, each of these elements must have specific characteristics, described in the following pages.

1.3.1. Rails

The first element here described is the rail which consists of longitudinal steel beams that evenly and continuously guide the train wheels. These elements must have sufficient stiffness to be used as structural beams and to induce load transfer from the wheel to several sleeper supports without excessive deflection between supports. It can also be used as an electrical conductor for signal circuit (each rail being a separate conductor connected by the train axles). Dahlberg (2003) stated that rails used in railway lines result from changes to an I profile where the flanges were converted (by the English engineer Charles Vignoles during 1830s) in order to provide a smooth running surface and allow the transmission of axle loads to the sleeper. The author also referred that high inertia is required in order to transfer the loads to neighbor sleepers without significative deformation of the rail under direct demand. In Europe, the most common section was created by the International Union of Railways and is designed by UIC60 (Fig. 1.2), where 60 refers to the mass of the rail in kilograms per meter (Dahlberg, 2003).

The standard rail length is 25 m, but continuous-welded rails, or longer rails, can be used on the main section to improve ride quality and reduce noise and vibration (Miura *et al.*, 1998). Selig and Waters (1994) reported that two types of rail connections can be employed: bolted joint union and welded union. Bolted joint unions are considered by the authors as good solutions to employ in curves in order to avoid lateral demands due to thermally induced length changes. Esveld (2001) referred that the use of joints prevents the development

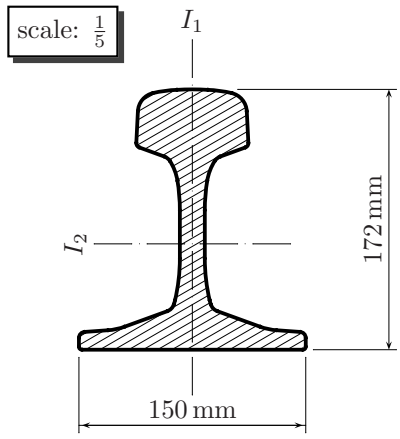

$I_1 = 512.9 \times 10^{-8}\,\mathrm{m}^4$
$I_2 = 3055.0 \times 10^{-8}\,\mathrm{m}^4$
$A = 76.8 \times 10^{-4}\,\mathrm{m}^2$

a) b)

Figure 1.2: (a) Rail section (UIC60) and (b) rail properties

of axial forces and the consequent risk of track buckling at high temperatures. However, the disadvantage of joints relies on the care for maintenance-intensive joints which generate high dynamic loads during train passage. These loads are responsible for many problems such as rapid deterioration of the vertical track geometry, plastic deformation of the rail head, dangerous rail cracks as well as damage to sleepers and fastenings. These problems increase progressively as the speed increases. As a rule, joints have a very important negative effect on the lifespan of all track components and cannot be used for high-speed railway lines.

Concerning welded rail, Selig and Waters (1994) pointed out that its functional efficiency is higher and maintenance cost lower but higher initial investments and difficulties in replacing faulty elements exists. Continuous-welded rails are useful to interrupted vibrations and reduce maintenance costs. Rails can be welded end-to-end using any of four processes (Miura *et al.*, 1998): flash butt, thermit, gas pressure, and enclosed arc. Miura *et al.* (1998) stated that Japan is the only country using the gas pressure process and the enclosed arc in addition to the other two, commonly used in other countries. According to this author, the gas pressure process is less efficient than the flash butt process, but it is widely used for both factory and track-side welding because the equipment is easily portable and joint quality is as good as that of flash butt process. Continuous welded rails do not, however, have only advantages (Esveld, 2001). Temperature stresses are especially responsible for failure of welds with small imperfections at low temperatures. On the other hand, lateral stability should be sufficiently high to resist compression forces developing at temperatures above the neutral temperature of 25°C, as buckling may otherwise occur. The principle of this phenomenon is sketched in Figure 1.3 showing the compressive forces and the resistance forces on the track and the resulting typical buckling shape. To avoid this phenomenon, reinforcements by means of fastening systems, sleepers and ballast are used (Miura *et al.*, 1998).

In design, the distance between the inside faces of a rail head, designated as rail gage, should be carefully chosen since distinct values are found from country to country and, sometimes, even inside a same country (Selig and Waters, 1994). For an international railway line, this simple detail achieves high importance. Finally, Brandl (2004) mentioned that the fatigue strength of rails drops during the long-term period to about 2/3 of their initial strength due to corrosion and wear, consequently reducing the resisting moment of the rail profile, thus increasing displacements.

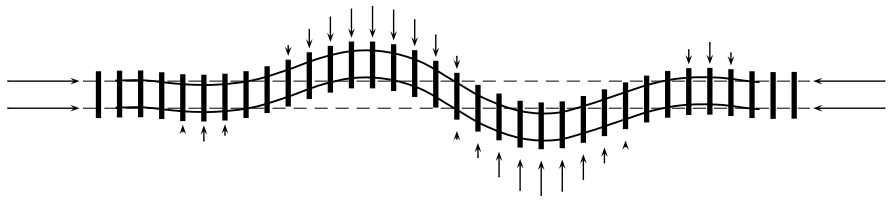

Figure 1.3: General buckling effect (Esveld, 2001)

1.3.2. Pads

The second element here described is the pad. Dahlberg (2003) referred that the pad consists of a rubber element to be placed between rails and concrete sleepers in order to protect sleepers from wear impact loads, to filter vibrations and to allow rail deformations. These elements perform an important role since its lower stiffness allows the rail to deform itself and, by this mechanism, to distribute loading over several sleepers. Ilias (1999) pointed out that a soft pad has less damping than a stiff one. Rubber pads (Fig. 1.4) are used with concrete sleeper to fulfill the following functions (Selig and Waters, 1994):

1. provide resiliency for the rail/sleeper system;
2. provide damping of wheel-induced vibrations;
3. prevent or reduce rail/sleeper contact friction;
4. provide electrical insulation for the track signal circuits.

Regarding wood sleepers, Selig and Waters (1994) referred that these consist of steel plates placed under the rail to distribute the rail force over the wood surface. These elements provide suitable bearing pressure for the wood and protect it from mechanical wear. The authors referred that, if the sleeper plate size is inadequate for the rail loading, the resulting pressure may exceed the compressive strength of the wood fiber and thus cause accelerated plate cutting and premature deterioration of the sleeper.

1.3.3. Fastening systems

The next element to be described is the fastening system whose main function consists of retaining the rail against the sleeper and avoiding vertical, lateral and longitudinal overturning movements of rail (Selig and Waters, 1994). According to Esveld (2001), the introduction of continuous-welded rails gave rise to the need for fastenings with greater elasticity, and in the case of concrete sleepers, which are prone to impacts, this is certainly an indispensable requirement. In early days, dog spikes or other simple devices were used to fasten the rail to wood sleepers. After the introduction of concrete sleepers, the spikes were replaced

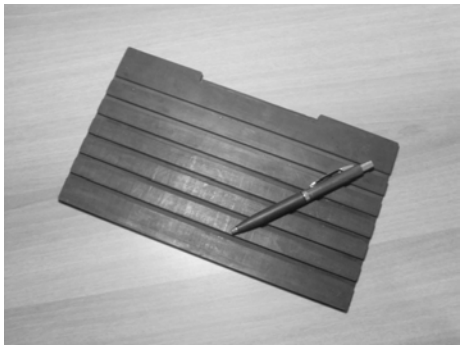

Figure 1.4: Rubber pad

by double elastic fastenings in which the rail is fastened by a spring and a rubber pad (concrete sleeper) or steel plates (wood sleepers) between the rail and the sleeper (Miura *et al.*, 1998). Rail fastening distribute loads and dampen vibrations and are an essential component in high-speed train operation. There are many types of fastening systems, namely: Nabla clip, Pandrol clip, Pandrol fastclip and Vossloh clip. Figure 1.5 illustrates these four fastening systems.

1.3.4. Sleepers

Regarding sleeper elements (or cross ties), the two most common types are wood and prestressed/reinforced concrete (Selig and Waters, 1994), concrete sleepers being heavier than wood sleepers and presenting a much more secure fastening system than wood sleepers. On the other hand, concrete sleepers are more difficult to handle than wood sleepers, and require pads to provide sufficient resiliency. Miura *et al.* (1998) referred that concrete sleepers, introduced in the early 1950s, are used on most lines today due to their longer lifespan and greater track stability. These elements can be monoblock or twin-block type (Fig. 1.6).

Although wood sleepers have good elasticity and are lighter and easier to handle than concrete sleepers, their main drawback is a short lifespan due to deterioration. Miura *et al.* (1998) referred that synthetic sleepers made of hard polyurethane foam and glass fiber are used in Japan, and were designed for long lifespan (more than 60 years) while maintaining the physical properties of wood sleepers. These were mainly developed for applications on steel girder bridges, switches and other sections where maintenance or replacement is difficult.

Summing up, the main purpose of the sleeper is to guarantee correct leveling and alignment of the rail and to contribute to a better distribution in the ballast

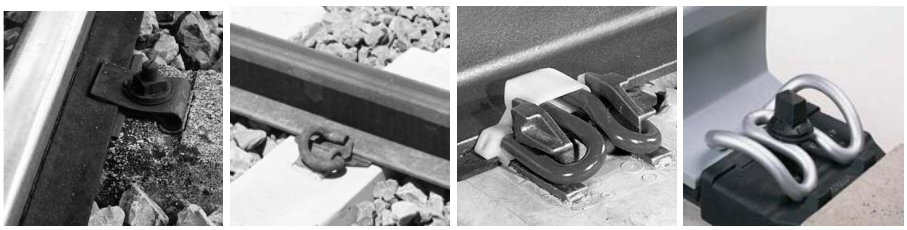

Figure 1.5: a) Nabla clip, b) Pandrol clip, c) Pandrol fastclip, and d) Vossloh clip

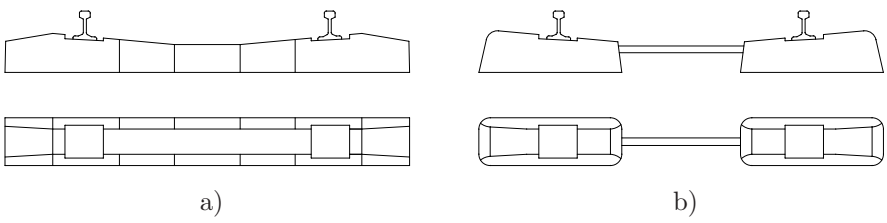

Figure 1.6: a) Monoblock and b) twin-block concrete sleeper

layer (Dahlberg, 2003). Selig and Waters (1994) referred the following as main functions:

1. receive the load from the rail and distribute it over the supporting ballast at an acceptable ballast pressure level;
2. hold the fastening system to maintain the proper track gage;
3. restrain the lateral, longitudinal and vertical rail movement by anchorage of the superstructure in the ballast.

1.3.5. Ballast

This highly-compacted layer, is composed of granular materials, evenly graded with angular shape and is produced from granite or limestone (Dahlberg, 2003). According to Selig and Waters (1994) it should be constructed from materials unaffected by frost. It should inhibit vegetation growth, absorb airborne noise, reduce pressure from sleepers to acceptable stress levels, provide drainage, facilitate maintenance surfacing and lining operations of sleepers, provide resiliency to absorb track energy, possess large voids to accommodate fouling material and resist to train excitations. To do that the authors referred that ideal mechanical properties of the ballast result from a combination of the physical properties of the individual ballast material and its *in situ* physical state. The physical state is defined by the in-place density, while the physical properties of the material are described by various indices such as particle size, shape, angularity, hardness, surface texture and durability. The initial unit weight is usually created by maintenance tamping, together with mechanical compaction.

Usually, only crushed rock or slag is used for rail track ballast. However, in areas of the world where it is difficult or too expensive to obtain such material, rounded coarse river gravel is used. From road engineering, it is well known that even a small change in angularity or surface roughness has a determinant effect on the stress-strain behavior of granular materials, even if the angularity (sharpness of corners) of the ballast leads to undesirable stress concentrations and heterogeneous stress distributions (Lu and McDowell, 2008). Indraratna *et al.* (2005) showed that most ballast degradation cannot be attributed to particle splitting, but it is instead primarily the consequence of corner breakage. Small amounts of rounded particles worsen the performance of rail track ballast (Brandl, 2004). This was confirmed by systematic test series performed by Raymond (2000), which demonstrated that even a very small percentage (by weight) of rounded aggregate added to the crushed aggregate causes a rapid drop in the ultimate bearing capacity (Fig. 1.7). This author performed tests on a 75 mm wide footing resting on materials with different crushing percentages but identical gradation, submitted to a repetitive loading of 100 kPa.

Lim (2004) referred that under traffic loading, the stresses in the ballast are sufficient to cause significant particle breakage. According to Selig and Waters (1994), stresses results from:

1. mechanical particle degradation during construction and maintenance, and under traffic loading;
2. chemical and mechanical weathering degradation resulting from environmental changes;

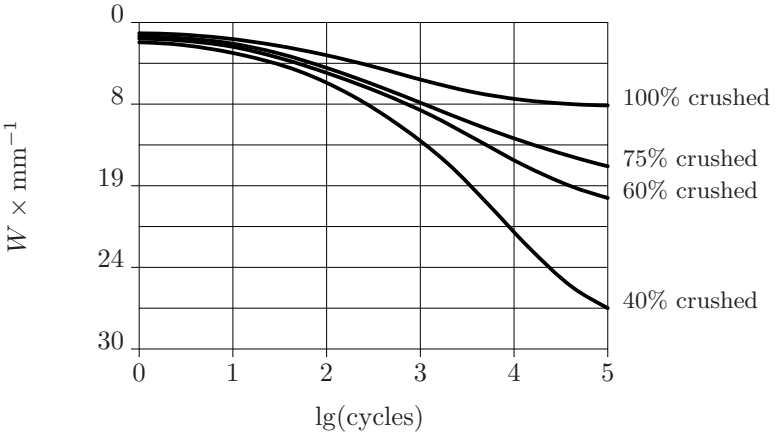

Figure 1.7: Effect of crushed particles on the static bearing capacity of the ballast (Raymond, 2000)

3. migration of fine particles from the surface and underlying layers.

This effect causes track settlement and therefore the track geometry will need to be restored by tamping. However, tamping causes further ballast breakdown. This maintenance cycle will eventually lead to the loss of strength and stiffness in the ballast, when fine material generated from ballast breakdown reaches a critical level and when the water fails to drain properly from the ballast. At this stage, the track needs to be maintained either by ballast cleaning or ballast renewal. Thus, it is important to use good quality ballast material in order to increase ballast life on the track and reduce waste ballast generated from ballast cleaning or ballast renewal. Ballast is the only track component used for external constraint of the superstructure and is also used for providing a fast and economical method of restoring track geometry (tamping).

Selig and Boucher (1990) referred that conventional ballast abrasion tests, such as the wet friction value, Los Angeles abrasion, and Micro-Deval friction, produce conflicting results and often fail to represent actual field performance. Furthermore, these tests involve revolving particles in a cylinder or drum to measure degradation, being the mechanics different from those beneath the railway track during traffic loading. Nevertheless, these tests are still considered as the best and most important indicators of ballast performance in service. Lim (2004) referred to another test, the aggregate crushing value test. However, since the test is performed on the small ballast particles (10 mm $\sim$ 14 mm), instead of normal sizes used in the ballast (28 mm $\sim$ 50 mm), it may also be considered inappropriate. A research performed by McDowell and Amon (2000) showed that the strength of soil particles varies according to size, and larger soil particles tend to have a lower average tensile strength compared to smaller particles. For this reason, aggregate crushing value will be uncertain.

To conclude, it should be noticed that even if ballasted tracks are the most common technology for railway construction, alternatives are available, namely by mean of slab-tracks. About 40 years ago, European railway engineers in countries with advanced railway technology were examining car and track systems for trains running at speed over 200 km h^{-1} to determine if it was possible

to repair the ballast frequently enough before it was loosened by the severe impact of the High-Speed Train operation (Miura *et al.*, 1998). Some countries (e.g., France) adopted the ballasted tracks, meanwhile others (e.g., Japan) decided to use slab-tracks. Railway lines without ballast (slab-tracks) were initially used in bridges and in tunnels but with the increasing requirements on the track bed of HST railway lines, this technique has been sometimes used along entire railway networks. A slab-track means a reinforced concrete slab laid on a viaduct or another rugged bed, and secured to the bed using cement asphalt (Fig. 1.8). According to the disposition of the rails and sleepers, it can present five typologies: embedded rail, resilient baseplate, booted sleeper, cast-in sleeper and floating slab. Miura *et al.* (1998) referred a 1990 comparison of the economic advantages of ballast and slab-tracks on the Tohoku Shinkansen train showing that slab-track cost 1.3 times more than ballasted tracks (in tunnels). Nevertheless, this difference is balanced out after about 9 years due to the lower maintenance costs of slab-tracks. Since slab-tracks are lighter than ballasted tracks as a whole, the construction cost of a new railway based on slab-tracks, including viaduct and tunnel sections, becomes lower. A more recent study, published by Brandl (2004), referred that the economical advantage of this system lies on low maintenance costs. However, since ballast maintaining has become more sophisticated during the past years, structures without ballast are actually only economical if their construction costs exceed those of ballast tracks by no more than about 30 % to 40 %. Esveld (2001) referred that recent applications tend more and more towards non-ballasted track due to low maintenance, high availability, low structure height and low weight. This author concluded that when designing the railway lines, factors like life-cycle cost, construction time, availability and durability play an increasingly important role and in this point non-ballasted track concepts offer good opportunities.

1.3.6. Subballast

Dahlberg (2003) referred that the subballast layer is used to prevent mixtures of the large particles from the ballast with the small ones existing in the capping layer. The possibility of using any sand or gravel to fill this layer is also pointed out, if frost insensitivity and drainage are ensured. Selig and Waters (1994)

Figure 1.8: Slab-track

indicated that this layer should prevent subgrade friction with ballast (which in the presence of water leads to slurry formation) and reduce induced stress in the subgrade to acceptable levels. Brandl (2004) referred that granular subballast should present sufficient resistance to weather conditions and to grain crushing. Grain crushing and friction/abrasion already occurs during compaction at the construction site and may continue due to the long-term influence of heavy dynamic traffic. Therefore, the soil (or other granular material) has to undergo suitability tests (Brandl, 2001).

In this way, Selig and Waters (1994) pointed out that the most common and suitable subballast materials are broadly-graded naturally occurring or processed sand-gravel mixtures, or broadly-graded crushed natural aggregates or slags. In some cases, improvements are required by means of stabilization (with lime, cement or asphalt), asphalt concrete layers or geosynthetics. According to Brandl (2004), grain size curves (Fig. 1.9) similar to the parabolic shape of the Fuller curve have proved to be more suitable as they can be easily compacted and exhibit minimum grain crushing or friction.

The bearing capacity and stiffness of subballast change seasonally, especially in areas where intensive freezing periods and numerous freezing-thawing cycles occur. According to Brandl (2004), laboratory tests and long-term *in situ* observations of roads and highways show a seasonal loss in bearing capacity of about 30 % to 60 % in relation to the maximum value (Fig. 1.10) even for non-frost susceptible bases. Consequently, in zones exposed to temporary frost periods, the subballast must exhibit not only proper bearing-deformation properties but also sufficient freezing-thawing resistance. Brandl (2001) referred that freezing-thawing resistance tests are only necessary for completely unknown materials or for bound layers and can be estimated by means of the mineral criterion. According to this author, the use of bound subballast layers (with cement or asphalt stabilization) can be used as a solution for the bearing capacity reduction since it show significantly less seasonal fluctuation than unbound soil or other granular material. Soil stabilization with cement needs careful post-treatment as it presents brittle behavior, undergoes reflective cracking and suffers long-term

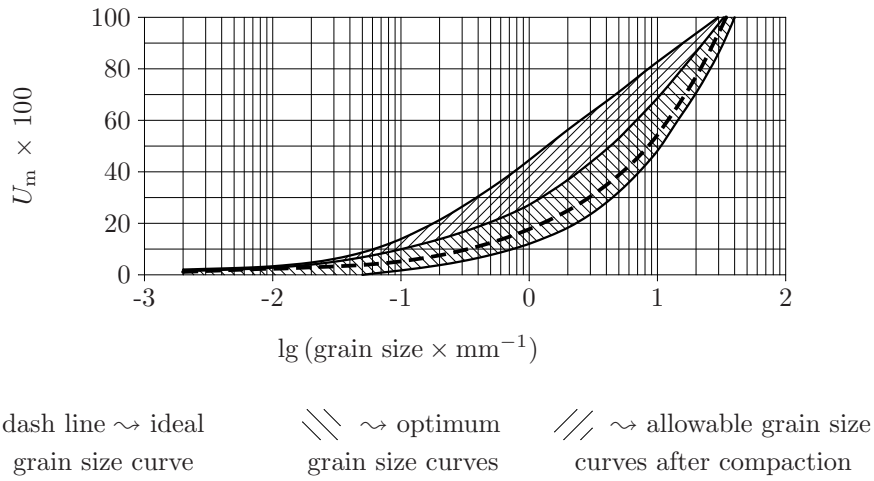

Figure 1.9: Optimum grain size curves (Brandl, 2004)

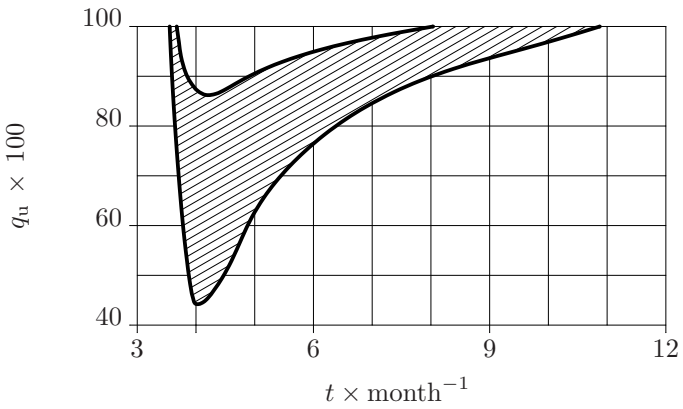

Figure 1.10: Seasonal fluctuation of the bearing capacity (given as a ratio percentage) of unbound road layers (Brandl, 2004)

fatigue under permanent load-cycling. Its *in situ* stiffness cannot be regulated during construction as precisely as for asphaltic layers. Asphaltic layers are therefore better than cement stabilization, at least for conventional rail tracks with ballast (Brandl, 2004).

According to Brandl (2004), the thickness of subballast layer for high-speed railway lines should be $d \geqslant 0.5\,\text{m}$ (for Central Europe countries $d \geqslant 1\,\text{m}$) and deformability modulus given by plate test (corresponding to reload cycle) should be between 120 MPa and 200 MPa.

1.3.7. Geosynthetics

Geosynthetics can be divided in three main groups, namely: geotextiles, geogrids and geomembranes. Geotextiles are permeable materials that guarantee the separation of layers, retention of the fines fraction, permeability in the geotextile plan (if its thickness allows it) and reinforcement. Geomembranes prevent percolation, ensure layer separation and should not be used as reinforcement. Finally, geogrids are used only for reinforcement.

Geosynthetics materials can be used to contribute, together with subballast, in the prevention of particles intermixing between different layers. They also improve drainage and can be used to reinforce soil with insufficient mechanical strength (Selig and Waters, 1994). This reinforcement of the structure makes possible a thickness reduction of the subballast, as long as freezing-thawing intensity, hydrological conditions and train speed are conveniently taken into consideration. However, Brandl (2004) pointed out that such a substitute should be limited to upgrading and renovation of old railway lines. It should not be performed for new railway lines, specially not for high-speed railway lines. This is due to the fact that geosynthetics cannot prevent frost heaves and only reduce the adverse effects of thawing.

Getting good aggregate material which needs design specification can sometimes be difficult, just because it involves long transport distances. Due to that, geosynthetics are a cost-effective alternative. The combined use of soil (good in compression and poor in tension) with a geosynthetics (good in tension and poor in compression) allows efficient soil reinforcement (Selig and Waters,

1994; Jamiolkowski *et al.*, 1999; Wu, 2003; Duncan-Williams and Attoh-Okine, 2008). Geosynthetics have proved to be a suitable reinforcement for all layers, i.e., from the embankment to the ballast layer, since their inclusion improves interlocking at the interface and consequently reduces the lateral spread of the soil (Duncan-Williams and Attoh-Okine, 2008). According to Brown *et al.* (2007), this reinforcement is higher if the foundation stiffness is low. Jamiolkowski *et al.* (1999) has studied the influence of a geogrid layer on top of the subballast layer (0.3 m bellow the sleeper) and found that the induced stress 0.9 m below the sleeper is reduced by 15 % to 20 % (Fig. 1.11). Brown *et al.* (2007) performed studies of ballast layer reinforced with geogrids and detected that the transient wheel loading is unlikely to be enhanced by the presence of geogrid reinforcement.

Montanelli and Recalcati (2003) referred that geogrid reinforcement functions can be summarized in five groups, namely:

1. create a stiff platform where horizontal shear strains and vertical settlements are controlled and minimized;
2. increase the bearing capacity and the load distribution by enlarging the foundation slip failure line, thus reducing vertical stresses;
3. increase the fill soil stiffness by enhancing the soil compaction, providing inner tensile strength and an apparent long-term cohesion of the fill soil even under high dynamic loads approaching the critical speed;
4. increase the damping efficiency of the embankment filling thus allowing higher railway speed;
5. reinforce, filter and separate soil components.

The same authors referred that the design of the structure reinforced with geosynthetics requires the consideration of a large number of factors, namely: type of reinforcement, number of reinforcing layers, depth below the ballast of the first reinforcement layer, spacing between reinforcing layers, dimensions of the reinforcement and type and placement of the fill.

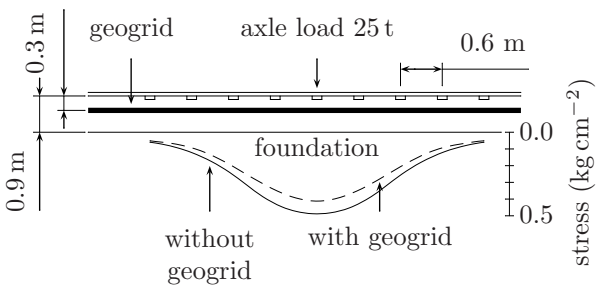

Figure 1.11: Settlement reduction induced by geogrid inclusion (Jamiolkowski *et al.*, 1999)

1.3.8. Capping layer

The capping layer is the platform on which the track structure is built and it should provide a stable foundation for the subballast and ballast layers. The range of stiffness of the capping layers stiffness range is believed to influence ballast, rail and sleeper deterioration. According to Selig and Waters (1994), the influence of the traffic induced stresses extends downwards as much as 5 meters below the bottom of the sleepers.

The subgrade may be divided into two categories: natural ground or placed soil. Selig and Waters (1994) indicated that soils other than those existing locally are generally expensive to use as capping layer. If natural mechanical properties are not satisfactory, stabilizations with lime or cement must be applied. The authors also referred that, due to impossibility of maintenance operations after construction, this layer constitutes the most important cause of track failure. Placed soil is used either to replace the upper section of unsuitable existing ground or to raise the platform to the required height for the rest of the track structure.

Selig and Waters (1994) indicated that the capping layer should not present the following failure modes:

1. excessive progressive settlement from repeated traffic loading;
2. consolidation settlement and massive shear failure under the combined weights of the train, track structure, and earth;
3. progressive shear failure from repeated wheel loading;
4. significant volume change (swelling and shrinking) from moisture change;
5. frost heave and thaw softening.

1.3.9. Foundation

The foundation is the last component of the structure and one of the least controllable. According to Heelis *et al.* (1999a), the foundation consists of a multi-layer in which the stiffness is highly dependent on the most flexible layer and, hence, the stiffness of ballast and subballast effect become secondary when compared to the influence of soft layers. Brandl (2004) pointed out that the foundation has a substantial influence on the geometry (settlement, lateral displacement) of the rails, especially in the case of very soft and heterogeneous ground and low embankments. This author recommends that slab rail tracks should not be constructed on such ground unless it was previously improved (by stabilization) or deep foundation elements were installed. To assess the long-term settlement behavior of soft foundations, oedometric tests can be used, which should clearly show a possible creeping tendency. To allow construction on these materials the author suggested the use of piled embankments while bearing in mind that a great number of heavy load-cycles may cause cumulative settlements at long-term. This occurs mainly with floating piles and less with end-bearing piles.

In matters of vertical displacement, Brandl (2004) referred that these may be caused by foundation consolidation, compaction under traffic, freezing-thawing action, swelling and shrinkage from moisture charge and by shear displacement.

1.4. Railway design behavior

As previously mentioned, the function of the railway system is to distribute the highly concentrated load at rail level to admissible low stresses at foundation level. In order to do so, Brandl (2004) pointed out that the reversible deflection of the ballast and subballast is an essential characteristic of the conventional railway track structure. Its deformability facilitates the load distribution from the rail to a higher number of sleepers. Consequently, stiff ballast and subballast layers cause higher stress concentrations, hence an increased grain friction/abrasion. This fact, in turn, gradually creates different local stiffnesses, hence differential rail deformations under traffic loads. These differential rail deflections cause an adverse rearrangement of the dynamic wheel forces which, in the end, progressively worsen the rail geometry, thus accelerating wheel/rail and rail/sleeper wear.

In this context, an efficient design should limit the maximum level of vertical and horizontal deformations, so that irreversible strains do not become uncontrollable, but at the same time assure a minimum deformation so that load distribution is made possible.

1.4.1. Vertical reversible deflection

According to Brandl (2004), in an ideal railway structure, rail deflection should be between an allowable upper and lower limit, being these limits a function of rail support, axle loads and train speed. This author referred that experience has shown that the elastic rail deflection W_e under a load of about 200 kN moving at a constant speed C should be in the range of:

$$W_\mathrm{e} \in \begin{cases} [1.0\,\mathrm{mm}, 2.2\,\mathrm{mm}] & : \quad C \leq 160\,\mathrm{km\,h^{-1}} \\ [1.5\,\mathrm{mm}, 2.0\,\mathrm{mm}] & : \quad C > 160\,\mathrm{km\,h^{-1}} \end{cases} \tag{1.1}$$

in order to avoid problems in rail geometry and wheel/rail/sleeper system. Moreover, too small deflection has an adverse effect on the load distribution, since less support sleepers contribute to the load transfer. In the case of very stiff ballast and subballast layers, the elastic deformations of the rail result only from the rail itself and its fixing system. *In situ* measurements have revealed that the elastic rail deflections decrease with increasing speed and, therefore, the allowable minimum values of W_e should be higher for High-Speed Trains (Brandl, 2004).

1.4.2. Vertical cumulative deflection

The elastic rail deflection widely depends on the resilient modulus of the entire structure (superstructure and substructure) and both can only be determined by *in situ* measurements since the individual layers interact with each other. Also cumulative deflection cannot be estimated by adding settlements of the individual layers. This is a direct consequence of the resilient moduli dependency on the stiffness of adjacent layers. Several national regulations limit the allowable cumulative deflections of railway embankments, being the less strict values for railway lines with a ballast layer (such a structure allows easy maintenance). Brandl (2004) referred that cumulative deflections W_p after construction of about 10 cm to 30 cm are considered acceptable, although re-leveling

and ballast tamping should be implemented at earlier stages of deformation. On the other hand, slab-tracks can suffer only very small (differential) settlements since re-leveling is extremely costly. According to Brandl (2004), the allowable cumulative rail deflection W_p should be limited as follows:

$$W_\mathrm{p} \in \begin{cases} [0.0\,\mathrm{mm}, 60.0\,\mathrm{mm}] & : \quad C \leq 160\,\mathrm{km\,h^{-1}} \\ [0.0\,\mathrm{mm}, 30.0\,\mathrm{mm}] & : \quad C > 160\,\mathrm{km\,h^{-1}} \end{cases} \tag{1.2}$$

Settlement limitation should also be applied to cumulative differential deflections along and between the rails. In the case of differential deflections between rail W_pd, Brandl (2004) indicated that these should be smaller than 3 mm.

1.4.3. Horizontal reversible deflection

Brandl (2004) pointed out that horizontal movements U_e and V_e can be induced by movements of the railway track if the construction is performed over an unstable slope, by differential settlements or spreading of the embankment or by high lateral forces along a curved alignment combined with low horizontal stiffness of the subballast, subgrade and/or the underlying layers. It can also be due to the 'wave' motion of the boogie, a necessary characteristic for ride comfort.

So, in order to limit wheel/rail and rail/sleeper wear and increase the allowable train speed, the author suggest that the horizontal displacements should be limited to:

$$\sqrt{U_\mathrm{e}^2 + V_\mathrm{e}^2} \in \begin{cases} [10.0\,\mathrm{mm}, 20.0\,\mathrm{mm}] & : \quad C \leq 160\,\mathrm{km\,h^{-1}} \\ [2.0\,\mathrm{mm}, 5.0\,\mathrm{mm}] & : \quad C > 160\,\mathrm{km\,h^{-1}} \end{cases} \tag{1.3}$$

Horizontal cumulative deflection also exists and its limit must be attended. However, since the vertical deflection is dominant and controls global behavior, horizontal movements will not be further studied.

1.5. Dynamic concepts of the moving load

Once the diverse components of the railway system and its ideal global behavior (in terms of deformation) are known, one should pay attention to an important fact: the excitation is not static and energy propagation exists and should be considered during design. In fact, loads moving along half spaces induce dynamic effects of great importance for the compaction of railway infrastructures. Numerical simulation, *in situ* testing and laboratory work should analyze these concepts. In this context, the propagation of energy waves, energy dissipation and particular moving load speeds in numerical models must be detailed.

1.5.1. Energy wave

Energy propagation has to be considered in dynamic analyzes of railways since trains are able to move as fast as energy waves, and consequently can induce high dynamic loads. To do so, the discretization of the layers is usually performed so that the theory of continuum medium mechanics can be applied. This mathematical tool requires, however, special attention since the material used in ballast and subballast exhibit large dimensions when compared to the

thickness of the layer. For this reason, the existence of an elementary volume representative of these layers is questionable. Alternatively, discrete elements could be used (topic detailed on page 23) but attending nowadays computational capacities.

Energy travels through soil in the form of body waves and surface waves (Kramer, 1996). The first ones can be subdivided into two groups: compression or primary waves (currently referred to as p-waves) and shear or secondary waves (currently referred to as s-waves). Primary waves origin particle displacements parallel to wave propagation direction; meanwhile, secondary waves originate perpendicular displacements to wave direction. Surface waves result from the interaction of body and surface waves and can also be divided into two major groups, Rayleigh and Love waves, respectively. The first one (Rayleigh) is composed of the vertical component of displacements introduced by s-waves together with the ones introduced by p-waves and originates elliptical anticlockwise movements at the surface. Love waves are composed only by the horizontal component of displacement introduced by s-waves.

The Equation of motion for an elastic, linear and isotropic solid can be written in terms of displacements (if Hooke's law is considered) for a generic direction as (Kramer, 1996):

$$\rho \frac{\partial^2 U}{\partial t^2} = (\Lambda + \mu) \frac{\partial \varepsilon}{\partial x} + \mu \nabla^2 U \tag{1.4}$$

where ∇^2 is the Laplacian operator, ε is the volumetric strain, and μ and Λ are Lamé's constants.

The solution of a system defined by the three equations of motion (one for each orthogonal directions) is composed of the velocities of primary and secondary waves. This pair of velocities C_p (for p-wave) and C_s (for s-wave) is presented in Equations 1.5 and 1.6.

$$C_\mathrm{p} = \sqrt{\frac{G(2-2\nu)}{\rho(1-2\nu)}} \tag{1.5}$$

$$C_\mathrm{s} = \sqrt{\frac{G}{\rho}} \tag{1.6}$$

where G is the shear modulus, ν is the Poisson's ratio and ρ is the mass density of the medium.

Equations 1.5 and 1.6 enable to conclude that s-wave velocity will always be smaller than the p-wave velocity and that soils with very low compressibility (Poisson's ratio near 0.5) will present extremely high p-waves velocities.

1.5.2. Energy dissipation

The energy transmitted along the soil as energy wave is dissipated by two distinct mechanisms (Kramer, 1996). The first one, designated as radiation damping, is due to the infinite dimension of foundation surface while the second mechanism, known as damping, is due to energy conversion into heat by friction between the particles. In radiation damping, energy distributes itself by a perimeter growing, from a center point, through radiation.

The mechanism of energy dissipation by damping is introduced in mathematical models generally by the form of Kelvin-Voigt solid. In this element shear stress is composed of two forces: a proportional reaction to displacement (idealized as an elastic linear spring) and a viscous damper proportional to frequency. Since the Kevin-Voigt solid presents shear resistance proportional to frequency, the model is defined as viscous. However, real soils dissipate energy through slippage of grains with respect to each other and by that reason independently of frequency ω. In order to remove this specificity it is necessary to introduce a new parameter ξ written as a function of frequency inverse. Clough and Penzien (1993) defined ξ as the ratio between damping of the system and the smallest amount of damping (referred as c_{c}) for which no oscillation occurs in free vibration response. This new parameter allows the definition of the fundamental equation of dynamics in frequency domain (Eq. 1.7) as a hysteretically damped discreet system, i.e., equally damped independently of frequency.

$$\left(-m\omega^2 + i\omega\frac{2k_{\mathrm{s}}\xi}{\omega} + k_{\mathrm{s}}\right)\cdot U(\omega) = P(\omega) \tag{1.7}$$

where m is the mass, ω is the circular speed, and k_{s} is the soil/spring stiffness.

The value of ξ can be obtained supposing a single degree of freedom system submitted to an imposed harmonic distortion in which the shear stiffness is given by:

$$\tau = k_{\mathrm{s}}\gamma_{\mathrm{e}}\sin(\omega t) + \omega c\gamma_{\mathrm{e}}\cos(\omega t) \tag{1.8}$$

where τ is the shear stress, γ_{e} is the elastic shear strain, t is the time and c is the damping.

Assuming that sinusoidal excitations originate elliptical answers (Fig. 1.12) and that the energy dissipated during one cycle will be given by its area (referred as Ψ), it is possible to write:

$$\Psi = \int_{t_0}^{t_0+\frac{2\pi}{\omega}} \frac{\tau\partial\gamma}{\partial t}\partial t = \pi c\omega\gamma_{\mathrm{e}}^2 \tag{1.9}$$

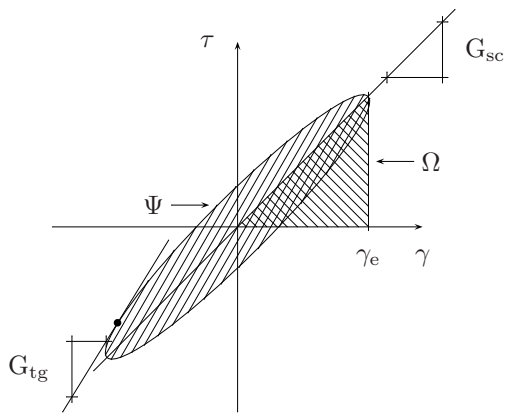

Figure 1.12: Stress-strain behavior induced by viscous damping

Peak energy stored in one cycle is given by the triangular area (referred as Ω) and can be expressed as:

$$\Omega = \frac{k_s \gamma_e^2}{2} \tag{1.10}$$

Assuming that the equation, in time domain (Eq. 1.11), that rules the response of an undercritically damped system is an homogeneous linear differential equation with conjugated unrepeated roots, the generic solution can be written as presented in Equation 1.12, with A_1 and A_2 parameters to be defined according to the initial conditions ($U(t=0) = U_0$ and $\dot{U}(t=0) = V_0$). Parameters a and b are real numbers obtained from the characteristic equation (Eq. 1.13) of Equation 1.12.

$$m\frac{\mathrm{d}^2U(t)}{\mathrm{d}t^2} + c\frac{\mathrm{d}U(t)}{\mathrm{d}t} + k_\mathrm{s}U(t) = 0 \tag{1.11}$$

$$U(t) = (A_1 \cos(bt) + A_2 \sin(bt))\,\mathrm{e}^{at} \tag{1.12}$$

$$ms^2 + cs + k_\mathrm{s} = 0 \tag{1.13}$$

Critical damping is reached when the imaginary components of roots s (Eq. 1.14) are equal to zero. That is achieved when damping cancels the radical in Equation 1.14, providing $c_\mathrm{c} = (4mk_\mathrm{s})^{0.5}$. Taking into account that $\omega^2 = k_\mathrm{s}m^{-1}$ one can define $c_\mathrm{c} = 2m\omega$.

$$s = -\frac{c}{2m} \pm \frac{\sqrt{c^2 - 4mk_\mathrm{s}}}{2m} \tag{1.14}$$

In order to determine the value of the damping ratio ξ recalling results from Equations 1.9 and 1.10, and since $\xi = c\,c_\mathrm{c}^{-1}$, it becomes necessary to calculate an auxiliary variable α. Its value is evaluated in Equation 1.15, which results on the relation given in Equation 1.16.

$$\xi = \frac{c}{cc} = \frac{c}{2m\omega} = \alpha\frac{\Psi}{\Omega} = \alpha\frac{\pi c\omega\gamma_e^2}{\frac{k_s\gamma_e^2}{2}} \Leftrightarrow \alpha = \frac{1}{4\pi} \tag{1.15}$$

$$\xi = \frac{\Psi}{4\pi\Omega} \tag{1.16}$$

1.5.3. Particular speeds of the moving load

Regarding the particular speeds of the moving load, there are two wave velocities that should be considered when modeling a load moving on a half space: the velocity of the Rayleigh surface waves and the minimum phase velocity of bending waves propagating in the foundation surface (this one usually refereed as critical speed) (Krylov *et al.*, 2000).

Krylov *et al.* (2000) showed that Trans-Rayleigh (i.e., a train that moves at a higher speed than Rayleigh wave velocity) induces ground vibration that propagate almost in the same direction producing a vibration boom and resulting in large deflections. It is also referred that critical speed results in a further

increase but not as drastic as the one described before. This deflection amplitudes may result in train derailment and it is limited by the damping of the railway system. Critical speed C_{cr} (Heelis *et al.*, 1999a; Krylov *et al.*, 2000) can be obtained through:

$$C_{\mathrm{cr}} = \sqrt[4]{\frac{4k_{\mathrm{s}}EI}{m^2}} \tag{1.17}$$

where E is the deformability modulus of the beam, I the inertia of the beam, m the mass per unit length of the beam and k_{s} is the stiffness of the foundation.

Even if simplified, Equation 1.17 is quite interesting as it is able to show that critical speed is enlarged by the increasing Winkler stiffness k_{s} of the foundation, increasing flexural stiffness of the rail EI or by reducing the mass per unit length m of the beam .

1.6. Testing

Railway maintenance costs can and should be reduced by efficient design systems. To do so, precise characterization of the reversible and irreversible mechanical properties of the geomaterials of all layers is fundamental. The rational design approach was divided by Burrow and Ghataora (2004) into two main processes. In the first one, stresses, strains and deflections of the applied loading should be measured so that the stress/strain distribution in the substructure can be formulated from a numerical model of the track system. Such a model requires the characterization of the track system in terms of engineering parameters by means of reliable testing. In the second process, it is necessary to determine the mechanisms causing the track support system to deteriorate over time. By setting limits to the amount of deterioration through serviceability requirements, allowable stresses, strains and deflections may be established.

According to Lu and McDowell (2008), the monotonic triaxial test is one of the most important laboratory tests for the investigation of the mechanical behavior of railway ballast since it provides an efficient way to study the stress-strain relation behavior and degradation characteristics. For the case of cyclic triaxial testing, irreversible behavior can also be correctly quantified. Regarding the foundation, and for the case of water-sensitive materials, oedometric tests are also required for a complete characterization. A major limitation is the reduced number of triaxial apparatuses able of characterizing geomaterials with large dimensions (e.g. ballast).

Burrow and Ghataora (2004) indicated that when defining triaxial test procedures, one should bear in mind that the forces applied to the track by moving vehicles are a combination of a static load and a dynamic component, often formulated from empirical models. In fact, during the design period the loads applied to the track system vary in magnitude, frequency and configuration. Consequently, in order to be able to establish the cumulative effect of traffic loading on the performance of the track, it is necessary to characterize the applied loading spectra. This is a potentially complex process and future methods may incorporate statistical techniques to quantify the loading spectra. Also, shear stress is not reproduced in triaxial tests, even if in-phase variation of deviatoric stress and chamber confining pressure is assured. For that, Powrie *et al.* (2007) carried out 3D numerical analyzes to identify the stress paths followed

by elements of soils in the sub-base below railway tracks, and discussed how these could be represented in the laboratory hollow cylinder apparatus.

1.7. Modeling

The understanding of the different track components, the definition of deformation limits, the consideration of dynamic effects and the precise characterization in the laboratory are fundamental and are here presented with a single purpose: the correct numerical formulation of models with load moving along an elastic/plastic half-space. This numerical simulation can focus on the quantification of stress/strain evolution during traffic and can be useful to quantify long-term behavior, by means of numerical or laboratory techniques.

For the simulation, one should consider the model simplifications and the choice of numerical techniques. Several simplifications can be made and distinct numerical techniques, with distinct advantages and disadvantages, can be used.

1.7.1. Simplifications

As a starting point it should be noticed that numerical simulations always require simplifications. This fact is always present and it must be performed with caution so that important aspects are not removed from the model. Several particularities related with railway lines models have been studied and their influence has been analyzed. For instance, Hildebrand (2001) referred that since the rotational stiffness of the pad is much smaller than its translational stiffness, it can be disregarded. The author also pointed out that the variation of the stiffness of the sleeper does not have a significant role in the response. Heelis *et al.* (2000) indicated that modeling the boogie as two axes instead of one decreases the defection in the subgrade, and that increasing the number of boogies raises the deflection (specially under the trailing boogie of the locomotive).

Other authors detected patterned responses that simplify the interpretation of the results. For instance, Krylov *et al.* (2000) pointed out that track deflection (in elastic computations) can be described as a stationary solution since it only depends on the $(x - C_{\mathrm{t}}t)$ combination (it presents a constant shape traveling at the surface at velocity C_{t}). Studies performed by Heelis *et al.* (1999a, 2000) showed that maximum defection due to the passage of High-Speed Trains is not located directly underneath the applied load. This effect is more apparent when the train speed exceeds critical speed.

Several simplifications can be performed during modeling, inducing a more or less important loss of accuracy. However, some elements of the track structure should always be considered. Hildebrand (2001) referred that to correctly evaluate vibration propagation in rails, the influence of both rails must be taken into account since a model with only one rail will overpredict attenuation. Studies performed by this author indicated that attenuation strongly depends on the relative phase of vibrations between the two rails. The frequency that corresponds to the first mode of a supported finite beam with a length equal to sleeper spacing is generally called pinned-pinned frequency and it is not affected by pads, sleepers or ballast characteristics. However, it is a function of sleeper spacing and bending stiffness of the rail (Hildebrand, 2001). Sleeper spacing must also be considered if the evaluation of corrugation is intended,

since their evolution depends on the initial profile phase. Studies performed by Ilias (1999) showed that if the initial irregularity does not fit the structural dynamics, the irregularity first moves to the 'correct' position in sleeper bay. Regarding pads, a stiffer pad induces higher stress levels in the sleeper, wayside noise and considerably increases the attenuation at frequencies beyond pinned-pinned frequency (Hildebrand, 2001). The stiffness grows at frequencies below pinned-pinned and also reduces vibration but not in a relevant way. This element presents high influence on the high-frequency content of the structure response. In the near field, however, its influence is not so relevant. The surface roughness, wheel impacts, wheels out-of-roundness, unsupported sleepers, rail manufacturing imperfections and inhomogeneous stiffness of track are also phenomena that should be considered in modeling when noise production and far field response are to be evaluated through numerical modeling (Ilias, 1999; Degrande, 2000; Krylov *et al.*, 2000). These induce propagation that decays with distance by energy transference to ballast and air (as airborne sound) (Hildebrand, 2001). Ilias (1999) referred that trains passing over rails having this kind of irregularity will produce forces that induce irregularities. After a million passages, a more or less regular pattern (corrugation) will appear. Usually, this imperfection is not considered in the models. However, wheel and rail defects can cause load amplification by factors as much as three times the nominal static wheel load. For that reason, Brandl (2004) recommended that the out-of-roundness of the wheels should be taken into account. This imperfection reduces riding stability, safety and comfort, and increases maintenance costs for vehicles and rail tracks. Figure 1.13.a represents an ideal model proposed by Knothe and Wu (2000) to simulate the interactions between vehicle and rail, in which the wheel out-of-roundness n (regarding a perfect circle) is supposed by the author to be in the 3rd to 5th order (Fig. 1.13.b) for a frequency generation between 50 Hz to 150 Hz.

Simplifications are also performed in the applied load which have vertical, lateral and longitudinal components. The vertical wheel force is often considered

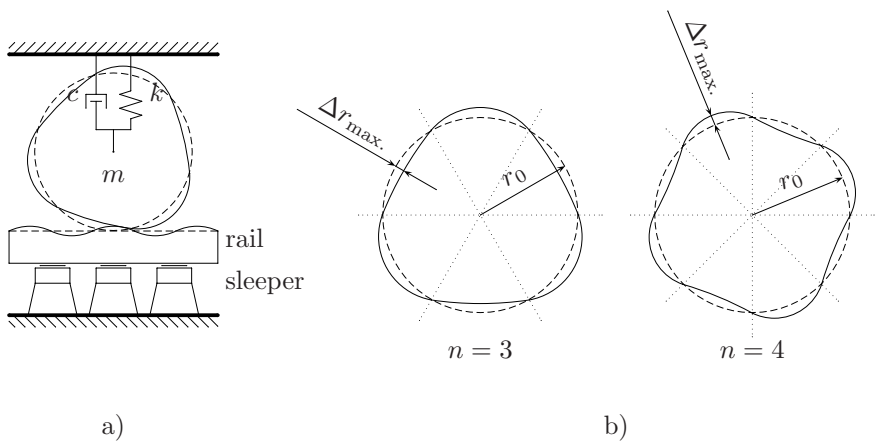

Figure 1.13: (a) Idealized model interactions between vehicle and rail and (b) consideration of wheel out-of-roundness n (Knothe and Wu, 2000)

as having a static component equal to the vehicle weight divided by the number of wheels plus a dynamic variation about the static value. The static values range from about 53 kN for light rail passenger service to 174 kN for trains in EUA (Selig and Waters, 1994). Lateral forces are parallel to the long axis of the sleepers and are produced by lateral wheel forces and/or buckling reaction forces. The lateral wheel force comes from the lateral component of friction force between the wheel and rail, and by the lateral force applied by the wheel flange against the rail. Sources of lateral wheel forces are the train reaction to geometry deviations, self-excited hunting motions which result from boogie instability at high speeds, and centrifugal forces in curves. Lateral wheel forces are very complex and much harder to predict than vertical forces. Longitudinal forces are parallel to the rails and result from (Selig and Waters, 1994):

1. locomotive traction force including force required to accelerate the train;
2. braking force from the locomotive;
3. thermal expansion and contraction of the rails;
4. rail wave action.

For the near field modeling of the induced stress in the structure, the consideration of the dynamic components of the vertical component is not required. However, for modeling far field, namely for noise and vibrations in distant constructions, lateral and dynamic vertical forces should be considered.

1.7.2. Techniques

Regarding modeling techniques, the first models consist of the simplest analytical equations to evaluate ground response due to a traveling train in a two dimensional model of a point load moving on an infinite beam resting on an elastic foundation composed of a series of discrete springs (Winkler's foundation). Damping was introduced as proportional to vertical speed (viscous model), with results highly depending on it. Since the model is linear, elastic superposition could be used to simulate a multi-axle train. The model does not take into account shear coupling between springs (Heelis *et al.*, 1999b). The equation that rules this model is presented in Equation 1.18 where $\delta(x - C_\mathrm{t}t)$ (Eq. 1.19 and 1.20) is the Dirac delta function (Clough and Penzien, 1993).

$$EI\frac{\mathrm{d}^4W(x,t)}{\mathrm{d}x^4} + \rho\frac{\mathrm{d}^2W(x,t)}{\mathrm{d}x^2} + 2c\frac{\mathrm{d}W(x,t)}{\mathrm{d}x} + k_\mathrm{s}W(x,t) = P\delta(x - C_\mathrm{t}t) \quad (1.18)$$

$$\delta(x - C_\mathrm{t}t) = \begin{cases} 0 & \text{if} \quad (x - C_\mathrm{t}t) \neq 0 \\ \infty & \text{if} \quad (x - C_\mathrm{t}t) = 0 \end{cases} \quad (1.19)$$

$$\int_{-\infty}^{+\infty} \delta(x - C_\mathrm{t}t) = 1 \quad (1.20)$$

The product EI could represent the bending stiffness of the rail alone or include the ballast and embankment (Heelis *et al.*, 1999b). Relationships between

k_s with elastic soil parameters have been presented by Biot (1937), Vlaslov (1957) and Vesic (1963) (Heelis *et al.*, 2000). By applying the load on the sleepers or ballast, one could estimate the vertical stress applied to underlying layers, determined from integrated forms of the Boussinesq equations derived for a point load acting on the surface of a semi-infinite, elastic, homogeneous, isotropic mass (Burrow and Ghataora, 2004).

More recently (with the advent of computers), design procedures have adopted models based on Layered Elastic Theory, Finite Element Method (FEM) with 2.5D and 3D simulations, or Discrete Element Method (DEM), for track structure submitted to moving vertical wheel loads (Burrow and Ghataora, 2004). Many of them overcome limitations of the beam-on-elastic foundation model as individual components of the superstructure and substructure can be modeled and shear cut and wave propagation (for 3D models) are taken into account. Additionally, these models have the potential to consider non-linear characteristics including plastic, viscous and viscoelastic deformations and strain rates which are non-linear functions of the stress level. These computer models can be constructed and run on a typical or measured track in a virtual environment, and a wide range of possible designs or parameters changes can be studied. The outputs of the models can be set up to provide accurate predictions of the dynamic behavior of the vehicle and its interaction with the track (Iwnicki, 2006).

The more accurate technique for railway modeling could be accepted as the Discrete Element Method. Since railway ballast generally comprises large particles of a typical size of 40 mm, it is difficult to treat such a material using continuum medium approach as the particle size is large regarding the geometry of loading. Lu and McDowell (2008) referred that the Discrete Element Method has been widely used to investigate the mechanical behavior of railway ballast for a few decades. In fact, Cundall and Strack (1979) used Discrete Element Method to investigate the response of ballast 30 years ago. Nevertheless three decades have passed and continuum modeling is still often used. This is due to the computer time-consuming limitation of this method. To reduce this computational effort, clumps have been used to model ballast particle shape and introduce interlock (McDowell *et al.*, 2006). A clump is a single entity of overlapping balls; it is internally rigid and deformable at the external boundary. This simplification can reduce, in fact, computational time but it induces an unreal and undesirable unbreakable condition.

Lim (2004) referred that the discrete element program PFC3D (Itasca Consulting Group, Inc., 1999) is believed to be the most suitable numerical model for investigating the micro mechanical behavior of ballast. PFC3D applies Discrete Element Method (DEM) to model the movement and interaction of stressed assemblies of spherical balls, which can overlap and displace independently from one another and interact only at contacts or interfaces between the balls. This program applies a contact constitutive law to each particle contact, such that the contact force is related to the amount of overlap, and accelerations are calculated from the contact forces via Newton's second law. These accelerations are integrated to determine velocities and displacements via a time-stepping scheme, and the resulting displacements are used to calculate the new contact forces via the contact constitutive law. The material constants for the contact constitutive law have explicit physical meanings. A crushable particle can also be modeled in PFC3D as an agglomerate of balls bonded together. Thus,

PFC3D can be used to investigate the heterogeneous stresses in the ballast in a way that cannot be achieved using continuum approaches.

1.7.3. Domains of analysis

When track dynamics is investigated in the time domain, deflections and displacements of the vehicle are calculated by numerical time integration as the vehicle moves along the track. The vertical motion of the wheelset should then match the vertical deflection of the rail, while taking the contact deformation between the wheel and the rail into account. This contact force should be considered unknown and determined in the calculation (Dahlberg, 2003). The track can be modeled by finite elements and in many cases a modal analysis (or eigenvalue analysis) of the track can be performed. This requires that the track is modeled over a finite length. In this type of analyzes, all systems with mass and stiffness can vibrate and these vibrations occur most naturally at certain frequencies called modal frequencies and in certain patterns called mode shapes. If the equation of motion is linear (or can be lineared for a certain balance positions of the bodies or length of vibrations) then an eigenvalue analysis can be carried out to determine the modal frequencies and mode shapes. The track is then described through its modal parameters, and the physical deflections of the track are determined by modal superposition, which requires linear consideration. The vehicle is often modeled by the use of rigid masses, springs (linear or non-linear) and viscous dampers. If a more detailed response of the vehicle is of interest, then a better vehicle model should be used and it might be convenient to use modal analysis also for the vehicle deformations (the vehicle is no longer composed of rigid bodies). This is a useful analysis for knowing the modes so that unwanted vibrations are reduced. In practice, the complex eigenvalues can easily be calculated for the particular equations of motions using MATLAB® 'eig' routine.

Regarding frequency-domain technique, only fully linear systems can be treated. The track response is assumed to be stationary, implying that singular events along the track, such as a rail joint, a sleeper hanging in the rail, varying track stiffness, and so on, cannot be treated (Dahlberg, 2003). Using the frequency-domain technique it is possible to investigate the track and wheel response due to a 'moving irregularity'. Instead of having a wheel moving along the rail, one investigates a stationary wheel. The rail and the wheel are then excited at the contact between wheel and rail. One may think of this excitation as if a strip of irregular thickness was inserted between the wheel and the rail. The strip is then forced to move between the wheel and the rail so that the irregularity of the strip will excite both wheel and rail (Dahlberg, 2003). The response of the wheel and the track is obtained in the frequency domain. Together with the Fourier transformation of the irregularity, the Fourier transformation of the response is obtained, and the inverse transformation provides the time-domain response.

1.8. Noise and vibration

In recent years, rail transport systems have increasingly received complaints from people living alongside lines and above underground lines (Esveld, 2001).

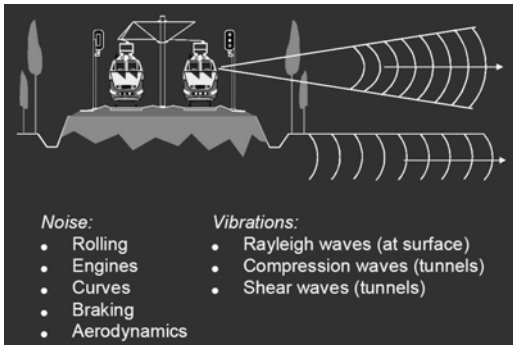

Figure 1.14: Noise and vibration produced by High-Speed Trains (Esveld, 2001)

The disturbance is usually caused by the direct emission of noise or vibration from the railway (Fig. 1.14), but sometimes noise in buildings is produced by the walls vibrating, which is referred to as re-radiated noise. Vibrations and structure-born noise mainly occur at lower frequencies, below 50 Hz. At higher frequencies, these vibrations attenuate increasingly fast. The energy at higher frequencies is radiated as noise mainly through the wheels and the rails. Roughly speaking, vibrations and structure-born noise occur in the frequency range of $0\,\mathrm{Hz} \sim 100\,\mathrm{Hz}$, and noise between $30\,\mathrm{Hz} \sim 2000\,\mathrm{Hz}$. The principle of noise and vibration radiation is illustrated in Figure 1.14.

There is a large amount of excitation sources that may induce oscillations, vibrations and noise in the train, in the track and in its surroundings. Long wavelength geometric irregularities in the track alignment will induce lateral displacements of the railway boogies, and this will induce traveling discomfort for the passengers. Short wavelength irregularities will produce vibrations and noise. Long wavelength irregularities are defined by Dahlberg (2003) as irregularities of a wavelength of 0.3 m or longer. These irregularities may be due to geometrical irregularities in the rail, irregularities of the track stiffness, sleeper spacing or wheel out-of-roundness (Dahlberg, 2003). In the case of sleeper spacing, even though the rail itself may not have an irregularity with a wavelength corresponding to the sleeper spacing, the wheel will be influenced by the varying stiffness of the track. As the track is stiffer at the sleepers, and softer in-between, the wheel will be excited with a frequency that corresponds to the speed C of the train and the sleeper spacing l. The excitation frequency f becomes $f = C\,l^{-1}$. The wheel out-of-roundness will excite the train-track structure with one or several frequencies corresponding to the wavelength of the wheel out-of-roundness. The rail manufacturing process also induces rail irregularities with a wavelength from one to several meters. These irregularities induce low frequency excitation on the train and the track. Regarding the variation of stiffness, it is not only due to the existence of sleepers. In fact, the existence of switches, turnouts and random variable stiffness of the foundation will induce low frequencies on the train.

Regarding short wavelength irregularities, their development is explained by the dynamics between the train and track system and linked to resonance effects in the combined rail and wheel system. It is assumed to be so, because the irregularities that develop are periodic of a certain wavelength, mostly in the range of 0.03 m to 0.3 m (Dahlberg, 2003). In fact, only long wavelengths can

be explained by the manufacturing process. Such short periodic irregularities are usually named corrugation. It should be noted that long wavelength irregularities may not be periodic, in opposition to corrugation which is periodic. The origin of corrugations on rails has not yet been fully explained but resonance effects between rail, wheel, and axle are believed to be involved (Dahlberg, 2003).

When the train speed increases, the dynamic interaction between the vehicle and the track becomes more and more pronounced and this gives rise to larger dynamic forces between the wheels and the rails. Once the rail corrugation has began to develop, the dynamic forces in the train-track system will be further magnified, and the deterioration rate of the track will increase. With time, an almost regular sequence of shiny peaks and dark troughs, generally spaced about 0.03 m to 0.08 m, will appear (the designated corrugation) which induces vibrations and noise.

A careful design of the track can minimize the vibrations in the surroundings. Andersen and Nielsen (2005) referred that open or infilled trenches may be constructed along the track, or the soil underneath the track may be improved to reduce induced vibrations. The analyzes indicate that open trenches are more efficient than infilled trenches or soil stiffening, even at low frequencies. However, the direction of the load is of great importance. For example, the response outside a shallow open trench may change dramatically when horizontal load is applied instead of vertical load. Analyzes performed by Andersen and Nielsen (2005) allow to conclude that the response of the ground surface is very different in the case of vertical and horizontal loads. This suggests that conclusions regarding the vibration caused by a force in one direction cannot be made from observations of the response to excitation in the other direction. Distinct advantages and disadvantages of possible mitigation methods are summarized and presented in Table 1.1.

1.9. Maintenance

Since track deterioration is quite different from the global failure of general geotechnical structures, such as spread footings or retaining walls, it is desirable and advantageous to understand how failure occurs, the difficulty to perform maintenance and its high cost.

In railway structures, the deterioration is induced by an accumulation of plastic deformations in the ballast, subballast and capping layer due to cyclic loading. These cyclic loads induce permanent settlement, primarily due to the compression of the capping layer and the compacted soil (Shin *et al.*, 2002), which induce frequent and expensive maintenance operations. In order to meet competition with other modes of transport, there is an increasing demand upon the railways to improve reliability, efficiency, and traffic times (Esveld, 2001). The requirements in speed and axle load mean that the demands made upon the track are becoming more onerous. Deterioration of the track geometry has been recognized as the main cause for track maintenance.

Table 1.1: Mitigation methods advantages and disadvantages (Andersen and Nielsen, 2005)

Mitigation method	**Advantages**
Vibration screening in general	More efficient than soil improvement.
Open trenches	Deep open trenches provide good vibration reduction, even at low frequencies. Cheap in terms of construction materials.
Concrete barriers	Great efficiency at low frequencies and low vehicle speeds for vertical loads. May be installed e.g. under pavements.
Soil improvement in general	Reduction of vibrations at all frequencies, vehicle speeds and distances from the track. Good solution for sites with soft original soil.
Soil replacement (or soil stiffening)	Particularly small response under a wheel set. Relatively inexpensive construction by means of, e.g, 'jet grouting'.
Inclusion of a 'tube'	Particularly small response far far behind and in front of a wheel set for vertical loading.

Mitigation method	**Disadvantages**
Vibration screening in general	Amplification of response inside trenches.
Open trenches	Shallow trenches may lead to amplification of the response outside the barrier. Expensive, if new material is to be used.
Concrete barriers	Amplification of response outside barrier at low frequencies for horizontal loads. Expensive construction.
Soil improvement in general	Generally less efficient than barriers. Not a possible solution if the existing ground already consists of stiff soil.
Inclusion of a 'tube'	Expensive construction.

The deterioration is mainly caused by the settlement of the substructure, which tends to depend on the site conditions (Lim, 2004). In the past, more attention has been given to the track superstructure consisting of the rails, the fasteners and the sleepers, than to the substructure consisting of the ballast, the subballast and the subgrade. Even though the substructure components have a major influence on the cost of track maintenance, less attention has been given to the substructure because the properties of the substructure are more variable and difficult to define than those of the superstructure (Selig and Waters, 1994).

The braking distance of trains is much longer than that of cars. Trains cannot be brought to a standstill in time if people or vehicles unexpectedly appear on the track. Similarly, it is not possible to halt traffic temporarily every time works are required on the track. This is why comprehensive stringent safety regulations apply to work within the railway structure. Firstly the track must always be in a safe condition for approaching trains and secondly the safety of the track maintenance crew must be ensured.

Kaynia and Clouteau (2007) referred that the majority of railway tracks in Europe rest on ballast. Low-speed trains with speeds of around 200 $\mathrm{km\,h^{-1}}$ or less have been operating for a long time on such tracks without any major problem. High-Speed Trains with more than 300 $\mathrm{km\,h^{-1}}$ of speed, have been operating on certain segments. Observations on railway performance have indicated that track problems, such as settlement and deterioration, tend to increase with train speed and lead to the need for maintenance (Kaynia and Clouteau, 2007). To make High-Speed Trains more competitive, it is necessary to reduce maintenance costs. Esveld (2001) referred that 25 % of the annual expenditure concerns mechanized track maintenance and 5 % manual track maintenance (Fig. 1.15). It is, therefore, obvious that the high expenses are caused by track renewal. The maintenance operations of railway company represent about 6 % of its annual turnover. Among those, 10 % comprise the maintenance of the geometrical quality of the lines, which is mainly carried out by tamping operations. Reducing the global volume of tamping operations could largely reduce the corresponding costs, and increase the availability of the lines.

For the maintenance of the structure, manual insertion of sand blankets is not only costly, but also the compactness and uniformity of the blanket cannot

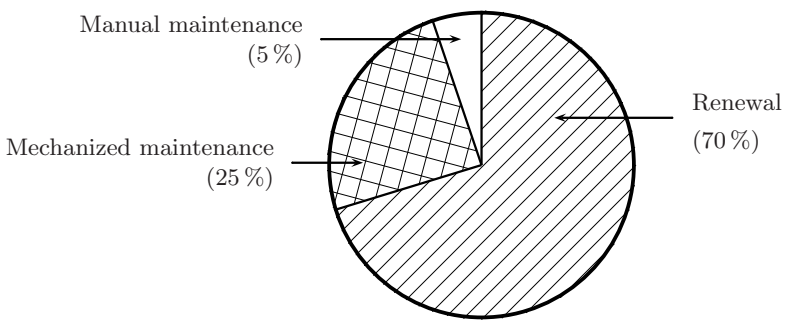

Figure 1.15: Total annual expenditure for maintenance and renewal (Esveld, 2001)

be maintained. Insertion of blankets by road construction equipment requires a close-down track during the rehabilitation process and, once more, the quality of the finished product is in many cases questionable. Different machines and machine systems are available, which can insert sand blankets, geosynthetics or other protection layers under the track, in track possessions, without the need to dismantle the track. For that, Esveld (2001) referred the aim of a completely continuous action. Production line treatment of the track with quality control of the completed work is achieved with the concept of a Mechanized Maintenance (e.g. Train MDZ - Fig. 1.16) consisting of the leveling, lining, tamping machine, the ballast regulator and the dynamic track stabilizer. In this modern system, the lining process is based on a 4-point measurement, or, if design lining is applied, on a 3-point measurement. In the 4-point system, the machine measures three ordinates, Y_1, Y_2, and Y_4 which together determine a second-degree curve by means of which local track alignment is approximated. At work-point C (see Fig. 1.16) the track is aligned so that it comes to lie on this curve. The correct position is verified by means of h and H, the quotient of which has a fixed value.

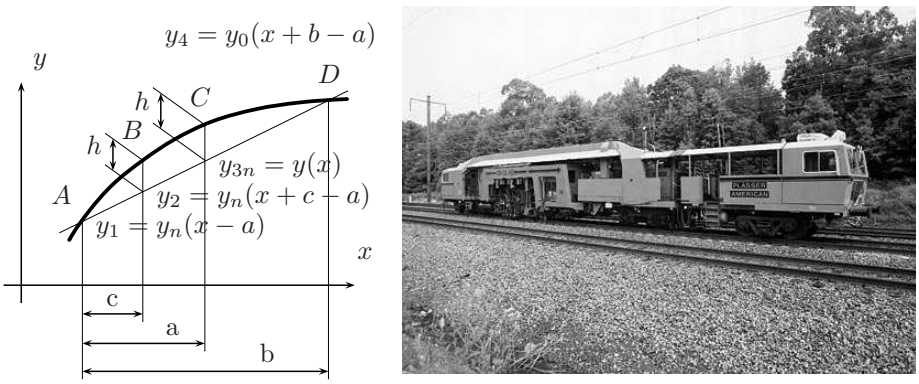

a) b)

Figure 1.16: a) Four-point system for lining process and b) Mechanized Maintenance Train (MDZ) (adapted from Esveld (2001))

1.10. Summary

This Chapter starts by presenting a global overview of railway technology, where the description of the contribution of each track component is given, as well as the design behavior of the railway structure, dynamic concepts of the moving load, laboratorial testing and consequence of simplifications in numerical models. It uses therefore a descriptive approach that allowed the identification of the major field of improvement in which this research work will focus.

Along this exposition, it was detected that railway structures should allow an efficient distribution to reduce the stress level to admissible values when applied to the foundation, the influence of wave propagation should be taken into account when modeling and, of great importance, it becomes unquestionable that maintenance costs are a crucial aspect to consider and require better design techniques. These techniques must become much more efficient in order to

allow maximum cost reduction. To do so, these must rely on solid numerical models that, in its turn, most rely on accurate laboratory procedures. Numerical model, to be able to allow moving excitations and dynamic analyzes (e.g. wave propagation), require FEM meshes with a high number of degrees of freedom. An alternative consists in the use of frequency domain models, which allow considerable reduction of computational effort but limits analyzes to the linear elastic case. Commonly, numerical simulations are performed assuming an elastic behavior of the entire railway structure, which may lead to an important question: the implication of this assumption in the induced stress field. It was possible to detect that for noise and vibration generation (far field response) the assumption of linear elastic analyzes can provide precise results, but for stresses and strains mobilized in the structure (near field response) the response may be unrealistic. It seems therefore fundamental that the evolution of induced stresses, for linear elastic and also for non-linear plastic cases, should be performed.

In sum, the precise numerical quantification of the stresses induced on a railway track by an HST, which may lead to a better design and respective reduction of maintenance costs, should be taken into account.

Elastic domain of soils

2.1. Introduction

Since numerical quantification of strain and stress evolution requires numerically robust models, all possible simplifications should be used. Due to that, 3D models of railway tracks submitted to HST commonly assume an elastic behavior for all layers, an assumption which is studied along this thesis. Since tracks are subjected to a high number of cycles without significative loss of its mechanical behavior (taking into account that only the ballast can be subjected to an 'easy' maintenance), low stress levels are expected at foundation level. Since this assumption will be made in all models, the quantification of the elastic domain is necessary to validate results. In order to do that, a possible track site foundation soil near the city of Porto was studied. It should be noted that since no sufficient data from instrumented railway sites was available, this assumption had to be made.

This Chapter starts by demonstrating the importance of the definition of the elastic domain (through a short bibliographic revision), even from non-elastic analyzes, and ends with the way found in UM to economically quantify it in laboratory. It is important to refer that all hardware was chosen taking into account its low cost and efficiency. Regarding software, it was developed at UM by the author and it is exposed in detail in the Appendix (see page 171). The study soil is described and three testing phases are presented so that a definition of its elastic domain could be achieved. The Chapter ends with the definitions of this domain, which is intended to corroborate (in the numerical models used in the following Chapters) the elastic assumption performed at foundation level. Future improvements on the laboratory system and testing programme are also described.

2.2. Elastic domain

Even if widely used, little attention has been paid to the mechanical behavior of geomaterials for low strain levels, in which physical and mechanical properties must be efficiently controlled, in distinct cases like dam constructions, embankments or foundations. According to Vinale *et al.* (1999), even if during construction high strains are reached, precise measurements of the low strains during service must be performed to correctly evaluate the stress state. After construction, deformations will be very small, in part due to the high stiffness

of the compacted soils, but their quantification is of great importance. Studies performed by Vinale *et al.* (1999) in a silty sand from El-Infiernillo dam, with a water content of 11.4 %, demonstrated that the use of a secant modulus associated with a deformation level of 1 % ($E_{\mathrm{sc}}(1\,\%)$) induces an overestimation of settlements W (comparatively with the ones obtained using the initial Young modulus - E_0) as shown in Figure 2.1.

Currently, is unquestionable the preponderance of the behavior of granular soils in the bearing capacity of shallow and deep foundations, as well as the confirmation of its efficiency when used in roads and railways. Due to that, it is of great importance to correctly define its characteristics of deformability. Even if the non-linear behavior and time influence in the strain-stress relation are not well known and considered in the project (Dan, 2001), it is fundamental to pay special attention to the soil behavior for strain levels lower than 0.1 % (Jardine *et al.*, 1984; Burland, 1989; Balay *et al.*, 1997; Gomes Correia and Biarez, 1999). With the exceptions of rare soft soils submitted to high loading, all soils present service strain levels between 0.01 % to 0.1 %. The same behavior is detected in soils under foundations or in road infrastructure when strongly compacted (Balay *et al.*, 1997; Dan, 2001; Gomes Correia, 2004b). In this domain of low strain levels, materials can be considered linear elastic since the response is independent of velocity and reversible when submitted to cyclic loading.

According to Jardine *et al.* (1991), soil behavior can be divided in four domains (Fig. 2.2.a):

1. A stress variation from O induces a linear elastic behavior until surface Y_1 is reached , i.e., until strain level ϵ_{Y_1} is reached (corresponding to the constant value in the secant modulus degradation curve - Fig. 2.2.b). The

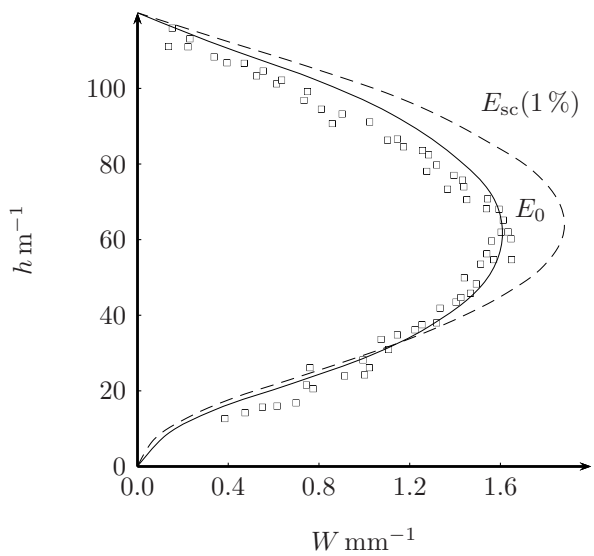

Figure 2.1: Comparison between measurements and simulated settlements in El-Infiernillo dam (Vinale *et al.*, 1999) along the height h of the dam

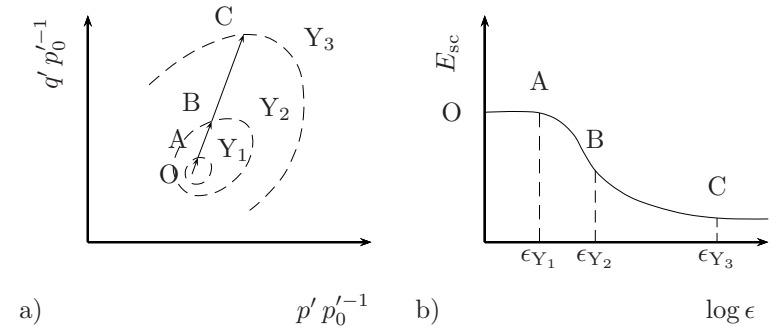

Figure 2.2: a) Domain surfaces and b) secant modulus degradation curve (Jardine, 1992)

strain level required to reach surface Y_1 is usually around 10^{-6} to 10^{-5}.

2. Increasing the stress variation in order to reach surface Y_2 (deformation level between ϵ_{Y_1} and ϵ_{Y_2}) still induces an elastic behavior. However, the relation strain/stress becomes non-linear and the trajectory between loading and unload presents hysteresis. A decrease in the secant modulus (interval $\overline{AB}$ in the degradation curve - Fig. 2.2.b) is also visible. There is no development of the interstitial pressure on undrained tests and, in cyclic loading, damping increases. Usually the value of ϵ_{Y_1} is about 5×10^{-4}.

3. A new grow in stress will induce a stronger decrease in the secant modulus (interval $\overline{BC}$ in the degradation curve - Fig. 2.2.b) and irreversible deformations, as larger and closer to the value of ϵ_{Y_3} the strain is. In this situation and for cyclic undrained tests, interstitial pressure starts to develop. Damping also assumes larger values.

4. Outside surface Y_3, i.e., for strains higher than ϵ_{Y_3}, irreversible deformation becomes preponderant. For the case of strong overconsolidated clays strain ϵ_{Y_3} (corresponding to maximum resistance) is around 7×10^{-3}.

Due to this non-linear behavior, the definition of four distinct modulus is possible, namely (Fig. 2.3.a):

E_0 designated Young's modulus or maximum deformability secant modulus - it corresponds to the linear elastic regime.

E_{sc} designated deformability secant modulus - it corresponds to the secant modulus associated with a certain strain or stress level.

E_{tg} designated deformability tangent modulus - it corresponds to the tangent modulus associated with a certain strain or stress level.

E_{eq} designated deformability equivalent modulus - it corresponds to the modulus associated with a load/unload cycle at a certain strain amplitude.

Also, the relation strain/stress of a soil submitted to a load/unload uniaxial action can be divided into four types, namely (Fig. 2.4):

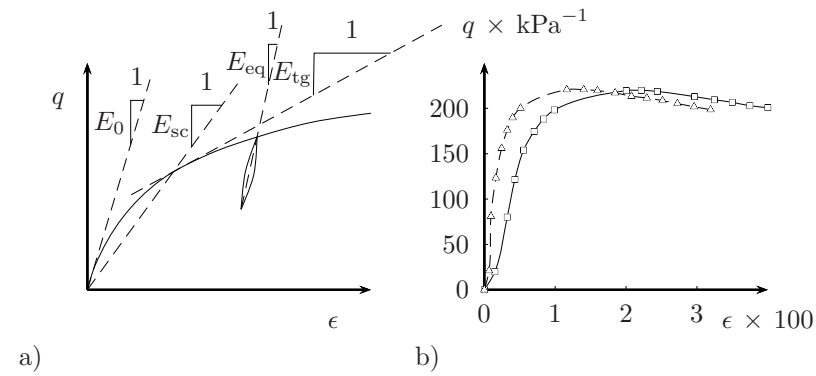

Figure 2.3: a) Modulus and b) influence of instrumentation in measurements using external instrumentation (solid line) and local instrumentation (dashed line) (Gomes Correia, 1985)

a) linear elastic;

b) non-linear elastic;

c) reversible with hysteresis;

d) irreversible.

The importance attributed by the geotechnical community to the small strains domain (behavior inside surface Y_1) has allowed a better prediction of foundation settlements under service vertical loads; has allowed the modification of traditional empirical testing to more scientific ones, both in laboratory and *in situ*; has increased the importance of seismic testing and the evolution of simplified models to more realistic ones by including new relevant factors (Gomes Correia, 2004a).

To correctly evaluate the first domain (surface Y_1 in Fig. 2.2.a), special attention must be paid in order to reduce errors induced by the laboratory technique. Gomes Correia (1985, 2004b) and Burland (1989) verified that, for strain levels below to 0.1 %, the traditional external instrumentation used in triaxial tests underestimates the real soil stiffness. For that reason it becomes necessary, in triaxial tests, to use local instrumentation (Fig. 2.3.b). Errors induced by external instrumentation are due to bending of the specimen, testing system

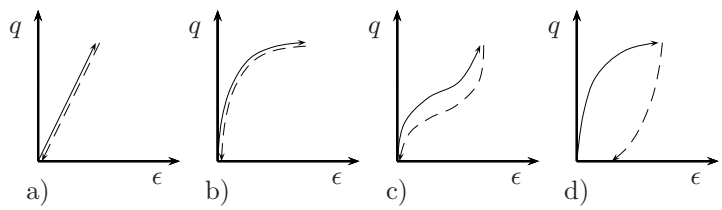

Figure 2.4: Strain/stress relations in soils

deformability, adjustments in the triaxial chamber and rotation/confining of specimen near the top or base (Jardine *et al.*, 1984; Goto *et al.*, 1991).

Alternatively to the triaxial test with local instrumentation, dynamic tests can be used to evaluate the low strain behavior of the soil. These dynamic tests can be the resonant column or the use of bender elements. Rampelo and Viggiani (1999) referred that the use of the resonant column demands back-analyzes in which the soil is assumed continuous, elastic and linear. The main advantage of this dynamic test is the direct measure of shear modulus for very low strain levels (around 10^{-6}). However, cyclic studies are not possible since it is unable to correctly control the number of applied cycles (Gomes Correia, 2004b). Regarding bender elements, it should be pointed out that for granular materials with large dimensions, the interpretation of wave propagations is not straightforward due to the fact that granular materials are discontinuous media. For that reason, the use of bender elements remains conditioned (Dan, 2001).

2.3. Instrumentation technique

2.3.1. Technique selection

As indicated, the use of external instrumentation is not compatible with the evaluation of an elastic domain. This task demands the use of local instrumentation, able to record strain levels as small as 10^{-6}. Actually there are several transducers capable of doing so, namely (Gomes Correia *et al.*, 2006): Piezoelectric transducers (bender elements), Hall-effect transducers, Linear Variable Displacement Transducer (LVDT) and Local Deformation Transducer (LDT).

Local instrumentation was born in the early 80's, representing at that time a big challenge for all geotechnical laboratories. Burland and Symes (1982), in an initial phase, were able to record strains as low as 10^{-5} using four electrolytic transducers. Other authors used different techniques with similar results: Clayton *et al.* (1989) used Hall-effect transducers, Gomes Correia (1985) used mini LVDTs and proximity sensors, and Gomes Correia and Gillet (1993) used LVDTs in a large triaxial chamber.

In the Geotechnical Engineering Institute of Industrial Sciences in Tokyo University, Satoshi Goto decided to developed a simple transducer, designated as Local Deformation Transducer able to record strains from 10^{-6} to 10^{-2} (Goto *et al.*, 1991). The transducer consisted on a thin, long and flexible strip of phosphor bronze, with a Wheatstone bridge in the middle.

The advantages of this transducer are its simplicity, low cost, small weight, insensibility to temperature (if constructed using full bridge) and the possibility to be used under water (Gomes Correia *et al.* (2006) and Goto *et al.* (1991)). Hall-effect transducers present insufficient resolution and high sensitivity to electrical noise and temperature, LVDTs are difficult to fix in the specimen due to its significative weight and piezoelectric transducers present difficulties in interpretation, namely with time and wave distance (Gomes Correia *et al.*, 2006).

For the proposed elastic domain evaluation, and considering the matter previously described, it was decided to introduce local instrumentation in a triaxial chamber existing at UM. The use of LDTs, originally developed by Goto *et al.* (1991) and capable of detecting strain increments of 10^{-6}, was adopted. All the necessary transducers were constructed (by the author) in the Civil Enginee-

ring Laboratory in UM. The only found disadvantage was the small deformation field, which according to Hoque *et al.* (1997), should not be higher than 2 %. Hoque *et al.* (1997) performed several tests to confirm the long term stability, hysteresis and durability under pressurized submersion. Only the used glue was not object of testing. The results presented by these authors were quite satisfactory and allowed the confident use of this technique without further testing.

2.3.2. LDTs

An LDT transducer consists of a thin, long and flexible strip of phosphor bronze with one or two gauges (Fig. 2.5) applied in each side, corresponding to LDTs in half or full bridge, respectively. It should be noted that the full bridge version presents improved sensibility and is insensitive to temperature.

For the construction of the LDTs, special attention was paid to the choice of the materials to be used, namely: strip, gauges, glue and conductors. The strip consisted of a mixture of phosphor bronze with thermo treatment (in order to improve its elastic behavior). Without this improved elasticity, the permanent deformations of the transducer would be unacceptable. Steel strips were not recommended due to the existence of carbon, even if in a very low percentage, which induces oxidation. Regarding the gauges, the ones used had a nominal resistance of 120 Ω, dimensions of 0.84 mm×2 mm (model Kyowa KFG-2N-120-C1-16) with high resistance to fatigue (allow 2×10^6 cycles for strain levels of $\pm 1500\mu\epsilon$). The glue, of premium quality, was also a material of great importance. The chosen one was Kyowa CC-33A. It consists of a glue with a resistance of 50 kPa to 100 kPa, able to hold temperatures from -196 °C to 120 °C. To guarantee its maximum efficiency, during the construction of the LDTs, a strong compression was applied during the 1st minute, followed by hardening at room temperature for 24 hours.

In a first phase, the LDTs constructed in UM did not have the waterproofing characteristics recommended by Goto *et al.* (1991) and Hoque *et al.* (1997). Since these were not intended to be used in water, the inexistent protection allow a weight reduction and improved flexibility. However, during testing it was noted that the electrical connections were exposed to handling and therefore easily damaged. For that reason, in a second phase, the protections were applied even if testing was not intended to be performed under water.

The work principle of the LDTs is based on the fact that variations in dis-

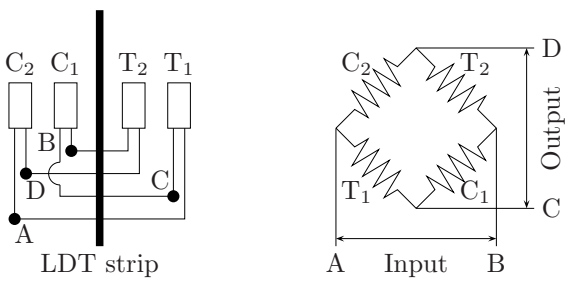

Figure 2.5: Scheme of a full bridge LDT (Goto *et al.*, 1991)

tance between the strip extremes induce a variation on the electrical gauges, and consequently, an unbalance of the Wheatstone bridge. This unbalance is related with specimen deformation by means of a squared relation obtained during calibration.

As already stated, LDT behavior was not analyzed since the technique was already object of study by Goto *et al.* (1991) and Hoque *et al.* (1997), namely in terms of hysteresis, long term stability, behavior in water medium and dynamic testing.

2.3.3. Radial instrumentation

The radial system has evolved in 3 phases. In the first phase, there was no radial instrumentation being the radial strain supposed equal to the axial (the material was assumed isotropic). In order to record radial deformations it became necessary to define a system capable to record this deformation in classical triaxial chambers, with little space between the specimen and the chamber wall. These classical chambers were developed this way in order to present the smallest volumetric changes. They used water as medium to apply confining pressure to the specimen so that volume change could be measured through the flow in/out of the chamber. The elimination of this system was required since it is not possible to measure small strains with it. Also, the use of compressed air made testing much easier and the purchase of automatic pneumatic systems was found to be less expensive than the ones for water. The use of air was also less demanding in terms of waterproofing of the transducers.

So, it became necessary to develop a system capable of recording the radial deformation taking advantage of the good resolution of the LDTs. First, since Goto *et al.* (1991) used half-bridge LDTs, changes were introduced in order to improve sensor resolution. It was considered, as a starting point, that the transducers should be in full bridge. In order to do so, the strip width was enlarged to 4 mm to allow the application of 2 gauges in each strip side. This increase in strip width induced high forces in the pseudo-articulations of the LDTs (Fig. 2.14.c). For that reason and also due the fact that the strip length was reduced (only 75 mm), the strip thickness was also reduced to 0.2 mm. With this combination, Goto *et al.* (1991) recommendations were accomplished. Secondly, two solutions were studied: the use of an articulated ring (similar to the one used with a Hall-effect transducer) in contact with the specimen in two opposite points or a belt in which a LDT measured perimeter variation of the specimen. The last option was adopted since it required less space between specimen and chamber, it presented less weight, the measuring diameter provided more representative values than diameter measuring and the outputs were increased by a factor of π.

The construction of the belt (Fig. 2.6) was possible with low cost and easily accessible materials. Attention was paid to the following topics:

1. the belt stiffness had to be high so that its deformability did not affect measurements. The wire used in the system also presented high axial stiffness and low bending stiffness;

2. all components were connected by means of a low flexibility and temperature/water insensitive glue. It was composed of two components (Devcon

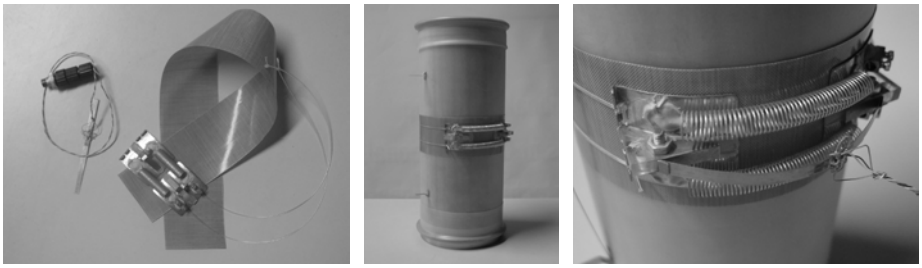

a) b) c)

Figure 2.6: a) Components of the belt radial system, b) belt radial system mounted in specimen and c) LDT installed in belt radial system

Epoxy Resin and Devcon Hardener), widely used in the Civil Engineering Laboratory at UM in tension tests;

3. a Teflon strip was introduced between the belt wires and the latex membrane in order to minimize friction.

This developed system presented pseudo-articulations adjustable to the initial positions of the LDT. However, these adjustments could only be performed during calibration of the system. In fact, the relation between LDT measurements and specimen diameter was not linear. The relation obtained (Eq. 2.1) could not be introduced in an automatic computer code so that an approximation using a third degree polynomial function was used. This approximation presented the best adjustment in a group of polynomial (degree 1 to 3), exponential, power and logarithmic.

$$C = D\pi - \arcsin \frac{\frac{B}{2}}{\frac{D}{2} + A} \tag{2.1}$$

During the testing programme A was set equal to 9 mm, C equal to 259 mm, and D obtained as a function of B (value presented by the radial LDT). The meaning of the variables is presented in Figure 2.7.

During testing, limitations were found in the developed radial system. The non-linear relation between diameter and LDT readings required the use of an approximate relation that induced a small error and did not allow further corrections in the pseudo-articulations of the LDTs. Moreover, adjustments between the latex membrane and Teflon induced unexpected behavior that interfered with radial strain measurements. Due to this fact, this system had to be replaced by a new one.

So, since reliable measurements had been obtained with the axial system, the idea of measuring radial deformation using the same principle was adopted. The problem relied on the fact that measurements had to be made in a non-plane surface. However, a linear relation between LDT measurement and diameter exists (Eq. 2.2 - see Fig. 2.8 for variable meaning). It should be pointed out that Equation 2.2 was obtained assuming that α remains constant.

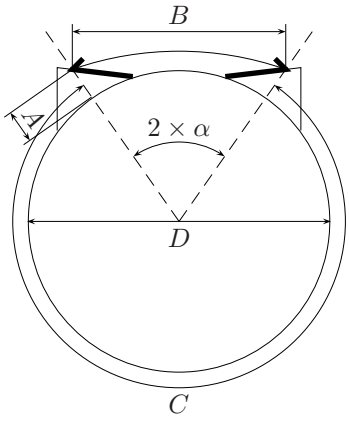

Figure 2.7: Scheme of the belt radial system with variables used in Equation 2.1 (Araújo, 2007)

$$D = A \times \left(\frac{B}{B_i} - 1\right) + D_i \times \frac{B}{B_i} \tag{2.2}$$

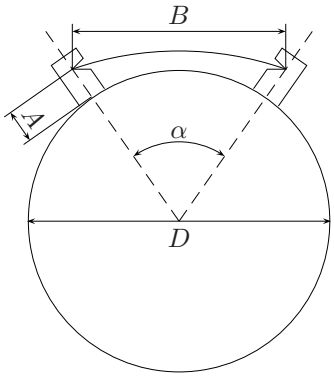

Figure 2.8: Direct radial measurement system with variables used in Equation 2.2

2.3.4. Axial instrumentation

Axial deformations were measured with the LDTs constructed (by the author) in the Civil Engineering Department at UM according to the recommendations presented by Goto *et al.* (1991), being the LDTs length the only chosen parameter. In these transducers, as in the radial ones, waterproofing was not applied in a 1st phase in order to increase flexibility and reduce weight. However, as already mentioned, this protection was later applied since it allows LDTs to be more easily handled.

2.4. Acquisition and control system

2.4.1. Acquisition

As a starting point in the assembling of the acquisition system, the characteristics presented by Hoque *et al.* (1997) were considered. In this author's system, the LDTs were excited with 2 V, being the output amplified through Kyowa DPM-600 amplifiers with a amplification factor of 10. The analog to digital conversion was performed using an AD 12 bit converter at an interval of ±5 V, which corresponded to a resolution of:

$$R = \frac{10}{2^{12} - 1} = 2.442\,\mathrm{mV} \tag{2.3}$$

In the system developed at UM, a 14 bit-AD converter from National Instruments (ref. NI USB-6009), 8 signal amplifiers for Wheatstone bridge (ref. SG-3016 CR-G) and a power supply of 24 V/2 A (ref. DP-540A CR) were used.

These components were chosen for their low price and good quality. The AD converter is also a DA converter since it also possesses 2 analog outputs and 12 digital outputs that allow the control of proportional servo-valves or precise stepper-motors. The converter was built with 14 bits for the analog input signals and 12 bits for the output analog signals. The amplifiers allowed a maximum amplification factor of 1000 with a precision of 0.1 %. During testing, the following transducers were used:

2 LDTs with 150 mm×4 mm×0.3 mm to measure axial deformation;

1 LDT with 75 ×4 mm×0.2 mm to measure radial deformation;

1 load cell;

1 pressure transducer.

All signals were amplified for an output voltage interval of ±10 V. Considering that it is a 14 bit converter, the resolution was set equal to 1.221 mV, smaller than the one used by Hoque *et al.* (1997). The converter allowed 4 or 8 band conversion as a function of the connection type, which could be differential (4 conversions) or sequential (8 conversions). Since it was intended to acquire signals from 5 transducers, the use of a sequential connection was initially adopted. This type of connection, in which the signals reference is common to all transducers, can present problems due to ground connections. In fact, this problem was detected and it was preferred to configure the transducers to be used in control (load cell and pressure transducer) with differential connections and the LDTs with sequential connections. With this configuration, testing was possible until a complementary converter was acquired. This complementary converter (model NI USB-6210 from National Instruments) provided 8 channels (in differential mode) at 16 bits and allowed all transducers to be configured with differential connections.

All LDT transducers were excited at 3 V, despite this voltage implicates an intensity current of 25 mA, a value slightly higher than the maximum recommended by the amplifier manufacturer (20 mA). This voltage level was adopted so that the output of the LDTs fulfilled the maximum amplifier interval (±10 mV).

As indicated by Goto *et al.* (1991), an analog filter could be and was used to reduce the noise of the LDTs noise, even if a slight phase shift in the signal was produced. Since all tests were performed at low rate (never above 10 kPa $\min^{-1}$) this phase was neglegible.

2.4.2. Control system

In an initial phase, tests were performed in a classical triaxial chamber, with manual control of the chamber pressure through a mechanical pneumatic-valve. The axial load was applied through a pneumatic cylinder with a second mechanical pneumatic-valve. This phase, with obvious limitations due to operator control, was used to evaluate the potentiality of a pneumatic system. Results were quite satisfactory and provided excellent guidelines for the development of an automatic system.

The automatic control system was initially developed by Araújo (2007) and was here improved (see Appendix for a precise description of the latest developed version of the software). Araújo (2007) made use of a stress-path chamber existing in the Civil Engineering Laboratory in UM (Fig. 2.9), already having a low friction pneumatic piston for the application of the axial load. The chamber was produced by Wykeham Farrance (model 12406), with a maximum working pressure of 1700 kPa.

In order to control air pressure, a proportional pneumatic-valve search was performed by Araújo (2007). This author performed tests with a model from FESTO (model VPPE) with a working pressure range of 600 kPa. With it, an open loop valve, the resolution was never inferior to 15 kPa, with is an unacceptable value for testing purposes. Other models were analyzed, with the best found models having a resolution of 0.2 kPa for a maximum range of 100 kPa. This resolution becomes unacceptable for high-pressure ranges and the cost of these equipments were extremely high. Due to these factors the option for a noncommercial solution was taken into consideration.

Since mechanical pneumatic-valves present excellent resolution (0.1 kPa for a full range pressure of 500 kPa), the automation of these elements was performed by Araújo (2007). For that, the use of accuracy stepper-motors was adopted.

a) b)

Figure 2.9: Stress-path chamber (model 12406 from Wykeham Farrance)

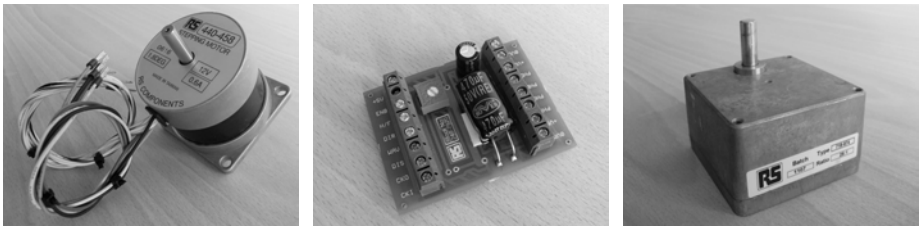

a) b) c)

Figure 2.10: a) Precise stepper-motor, b) electronic device to digitally control the stepper-motors and c) reduction system to reduce step-angle

These motors are developed for applications in which high precision is required, namely robotics and coordinates plotters. For that, a model commercialized by RS-Amidata with reference number 440-458 (Fig. 2.10.a) and the following characteristics, was chosen: step-angle of 1.8°, maximum binary of 0.5 Nm and step-precision of 5 %.

For the control of the stepper-motor, it was necessary the acquisition of an electronic device RSSM2 (Fig. 2.10.b), also commercialized by RS-Amidata with the reference number 240-7920. It consists of a board capable of stepper-motor control through digital inputs for speed, rotation direction and step-type definition.

Since the mechanical pneumatic-valves require a maximum binary of 3.5 Nm, and also a step-precision improvement, a reduction system was used. The chosen one (Fig. 2.10.c), commercialized by RS-Amidata with the reference number 718-874, allows a maximum torque of 4 Nm and a step-angle of 0.036°.

Araújo (2007) performed, with this system, distinct paths to check its efficiency. Control software was developed using LabVIEW® and MATLAB® languages, and two distinct paths were efficiently controlled. For high pressure values a precision reduction was detected but not compromising the efficiency of the system. However, a severe limitation was detected when the applied path involves the simultaneous variation of the mean p and deviatoric q stresses. This limitation was due to adjustments in the reduction system (Fig. 2.9.c) and to the slow response of the stepper-motors. Summing up, the system was able to maintain one of the variables constant while the second one was used to induce cyclic testing.

In order to overcome this limitation, a proportional servo-valve had to be used. In this way, a new search for a high precision proportional pneumatic servo-valve was performed, the solution being found in the commercial model MPV1MFEE060AXL from Proportion-Air, Incorporated (Fig. 2.11). It consists of a close-loop proportional pneumatic-valve with a typical resolution of ±0.02 % for a full range above 600 kPa.

This proportional pneumatic-valve was used to control q stress, while the stepper-motor solution was maintained for p stress. This combination was used since the automated mechanical pneumatic-valves solution presented less oscillation when applying cyclic loading and the proportional pneumatic-valve solution

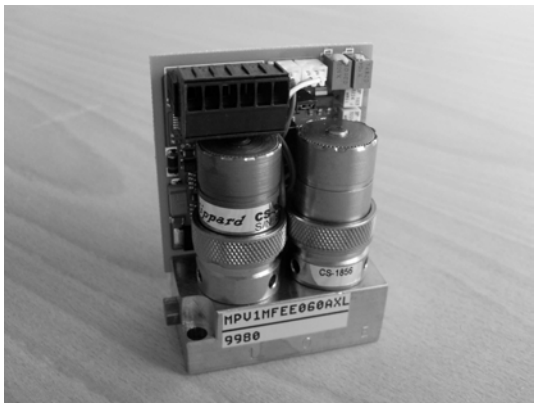

Figure 2.11: Proportional close loop valve from Proportion-Air

presented an excellent behavior when rapid inversion in air pressure is needed. The control signal of this element was computed from the applied value of the stepper-motor so that maximum precision in controlling was achieved.

As performed by Araújo (2007) for the solution with two stepper-motors, several distinct paths were programed in order to evaluate the efficiency of the system. As indicated in Figure 2.12, all paths could now be applied. The only 'limitation' was the slow testing speed. However, this limitation could easily be

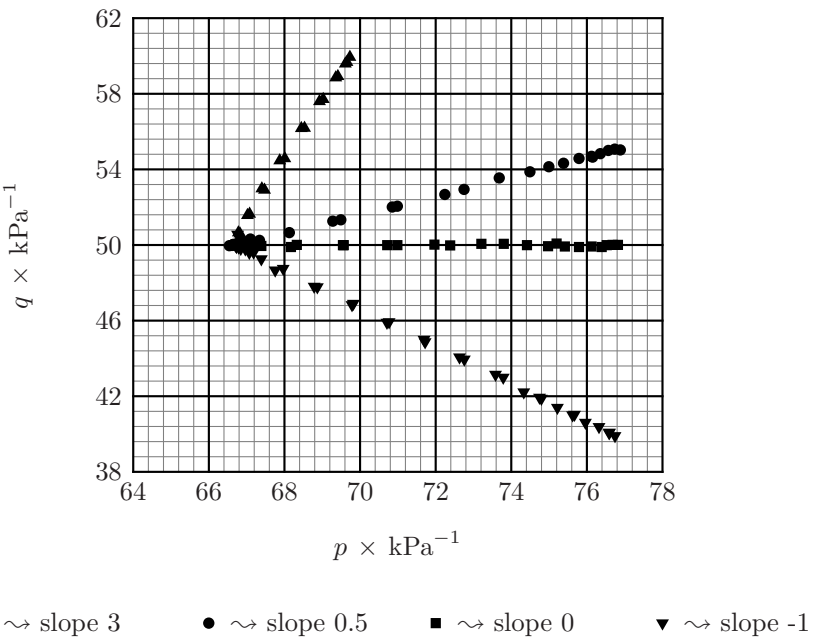

Figure 2.12: Tested stress-paths using one mechanical pneumatic-valves and one proportional pneumatic-valve

overcome with the replacement of the mechanical pneumatic-valves solution for a second proportional pneumatic-valve. Note that this change was not introduced for the previously mentioned reasons. It is however important to refer that the last version of the developed software (see Appendix) allows the simultaneous control of 2 proportional servo-valves and one stepper-motor.

2.5. Study soil

It was intended to study the behavior, in the small strain domain, of a sand designated Perafita sand. It consists in a silty sand, already studied in a bilateral France-Portugal cooperation project, in a 1st phase through 'Instituto Superior Técnico' and in a 2nd phase through UM, with 'Ecole Centrale Paris' (Hadiwardoyo, 2002; Fleureau *et al.*, 2002; Reis Ferreira, 2003).

Based on results presented by Reis Ferreira (2003), the study soil was defined as nonplastic with an uniformity coefficient $U_C = 17$ and a curvature coefficient $C_C = 1.85$ (Fig. 2.13). The specific density was set equal to $G_s = 2.69$. Compaction parameters relative to the modified Proctor test were (Fleureau *et al.*, 2002): optimum water content $\omega_p = 13.2\,\%$, dry unit mass $\gamma_{dmax} = 1890\,\mathrm{kg\,m^{-3}}$ and void ratio $e = 0.42$.

Figure 2.13 shows that a high percentage of small dimension particles, when compared with the grain size curve from previous studies, was present. Grain size studies were performed after removal of particles retained in seeve ASTM #4 in order to remove all gravel particles. In this work all specimens were constructed using the following state conditions: void ratio $e = 0.56$, apparent unit weight $\gamma_n = 18.9\,\mathrm{kN\,m^{-3}}$, degree of saturation Sr = 0.615 and water content $\omega_n = 13\,\%$. The specific density was assumed constant and equal to $G = 2.69$.

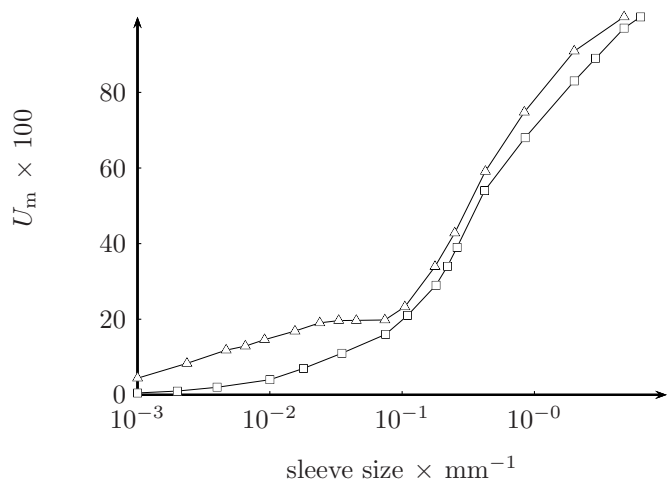

Fleureau *et al.* (2002) $\rightsquigarrow \square$ Araújo (2007) $\rightsquigarrow \triangle$

Figure 2.13: Grain-size distribution studies performed in Perafita sand (Fleureau *et al.*, 2002; Araújo, 2007)

These lower compaction parameters (when compared with the ones presented by Fleureau *et al.* (2002)) were considered to better represent *in situ* conditions, in which unit mass and water content are lower than the ones obtained with the modified Proctor.

2.6. Sample construction and instrumentation

Since there were no specific standards written to define testing procedures for the evaluation of the elastic domain surface, principles from EN 13286-7 'Unbound and hydraulically bound mixtures - Part 7: Cyclic load triaxial test for unbound mixtures' and EN 13286-43 'Unbound and hydraulically bound mixtures - Part 43: Test method for the determination of the modulus of elasticity of hydraulically bound mixtures' were adopted.

Sample construction was performed using a 100 mm diameter by 200 mm height mold (Fig. 2.14.a). In order to guarantee a constant unit mass, its compaction was divided into 5 layers with 4 cm each. Using a mechanical press, and knowing the weight of the material per layer, it was possible to compress the soil until the desired layer thickness was reached. To avoid discontinuity surfaces, before compaction of a new layer, the top surface of the previous layer was subjected to several orthogonal cuts.

Once the compaction of the specimen was completed, it was necessary to create the pseudo-articulations of the LDTs. The use of a small metallic element (Fig. 2.14.b) was necessary in order to guarantee the unification between the latex membrane and the soil. This metallic element was riveted in the soil and glued to the membrane through a low flexibility glue. With this procedure, a fixed point (Fig. 2.14.c) was created, which allowed the use of LDTs for correct measurement of specimen deformation.

The initial height and diameter of the specimen were obtained through an

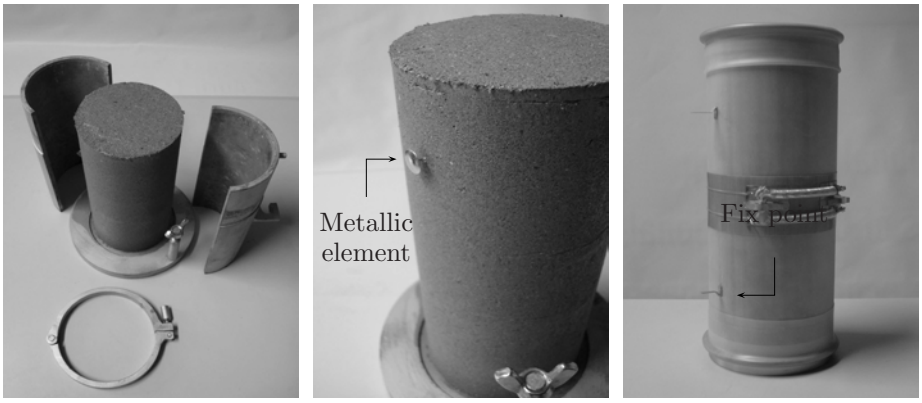

a) b) c)

Figure 2.14: a) Mold used for specimen construction, b) metallic element and c) LDTs pseudo-articulation points

average of 3 measurements, directly made on the specimen after mold removal. After that, the specimen was placed in the triaxial chamber and before starting testing, the initial readings of the transducers were recorded as reference points for the strain calculation. For this step an initial mean stress of 5 kPa was applied to avoid undesirable adjustments in the pseudo articulations of the LDTs. In the initial radial system, specimen diameter could be obtained directly from the LDT existing in the radial measurement system (Fig. 2.15.a). In the direct radial system (Fig. 2.15.b), the initial diameter of the specimen was necessary to calculate the value of α (Fig. 2.2).

Finally, before starting testing, the specimen was consolidated for the intended initial stress state. This consolidation was maintained for a period of a few hours, usually during night period, until strain stabilization was achieved.

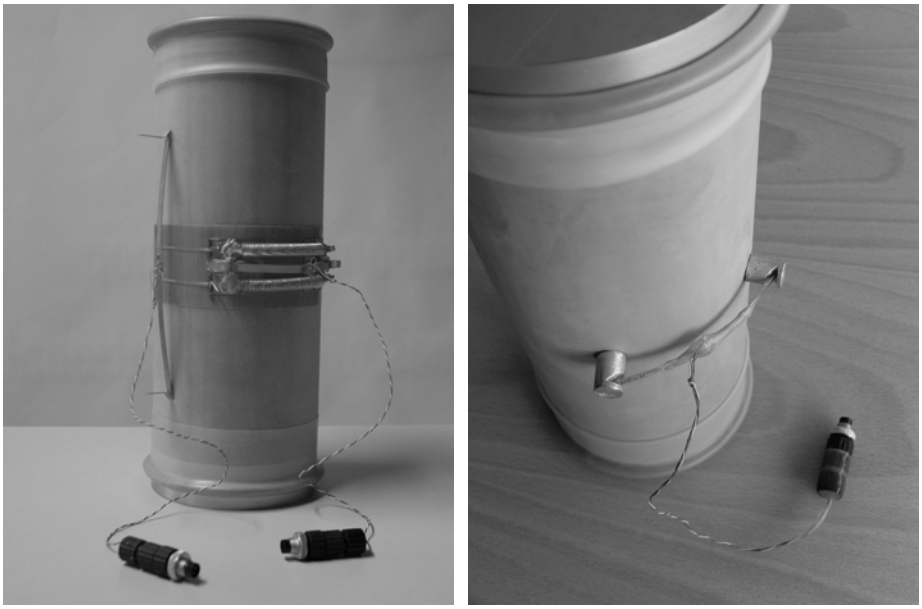

a) b)

Figure 2.15: a) Belt radial measuring system and b) direct radial measuring system

2.7. Testing program

The evolution of the system, as previously referred, was performed in three phases. The first phase, without radial instrumentation and manual control of the applied paths, was performed on three specimens (A, B and C). Results from this testing phase are presented in Araújo (2007) and the testing sequence is indicated in Figure 2.16.a. At this phase, since no automatic control was available, small corrections were not executed and only two distinct stress-paths could be applied (isolated variation in the q stress or in the hydrostatic pressure).

It was also difficult to execute a high number of cycles due to human control.

This initial system was improved by Araújo (2007) with a belt radial system and an automatic control system. In this second phase, human limitations were removed, precision was improved and the applied stresses were effectively controlled. The system was originally developed to allow the application of all stress-paths. However, when the stress-paths required synchronization in the variation of the mean p and deviatoric q stresses, the control was not acceptable. This limitation was due to the use of two automated mechanical pneumatic-valves, unable to apply fast and precise changes in air pressure. Nevertheless, it becomes possible to improve precision in the application of the paths and the execution of a larger number of cycles. Tests performed during this phase are presented in Figure 2.16.b, on 5 specimens (a to e).

During this work, the introduction of an improved radial measuring system and the use of a high precision proportional pneumatic-valve allowed the correct evaluation of ϵ_v strain and the application of any desired path (Fig. 2.12). Testing was performed over 2 specimens (α and β) with a synchronized stress-path (slope equal to 0.5 in $q-p$ space) efficiently controlled on 4 distinct paths (Fig. 2.16.c).

Results from the 1st and 2nd phases are presented in Araújo (2007). Results from the third phase are presented in Figure 2.17 (page 49). Regarding testing order, produced on a same specimen, an index was added to serve as reference (Fig. 2.16). Table 2.1 summarizes the initial state for specimens α and β and ω. Sample ω was used to validate the operationality of the direct radial system. This was achieved with a cyclic test with constant chamber pressure σ_3 of 50 kPa and a cyclic variation of q stress of 4 kPa (Fig. 2.18 in page 50). The range of q stress was chosen so that linear elastic behavior was assured.

It is important to point out that Table 2.1 contains the unit mass and water content measured after specimen preparation and strains related with the initial stress state (before starting cyclic testing).

2.8. Analysis of the results

The analysis of the results was performed to allow the definition of an elastic domain of the material. This elastic domain was defined as the domain in which, during a loading/unloading cycle, the relation between stress and strain remains linear without hysteresis and no permanent strain occurs.

It should be noted that during the 1st and 2nd phases, since the radial system was not truly trustworthy, the elastic domain evaluation was performed with ϵ_a. During the 3rd phase, since good behavior was recorded in the radial measuring system (Fig. 2.18), ϵ_v was used. Nevertheless, it should be noted that since the analyzes are performed in the elastic domain, induced linear variations of ϵ_{a} will induce linear variations of ϵ_{v} and ϵ_{r}.

In Araújo (2007), since modulus definition was intended, stress/strain relation related with slope path of 3 were represented using q stress and for the case of slope equal to 0 (without variation of the q stress) using p stress. In Figure 2.17 all relations are presented in terms of $(p-\epsilon_r)$.

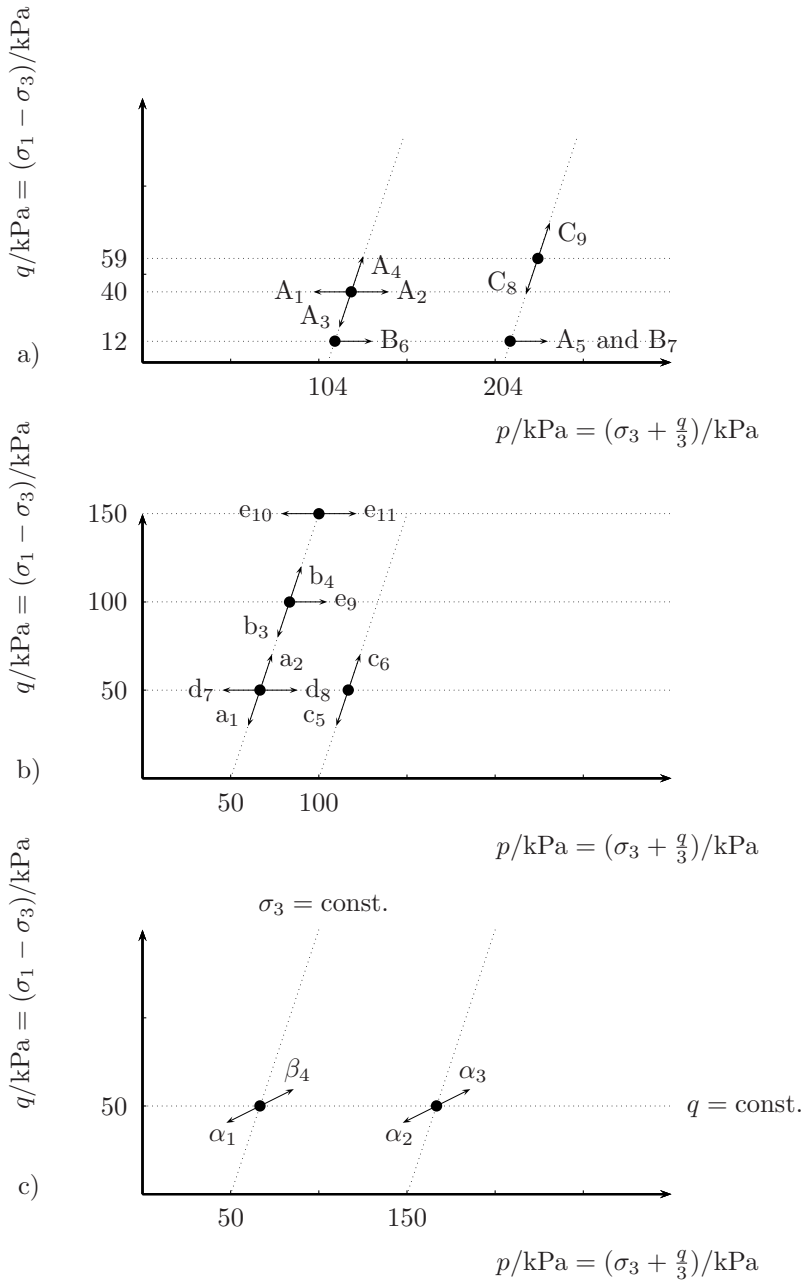

Figure 2.16: a) 1st phase, b) 2nd phase and c) 3rd phase applied stress-paths

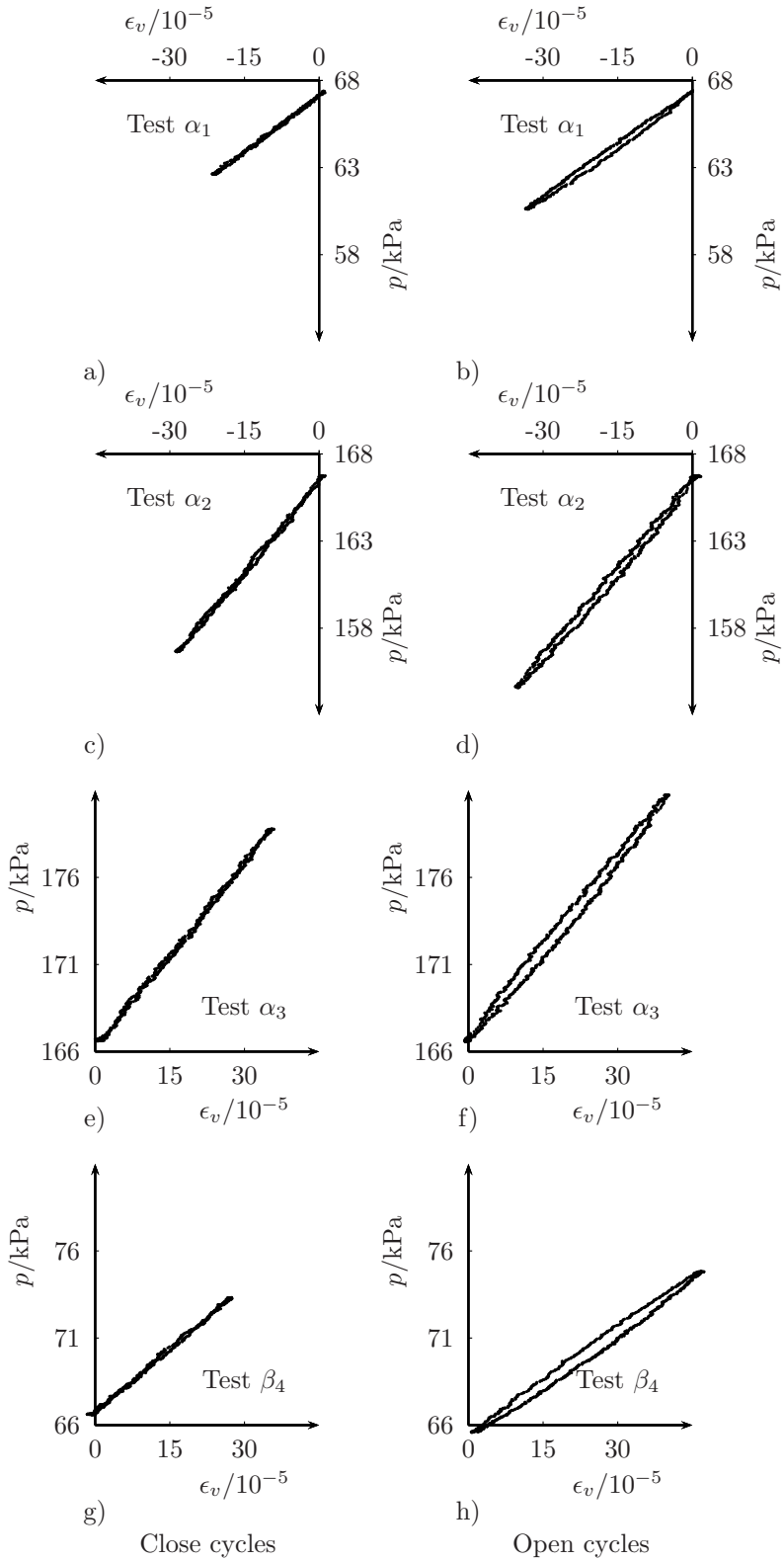

Figure 2.17: Elastic domain evaluation during the 3rd phase

Table 2.1: State conditions of the third-phase specimens during elastic domain evaluation and Poisson's evaluation

Study case	$\gamma/(\mathrm{kN/m^3})$	$\omega \times 100$	$\epsilon_a \times 100$	$\epsilon_r \times 100$
α_1	18.19	12.90	1.38	0.93
α_2	18.19	12.90	1.70	1.70
α_3	18.19	12.90	1.77	1.73
β_4	18.19	12.83	1.16	0.20
ω	18.21	12.66	1.53	0.77

Figures 2.17.g and 2.17.h are used to clarify, for the case of an unloading/loading cycle with an initial stress level of $(p_0, q_0) = (66.7\,\mathrm{kPa}, 50\,\mathrm{kPa})$ and $\Delta q/\Delta p = 0.5$, that an amplitude of 7 kPa in cyclic p induces an elastic behavior but with hysteresis. With a cycle of 5 kPa (also on p) the behavior remains also linear. In this case, the elastic domain was defined as $\Delta p = 5\,\mathrm{kPa}$, $\Delta q = 2.5\,\mathrm{kPa}$ and $\Delta\epsilon_v = 22 \times 10^{-5}$.

All available results obtained for Perafita sand are represented in Figure 2.19. For each initial stress state (• marks in Fig. 2.19) the applied path and the corresponding last elastic linear domain increment was represented. In this Figure it is possible to see that the results obtained in the 1st phase are in accordance with the results of the 2nd phase, thus validating the use of the manual testing procedure. This agreement was expected due to the non influence

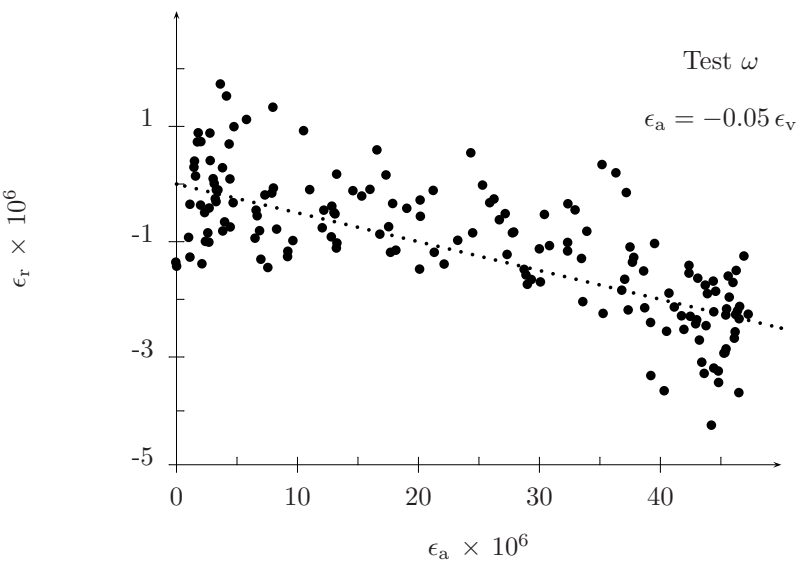

Figure 2.18: Poisson ratio evaluation for radial system validation

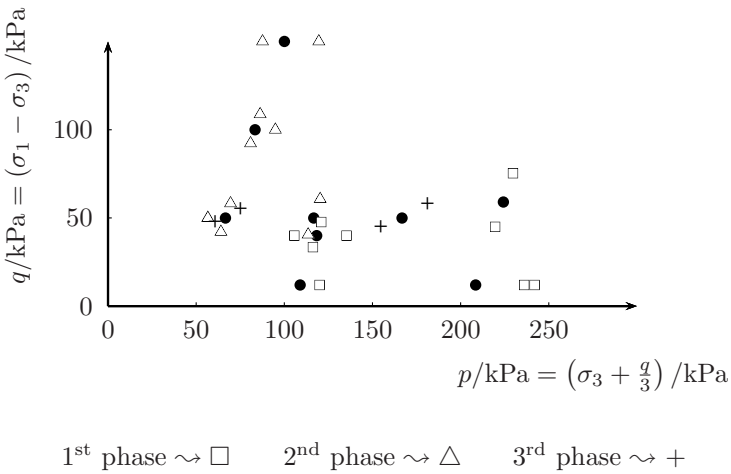

Figure 2.19: Increments that induced elastic domain limits

of the loading velocity on the elastic domain.

The results of Figure 2.19 were divided into three distinct groups in order to become easier to detect major tendencies. In that way, in a first approach, several paths applied from a same initial stress state were analyzed. Subsequently, the influence of p and q stresses in the path increment range was evaluated. Finally, the simultaneous influence of p, q stress and initial stress state was analyzed.

In the analysis of the elastic domain for any given initial stress state (p_0, q_0), it was easily detected that increasing paths require higher increments than decreasing trajectories to reach a hysteretic behavior. Regarding the influence of the p and q stresses, it was detected (particularly in the automated test) that the tendency of variations in p stress was more important to require higher path increments than variations in the q stress to reach the linear elastic domain surface. Taking into account all variables, it was observed that the increasing initial mean stress p_0 required larger increment ranges, for all stress-paths, to reach linear elastic surface, than increasing the initial deviatoric stress q_0.

The definition of the elastic domain was not possible without the simultaneous consideration of the initial stress state and the direction of the applied path. Since the influence of p stress presents a much higher influence that q stress, a normalized surface was produced using the initial value of the mean stress p_0 as reference. A satisfactory surface was obtained, with great practical interest, namely in the perspective of the definition of the constitutive law for the material.

2.9. Summary

Since the stress degrades through the structural layers of the track, a first attempt was made assuming elastic foundation behavior in the numerical model. To check this assumption a laboratory test equipment was developed. For that

it was necessary to select a strain measurement system and to develop a fully automated stress-path triaxial system. The selected transducer was the LDT due to its low cost and high precision. Regarding the stress-path system, it was fully automated by means of proportional close loop valve controlled by means of LabVIEW® software.

The results obtained with this developed equipment have allowed to conclude that the elastic domain limit depends on the initial stress state as well as on the applied stress-path. The initial mean stress p_0 presents a higher influence than the initial deviatoric stress q_0. Also, increments of the applied stress induce larger elastic domains in all path applied in this study. An attempt to obtain a standardized surface was performed using normalized values with the initial mean stress p_0. Even if other trajectories would improve the definition of this surface, all tendencies are already detectable in the present standardized elastic domain surface.

Taking into account the evolution of the domain radius r presented in Figure 2.20 the elastic domain of Perafita sand can be written as Equation 2.4 and is represented in Figure 2.21.

$$r(\alpha) = 0.13 + 0.02\cos(\alpha) - \sin^2(\alpha)\frac{3\alpha + 55}{10^3} \;\; \forall\, \alpha \in [0, 2\pi] \tag{2.4}$$

with r the radius of the elastic domain in $q\,p_0^{-1} : p\,p_0^{-1}$ space and α (in radians) the angular position given in accordance with Figure 2.20.

In the future, it would be desirable to perform tests at higher confining pressures to confirm that the detected tendencies remain. Difficulties were detected when trying to apply them due to limitations of the supply network (limited to 600 kPa) and the use of only half course of the proportional valves (these require an analog input from 0 to 10 V instead of the 0 to 5 V analog output provided by the AD converter). It should also be introduced on the equipment a device to measure suction since these tests were performed on samples with a water content of about 12.8 % water content. Alternatively, future testing should be performed on dry or saturated specimens. Regarding hardware improvements, it could be advantageous to change the specimen geometry from

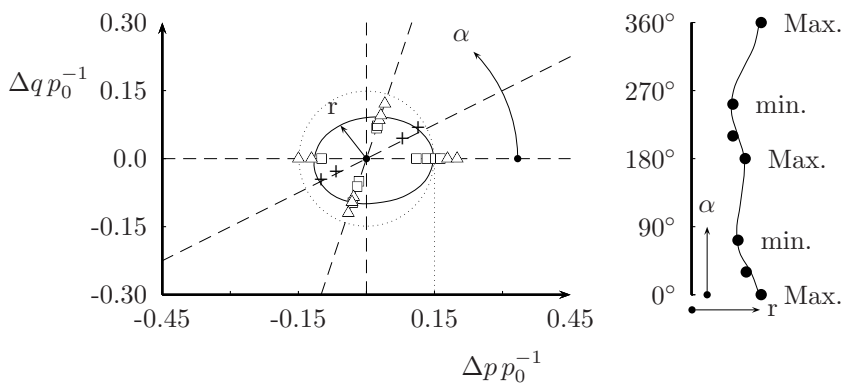

1st phase ⇝ □ 2nd phase ⇝ △ 3rd phase ⇝ +

Figure 2.20: Normalized elastic domain surface

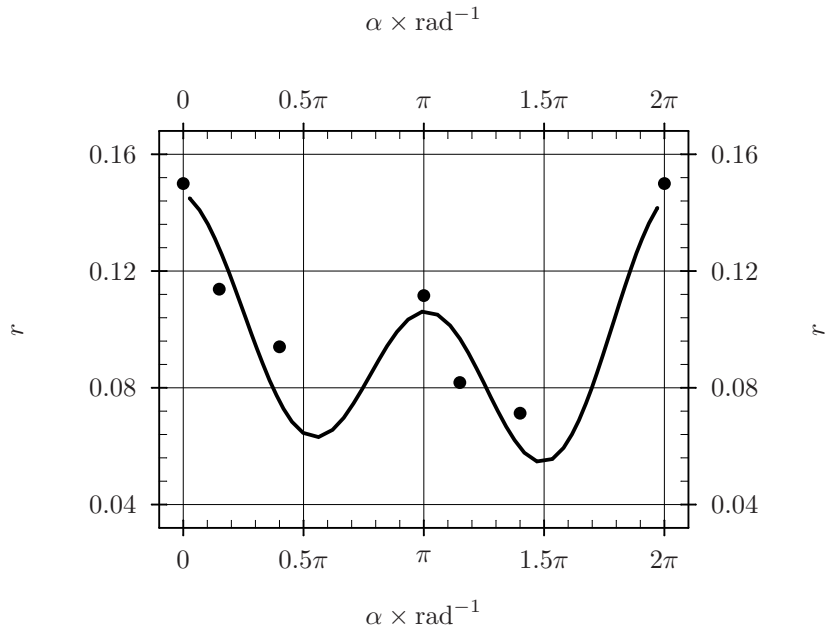

Figure 2.21: Mathematical elastic domain radius of Perafita sand

cylindrical to prismatic (althrough it requires modifications to the stress-path chamber) which allow larger LDT ranges. To conclude, testing with the latest developed software (see Appendix - page 171) should be performed to verify the efficiency of the simultaneous use of two proportional servo-valves (mainly in terms of testing speed).

This page was intentionally left blank.

Stress-path evaluation: elastic behavior

3.1. Introduction

As referred in Chapter 1, the development of calculation methods aimed at predicting the behavior of geotechnical structures (as HST railway lines) to repeated loading requires the formulation of a cyclic constitutive law for the constituent soils. Such a law may be expressed within the framework of (visco)-plasticity, involving the usual concepts of yield conditions, hardening and flow rules. The essential parameters governing the cyclic behavior may be experimentally identified, based on repeated triaxial loading tests performed on homogeneous specimens of material. Actually a significant amount of experimental data is available for describing the cumulative permanent deformations of granular materials subject to cyclic loading. Nevertheless, the calculation methods derived from the incorporation of such data remain somewhat crude. This is due to the fact that most of the cyclic constitutive laws only used the evolution of the axial permanent strain as a function of the number of load cycles. Very few indication is given regarding the lateral component, an essential information for formulating a fully three-dimensional constitutive law (Abdelkrim *et al.*, 2003).

Summing up, the efficient determination of the residual state of the structure and the cumulated settlement as functions of the traffic load require the combination of three elements (Abdelkrim *et al.*, 2003):

1. a computational tool for determining the reference stress-path cycle at any point of the structure as a function of the traffic loading characteristics;

2. the formulation of a cyclic constitutive law derived from laboratory tests conducted for each type of material and for various cyclic loadings;

3. a numerical procedure for calculating the residual state of the structure, and more particularly the residual settlement, from the knowledge of the cumulated permanent strain field.

Thus, in order to predict the residual state of HST railway lines, the reference stress-path must be determined. In this Chapter, measurements in a real railway line are presented and used in the calibration of a frequency domain numerical model. Parametric studies were performed to evaluate the influence

of the soil impedance in the direction of the reference stress-path. Results are then discussed and the influence of linear elastic constitutive law assumption analyzed.

3.2. Mathematical formulation

The problem of moving load has received considerable attention in the field of train induced vibrations (e.g. HST). Several analytical and numerical models using the finite elements (FEM) and boundary elements method (BEM) are actually under development. They mainly differ in two aspects (Clouteau *et al.*, 2001): the excitation mechanisms that are incorporated (quasi-static axle loads, parametric excitation, transient excitation due to rail joints and wheel flats and excitation due to wheel and rail roughness) and the way dynamic soil-structure interaction is accounted for (through soil coupling of the sleepers and the ballast).

In this work, the mathematical formulation assumes that the vehicle is moving at a constant speed C_{t}, in a fixed direction y, that the properties of the track and soil do not change in that direction (in this cases, the track-soil system is called translation invariant), that soil is horizontally layered and unbounded in the normal direction z, that displacements and strains remain sufficiently small (inside surface Y_1 in Figure 2.2.a) to allow the use of linear models and that excitations due to wheel flats and/or rail roughness is neglectable.

Since the system is translation invariant, the analyzes for the overall system is replaced by a generic periodic cell using the Floquet decomposition method. In order to take into account a structure interacting with a soil half-space, Clouteau *et al.* (2000) proposed a new method which allows 3D unbounded generic cells. This approach, initially developed for the study of the dynamic response of structures subjected to 3D seismic loading, was extended to the case of moving loads by Chebli *et al.* (2004, 2006).

Thus, since the model takes advantage of the Floquet and Fourier transformations, these mathematical formulations are exposed in the Appendix (see page 165). The periodic formulation; the track-soil interface; and the moving load mathematical principles are also presented in Appendix. Notice that the model was developed to compute the dynamic response (assuming linear elastic behavior) and neglected static excitations, i.e., it computed the increments of displacement induced by the dynamic load but ignore those induced by the weight of the structure and foundation. For that reason no stress field initialization is present in this Chapter.

3.3. Site characterization

In order to validate the numerical model, a HST railway line site had to be chosen. Special attention was paid to soil characterization and published *in situ* measurements. So, since six weeks before the inauguration (in December 1997) of the HST railway line between Brussels and Paris, the Belgium railway company required to Katholieke Universiteit Leuven (KUL), homologation tests during the passage of a Thalys HST at speeds ranging from $160\,\mathrm{km\,h^{-1}}$ to $330\,\mathrm{km\,h^{-1}}$, the site was chosen for model calibration.

That unique opportunity was used by Degrande (2000), professor at KUL, to perform free field vibration measurements on the track and in the far field. The *in situ* measurements were performed near Ath, 55 km south of Brussels, where train reaches its maximum speed. A complete characterization of the train, track and foundations was made by that author and is presented in the following Sections. *In situ* measurements were also made available and used for validation.

3.3.1. Thalys HST characteristics

According to Degrande (2000), a Thalys HST (Fig. 3.1) consists of 2 locomotives with 8 carriages, with a total train length of 200.18 m. The locomotives are supported by 2 boogies and have 4 axles. The carriages next to the locomotive share one boogie with the neighboring carriage, while the other 6 carriages share both boogies with neighboring carriages. The total number of boogies is 13 and, consequently, the number of axles on the train is 26. The carriage length l_t, the distance l_b between boogies, the axle distance l_a, the total axle mass m_t, the sprung axle mass m_s and the unsprung axle mass m_u of all carriages are summarized in Table 3.1.

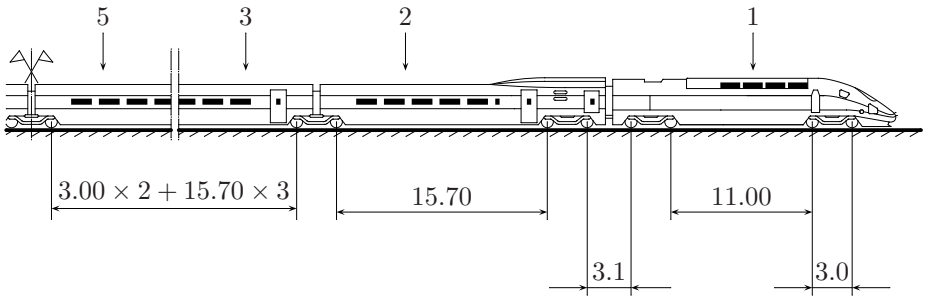

Figure 3.1: Thalys geometry

Table 3.1: Thalys physical and geometrical characteristics (Degrande, 2000)

Thalys component	Locomotive	Side carriage	Side carriage
# components	2	2	6
# axles	4	3	2
l_t/m	22.15	21.84	18.70
l_b/m	14.00	18.70	18.7
l_a/m	3.00	3.00	3.00
m_t/kN	166.77	142.25	166.77
m_s/kN	149.77	124.33	148.82
m_u/kN	17.00	17.95	17.91

3.3.2. Track characteristics

The HST railway line between Brussels and Paris is a classical ballast track. Degrande (2000) described it as having continuously welded UIC60, with a mass per unit length of $60\,\mathrm{kg\,m^{-1}}$ and a maximum moment of inertia of $0.3038 \times 10^{-4}\,\mathrm{m^4}$, fixed with Padroll E2039 rail fixation system on precast prestressed concrete monoblock sleepers with 2.5 mm length, 0.285 m width, 0.205 m height (under the rail) and a mass of 300 kg. Flexible rail pads with 0.01 m thick and a static stiffness of about $100\,\mathrm{MN\,m^{-1}}$, for a load ranging from 15 kN to 90 KN, are placed between the rail and the sleeper. The track is supported by a porphyry ballast layer (caliber 25/50, layer thickness 0.3 m), a limestone or porphyry layer (caliber 0/32, layer thickness 0.2 m) and a limestone supporting layer (caliber 0/80 to 0/120, layer thickness 0.5 m to 0.7 m).

3.3.3. Foundation characteristics

During the homologation tests, geophysical prospection tests have been performed, allowing an estimation of the variation and of the dynamic stiffness in the top layers and of a material damping ratio for an 'equivalent' homogeneous half-space that exhibits similar attenuation at the surface of the test site.

A SASW was performed to determine the dynamic soil characteristics of the site (Dewulf *et al.*, 1996). A transient excitation was generated by dropping a mass of 110 kg from a height of 0.9 m on a square (side 0.7 m) steel foundation with a mass of 600 kg.

Three horizontally stratified half-spaces were detected, with the top layer having a thickness of 1.4 m and a shear wave velocity of $80\,\mathrm{m\,s^{-1}}$, the middle layer a thickness of 1.9 m and a shear wave velocity of $133\,\mathrm{m\,s^{-1}}$, and a half-space layer with a shear wave velocity of $226\,\mathrm{m\,s^{-1}}$, all in good agreement with the layering revealed by borehole experiments. The track was built after an excavation with a depth of a few meters, where the soil was stabilized. As the SASW was performed on the unexcavated soil away from the track, Degrande (2000) suggested that the soil under the track could be assumed stiffer than the soft shallow layer revealed by the SASW test.

Apart from the variation of the stiffness with depth, an estimate of the hysteretic material damping was required. The cone penetration tests and the SASW tests reveled that the site was not homogeneous, ξ being expected to vary with depth. However, a classical Barkan expression for a homogeneous half-space was used by Degrande (2000). With it a simple inversion problem was solved in order to allow the definition of ξ equals to 3 %.

3.3.4. Site geometry

Figures 3.2 and 3.3 present the assumed geometrical characteristics of the HST railway line and the foundation. It consists of a symmetrical two-line ballast track with an assumed capping layer thickness of 0.5 m. These figures summarizes the information provided by Geert Degrande.

Other required physical and geometrical characteristics were not quantified during site characterization, but assumed based on published data on HST railway lines, namely in Schmitt (2005). These characteristics can be found in Tables 3.2 and 3.3, in which the assumed values are marked with *. Notice that

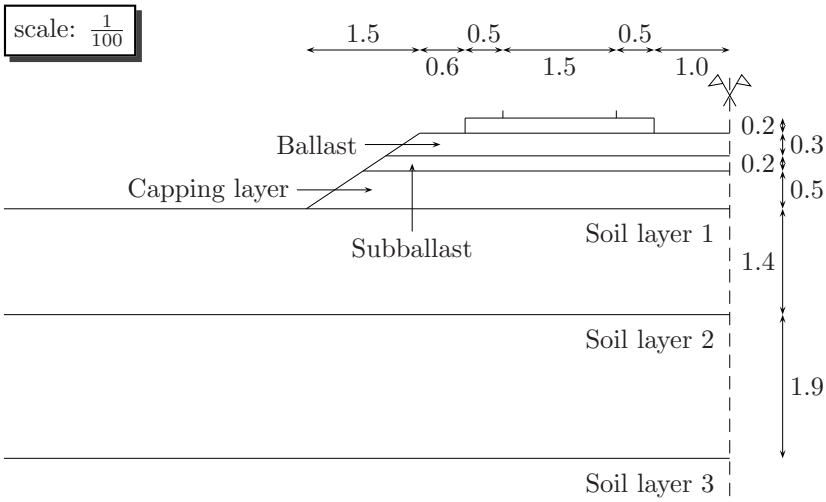

Figure 3.2: Section geometry of the two lines HST railway line between Brussels and Paris

a low value of damping ratio (around 1%) since low strains levels were admitted to occur in the structure and foundation layers.

3.4. Model construction

Model construction was done with the assumption of modeling both track lines. The HST railway line is composed of two lines, in which a HST train moves along one of them. However, during model calibration it was detected that accelerations in the unloaded line were present, this behavior being undetected in the *in situ* measurements presented by Degrande (2000). This inadequates behavior was due to the assumed linear elastic constitutive law that allow traction as well inadequate periodic modes used to obtain the final response. So,

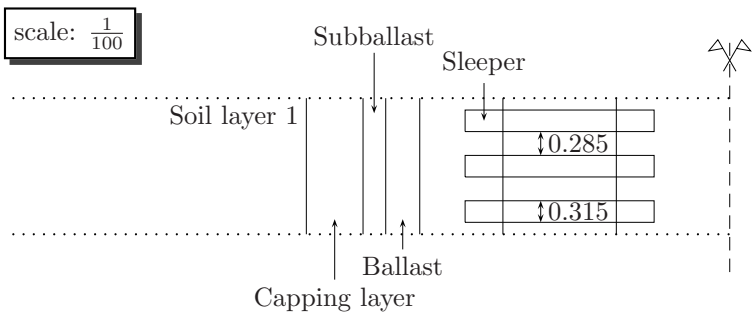

Figure 3.3: Plan geometry of the two lines HST railway line between Brussels and Paris

Table 3.2: Geometrical, physical and geotechnical characteristics of the track

Component	Parameter	Value
sleeper	ν	$0.2^\star$
	E_0/GPa	$30.0^\star$
	$\gamma_n/(kN/m^3)$	20.15
pad	k/(MN/m)	100.0
rail	A/m^2	76.8×10^{-4}
	$I_2^\dagger/m^4$	3055.0×10^{-8}
	$I_1^\dagger/m^4$	512.9×10^{-8}
	I_t/m^4	$100.0^\star$
	$\gamma_n/(kN/m^3)$	$76.52^\star$
	ν	$0.3^\star$
	E_0/GPa	$210.0^\star$
ballast	d/m	0.3
	$\gamma_n/(kN/m^3)$	$17.66^\star$
	ν	$0.1^\star$
	E_0/MPa	$200.0^\star$
	ξ/%	$1.0^\star$
subballast	d/m	0.2
	$\gamma_n/(kN/m^3)$	$21.58^\star$
	ν	$0.2^\star$
	E_0/MPa	$300.0^\star$
	ξ/%	$1.0^\star$
capping layer	d/m	0.5
	$\gamma_n/(kN/m^3)$	$21.58^\star$
	ν	$0.2^\star$
	E_0/MPa	$400.0^\star$
	ξ/%	$1.0^\star$

(see Fig. 1.2) † (admitted value) *

in order to improve simulation, only one track was represented using the geometry presented in Figures 3.4 and 3.5. With this consideration the incorrect influence of the unloaded line was removed since the periodic modes used in the computation became more realistic.

As previously referred, the domain decomposition method was used to independently simulate the track-structure and soil sub-domains. In that way the track-structure domain, composed by rail, sleeper, pad, ballast, subballast and capping layer was modeled using FEM elements. The two rails were simulated

Table 3.3: Physical and geotechnical characteristics of the foundation

Component	Parameter	Value
soil layer 1	ν	0.3
	$\xi/\%$	3.0
	$C_\mathrm{p}/(\mathrm{m/s})$	187.0
	$C_\mathrm{s}/(\mathrm{m/s})$	100.0
	$\gamma_\mathrm{n}/(\mathrm{kN/m^3})$	18.15
soil layer 2	ν	0.3
	$\xi/\%$	3.0
	$C_\mathrm{p}/(\mathrm{m/s})$	249.0
	$C_\mathrm{s}/(\mathrm{m/s})$	133.0
	$\gamma_\mathrm{n}/(\mathrm{kN/m^3})$	18.15
soil layer 3	ν	0.3
	$\xi/\%$	3.0
	$C_\mathrm{p}/(\mathrm{m/s})$	423.0
	$C_\mathrm{s}/(\mathrm{m/s})$	226.0
	$\gamma_\mathrm{n}/(\mathrm{kN/m^3})$	18.15

using Bernoulli beams while pads were represented as springs. All volume elements were simulated with 8 node volumetric elements. Since only a reference periodic cell was needed in the simulation, the number of used elements was

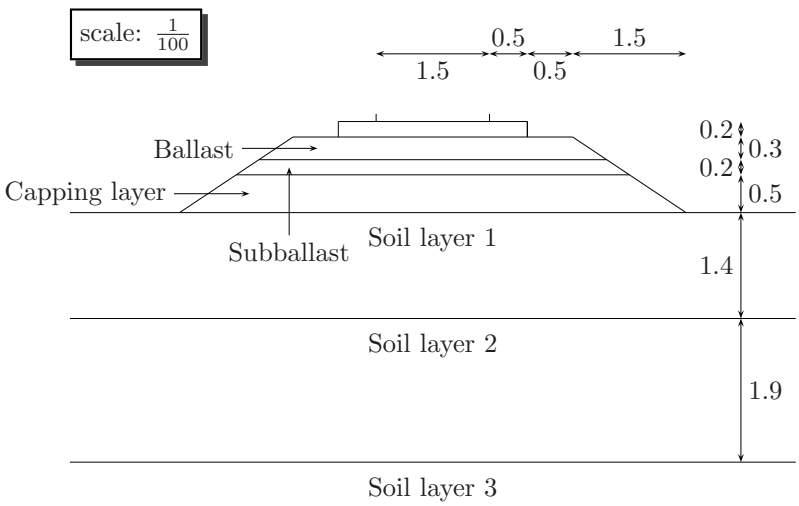

Figure 3.4: Section geometry used in the simulation

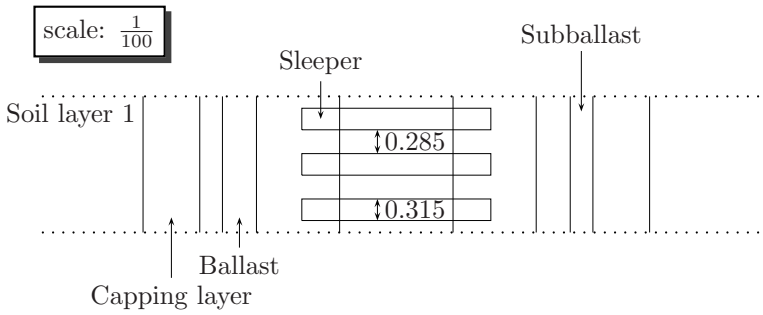

Figure 3.5: Plan geometry used in the simulation

considerably reduced without any loss of precision: 8 beam elements for the rail, 6 springs for the pads and 920 volumetric elements for the remaining track components. From this last ones 48 were used to simulate the sleeper, 264 the ballast, 176 the subballast and 440 the capping layer. Notice that no particular attention was needed during the definition of the mesh since few elements were needed to define with high precision all the elements of the structure (in opposition to the model developed in Chapter 5)

Figure 3.6 presents a perspective view of the reference periodic cell mesh used in the simulation. It becomes apparent that even with few elements used, the model allows the definition of sleeper geometry, spacing between sleepers, rail gage and embankment geometry.

After mesh building, the evaluation of the periodic modes was required. To do so, the evaluation of the eigenvalues and eigenvectors was performed, attending that only some particular eigenvectors could be used. Since periodic condition was assumed during the mathematical formulation, stiffness and mass matrices were modified in order to introduce this condition.

Eigenvectors were evaluated in MATLAB® after imposing, in the stiffness and mass matrix, a horizontal displacement equal in both sides of the elementary cell perpendicular to rail direction. The number of periodic modes to be used had also to be defined, in this case as a function of the frequency range that the model should represent. As the train load was considered as quasi-static and corrugation was despise, high frequency responses were not considered in the model. It should be noted that high frequencies contents are much more relevant in the far field, mainly in the form of vibration and noise, than in points near the rails.

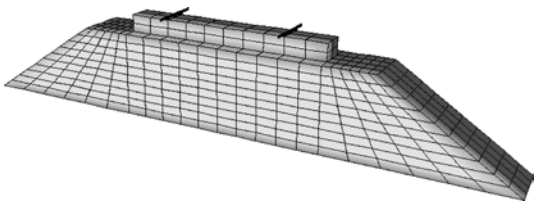

Figure 3.6: Reference periodic mesh

Due to this, an analysis up to 120 Hz was considered sufficient and the periodic modes necessary to correctly represent the response in this frequency range were calculated. According to Rubin criterion, all modes with eigenvalues inferior to 180 Hz should be considered to correctly simulate the response from 0 Hz to 120 Hz. In all performed simulations 58 periodic modes were considered, being the first 4 rigid modes (3 translations and 1 rotation). Figure 3.7.a illustrates the first nonrigid periodic mode used in the simulation presenting an eigenvalue of 17 Hz. The value of the eigenvalue associated to the last periodic mode (Fig. 3.7.b) was 268 Hz, superior to the value provided by Rubin criterion.

Some particular periodic modes were also introduced and are noted in this work as static modes. These, characterized by presenting high eigenvalues, were obtained assuming that the eigenvector was periodic and the horizontal displacements in the 2 nodes of the springs that represent pads were equal. Since 6 springs with 2 degrees of freedom were used, 12 static modes were obtained. The first one, illustrated in Figure 3.8.a, presents an eigenvalue of 380 Hz while the last one (Fig. 3.8.b) presents an eigenvalue of 9466 Hz. These modes, with high eigenvalues, were considered since they allow model to take into account the rail and sleeper vibration modes. This inclusion was performed since this periodic modes were assumed to influence the low frequency response (even if they present eigenvalues quite superior to those study by the numerical model). However, in this particular case, its contribution was quite small. Regarding the half-space, special Green functions were used (through MISS) to allow energy propagation.

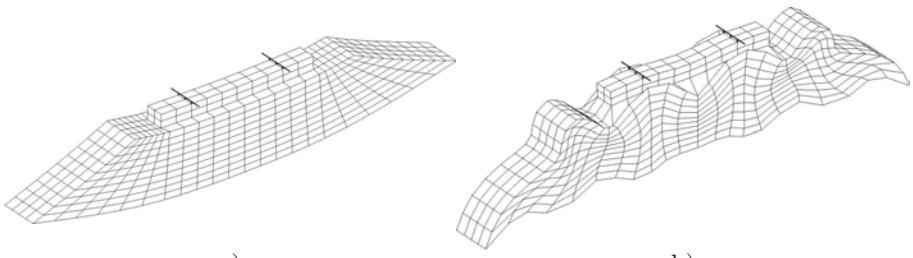

a) b)

Figure 3.7: a) First and b) last nonrigid periodic modes used in the simulation, with eigenvalues of 17 Hz and 268 Hz

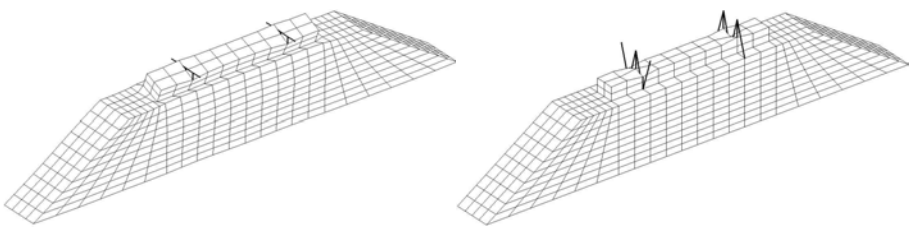

a) b)

Figure 3.8: a) First and b) last static modes used in the simulation, with eigenvalues of 380 Hz and 9466 Hz

As last remark, the following periodic modes presented the following eigenvalues (in Hertz): 17.2, 26.6, 28.9, 42.9, 47.5, 53.8, 69.1, 69.1, 72.8, 90.7, 91.8, 107.8, 111.4, 113.0, 116.8, 119.1, 132.3, 132.4, 135.5, 140.2, 153.7, 154.0, 154.4, 162.1, 163.6, 167.7, 174.9, 176.4, 179.6, 180.0, 190.9, 194.7, 196.6, 201.7, 203.7, 207.0, 209.8, 218.8, 219.2, 222.6, 226.5, 227.0, 229.9, 231.0, 237.7, 243.8, 245.2, 247.9, 248.2, 254.8, 257.4, 262.5, 266.7 and 268.6. Regarding the static modes, the eigenvalues were: 380, 395, 420, 496, 636, 691, 2394, 2394, 2422, 2422, 9466 and 9466.

3.5. Model validation

During the validation process, was noticed a high influence of soil stiffness on the overall system response. Due to that and since track stiffness was controlled during construction, four distinct cases were studied for soil stiffness in order to quantify its influence in the evolution of the stress-path. Degrande (2000) also referred that, due to foundation treatment, its stiffness could be considered higher than the values presented by the *in situ* tests.

Thus, 4 distinct cases were defined to analyze model reliably. The first of them assumed the conditions published by Degrande (2000), with 3 soil layers, the last one being considered infinite. A second one was used to quantify the sensitivity of the model to the presence of a bedrock layer. For that, a simplified case was studied, assuming that track structure was resting directly on the bedrock. The last two cases were used to consider the low strain level in the foundation (possible in linear elastic domain). For that, high value for the Young modulus was assumed. The difference between these two cases rests on the presence, at a depth of 10 m, of a bedrock layer.

3.5.1. Measurements filtering

In order to perform a valid comparison, it should be noted that numerical modeling was defined for a maximum frequency of 120 Hz. For that reason, measurements performed *in situ* were previously filtered in order to allow a reliable comparison.

During this process and from a first interpretation of the *in situ* results presented by Degrande (2000), attention recalls in the peak value present for sleeper acceleration, around 3g (Fig. 3.9), i.e., 3 times the gravitational acceleration. With this value of acceleration, it is expected to occur projection of the ballast nearby the sleeper.

Truncation was applied to obtain the response from 0 Hz to a maximum frequency of 120 Hz. This process was performed in MATLAB® by means of a Fast Fourier Transform (FFT). After this step, all values higher tan 120 Hz were removed before adding the conjugate part of the spectrum. In the end, through the use of an Inverse Fast Fourier Transform (IFFT), filtered measurements were converted to time domain.

From the analyzes of Figure 3.9, it becomes clear that the frequency range between measurement and simulation must agree. For this case study, filtering the *in situ* measurement induced a reduction in the amplitude of almost 300 %, clearly relevant for the comparison.

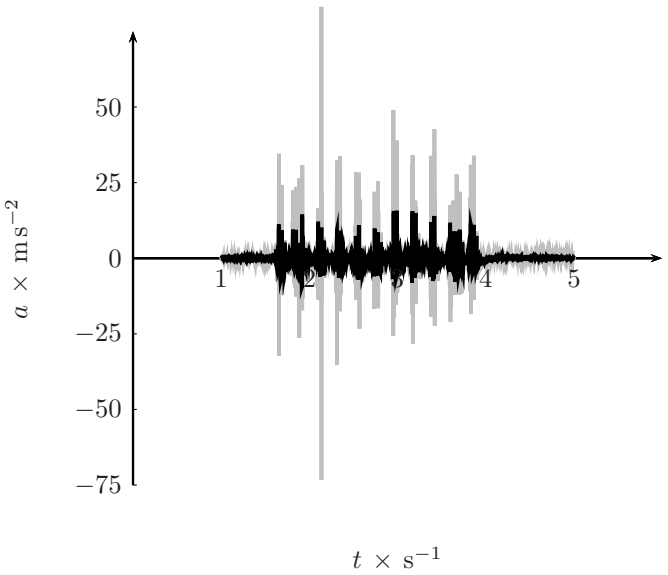

In situ measurements ⇝ gray (without filter) — In situ measurements ⇝ black (with 120 Hz lowpass filter)

Figure 3.9: Influence of signal filtering in sleeper acceleration

3.5.2. Simulation efficiency

For the validation process, and considering that stress-paths are controlled by displacements and not by accelerations, it would be advised to use is situ results in terms of displacements. However, test campaigns are usually performed with accelerometers. This is due to difficulties in obtaining a fix reference point for the displacement transducers, an inexistent problem when using accelerometers.

Degrande (2000) performed measurements using accelerometers and, through integration, obtained velocities in several points in track structure and far field. The integration process was performed using MATLAB® scripts developed at KUL and based on Fourier transformations (i.e., integration in the frequency domain). These scripts were also used in this work to obtain sleeper velocity. It could also be used to obtain sleeper displacement but, since it requires double integration, results were not considered reliable. It should be pointed out that this response in terms of velocity must be used with caution since it is not a direct measure. It consists on a transformation from the acceleration response, presenting that way influences on the used technique (in this case the KUL scripts) and also from measurement noise that produces signal drift. The ideal solution would be the *in situ* measurement of displacement transducers for deflections and geophones for the velocities.

Figures 3.10 to 3.13 (pages 66 to 67) allow the comparison, in terms of acceleration and velocity, between model simulations and *in situ* measurements. The FFT was performed using MATLAB®, that does not take into consideration the signal time step. Since the output of the FFT transformation was considered without the multiplication factor included by the time step, a double *yy* axle graphic was used.

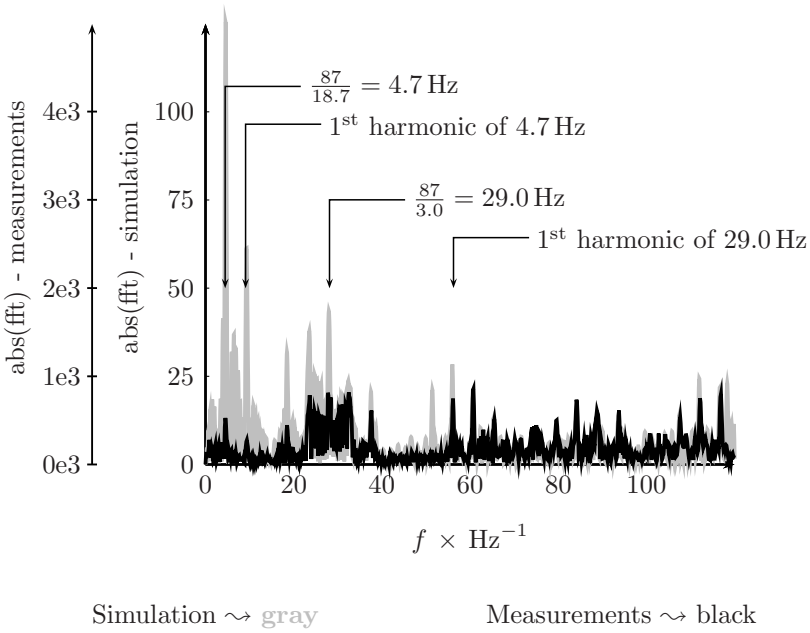

Simulation ⇝ gray Measurements ⇝ black

Figure 3.10: Comparison, in the frequency domain, between the measured and simulated acceleration

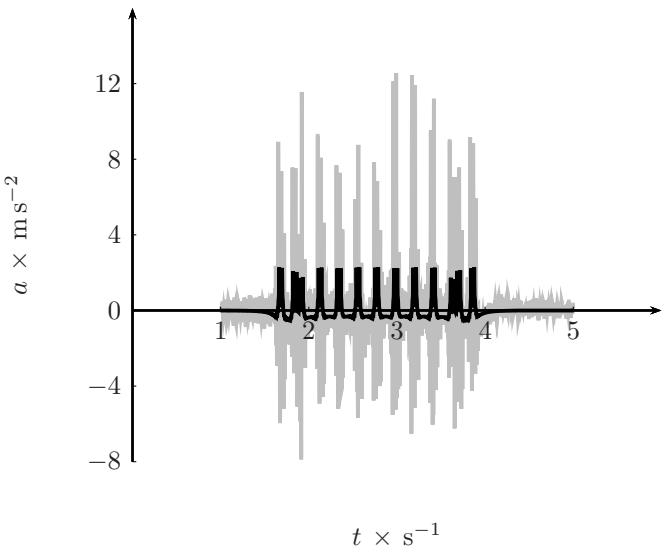

In situ measurements ⇝ gray (with 120 Hz lowpass filter) Simulation ⇝ black

Figure 3.11: Comparison, in the time domain, between the measured and simulated acceleration

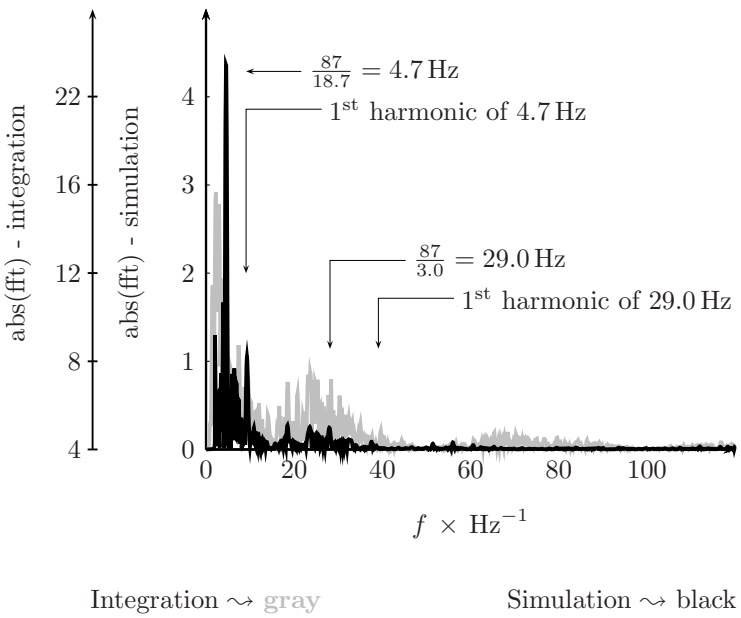

Figure 3.12: Comparison, in the frequency domain, between the simulation and integrated velocity

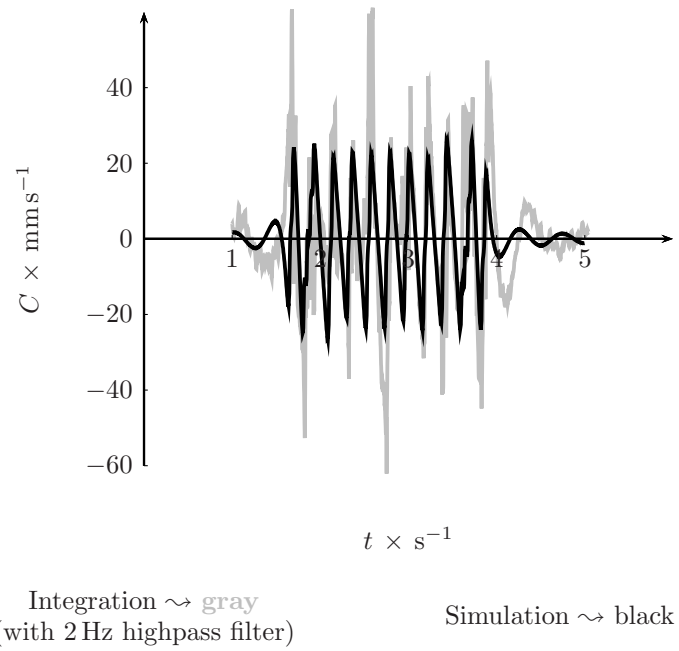

Figure 3.13: Comparison, in the time domain, between the simulation and integrated velocity

The comparisons were performed in the sleeper, the best element in the railway structure to obtain reliable measurements. Nevertheless, comparisons in the ballast, subballast and capping layer were also desirable but not performed since *in situ* measurements were not available. This is due to the difficulty of correctly measuring acceleration in a discontinuous medium, mainly in one like the ballast layer.

Measurements in the far field were performed but were not used in this work since, as previously indicated, the model is not developed for that purpose. It should be pointed, however, that it possesses the potentiality to predict vibrations in far points from the railway structure. In order to do that, modifications were required, mainly in terms of a variable train load and rail imperfections consideration (e.g., corrugation, wheel out-of-roundness). However, since the study of the far field response was not the purpose of this thesis, but the stress evolution near the rail, these modifications were not introduced.

From the analysis of Figure 3.11 it was detected a low level on the acceleration peaks (around $3\,\mathrm{m\,s^{-2}}$) when compared with the one from the *in situ* filtered measurements (around $8\,\mathrm{m\,s^{-2}}$). This low level in the acceleration is due to the low values, when compared with the ones from the measurements presented in Figure 3.10, in the frequency spectrum bellow 20 Hz. Regarding the fundamental frequencies, one can see that the ones correlated with the distance between axles (29 Hz) and boogies (4.7 Hz), were well captured. Also its harmonics were reasonably captured.

The low level detected in sleeper acceleration can be due to the influence of mechanism that produces high frequency contents, not considered in the simulation but which influences the study in the frequency range. It should be pointed out that some were considered in the simulation (rail and sleeper vibration) through the use of the static modes. The consideration of this mechanics should improve the simulation in terms of acceleration. However, considering that adjustment in terms of acceleration does not necessarily affect the response in terms of displacement (which effectively controls stress-path), it was decided to focus attention on the adjustment in terms of velocity. This consideration was performed since, for velocity, even for high frequencies, the influence of those mechanisms is not so relevant. Their influence is reduced since the velocity spectrum is correlated with the acceleration by means of the inverse value of the frequency. In case of the displacement field, the influence of the high frequencies content is even smaller since it is correlated with the acceleration spectrum by means of the inverse power value of the frequency.

From the analyzes of the fundamental frequencies in the velocity spectrum (Fig. 3.12), a very good adjustment is detected on axle and boogie fundamental frequencies. Regarding harmonics, adjustment is reasonable. In terms of comparison in time domain (Fig. 3.13) a good adjustment was also obtained. This comparison, even if performed with an integrated signal from the acceleration measurement, provides a good entrust on model operationality. Considering that the influence of high frequencies is even smaller in the displacement field, model was considered proper to predict stress-path evolution.

To conclude the validation, one last verification was performed, since the integration of measured acceleration had required a lowpass filter of 2 Hz to avoid velocity drift. Since in Figure 3.13 the predicted velocity was previously subject to a highpass filter, the influence of this filtering was quantified in Figure 3.14. For that, the comparison between the original signal (without the highpass filter)

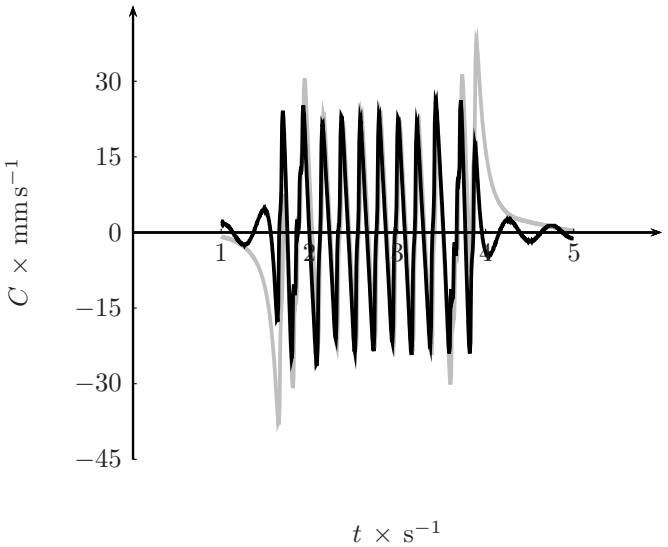

Simulation ⇝ gray (without filter) | Simulation ⇝ black (with 2 Hz highpass filter)

Figure 3.14: Influence of signal filtering in velocity simulation

and the filtered one (with a highpass filter of 2 Hz) was performed. As expected, the use of a highpass filter does not significantly changes the response since it is only used to remove drift and does not compromises the use of the integration technique.

3.6. Model parametric studies

Once the model validation process completed, a parametric study based on the foundations stiffness was performed. This study was performed in order to verify the numerical model capacity to properly consider the influence of the foundation stiffness on the evolution of the stress-path due to the passage of a HST. The parametric study was divided, as previously referred, into 4 distinct cases. These cases are:

1. Foundation assumed with the characteristics presented by Degrande (2000) and Degrande and Lombaert (2000). No bedrock was detected in the *in situ* testing and all soil layers presented low Young modulus values, around 70 MPa. This case is graphically represented in Figures 3.15 to 3.18 by means of a solid line.

2. Foundation assumed as a stiff soil, with a Young modulus of 200 MPa. This case, represented by a bold dash line, was considered to quantify the influence of a possible foundation treatment that increases soil stiffness, and even due to the assumption that low strain levels were reached in the foundation, consequently inducing high values of the Young modulus.

3. Foundation assumed as a stiff soil (equal to the one presented in case study 2) and resting over a bedrock layer at 10 m depth. The Young modulus of the bedrock layer was assumed equal to 30 GPa and the case study represented by a dash line.

4. Track structure resting directly on the bedrock layer. This case, represented by a dotted line, was considered to allow the interpretation of the stress-path from soft (case 1) to stiff (case 4) foundation.

All results are presented in Figures 3.15 to 3.18 (pages 70 and 72) and it interpretation was performed in terms of acceleration, velocity and displacement. Regarding acceleration, Figure 3.15 presents the acceleration obtained due to the passage of the entire train for the first 5 axles. From it analyzes it can be pointed out that the model was not sensitive to modifications in the foundation stiffness. This limitation reveals that the model requires the introduction of a new mechanism in order to improve acceleration prediction. However, the implementation of such mechanisms was not performed since the efficiency of the model to predict velocity and displacement was considered correct (and consequently stress). Such implementation would require developments that were beyond the objective of this thesis, that is the stress-path evolution due to the passage of a HST.

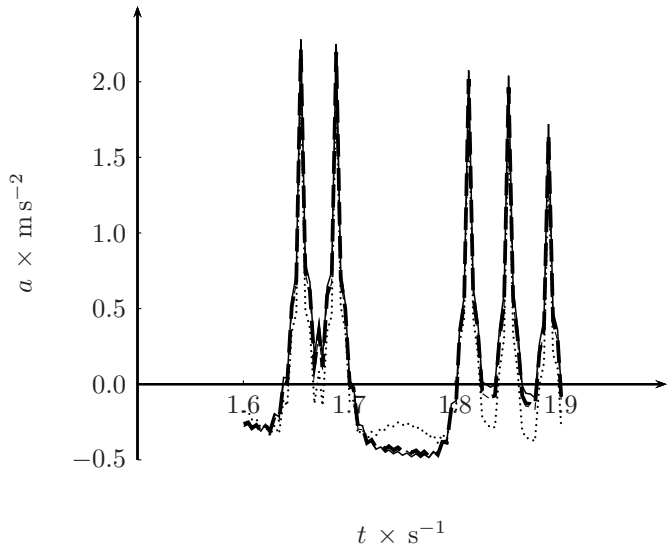

Soft soil ⇝ line | Stiff soil ⇝ **dash** (without bedrock) | Stiff soil ⇝ dash (bedrock at 10 m) | Bedrock ⇝ dots

Figure 3.15: Vertical acceleration of the sleeper (first 5 axles)

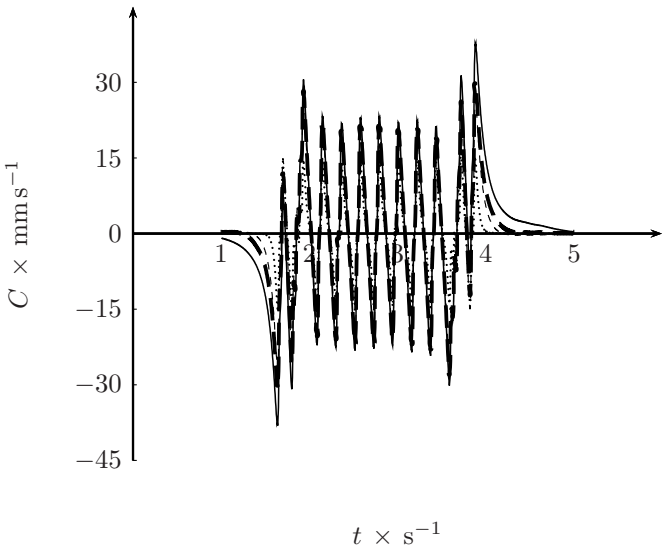

Soft soil ⇝ line | Stiff soil ⇝ **dash** (without bedrock) | Stiff soil ⇝ dash (bedrock at 10 m) | Bedrock ⇝ dots

Figure 3.16: Vertical velocity of the sleeper

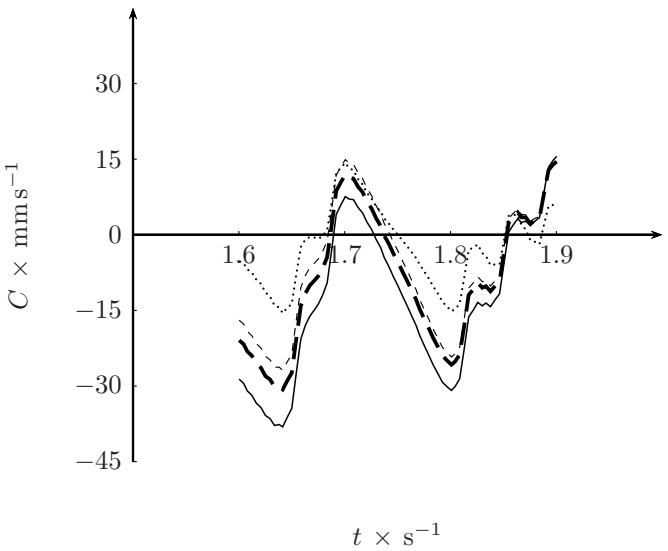

Soft soil ⇝ line | Stiff soil ⇝ **dash** (without bedrock) | Stiff soil ⇝ dash (bedrock at 10 m) | Bedrock ⇝ dots

Figure 3.17: Vertical velocity of the sleeper (first 5 axles)

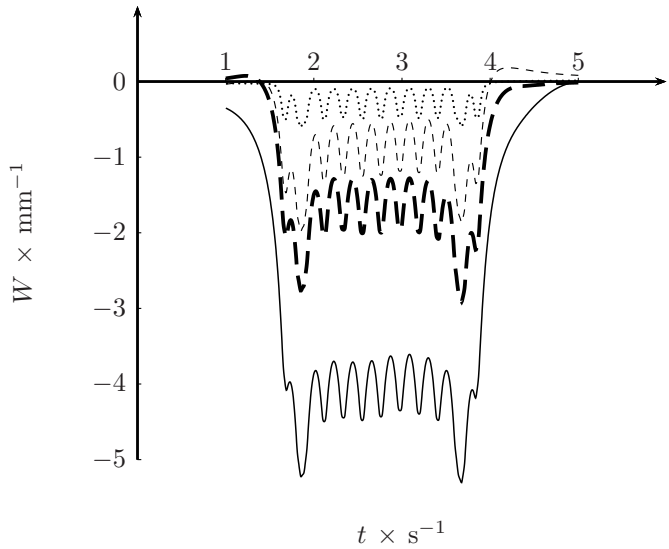

Soft soil ⇝ line | Stiff soil ⇝ **dash** (without bedrock) | Stiff soil ⇝ dash (bedrock at 10 m) | Bedrock ⇝ dots

Figure 3.18: Vertical displacement of the sleeper

From the interpretation of Figures 3.16 and 3.17, significative influence of the foundation stiffness were obtained, namely, that a stiff foundation induces smaller velocities. This behavior can easily be understood since sleeper displacement is smaller. The introduction of a higher value of the Young modulus (case study 2) induces a velocity reduction of nearly 25 % (Fig. 3.17) when compared with the foundation configuration presented by Degrande (2000) (case study 1). The 'predicted' low strain level in the foundation corroborates the neglectable reduction in velocity recorded with the introduction of the bedrock layer at 10m depth (case study 3). As pointed out in Chapter 2, the precise quantification of the Young modulus of the material can significantly improve the quality of the simulation and, consequently, reduce costs during construction by improving design capacities. Regarding case study 4, as expected, the velocity level presents its smallest values.

Figure 3.18, the most relevant since displacements induce direct variations of the stress field, presents most interesting results. Starting by the case configuration presented by Degrande and Lombaert (2000) (case study 1), maximum deformation reached by the sleeper (around 5 mm) is assumed overdo. This assumption is based on results obtained in other sites for which HST provides an average deformation level around 3 mm. With the assumption of a high foundation stiffness (case study 2) with a Young modulus of 200 kPa, a reasonable deformability modulus (assuming low strain levels) for a stiff foundation, maximum sleeper displacement is reduced by 40 %. Regarding case study 3, with the consideration of the bedrock layer at 10 m depth, the reflection of energy waves was observed. This effect is visible in the positive displacements presented in Figure 3.18 after train passage. The inclusion of the bedrock also reduces the deformation level to around 0.8 mm.

Summing up, a high value of foundation stiffness appears to be needed, as indicated by Prof. Degrande. About the existence of a bedrock layer, no conclusion can be taken since displacement measurements do not exist to verify the existence of wave reflection. Nevertheless its presence was well captured by the numerical model. Predicted results corroborated HST railway line expected behavior regarding foundation stiffness and, with it, confirmed the model capacity to study the stress-path evolution due to the passage of a HST.

3.7. Stress-path evaluation

The main purpose of this Chapter is to present and discuss the representative stress-path induced by the passage of a HST. For that, 5 points under the intersection rail/sleeper were used in the simulation. For each one of these points, 4 distinct stress-paths were obtained as result of the parametric study. The value of the foundation stiffness changed according to the cases described in page 70. These case studies were used to quantify the influence of the foundation stiffness on the slope of the representative stress-path.

Three of the five studied points were placed in the middle of the railway structure components, namely: ballast, subballast and capping layer. The 2 remaining points were studied in the capping layer; one in the top and a second one in the bottom of this layer. These extra points were added since capping layer presents the higher thickness and also because during this study path slope on this layer was highly influenced by the stiffness of the foundation.

Results are presented in Figures 3.19 to 3.23 (pages 74 to 76), in a $q : p$ space (see Eqs. 3.1 and 3.2, where σ_1, σ_2 and σ_3 are the principle stresses), being each of them used to represent all paths obtained in a certain point. In order to clarify interpretation, a Critical State Line (CSL) with slope $M_{\text{cs}}(\phi)$ (Eq. 3.3) and a Natural State Line (NSL) with slope M_0 (Eq. 3.4) were added to the representation. This critical state line was represented assuming ϕ equal to 45 ° and the natural state line with an impulse coefficient of $k_0 = 0.5$. Attend that the numerical model just provide the dynamic response, being the initial stress state defined as function of depth and k_0.

$$p = \frac{\sigma_1 + \sigma_2 + \sigma_3}{3} \tag{3.1}$$

$$q = \sqrt{\frac{(\sigma_1 - \sigma_2)^2 + (\sigma_2 - \sigma_3)^2 + (\sigma_3 - \sigma_1)^2}{2}} \tag{3.2}$$

$$M_\phi(\phi) = \frac{6 \sin \phi}{3 - \sin \phi} \tag{3.3}$$

$$M_0(k) = \frac{3(1-k)}{1+2k} \tag{3.4}$$

In a first approach, comparison was performed assuming that foundation stiffness, on any study point, was not relevant for the definition of the stress-path slope. With this assumption in mind, two analyzes were performed.

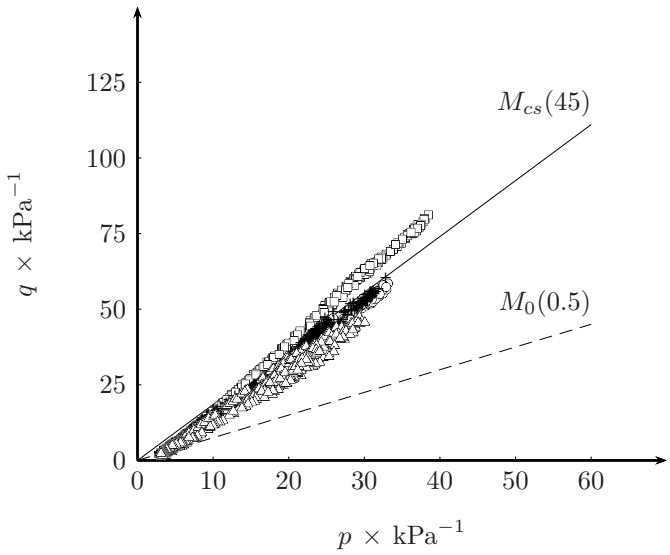

Soft soil $\rightsquigarrow \triangle$ Stiff soil $\rightsquigarrow \circ$ (without bedrock) Stiff soil $\rightsquigarrow +$ (bedrock at 10 m) Bedrock $\rightsquigarrow \square$

Figure 3.19: Ballast stress under the external rail

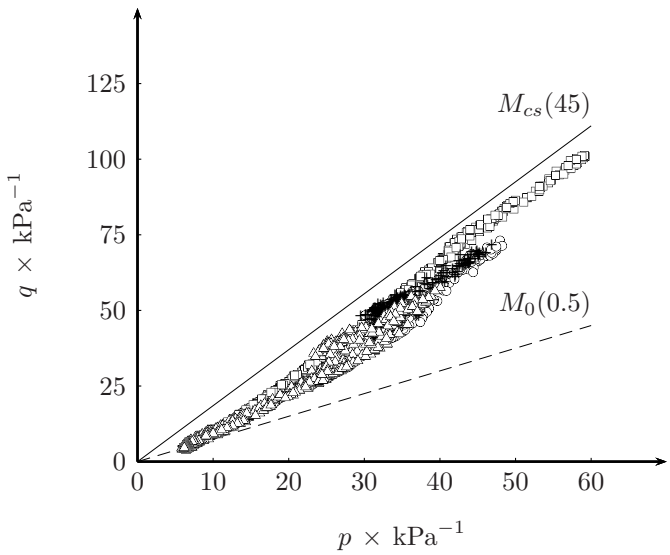

Soft soil $\rightsquigarrow \triangle$ Stiff soil $\rightsquigarrow \circ$ (without bedrock) Stiff soil $\rightsquigarrow +$ (bedrock at 10 m) Bedrock $\rightsquigarrow \square$

Figure 3.20: Subballast stress under the external rail

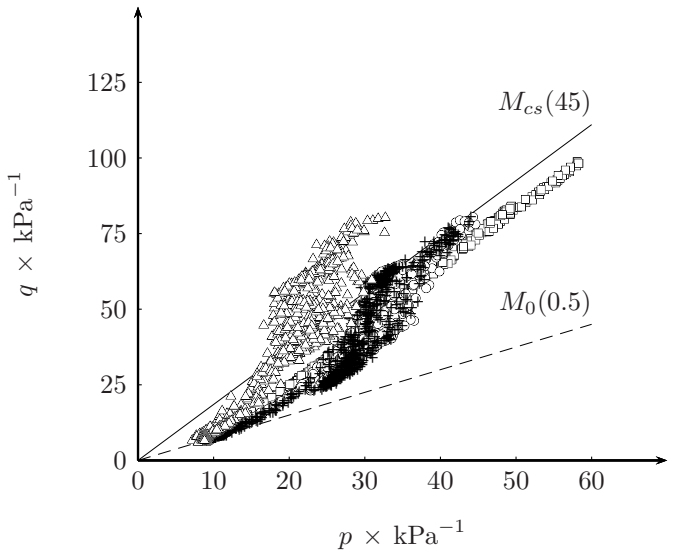

Soft soil $\rightsquigarrow \triangle$ Stiff soil $\rightsquigarrow \circ$ (without bedrock) Stiff soil $\rightsquigarrow +$ (bedrock at 10 m) Bedrock $\rightsquigarrow \square$

Figure 3.21: Capping layer stress (top) under the external rail

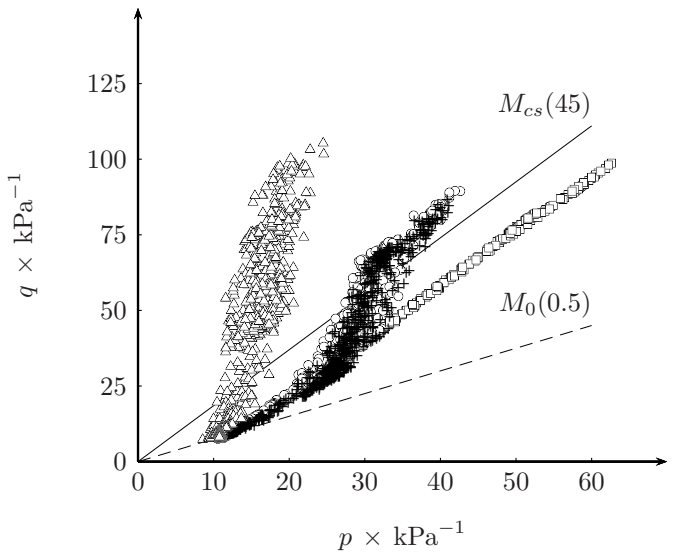

Soft soil $\rightsquigarrow \triangle$ Stiff soil $\rightsquigarrow \circ$ (without bedrock) Stiff soil $\rightsquigarrow +$ (bedrock at 10 m) Bedrock $\rightsquigarrow \square$

Figure 3.22: Capping layer stress (middle) under the external rail

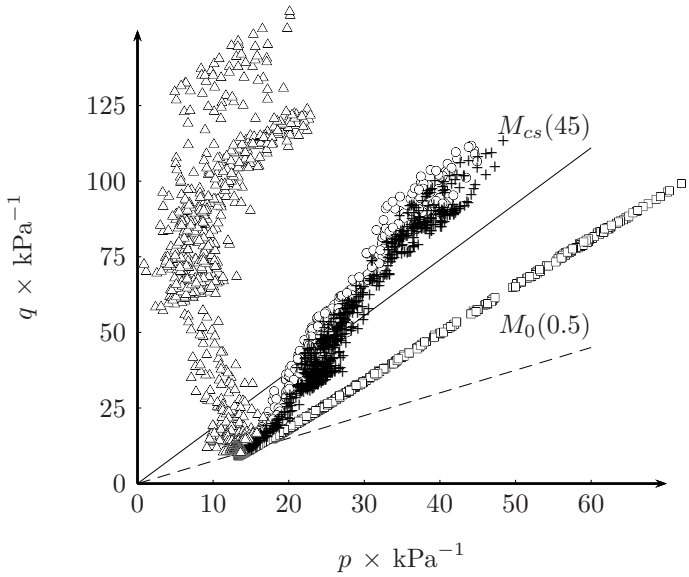

Soft soil ⇝ △ Stiff soil ⇝ ○ (without bedrock) Stiff soil ⇝ + (bedrock at 10 m) Bedrock ⇝ □

Figure 3.23: Capping layer stress (bottom) under the external rail

1. Assuming that the study point is not relevant for path definition, results cannot be generalized since opposed tendencies appear. In fact, based on results obtained in the ballast layer, maximum path slope was obtained when foundation stiffness was also maximum. However, based on results on the capping layer, this trend is inverted, i.e., maximum path slope was obtained with minimum foundation stiffness.

2. Assuming a fixed foundation stiffness in all study railway points produces same incongruence. If foundation stiffness is low (case study 1), slope increases from the capping layer to the ballast layer but, if the foundation is stiff (case study 4), slope decreases.

This analysis clarifies that path slope cannot be interpreted from the individual analysis of the railway study point or from the foundation stiffness. The interpretation must take into consideration both parameters simultaneously. In order to do so, the railway track structure was considered as a large 'beam' resting on the foundation. So, due to the passage of the HST, this 'beam' introduces horizontal stress due to bending. Taking as reference point the case of a stiff foundation (case 4), were bending of the railway structure is highly conditioned, horizontal stress appears by means of Poisson effect. Due to it, slope variation was not so significative and the highest value was found on the ballast layer. A reduction on the foundation stiffness introduces the bending 'effect' on the HST railway line. This 'effect' produces extra horizontal compression on the ballast layer and horizontal tractions on the capping layer. Due to this, the horizontal stress decreases from top to bottom if foundation stiffness decreases, and induces a path slope grow. This 'effect' was so more visible and significative as more flexible the foundation becomes.

3.8. Summary

Using a 3D frequency domain model with the objective to evaluate stress-path and validate the assumption of elastic behavior of materials it was possible to identify several limitations of the elastic model to reproduce field data of the case study. That data was collected near Ath, on the HST railway line from Paris to Brussels and used for model validation. From it comparison with simulation results, one notice that fundamental frequencies of the measurement signals were captured but the range of the simulated acceleration was low. Regarding velocity, simulation measurements match with accuracy the results obtained from the integration of acceleration response. The difference between measured and simulated acceleration are due to the incapacity of the model (as defined) to simulate high frequency modes. However, since only the near field (with a main response defined by low frequencies) was here subject of study and since velocity simulation presents good accuracy, the model was considered valid for stress evaluation. In fact, since the frequency contend of displacement and stress is even lower than the one present in velocity, model can be considered valid. Regarding the displacement response in time domain, no *in situ* measurements were available for calibration. Double integration was not used because signal was filtered near zero, which removes the static component of the response, and measurement noise induces excessive drift.

Focusing on the interpretation of the mobilized stress, bending on the structure occurs and induces a reduction of the mean stress. This effect does not exist if foundation is assumed stiff but is pronounced if foundation is soft. This behavior was expected but it may be amplified due to the elastic assumption. This increase in path slope can induce unrealistic slopes such as the one present in the capping layer for the case of a low stiffness foundation, where stress-path overcomes an assumed failure envelope ($\phi = 45°$).

Summing up, in cases where the deformability of the foundation is high, stress-path was found constant for all points of the track structure with a slope, in $\Delta q/\Delta p = 1.85$. When foundation stiffness is low, path slope remains equal to 1.85 on the ballast layer and grows, with depth, for a pure deviatoric stress on the capping layer. This characteristic path is intended to be used in laboratory but, for more reliability and to clarity why an overcoming of the critical state line occurs, plastic studies are found desirable to validate tendencies found along this Chapter.

This page was intentionally left blank.

Cyclic plastic modeling

4.1. Introduction

In order to overcome the limitations and validate the tendencies observed in the linear elastic model used in the previous Chapter, a more realistic numerical model must be used. I order to do so, a constitutive law able to correctly simulate the non-linear relation between stress and strains, as well as correctly quantify volumetric variations of the materials that compose the railway structure, was adopted. Through out this Chapter the bases of the model, as also a description of its parameters was exposed. The model was used to simulate three distinct materials, each one introduced to represent one railway layer, namely: ballast, subballast and capping layer. All of them were aims of the manual calibration and, as for the case of the capping layer, it was also part of a preliminary study with an optimization technique. The calibration performed in this work were performed to allow the development of an 3D non-linear model (Chapter 5).

4.2. Fundamental concepts

It is accepted by the scientific community that the granular materials show special deformation characteristics such as (Zhu *et al.*, 2006): anisotropy, dilatancy/contractancy, hardening/softening and complex behavior under cyclic loading. Consequently, constitutive laws should be able to simulate these behaviors. To clarify, and before exposing the models definition, the characteristic of each one is presented:

1. regarding dilatancy/contractancy, and assuming for the sake of clarity a moderate packed granular specimen undergoing continued deformation, an initial densification is usually followed by a dilatation. Any volumetric change is usually expressed by the so called dilatancy coefficient which is defined as the ratio of the velocity normal to the slip line to the velocity along the slip line (Zhu *et al.*, 2006). This dilatancy coefficient depends on the stress level and the density, and is therefore not constant.

2. granular materials exhibit an anisotropic response when subjected to elastic or inelastic strains since the response is dependent on the study direction. Since the fabric of granular materials evolves, in the course of

deformation to increase its resistance to the continued deformation, hardening occurs. Dense granular material specimens have a higher strength than loose ones, thus in the course of deformation, dilatancy transforms a specimen from dense to loose and leads to material softening.

3. experimental observations suggest that upon unloading, a granular specimen exhibits a plastic response and that the dilatancy rate suffers a discontinuous change from a positive value to a negative one. The microstructure of the granular materials adjusts itself so as to increase its resistance to the applied deformation (loading). This is the source of material hardening.

To allow the simulation of this complex behavior, the development of modern soil plasticity laws were started based on the pioneering work of Drucker, Gibson and Henkel, who first introduced the ideas of volumetric hardening and closed yield surface, and on the theoretical and experimental work of researchers from the University of Cambridge (Roscoe *et al.*, 1958), who provided the framework of critical state soil mechanics, in which elastoplastic models for soils could be developed. Based on their work, and during the last decades, significant progress has been made in the improvement of these models to predict the mechanical behavior of soils, namely by introducing various concepts such as: the double yield surfaces (Lade, 1977), the bounding surface (Dafalias and Herrmann, 1982), the anisotropic hardening rule (Mroz and Pietruszczak, 1983) and the endochronic intrinsic time (Valanis and Peters, 1991). Despite all these important contributions, three basic ingredients of critical state soil mechanics should always be considered:

1. there is a line in $e : \ln p'$ space in which all stress-paths of a normally consolidated clays lie, which is referred to as the normal consolidation line (NCL). The interest of this line is that it provides a volumetric hardening rule which can be generalized to general stress conditions;

2. there is a line in $e : \ln p' : q$ space where all residual states lie, regardless of the type and the initial conditions, which is referred to as the critical state line (CSL). The projection of this line on the $(e, \ln p')$ plane is parallel to the NCL, and divides initial states into 'wet' and 'dry', depending on whether they lie in the space between both lines or not. At this line, shear deformation takes place without change of volume;

3. stress-paths resulting either from consolidated drained and undrained tests lie on an unique state surface referred to as the 'Roscoe Surface'. This fact was found experimentally by Henkel during the 60's, who plotted the water content contours obtained in drained tests and found that undrained tests paths followed these lines as well. This fact is not directly applicable by elastoplastic models, as these isolines are not yield surfaces corresponding to constant values of the hardening parameter but it provides a hint of the type of yield surface.

Even though modern plasticity models are based on a rational mechanical process, a simplified method for dynamic analyzes, based on the pioneer works of Seed and I.M. (1970), and designed by equivalent-linear approach, is still used

in practical engineering applications. It only requires the knowledge of the variation of shear modulus and material damping ratio with shear strain by means of $G : \gamma$ and $\xi : \gamma$ curves, in opposition to modern plasticity models, in which the parameters definition is hard. Lopez-Caballero *et al.* (2007) referred that in some cases the rheological models do not necessarily have physical parameters possible of laboratory characterization. Simultaneously, dynamic properties of the soils are not usually available due to high cost of *in situ* laboratory testing. Wu *et al.* (1996) performed an inspection of the relevant literature and detected that the capacity of plastic models is gained by sacrificing the simplicity. This is manifested by the involved mathematical formulations and the increasing number of material constants due to the complex behavior of granular materials, namely: strong non-linear stress-strain relations, pressure sensitivity, shear and volumetric coupling and dilatancy volume change. Regardless of this hard parameter definition, the use of simplified methods as the equivalent-linear approach should be avoided. For instance, Wu *et al.* (1996) performed a literature review and detected that void ratio or other equivalent variables (e.g. density) have rarely been included in the constitutive models, being that an unsatisfactory situation. As an exception, the author referred the Cam-Clay model developed by the Cambridge soil mechanics school (Roscoe *et al.*, 1958), where the size of the yield surface is allowed to change with the void ratio. Wan and Guo (1998) also referred that the role of void ratio and stress in granular soil behavior is fundamental in modern plasticity.

In opposition to the equivalent-linear approach, one can refer to the development of micromechanical models (Liao *et al.*, 2000; Kruyt and Rothenburg, 2002; Chang and Hicher, 2005). According to Chang and Hicher (2005), micromechanical models could generally be classified into two categories. The first category is plasticity models with a fabric tensor, in which the material parameters of plasticity are defined at the macro (particle assembly) level. A fabric tensor is used to represent the anisotropy of the packing structure and material parameters are made to be functions of the fabric tensor so that the effects of the packing structure for granular materials are included. The second category is the microstructural plasticity model, in which the material parameter is defined at a micro (inter-particle) level. The basic idea is to view the packing as represented by a set of micro-systems. The inelastic behavior of each micro-system is characterized and the overall stress/strain relationship of the packing is obtained from an average of the behaviors of micro-systems. If the micro-systems are regarded as inter-particle planes (or mobilized planes) in the packing, then the approach is similar to that used in the modeling elastic behavior.

According to Chang and Hicher (2005), the microstructural approach is attractive conceptually, because it dispenses in having to deal with relations between the stress and strain tensors. Only a simple relation between the vectors of forces and relative displacements on a contact plane is required, which thus requires fewer material parameters. The stress and strain tensors are automatically obtained by integration over all spatial orientations. Aside from the modeling simplicity, the microstructural approach is more realistic, especially for the stress induced by the inherent anisotropy. Furthermore, it can capture the slip deformation on each plane, thus developing automatically the anisotropy induced from a stress application. Nevertheless, according to Wan and Guo (1998), a continuum approach which consists of using a macroscopic constitutive model based on plasticity theory, together with some stress dilatancy rule,

still remains the most useful framework due to its flexibility towards finite element modeling. The use of a microstructural model is still very demanding in matters of time and computational effort.

Inside modern continuum plastic constitutive models, some aspects are still part of the targets of discussion. For instance, according to Wu *et al.* (1996), there are some potential difficulties in applying elastoplasticity theory to granular materials since they do not show any purely elastic range. As a consequence of this assumption, the decomposition of deformation into elastic and plastic parts seems to be questionable and may not reflect the reality. To corroborate this fact (Wu *et al.*, 1996) presented a simple hypoplastic constitutive model without any elastic range.

A large number of constitute models are available in literature. Being impossible to describe all of them in this work, the most important concepts will be presented, namely: elastic domain, failure surface, yield surface and flow rule.

4.2.1. Elastic domain

The elastic domain is usually computed by means of a generalized Hooke's law (Eq. 4.1). In Wan and Guo (1998) article, the elastic strain increments (recoverable upon unloading) was calculated from that law by using a non linear shear modulus G proposed by Hardin and Richard (1963) (Eq. 4.2):

$$\sigma_{ij} = 2\mu\epsilon_{ij} + \lambda \mathrm{tr}(\epsilon_{kl})\delta ij \tag{4.1}$$

$$G = G_0 \frac{(2.17 - e)^2}{1 + e}\sqrt{p} \tag{4.2}$$

where G_0 is a material constant referring to the shear modulus at very small amplitudes of shear strains (1×10^{-6}).

4.2.2. Failure surface

Regarding the failure surface, Wan and Guo (1998) used the Mohr-Couloumb criterium (Eq. 4.3) in which ϕ is the friction angle.

$$F = \frac{1}{2}(\sigma_1 - \sigma_3) - \frac{1}{2}(\sigma_1 + \sigma_3)\sin\phi \tag{4.3}$$

There are several types of failure surfaces, namely: Tresca (Eq. 4.4), Mohr-Couloumb (Eq. 4.5), Von-Mises (Eq. 4.6) and Drucker-Prager (Eq. 4.7).

$$F = (\sigma_1 - \sigma_3) - 2c\cos\phi \tag{4.4}$$

$$F = (\sigma_1 - \sigma_3) - (\sigma_1 + \sigma_3) - 2c\cos\phi \tag{4.5}$$

$$F = I_2(\sigma_{ij}) - k^2 \tag{4.6}$$

$$F = \sqrt{I_2(\sigma_{ij})} + \alpha I_1(\sigma_{ij}) \tag{4.7}$$

For the case of Mohr-Coulomb in the field of principal stresses $(\sigma_1, \sigma_2, \sigma_3)$, surface F corresponds to a hexagonal pyramid with its axle coinciding to the

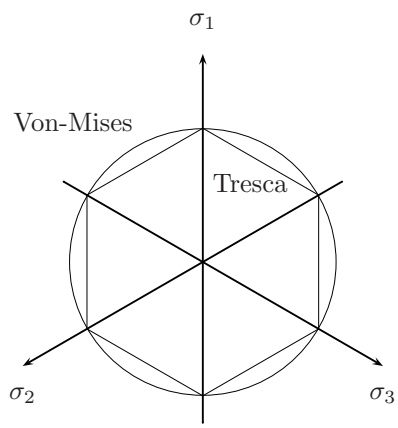

Figure 4.1: Tresca and Von-Mises failure surfaces in the deviatoric plane

equation $\sigma_1 = \sigma_2 = \sigma_3$. This pyramid evolves to a hexagonal prism in the case $\phi = 0°$, leading to Tresca surface (Fig. 4.1). Von-Mises surface corresponds to a cylinder with its axle coinciding in the equation $\sigma_1 = \sigma_2 = \sigma_3$. Drucker-Prager surface corresponds to a circumferential pyramid with its axle coinciding to the equation $\sigma_1 = \sigma_2 = \sigma_3$. In the deviatoric plane these surface can be represented as:

4.2.3. Yield surface

Yield surfaces can be idealized as surfaces representing contours of equal plastic work in which the plastic shear yield corresponds to a continuous mobilization of the friction angle resulting into an isotropic expansion of the yield surface in the stress space. In Wan and Guo (1998) the shear yield surfaces was given by:

$$F_{\mathrm{s}} = (\sigma_1 - \sigma_3) - (\sigma_1 + \sigma_3)\sin\psi \tag{4.8}$$

As another example, one can refer to the Cam-Clay model. The Cam-Clay model has been generalized by assuming a circular section of the yield surface. The mean stress $p = 3^{-1}\mathrm{tr}(\sigma_{ii})$ and deviatoric stress $q = (\frac{3}{2}S_{ij}S_{ij})^{-0.5}$ are used as the stress parameters in the models, where $S_{ij} = \sigma_{ij} - p\delta_{ij}$ is a deviatoric stress tensor and δ_{ij} is Kroneckers delta. In this configuration the shear yield is caused by an increase in stress ratio $q\,p^{-1}$, while the compressive yield is caused by an increase in the mean stress p. The essential concepts underlying Cam-Clay models derive from the observation of the soil in laboratory tests. Thus, laboratory tests show that soils loaded from some initial condition eventually reach a critical state characterized by the ability to sustain plastic deformation at a constant volume. Cam-Clay models are traditionally predicated on assumed forms of the CSL, yield surface and consolidation law. Assuming associative plasticity, the yield surface additionally determines the direction of the plastic flow. The soil is typically assumed to possess internal friction, and to exhibit oedometric and consolidation behavior in hydrostatic compression. The analytical forms of the CSL, yield surface and consolidation law, which characterize different versions of the Cam-Clay model, have variously been obtained empirically, by fitting

it to laboratory test data, or theoretically, by energy considerations pertaining to the mechanics of granular materials (Ortiz and Pandolfi, 2004). The model is characterized by CSL in the form of logarithmic spirals, and is notable for its simplicity and elegance. Improvements to this model were performed by several authors (Newson, 1998; Voyiadjis and Song, 2000; Graham *et al.*, 2001). This model has been applied successfully to cohesive soils but it fails to predict strain softening and the dilatancy behavior of frictional granular materials (Wu *et al.*, 1996). Traditionally, the plastic volumetric strain $\epsilon_{\mathrm{v}}^{\mathrm{p}}$ is taken as the hardening parameter in the Cam-Clay model, which is not appropriate for dilatancy sand (Yao *et al.*, 2008).

4.2.4. Flow rule

The plastic strain increments are calculated from the flow rules, for example $\mathrm{d}\epsilon^{\mathrm{p}} = \lambda \frac{\partial Q}{\partial \sigma}$, where λ^{p} is the plastic multiplier and Q the plastic potential function. In case the $Q = F$ the flow rule is designed associated. Otherwise the flow rule is non-associated.

As an example of a flow rule, one can present the original Rowes stress dilatancy equation, in which the dilatancy factor $D_{\mathrm{s}} = 1 - \mathrm{d}\epsilon_{\mathrm{v}}^{\mathrm{p}}/\mathrm{d}\epsilon_{\mathrm{a}}^{\mathrm{p}}$ is coupled to the effective stress ratio $R = \sigma_1/\sigma_3$, so as $R = K_{\mathrm{cs}}D$. The factor $K_{\mathrm{cs}} = \tan^2(\frac{\pi}{4} + \frac{\phi_{\mathrm{cs}}}{2})$ is a material constant derived from energy dissipation considerations, and ϕ_{cs} represents the friction angle at constant volume deformations. When written in terms of mobilized dilatation and friction angles, Rowes stress dilatancy equation takes the classical form:

$$\sin\psi = \frac{\sin\psi - \sin\phi_{\mathrm{cs}}}{\sin\psi \sin\phi_{\mathrm{cs}}} \tag{4.9}$$

Rowe's basic theory, which explains how the geometrical interlocking of the particles influences the strength of the material, provided a simple relationship between stress ratio and dilatancy factor which basically quantifies the geometrical effect (Wan and Guo, 1998). Rowes stress dilatancy relationship represents a flow rule which determines the direction of plastic strains. Wan and Guo (1998) referred that as a limitation it cannot describe the density or void ratio dependency during the deformational process, neither the difference between pre-peak and post-peak regimes for dense sands.

4.3. Multimechanism elastoplastic model

As exposed, both simplified to heavy micromechanical models could be used to simulate soil behavior, but they are less attractive then that of continuum models due to excessive simplicity of the high computational efforts. In this context a continuum model had to be select, one designed by Hujeux law, defined and enhanced by Aubry and co-workers since the early 80's (Aubry *et al.*, 1982; Hujeux, 1985) for modeling 3D cyclic soil behavior, chosen. This selection was based on its long development history, powerful mathematical formulation and vast application on scientific work, as evidenced in the work of Costa D'Aguiar (2008). Regarding model proprieties, this author presents it as an elastoplastic continuum approach model:

1. written in terms of Terzaghi effective stress in the case of saturated soils and with incremental plasticity;
2. yield criterium of Coulomb type;
3. taking into account the influence of compressive effective pressure (as also dilatancy/contractancy and critical state concept);
4. hardening evolution dependent on the plastic strains (deviatoric and volumetric);
5. cyclic kinematic hardening behavior in function of the state parameters in the previous loading;
6. written in the frame of infinitesimal transformations.

The model consists of a multimechanism approach with four plastic elementary mechanisms: three plastic mechanisms for the deviatoric deformations and one plastic mechanism for the isotropic deformation (Lopez-Caballero, 2003; Santos *et al.*, 2003). The deviatoric mechanism corresponds to plane deformations in three orthogonal plans, being a mechanism k defined in the plan that contains axles e_i and e_j and is perpendicular to axle e_k. The projection of any tensor T on the plan k only presents T_{ii}, T_{jj} and T_{ij} components. The vectorial formulation of the constitutive model allows plastic coupling effects between shear and plastic volumetric strain to be taken into account. The stress and strain state of the mechanism k is defined, according to Lopez-Caballero (2003), as:

$$p_k = \frac{\sigma_{ii}^{'} + \sigma_{jj}^{'}}{2} \tag{4.10}$$

$$q_k = \left[\left(\frac{\sigma'_{ii} - \sigma'_{jj}}{2} \right)^2 + (\sigma'_{ij})^2 \right]^{\frac{1}{2}} \tag{4.11}$$

$$\epsilon_{\mathrm{v}k} = \epsilon_{ii} + \epsilon_{jj} \tag{4.12}$$

$$\overline{\epsilon}_k = \left[\left(\frac{\epsilon_{ii} - \epsilon_{jj}}{2} \right)^2 + \epsilon_{ij}^2 \right]^{\frac{1}{2}} \tag{4.13}$$

The constitutive model allows modeling isotropic tests since it possesses one mechanism of consolidation. This mechanism is activated by isotropic loading and it only produces volumetric strain. The loading function for this mechanism is associated and it is defined as:

$$f_{\mathrm{iso}} = |p'| + dp_{\mathrm{c}} r_{\mathrm{iso}} \tag{4.14}$$

$$r_{\mathrm{iso}} = r_{\mathrm{iso}}^{\mathrm{ela}} + \frac{\int_0^t |(\dot{\epsilon}_v^p)_{\mathrm{iso}}| \mathrm{d}t}{c \frac{p_c}{p_{\mathrm{ref}}} \int_0^t |(\dot{\epsilon}_v^p)_{\mathrm{iso}}| \mathrm{d}t} \tag{4.15}$$

For the deviatoric yield surface of the mechanisms k, elasticity is controlled by:

$$K_0 = K_{\text{ref}} \left(\frac{p'}{p'_{\text{ref}}} \right)^{\text{ne}} \tag{4.16}$$

$$G_0 = G_{\text{ref}} \left(\frac{p'}{p'_{\text{ref}}} \right)^{\text{ne}} \tag{4.17}$$

Elasticity is assumed to be isotropic non-linear, with the bulk and shear modulus (K_0 and G_0) functions of the mean compressive stress p'. Non linearity is introduced by means of K_{ref} and G_{ref}, the elastic bulk and shear modulus measured at the mean reference pressure p_{ref}, and ne as the degree of non-linearity.

The yield surface of the model can be considered as a generalization of Coulomb Friction law, in which some aspects, such as the dependency on the state of compactness and the evolving friction mobilization, are included. In Hujeux law the yield surface is defined as:

$$q_k + \sin(\phi'_{pp}) p'_k F_k r_k < 0 \tag{4.18}$$

with

$$F_k = 1 - b \ln(\frac{p'_k}{p_c}) \tag{4.19}$$

$$p_c = p_{\text{c0}} \exp^{\beta \epsilon_v^p} \tag{4.20}$$

$$r_k = r_k^{\text{ela}} + \frac{\overline{\epsilon}_k^p}{a + \overline{\epsilon}_k^p} \tag{4.21}$$

$$a = a_1 + (a_2 - a_1)\alpha_k(r_k) \tag{4.22}$$

and dilatancy by:

$$\dot{\epsilon}_{\text{v}k}^p = \dot{\lambda}_k^p \psi_{\text{v}} \tag{4.23}$$

$$\psi_{\text{v}} = -\alpha_\psi \alpha_k(r_k) \left(\sin(\phi) + \frac{q_k}{p_k} \right) \tag{4.24}$$

$$\alpha_k(r_k) = \begin{cases} 0 & : \quad r^{\text{ela}} < r_k < r^{\text{hys}} \\ \left(\frac{r_k - r_k^{\text{hys}}}{r_k^{\text{mob}} - r_k^{\text{hys}}} \right)^m & : \quad r^{\text{hys}} < r_k < r^{\text{mob}} \\ 1 & : \quad r^{\text{mob}} < r_k < 1 \end{cases} \tag{4.25}$$

These mechanisms are coupled by means of the hardening variable ϵ_v^p:

$$\epsilon_v^p = \sum_k = 1^3 (\epsilon_{\text{v}k}^p) + (\epsilon_v^p)_{\text{iso}} \tag{4.26}$$

Regarding the cyclic yield surface, it is necessary to define the stress tensor and the direction associated to each mechanism. This is done though T_k^h and t_k^h that represent the deviatoric at the time of the last unload and its direction.

According to Costa D'Aguiar (2008) the cyclic yield surface is described by means of equations:

$$\mathsf{T}_k^h = \frac{s_k^h}{p'^h_k F \sin\phi'_{pp}} \tag{4.27}$$

$$t_k^h = \frac{s_k^h}{q_k^h} \tag{4.28}$$

So the deviatoric mechanisms for the cyclic yield surface are defined as:

$$f_k^c = q_k^c - p'_k r_k^c F_k(p'^*, p_c)\sin\phi'_{pp} \quad k \in [1,2,3] \tag{4.29}$$

where q_k^c is computed using:

$$s_k^c = s_k - (\mathsf{T}_k^h - t_k^h r_k^c) F_k \sin\phi'_{pp} \tag{4.30}$$

Regarding the isotropic mechanism the yield surface is written as:

$$f_{\text{iso}}^c = |p'^c| - dp_c r_{\text{iso}}^c \tag{4.31}$$

with

$$r_{\text{iso}}^h = \frac{p'^h}{dp_c^h} \tag{4.32}$$

$$p'^c = p' - r_{\text{iso}}^h dp_c \tag{4.33}$$

The evolution of the degree of mobilization of the mechanism r_{iso} is the same as that for the monotonic case but it is affected by the cyclic parameter c_2

$$r_{\text{iso}} = r_{\text{iso}}^{\text{ela}} + \frac{(\bar{\epsilon}_v{}^p)_i so}{c_2 + \frac{p_c}{p_{\text{ref}}} + (\bar{\epsilon}_v{}^p)_i so} \tag{4.34}$$

Summing up, this model uses 19 parameters, as presented in Table 4.1.

Table 4.1: Hujeux law parameters

Elasticity	**Loading function**	**Hardening**	**Soil domain**	**Initial state**
K_{ref}	ϕ'_{pp}	a_1	r^{ela}	p_{c0}
G_{ref}	β	a_2	r^{hys}	
ne	b	ψ	r^{mob}	
	d	α_ψ	$r_{\text{iso}}^{\text{ela}}$	
		m		
		c		
		c_2		

4.4. Hujeux law parameters

Hujeux law presents 19 parameters that can be divided into 5 groups concerning its role in soil behavior, respectively: 4 parameters that determine the elasticity, 4 parameters concerning the soil state during loading (yield surface), 7 parameters governing the hardening, 4 parameters defining the threshold domain and 1 parameter defining the initial state.

Elastic parameters

K_{ref} elastic bulk modulus for the reference pressure p_{ref};

G_{ref} elastic shear modulus for the reference pressure p_{ref};

ne power scalar to correlate the modulus with the mean stress p by means of a power law.

Yield surface parameters

Φ'_{pp} critical state (perfect plasticity) friction angle;

β plastic compressibility modulus that introduce the influence of the densification of the material in the final resistance;

b scalar value to define the type of yield surface;

d distance of the NCL to the CSL in $e : \ln p$ space.

Hardening parameters

a_1 scalar for controlling the evolution of the yield surface;

a_2 scalar for controlling the evolution of the yield surface;

ψ dilatancy angle of the characteristic state line;

α_ψ scalar representing the amplitude of dilatancy;

m power scalar for the definition of $a_k(r_k)$;

c_1 scalar for controlling the isotropic hardening;

c_2 scalar for controlling the isotropic hardening.

Threshold domain parameters

r^{elas} elastic ratio that determines the size of the elastic deviatoric domain;

r^{hys} hysteretic ratio that determine the size of the pseudo elastic and hysteretic deviatoric domain;

r^{mob} mobilized ratio that determines the size of hysteretic and mobilized deviatoric domain;

$r_{\text{iso}}^{\text{ela}}$ isotropic elastic ratio that determines the size of the elastic volumetric domain.

Initial state parameter

p_{c0} critical mean effective stress that corresponds to the initial state, defined by the initial void ratio.

Modaressi and Lopez-Caballero (2001) proposes a second classification by taking into consideration the fact that parameters can be measured by laboratory or field tests (direct parameters) or not (indirect parameters). In this way the direct parameters are K_{ref}, G_{ref}, ne, Φ'_{pp}, β, ψ and p_{c0}. The indirect parameters are b, d, a_1, a_2, α_ψ, m, c_1, c_2, r^{elas}, r^{hys}, r^{mob} and $r_{\text{iso}}^{\text{ela}}$.

4.5. Parameters influence and calibration

In this work the calibration of the model was performed along with the study of the influence of the parameters. It should be pointed out that an optimization technique for model calibration was also used, namely by means of an evolutionary algorithm. Nevertheless, an initial manual adjustments was performed due to the high number of parameters and some missing data (e.g. no data is available for undrained tests). This manual adjustment was useful for a better description of the role of each parameter and also for achieving sensitivity. During this phase the behavior of the chosen set of parameters was analyzed for drained, undrained, oedometric and cyclic shear tests even if no laboratory data was available.

4.5.1. Yield surface shape

Regarding parameter b, it governs the influence of the density or overconsolidation of the material and also the shape of the yield surface. It varies from 0 to 1 passing from Coulomb type surface (sands) to a Cam-Clay type one (clays). For and usual sand b takes a value between 0.1 and 0.2. Figure 4.2 presents the yield surfaces for b values of 0, 0.2 and 1. This is an indirect parameter and its adjustment requires an iterative process.

4.5.2. Deviatoric soil domains

The passage from the elastic to the hysteretic and mobilized domains is controlled by Equation 4.21. In this equation the internal variable a (Eq. 4.22) controls the hardening evolution, by controlling r_k. It is an important parameter of the model because it controls the rigidity when in plastic domain. The internal variable r_k is called degree of mobilized friction and varies from the initial values of r^{elas} to a limit unit value in perfect plasticity. It defines the degree of the mobilized friction associated with each k deviatoric mechanism. The degree of the mobilized friction is related with the plastic shear strain by the following incremental relationship:

$$\mathrm{d}r_k = \frac{\mathrm{d}\lambda(1 - r_k)^2}{a_k(r_k)} \tag{4.35}$$

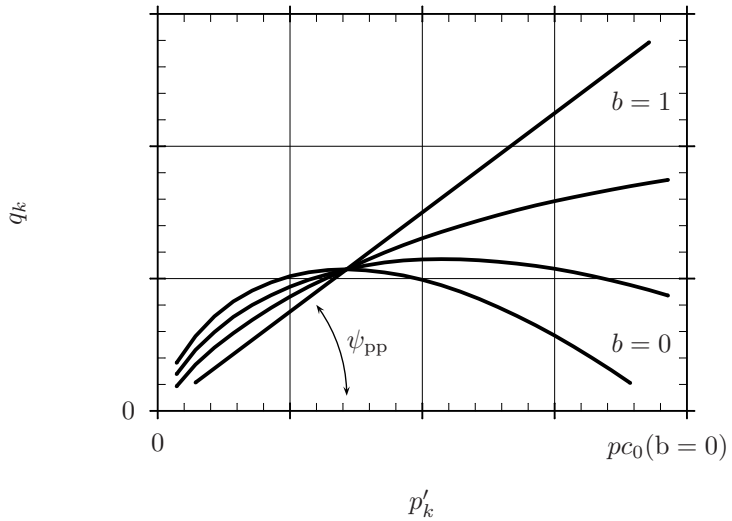

Figure 4.2: Influence of parameter b in the definition of the yield surfaces (Costa D'Aguiar, 2008)

in which $\mathrm{d}\lambda$ is the plastic multiplier obtained from the consistency condition $\mathrm{d}f_k = 0$. This internal variable r_k allows the division of the soil behavior into four domains: elastic, pseudo-elastic, hysteretic and mobilized. These domains are limited by:

1. elastic domain if $r_k = r^{\mathrm{ela}}$
2. pseudo-elastic domain if $r^{\mathrm{ela}} < r_k < r^{\mathrm{hys}}$
3. hysteretic domain if $r^{\mathrm{hys}} < r_k < r^{\mathrm{mob}}$
4. mobilized domain if $r^{\mathrm{mob}} < r_k < 1$

These indirect parameters can be adjusted by means of undrained cyclic shear tests. In the elastic domain $r_k = r^{\mathrm{ela}}$, the soil behavior is described by the elastic properties which are defined as a function of mean stress p. Santos *et al.* (2003) proposes an equation for the calculus of this indirect parameter by means of the equation:

$$r^{\mathrm{ela}} = \frac{G_{\mathrm{ref}}\gamma_t^c}{p' \sin\phi' F_k} \tag{4.36}$$

The value of r^{hys} can be adjusted to define the beginning of the behavior of the soil with volumetric deformation or pore pressure variations (Lopez-Caballero, 2003). The value of r^{mob}, between 0.8 and 0.9, is used to define stabilization, i.e., the end of volumetric deformations.

4.5.3. Isotropic soil domains

Parameter c, written as c_1 or c_2 (c_1 for the monotonic loading and c_2 for isotropic unloading), produces the evolution of the volumetric hardening. It represents the stiffness of the mechanism for the isotropic consolidation. According to Lopez-Caballero (2003), its value can be calibrated by means of undrained triaxial test being the obtained answer compared with the reference curve in plan $\eta/M : \epsilon_1$ (with $\eta = q\,p'^{-1}$). Figures 4.3 and 4.4 show the influence of this parameters in a simulation performed by Lopez-Caballero (2003) over a clay, respectively in an undrained triaxial test and in an isotropic consolidation triaxial test. As one can see in Figure 4.4, parameters c controls the swelling index. Lopez-Caballero (2003) suggest, as a first approximation, that c_2 should be considered equal to 50 % of c_1.

4.5.4. Dilatancy behavior

Parameters ψ and α_ψ are used for the evolution of the volumetric plastic deformation given by a flow rule based on a Roscoe's dilatancy rule (Eq. 4.37). ψ (a direct parameter) is the characteristic angle defining the limit between dilatancy and contractancy (Fig. 4.5). For the evolution of the plastic deviatoric deformation an associated flow rule is used (Eq. 4.38), where $\dot{\lambda}_k^p$ is the plastic multiplier.

$$\dot{\epsilon}_{\mathrm{v}k}^p = \dot{\lambda}^p \alpha_\psi \alpha(r) \left(\sin\psi - \frac{q_k}{p_k} \right) \tag{4.37}$$

$$\dot{\epsilon}_k^p = \dot{\lambda}_k^p \frac{\partial f_k}{\partial s_k} \tag{4.38}$$

According to Lopez-Caballero (2003), if no information is available for the definition of ψ, the same value used for ϕ_{pp} is recommended. This direct parameter plays an important role in the definition of the volumetric deformation. Its reduction induces a relevant growth in the dilatancy behavior of the model.

Parameter α_ψ allows that for drained conditions, no volume variations appear until a certain level of shearing is achieved. In addition, for undrained conditions, it allows that the evolution of pore pressure depends on the level of deformations (Costa D'Aguiar, 2008). It is usually considered equal to 1. Regarding m parameter, it is usually considered equal to 1 and used to change the evolution in the pseudo-elastic domain.

The internal variable r_k introduced on the yield surface (Eq. 4.18) is a hardening variables as the internal variable F_k. However, they present different evolution rules and represent different physical phenomenon. Variable F_k takes into account the volumetric hardening or softening with respect to the critical state, due to volumetric plastic strains (ϵ_v^p in Eq. 4.20), whereas r_k accounts for the isotropic hardening generated by plastic deviatoric strains ($\bar{\epsilon}_k^p$ in Eq. 4.21).

4.5.5. Initial and critical state definition

Results obtained from isotropic triaxial tests allow a directly definition of three Hujeux law parameters (β, d and p_{c0}) and two auxiliary parameters (k and λ). These parameters are represented in Figure 4.6 and its meaning is exposed above.

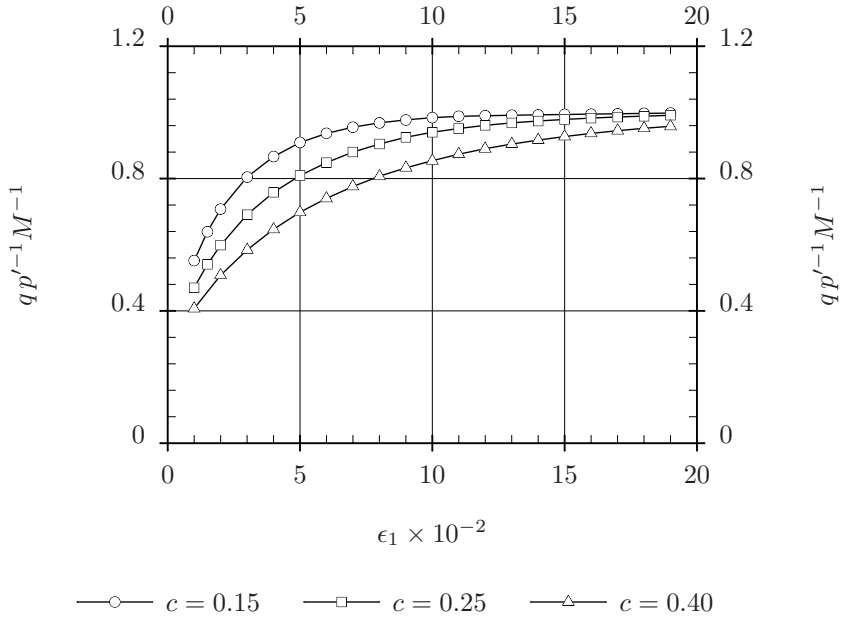

Figure 4.3: Calibration of parameter c by means of an undrained triaxial test (Lopez-Caballero, 2003)

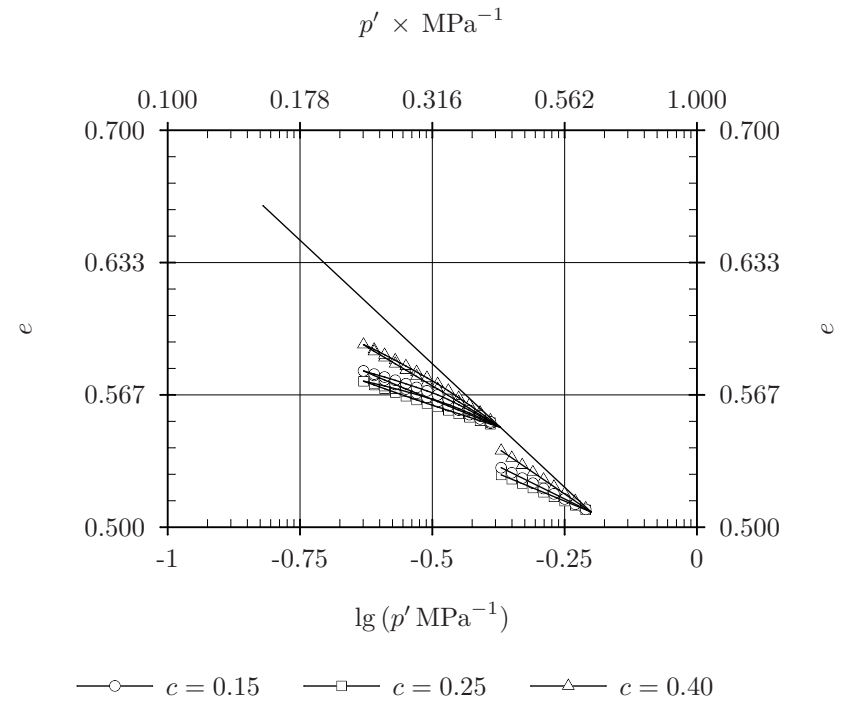

Figure 4.4: Calibration of parameter c by means of an isotropic triaxial test performed over a clay with OCR = 1 (Lopez-Caballero, 2003)

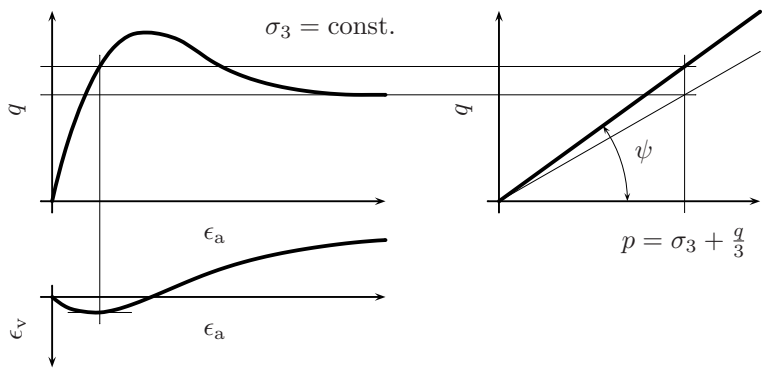

Figure 4.5: Method for ψ evaluation (Lopez-Caballero, 2003)

Variable d defines the distance between the NCL and the CSL in $e : \ln p$ plane. If no data is available for its quantification, results presented by Saïm (1997) showed that for clays and sands the vertical separation between these two lines can be taken proximally equal to $\Delta e \approx 0.1$. This relation is not acceptable for coarse material since NCL and CSL are not parallel. From previous studies, it was observed that d should take values around 2 for clays, 4 for the case or sand and 10 for the case of coarse materials.

The initial state of the soil is represented by the coefficient between the mean stress p' and the critical mean stress p_{c0}. If the elastic part of the deformation is ignored, its value can be defined by relation with the CSL and the initial void ratio.

The plastic compressibility module β represents the slope of the CSL in plane $\epsilon_v^p : \ln p'$, in which ϵ_v^p represents the plastic volumetric deformation, p' the mean stress and p'_{c0} the critical initial mean stress. Parameter β can be evaluated from oedometric tests by relations with the compressibility c_c and swelling c_r indexes, respectively: $c_c = 2.3\lambda$ and $c_r = 2.3K$. The calculus of β is performed with the Equation:

$$\frac{1}{K} + \frac{1}{\beta} = \frac{\lambda}{1 + e_0} \tag{4.39}$$

being K the slope of the swelling and λ the slope of the compressibility part.

4.6. Laboratory data

Since the constitutive law was chosen, its mathematical formulation exposed and parameters role interpreted, one can focus on the required laboratory data. In order to perform calibration, laboratory data presented by Suiker *et al.* (2005), Coronado (2005) and Martins (2011) were used respectively for the ballast, subballast and capping layer.

Regarding the ballast material, Suiker *et al.* (2005) performed studies on a material with particles resulting from crushed basalt and posterior sieving to limit the largest grain size particle to 38 mm (see Table 4.2). This author classifies this material as an uniformly graded gravel and referred that the characteristics

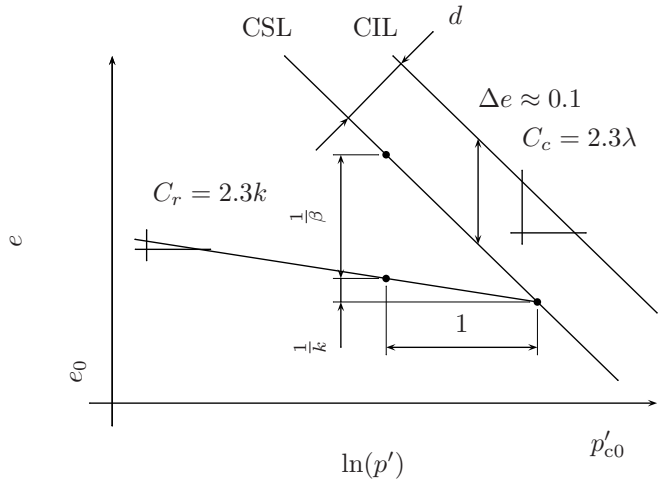

Figure 4.6: Definition of model parameters by means of the CLS

of the specimens were defined to simulate those reported by Selig *et al.* (1981) in a test track in Pueblo, Colo. Consequently, for his study, 3 specimens were used (Table 4.3) and from its results Suiker *et al.* (2005) found a peak friction angle ϕ of 48 ° (according to Mohr-Coulomb criterion without cohesion).

Specimen were prepared with a height h of 645 mm and a diameter ϕ of 254 mm resulting on an aspect ratio $h\,\phi^{-1} = 2.53$. For the instrumentation, an external displacement transducer clamped onto the piston rod was used for acquiring axial strain. It should be notice that deformation of the system is included in the recorded data and, thus, initial deformations should be expected excessive. For the radial deformation system, the author referred that a belt system, similar to the one used in Chapter 2, was used. It consists on a teflon multi-stranded steel cable of 1 mm diameter, which encloses the specimen circumference and is wound up by a small aluminum cylinder of 24 mm diameter. To reduce friction between the cable and the membrane, teflon tubes were introduced . Since the cable needs to be kept under a small tension in order to maintain the contact between the teflon tubing and the specimen, a rotational spring was placed inside the aluminum cylinder. Data was acquired by means

Table 4.2: Grain size distribution of ballast material (Suiker *et al.*, 2005)

Slieve designation	$d \times \mathbf{mm}^{-1}$	$U \times 10^2$
1/2”	38.10	0
1”	25.90	45
3/4”	19.00	85
1/2”	12.70	95
1/4”	6.35	100

Table 4.3: Characteristics of the static triaxial tests performed over the ballast material (Suiker *et al.*, 2005)

Test	$\sigma_3 \times \mathbf{kPa}^{-1}$	$\gamma_\mathbf{d} \times \mathbf{kN\,m}^{-3}$
1	-10.3	16.1
2	-41.3	17.0
3	-68.9	16.2

of a potentiometer with a relative resolution of 4.4×10^{-4} V. Attending to the large dimension of ballast material particles, 3 circumferential displacements devices equal to the one described were used at $0.33\,h$, $0.50\,h$ and $0.67\,h$, being h the specimen height.

Figures 4.7 to 4.11 are here present to summarize the important data used in the calibration of the model. Regarding this information, one notices that the radial measuring presented inadequate behavior. In fact, in Figure 4.8 one can see that no aceptable tendency is presented between the monotonic triaxial test, and for that no numerical adjustment was considered possible. Due to that fact, calibration mainly focuses on the representation of the behavior during cyclic testing (Figures 4.9 and 4.10). Figures 4.7 and 4.11, regarding monotonic triaxial tests, are presented since they will be used to see if specimen hardening was well simulated.

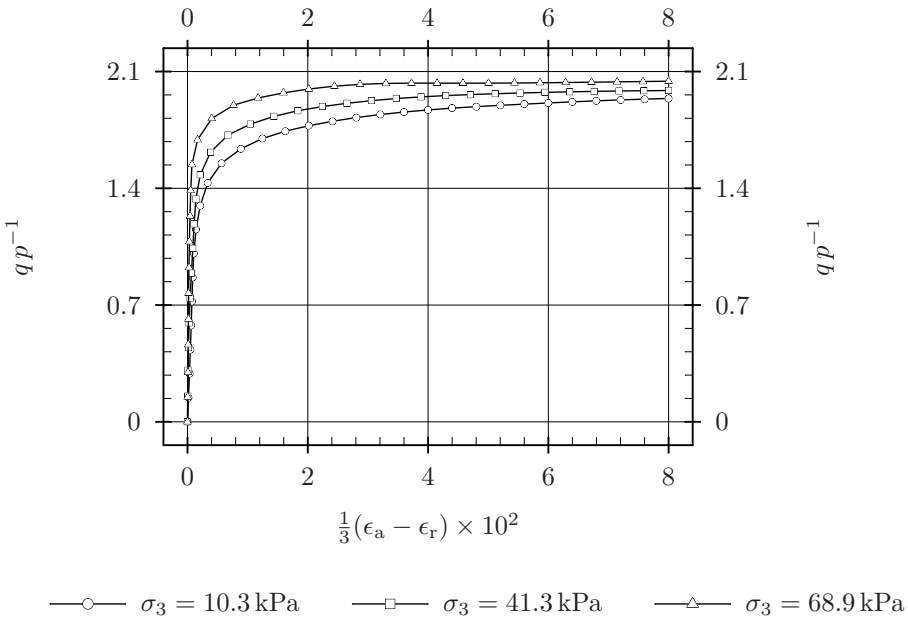

Figure 4.7: Consolidated drained triaxial tests performed over the ballast material with $q\,p^{-1} = 3$ and represented in $q\,p^{-1} : 3^{-1}(\epsilon_\mathrm{a} - \epsilon_\mathrm{r})$ space (adapted from Suiker *et al.* (2005))

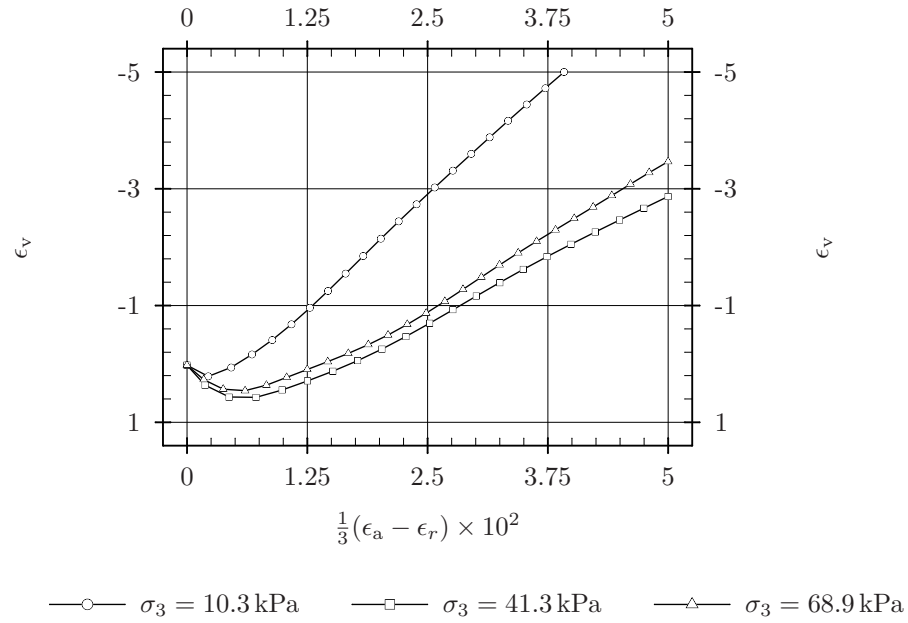

Figure 4.8: Consolidated drained triaxial tests performed over the ballast material with $q\,p^{-1} = 3$ and represented in $\epsilon_v : 3^{-1}(\epsilon_a - \epsilon_r)$ space (adapted from Suiker *et al.* (2005))

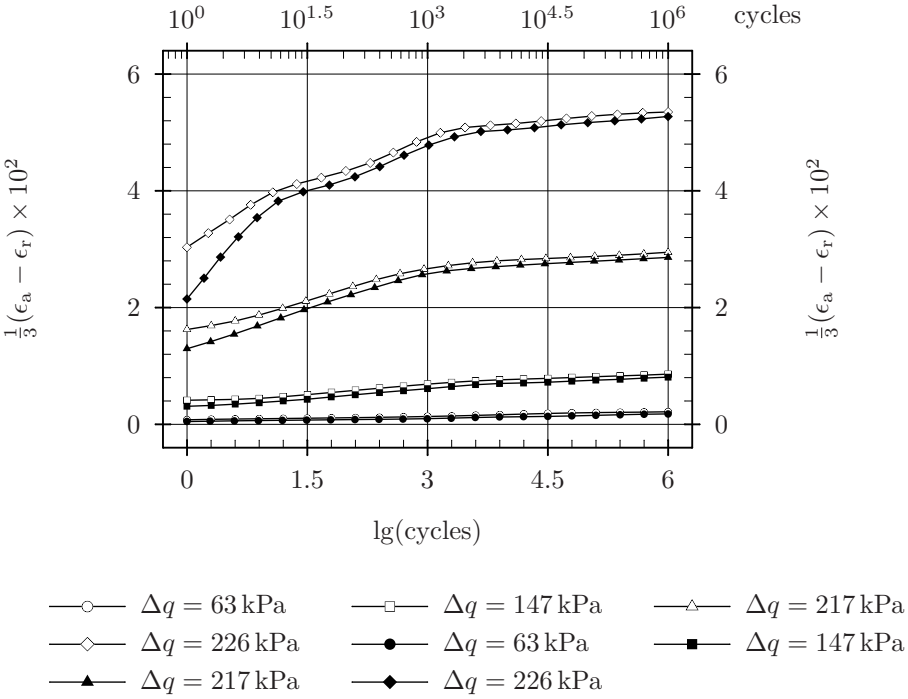

Figure 4.9: Cyclic drained triaxial tests performed over the ballast material with $q\,p^{-1} = 3$, $\sigma_3 = 68.9\,\text{kPa}$ and represented in $3^{-1}(\epsilon_a - \epsilon_r)$: cycles space with close marks for irreversible strain and open marks for total strain (adapted from Suiker *et al.* (2005))

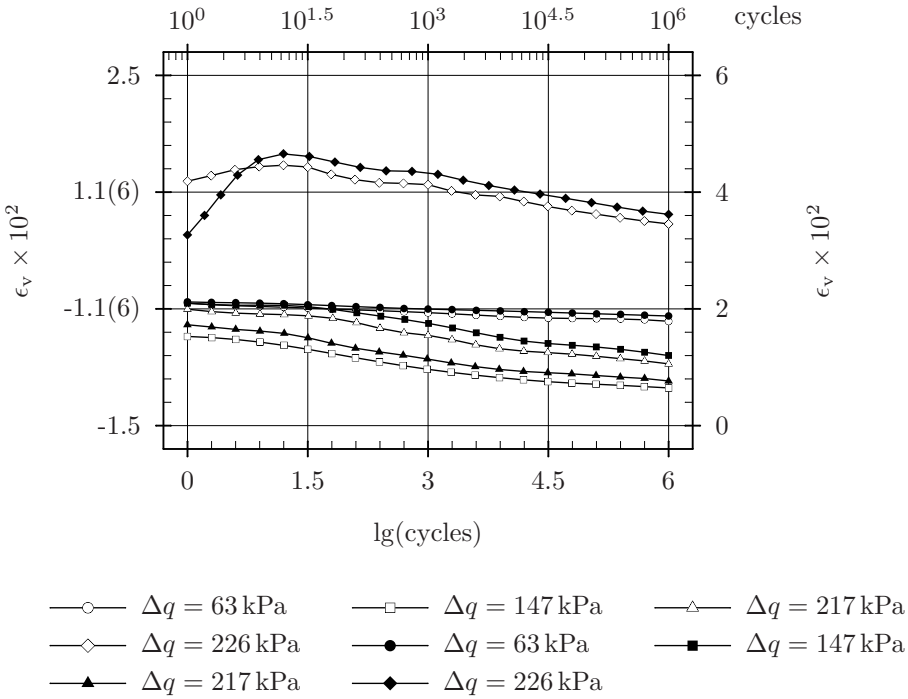

Figure 4.10: Cyclic drained tests performed over the ballast material with $q\,p^{-1} = 3$, $\sigma_3 = 68.9\,\mathrm{kPa}$ and represented in $\epsilon_\mathrm{v} : N_\mathrm{c}$ space with close marks for irreversible strain and open marks for total strain (adapted from Suiker *et al.* (2005))

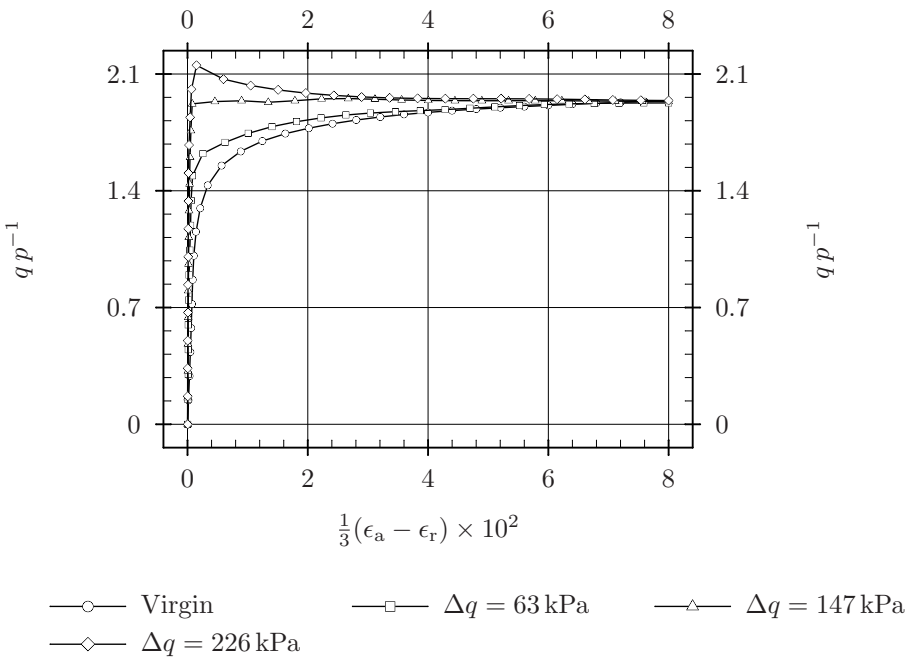

Figure 4.11: Drained triaxial test performed over the ballast material with $q\,p^{-1} = 3$, $\sigma_3 = 68.9\,\mathrm{kPa}$, after cyclic conditioning and represented in $q\,p^{-1} : 3^{-1}(\epsilon_\mathrm{a} - \epsilon_\mathrm{r})$ space (adapted from Suiker *et al.* (2005))

Regarding subballast, a natural crushed aggregate widely used in transportation geotechnical constructions and study by Coronado (2005) was used. This geomaterial is well described by means of gthe rain size curve, compaction tests and triaxial tests, whose results for the monotonic and cyclic cases are presented above and used for model calibration. One may start by referring that the studied material was designed by Coronado (2005) as 'Maraicheres' gravel. It is composed by a mixture of five different materials, respectively one sand 0/4 and four gravels 2/6.3 4/10 10/20 and 14/20. In the case of the sand 0/4, it is referred by the author that it results from a metamorphic rock, it presents a continuous grain size curve and a significant particles content (around 22 %). Regarding the gravels, they result from crushed rock, and present an uniform grain size curve and a small percentage of small particles (inferior to 6 %). Figure 4.12 shows the grain size curve of the 'Maraicheres' gravel, built from the five described materials according to AFNOR (1994).

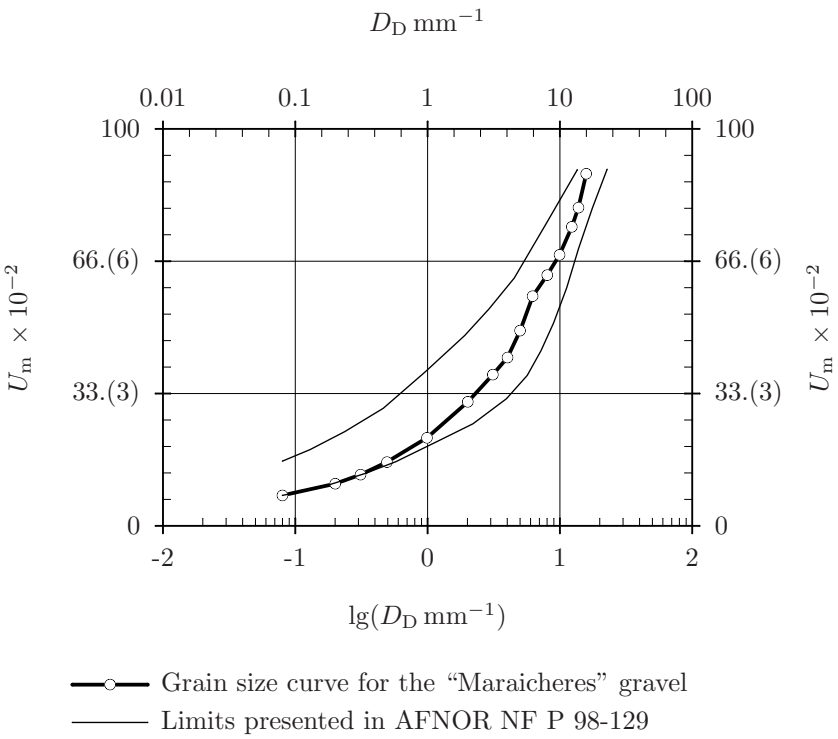

Figure 4.12: Grain size curve of the 'Maraicheres' gravel (adapted from Coronado (2005))

Once defined the grain size curve, Coronado (2005) performed compaction tests in order to quantify optimum water content and maximum dry unit weight. For that, the author performed modified Proctor tests obtaining $\omega_{\mathrm{opt}} = 6.0$ and γ_{dmax} =21.5 kN/m^3.

For testing the author used, in ECP laboratory, a classic triaxial chamber with instruments able to measure stiffness and Poisson ratio from small to medium strains (10^{-6} to 10^{-3}). In this equipment the measurement of the force

and deformation was acquired directly on the specimen. The radial deformation was acquired with a deformation transducer (LDT) placed in the middle of the specimen and the vertical deformation by means of three deformation transducers (LDT).

The compaction of the specimen, with 150 mm diameter and 300 mm height, was performed in twelve layers, being 56 drops applied in each layer (using modified Proctor testing configuration). To simulate *in situ* conditions the water content was defined 2 % inferior to the optimum one, resulting in specimens with $\omega = 3.86$ and $\gamma_d/\gamma_{dmax} = 0.97$.

After compaction, specimens were submitted to 4 distinct tests: one cyclic test and 3 monotonic tests. The monotonic tests were performed in drained conditions with suction measurement until an axial deformation of 8 % was achieved. In all cases small values of the intersticial pressure were recorded and for that reason results obtained in total stresses were considered equal to the effective ones. Figures 4.13 to 4.16 presents the summary of these monotonic tests. Regarding the CSL (obtained with the monotonic triaxial tests), it should be pointed out that with an axial strain of 8 % the stabilization on the deviatoric stress and the volumetric strain was not achieved. However, paying attention to the observed tendencies, the CSL presented in Figure 4.15 was assumed (for use in the Hujeux law) with $\beta = 120$.

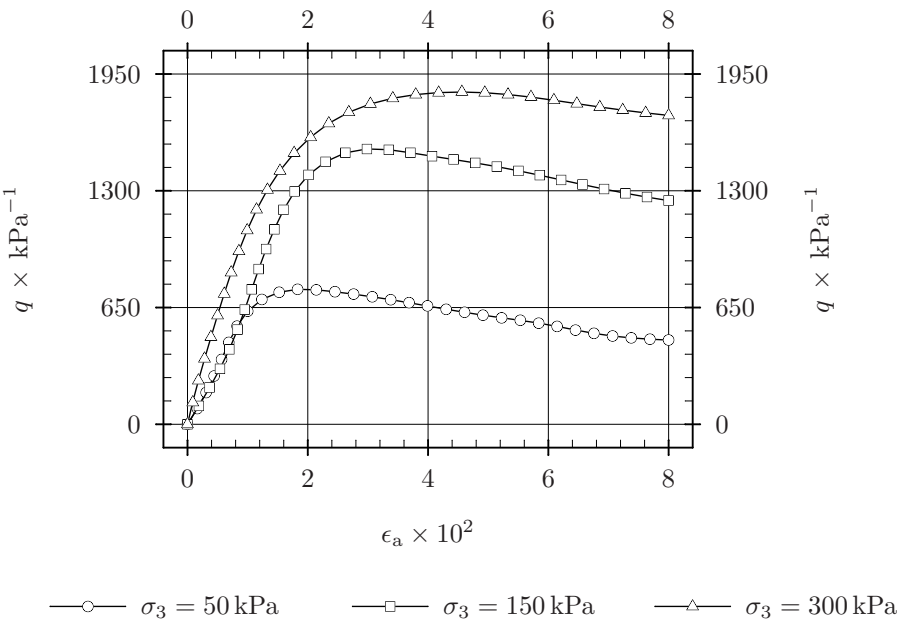

Figure 4.13: Drained monotonic triaxial test performed over the 'Maraicheres' gravel with $q\,p^{-1} = 3$ and represented in $q : \epsilon_\mathrm{a}$ space (adapted from Coronado (2005))

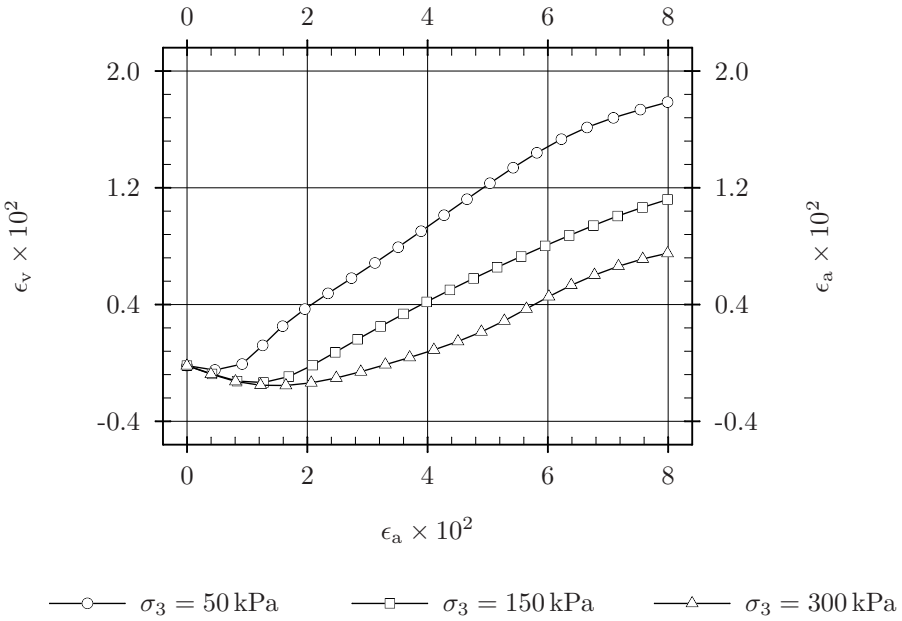

Figure 4.14: Drained monotonic triaxial test performed over the 'Maraicheres' gravel with $q\,p^{-1} = 3$ and represented in $\epsilon_v : \epsilon_a$ space (adapted from Coronado (2005))

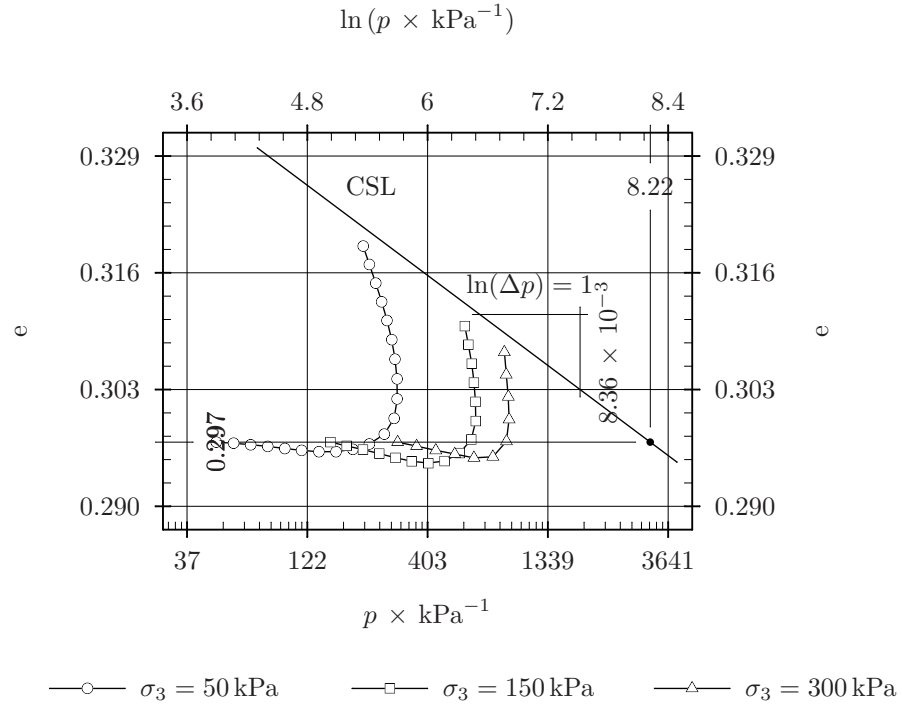

Figure 4.15: $e : \ln(p)$ relations obtained from the drained monotonic triaxial test performed over the 'Maraicheres' gravel (adapted from Coronado (2005))

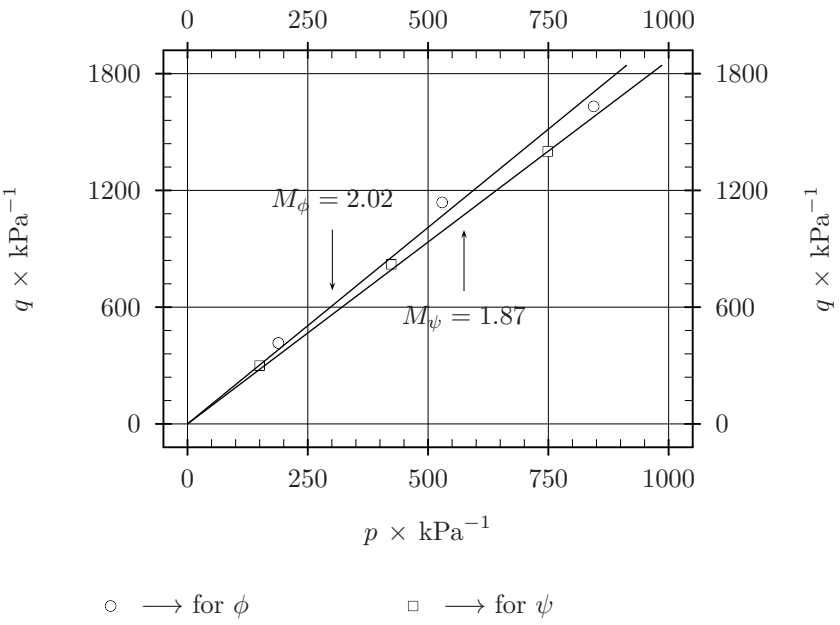

Figure 4.16: Quantification of ϕ and ψ values from results obtained in the 'Maraicheres' gravel (adapted from Coronado (2005))

From the results presented in Figure 4.16 one can also advert that this geomaterial presents a residual friction angle of 49°. Regarding the cyclic test, test procedure is composed by two main steps. In the first one, the specimen was submitted to a conditioning to simulate construction loading. This phase is composed by $2 \cdot 10^4$ cycles under a chamber confining pressure of 40 kPa and a deviatoric stress changing cyclically from 0 to 280 kPa. During the second phase several distinct stress-path were applied to study the behavior of the material. For each distinct stress-path 100 cycles were applied. Table 4.4 summarizes all the distinct stress-paths applied during the second phase. Figures 4.17 to 4.20 present a summary of cyclic tests results.

Table 4.4: Stress-path applied during the second phase of the cyclic triaxial tests (Coronado, 2005)

n.° cycles	**test number**	$\sigma_3 \times \text{kPa}^{-1}$	$q \times \text{kPa}^{-1}$
100	1	10	30
100	2	10	40
100	3	10	50
100	4	10	60
100	5	10	70
100	6	20	40
100	7	20	65
100	8	20	90

Continued on next page...

Table 4.4 – *Continued*

n.° cycles	**test number**	$\sigma_3 \times \mathrm{kPa}^{-1}$	$q \times \mathrm{kPa}^{-1}$
100	9	20	115
100	10	20	140
100	11	30	50
100	12	30	90
100	13	30	130
100	14	30	170
100	15	30	210
100	16	40	60
100	17	40	115
100	18	40	175
100	19	40	225
100	20	40	280

Finally, regarding capping layer, a foundation soil study by Martins *et al.* (2008); Martins (2011) was used. It consists on the foundation soil of a testing railway structure built near Évora, 2.5 km from 'Monte das Flores' station. This testing site was studied under a cooperation protocol between REFER and TecMinho, as the representative consortium UM/LNEC/IST/FCT-UNL (project 'POCI/ ECM/6114/2004: Interacção solo−via férrea para comboios de alta velocidade').

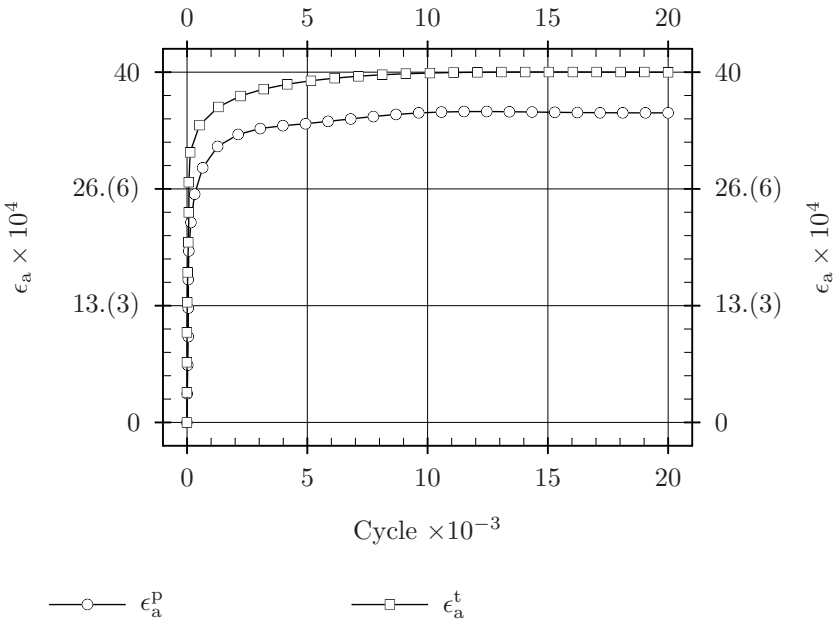

Figure 4.17: Cyclic drained triaxial test performed over the 'Maraicheres' gravel with $q\,p^{-1} = 3$, confining pressure $\sigma_3 = 40\,kPa$ and representation of the irreversible ϵ_a^p and total ϵ_a^t axial strains during the 20 000 loading cycles (adapted from Coronado (2005))

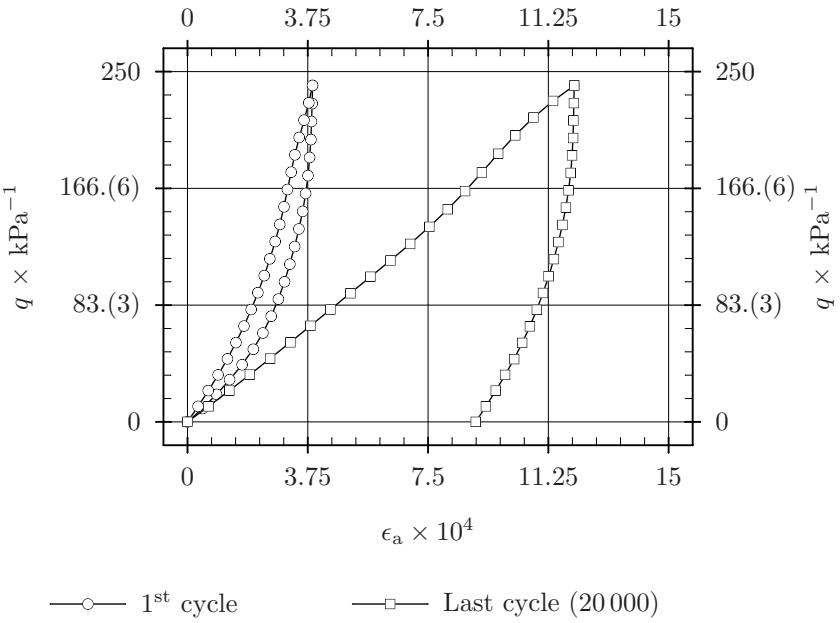

Figure 4.18: Detail of the first and last cycle obtained during the conditioning of the 'Maraicheres' gravel (adapted from Coronado (2005))

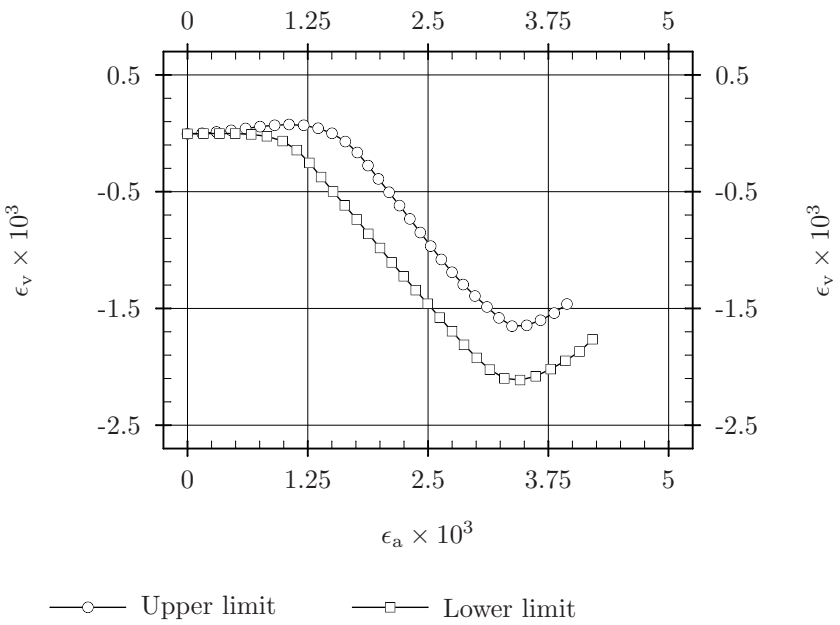

Figure 4.19: Cyclic drained triaxial test performed over the 'Maraicheres' gravel with $q\,p^{-1} = 3$, confining pressure $\sigma_3 = 40\,kPa$ and representation of the volumetric strain ϵ_v limits during the 20 000 loading cycles (adapted from Coronado (2005))

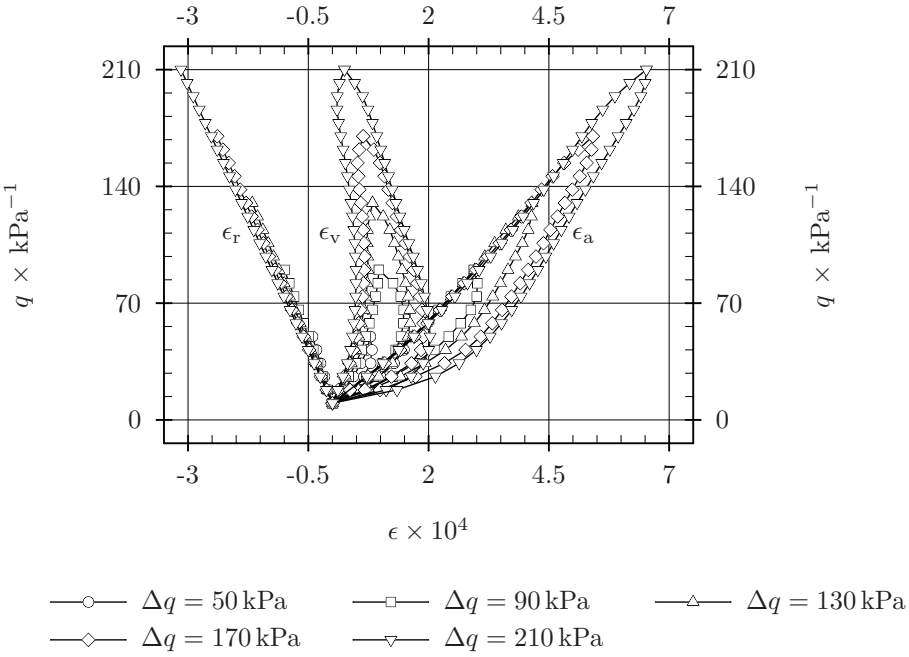

Figure 4.20: Cyclic triaxial tests performed with $q\,p^{-1} = 3$ and $\sigma_3 = 30\,kPa$ in order to evaluate reversible behavior (adapted from Coronado (2005))

Soil specimens were collected, characterized in laboratory and published by Martins *et al.* (2008); Martins (2011). These authors presented the material as having a plastic limit L_p of 21, liquid limit L_l of 32, liquidity index I of 11 (NP, 1969), methylene blue sulfide test result of 0.96 (AFNOR, 1993), sand equivalent test of 24 % (LNEC, 1967) and particle specific density G of 2.65 (NP, 1965). Regarding the grain size distribution (Tab. 4.5), and according to the Unified Soil Classification System (ASTM, 1975), the soil is defined as a clayey sand. It should be noticed that a high percentage of fine material is present (16 %).

Table 4.5: Grain size distribution of 'Évora' sand (Martins *et al.*, 2008)

Slieve designation	$d \times \mathbf{mm}^{-1}$	$U \times 10^2$
#200	0.074	16
#140	0.105	18
#80	0.177	25
#60	0.25	29
#40	0.42	36
#20	0.841	48
#10	2	76
#4	4.76	98
3/8"	9.51	100

During the construction of the railway testing structure, near 'Monte das Flores' station, compaction tests were performed to quantify optimum water content and dry unit weight. Using the test procedure described in LNEC (1966), optimum water content ω and maximum dry unit weight γ_d were 8.6 % and 20.5 kN m^{-3} for modified Proctor and 10.1 % and 19.9 kN m^{-3} for the standart Proctor compaction test. Tests used for calibration of the Hujeux law, performed in the geotechnical laboratory of UM, were performed over four specimens built to allow the execution of two oedometric tests and two monotonic multi-stage triaxial test. All specimens presented $\gamma_d = 19.9$ kN m^{-3}.

Regarding the oedometric tests, 2 hydric states were used and are represented in Figure 4.21, respectively a saturated one (Sr = 1) and a second one with optimum water content $\omega = 10.1$ % (Sr = 0.7). Tested specimens presented 70 mm diameter and 20 mm height. From the analysis of these results one can notice that the saturation of the specimen, which removes soil suction, increases compressibility c_c and recompressibility c_r indexes. These indexes are $c_c = 0.222$ and $c_r = 0.044$ for the saturated specimen, and c_c=0.161 and c_r=0.014 for the unsaturated one.

Regarding the triaxial tests, specimens were built by means of a vibration hammer, in molds with 100 mm diameter and 200 mm height. For compaction, the specimens were divided into 4 layers of 50 mm each to assure homogeneous compaction. As in the case of the oedometric test, also a dry unit weight of 19.9 kN m^{-3} was used. A hydric state was chosen to match those in the oedometric tests so that tendencies could be compared. With the two constructed specimens, two multi-stages monotonic triaxial tests were performed and, the results are presented in Figures 4.22 to 4.24.

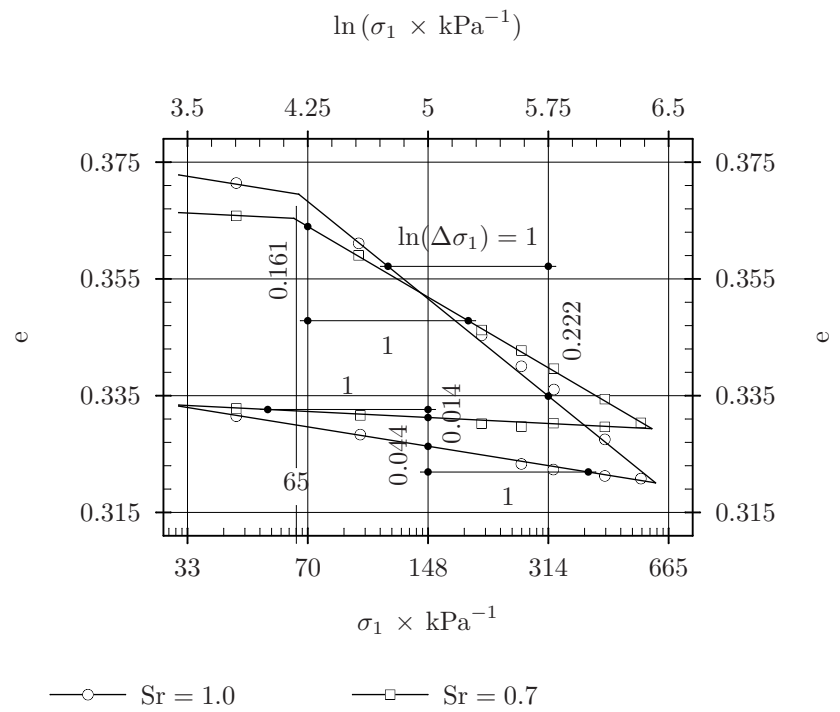

Figure 4.21: Oedometric test results obtained on 'Évora' sand

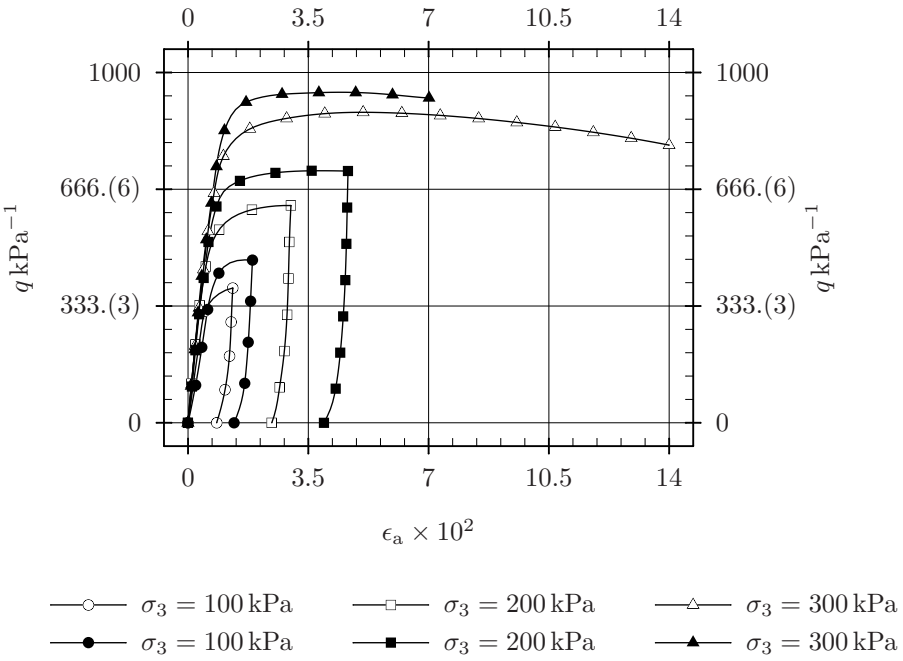

Figure 4.22: Multi-stage monotonic drained triaxial tests performed over 'Évora' sand using $q\,p^{-1} = 3$, confining pressure $\sigma_3 = \{100, 200, 300\}$ kPa and represented in $q : \epsilon_\mathrm{a}$ space with close marks for Sr = 0.7 and open marks for Sr = 1.0

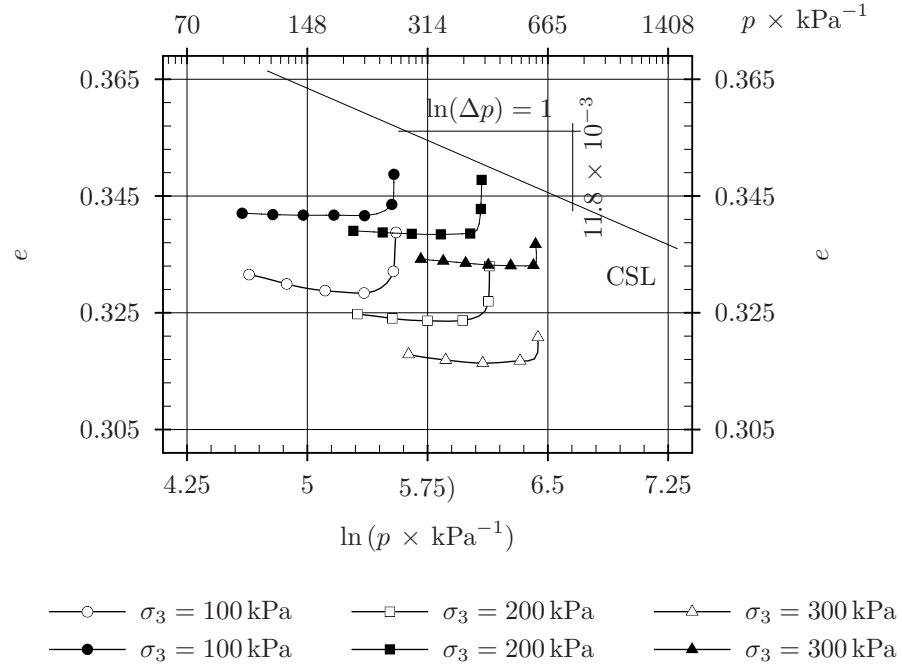

Figure 4.23: Multi-stage monotonic drained triaxial tests performed over 'Évora' sand using $q\,p^{-1} = 3$, confining pressure $\sigma_3 = \{100, 200, 300\}$ kPa and represented in $e : p$ space with close marks for Sr = 0.7 and open marks for Sr = 1.0

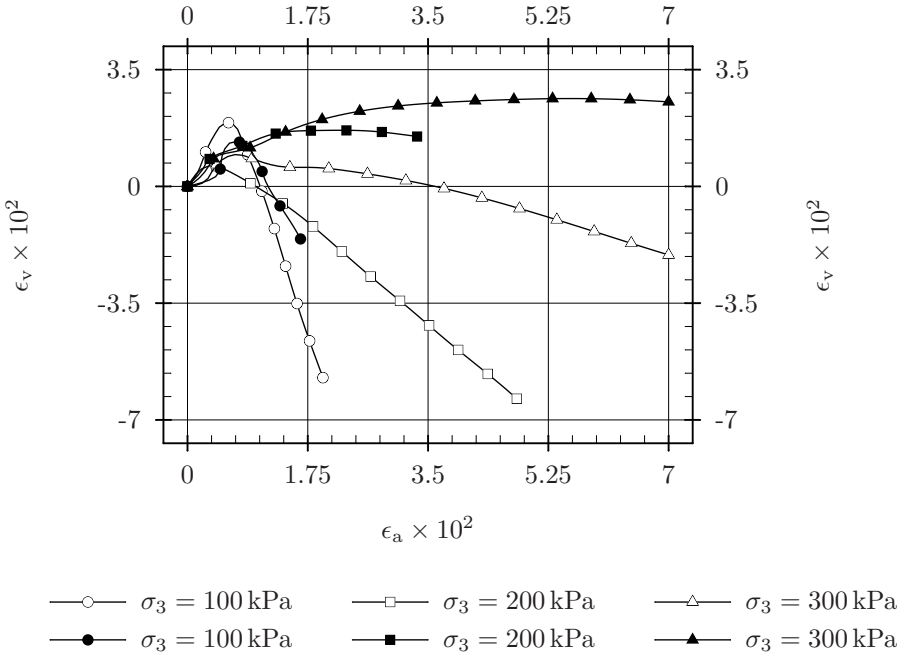

Figure 4.24: Multi-stage monotonic drained triaxial tests performed over 'Évora' sand using $q\,p^{-1} = 3$, confining pressure $\sigma_3 = \{100, 200, 300\}$ kPa and represented in $\epsilon_v : \epsilon_a$ space with close marks for Sr = 0.7 and open marks for Sr = 1.0

From the interpretation of these results from Hujeux law β parameter was estimated around 50 and peak friction angle around 37 °, or $\beta = 85$ and peak friction angle around 39 °, respectively for the saturated or unsaturated case. Regarding test monitoring, an external position transducer was used for recording axial strain. Radial strain was obtained by means of acquiring chamber volume variations and axial load by means of a local load cell.

4.7. Manual calibration process

Once all the required laboratory data was treated and presented in the previous section, one could focus on the calibration of the model for the distinct materials. For that a MATLAB® graphical interface script was developed to assist on the process. This script (see Appendix for more details) was developed to allow simultaneous analyze of a certain set of parameters to all available laboratory data and to quantify the adjustment error E_a by means of a square power error equation. For that, Equation 4.40 and 4.41 were defined, in which j represents the number of points used to define each laboratory relation, x_i^l the points of the laboratory data and x_i^s the points of the simulated relation.

$$E = \frac{\sum_{i=1}^{j} \left[x_i^l - x_i^s\right]^2}{jb} \tag{4.40}$$

$$b = \min(\max\{|x_i^l|\}, \max\{|x_i^s|\}) \tag{4.41}$$

Along the manual calibration, it was detect that Hujeux law had difficulties to simulate the stabilization of irreversible strain during cyclic testing. For that an extra parameter N (Eq. 4.42) was added to those given in Table 4.1, so that Hujeux law parameter ne could change in function of the number of performed cycles. This parameter was implemented in MATLAB® code by means of Equation 4.42.

$$ne_{\text{var}} = ne\left(1 - \frac{j}{j+N}\right) \tag{4.42}$$

Once the automatization of the process was completed to compute adjustment error E_{a} and a simultaneous visualization of all responses (for all laboratory data) produced, manual calibration was performed. One last detail remains to be exposed, which is the fact that since laboratory data for some important tests were not always available, some simulations are presented without the respective laboratory data. These 'artificial' tests are mainly the triaxial isotropic consolidation test, the oedometric test and the cyclic shear test. Regarding the 'artificial' isotropic consolidation test, it was defined to start at $p = 0.1\,\text{MPa}$ and increased to $p = 5.1\,\text{MPa}$. After that p was reduced to $0.1\,\text{MPa}$ and again increased to $9.1\,\text{MPa}$. Regarding the 'artificial' oedometric test, it started at $\sigma_1 = 0\,\text{MPa}$ and increases to $\sigma_1 = 6\,\text{MPa}$. After that σ_1 was reduced to $1\,\text{MPa}$ and again increased to $10\,\text{MPa}$. The last 'artificial' test, the cyclic shear, consisted of 3 cycles performed under constant confining pressure $\sigma_3 = 100\,\text{kPa}$ and cycle amplitude of 10, 20 and $30\,\text{kPa}$. These 'artificial' simulations are important and must be analyzed, even if no validation can be performed, since the chosen set of parameters must reproduce any test conditions.

Table 4.6 and Figure 4.25 demostrate, respectively, a summary of all test conditions used in the calibration process of ballast material and the obtained simulations response for the best set of parameters (see page 118). Detailing, Table 4.6 presents the initial stress condition, applied stress-path, drained condition and test type (monotonic/cyclic) of the laboratory data relative to ballast material while Figure 4.25 presents, graphically, the laboratory data and simulated Hujeux law response by means of the developed MATLAB® graphical script, with the set of parameters presented in page 118. This Figure (as Figures 4.26, 4.27 and 4.29) present results assuming traction/extension with a positive signal.

This set of parameters was obtained mainly for a precise simulation of total permanent deformation evolution and triaxial answer after stress stabilization. As previously referred (page 95), volumetric tendencies presented in Suiker *et al.* (2005) cannot be simulated. As showed in Figure 4.8, no relation exists between the volumetric strain and mean stress p. Consequently, calibration focuses mainly on limiting the rate evolution of the total permanent axial strain during along specimen conditioning. For that, the value of ne was progressively decreased until zero. It should be observed that even in this extreme situation, total permanent axial strain obtained in simulation always overcomes the values presented at laboratory. Regarding triaxial tests, adjustment between data obtained in tests performed without conditioning and Hujeux law simulation was poor. However, after conditioning the deviatoric stress associated with the residual state was well acquired.

Table 4.6: Laboratory data used in MATLAB® software for manual calibration of ballast material and presented in Figure 4.25

Figure position	**Test number**	**Initial stress** $(\sigma_3\,, q)$	**Trajectory**	**Test type**	**Drain condition**	**Restrain strains**	**Space**
(1,1)	1	(-10.3 kPa,0 kPa)	$q\,p^{-1} = 3$	Monotonic	Drained	None	$q : \epsilon_{\mathrm{a}}$
(1,2)	2	(-68.9 kPa,0 kPa)	$q\,p^{-1} = 3$	Monotonic	Drained	None	$q : \epsilon_{\mathrm{a}}$
(1,3)	3	(-68.9 kPa,0 kPa)	$q\,p^{-1} = 3$	1000 cycles ($\delta q = 63$ kPa)	Drained	None	$\epsilon_{\mathrm{a}}^{\mathrm{t}} : N\mathrm{c}$
(2,1)	3	(-68.9 kPa,0 kPa)	$q\,p^{-1} = 3$	Monotonic	Drained	None	$q : \epsilon_{\mathrm{a}}$
(2,2)	4	(-68.9 kPa,0 kPa)	$q\,p^{-1} = 3$	1000 cycles ($\delta q = 147$ kPa)	Drained	None	$\epsilon_{\mathrm{a}}^{\mathrm{t}} : N\mathrm{c}$
(2,3)	4	(-68.9 kPa,0 kPa)	$q\,p^{-1} = 3$	Monotonic	Drained	None	$q : \epsilon_{\mathrm{a}}$
(3,1)	5	(-68.9 kPa,0 kPa)	$q\,p^{-1} = 3$	1000 cycles ($\delta q = 226$ kPa)	Drained	None	$\epsilon_{\mathrm{a}}^{\mathrm{t}} : N\mathrm{c}$
(3,2)	5	(-68 kPa.9,0 kPa)	$q\,p^{-1} = 3$	Monotonic	Drained	None	$q : \epsilon_{\mathrm{a}}$
(3,3)¶	6	(-100 kPa,0 kPa)	$q\,p^{-1} = 3$	Monotonic	Undrained	None	$q : \epsilon_{\mathrm{a}}$
(4,1)¶	6	(-100 kPa,0 kPa)	$q\,p^{-1} = 3$	Monotonic	Undrained	None	$u : \epsilon_{\mathrm{a}}$
(4,2)¶	7	(-100 kPa,0 kPa)	$q = 0$	Monotonic	Drained	None	$\epsilon_{\mathrm{v}} : p$
(4,3)¶	8	(0 kPa,0 kPa)	$q = kp^*$	Monotonic	Drained	ϵ_{r}	$e : \epsilon_{\mathrm{a}}$
(5,1)¶	9	(-100 kPa,0 kPa)	$\sigma = 0$	1 cycle each ($\delta\tau_{\mathrm{xy}} = \{10, 20, 30\}$ kPa)	Drained	None	$\tau_{\mathrm{xy}} : \gamma_{\mathrm{xy}}$

* With k the natural impulse coefficient
¶ No laboratory data available

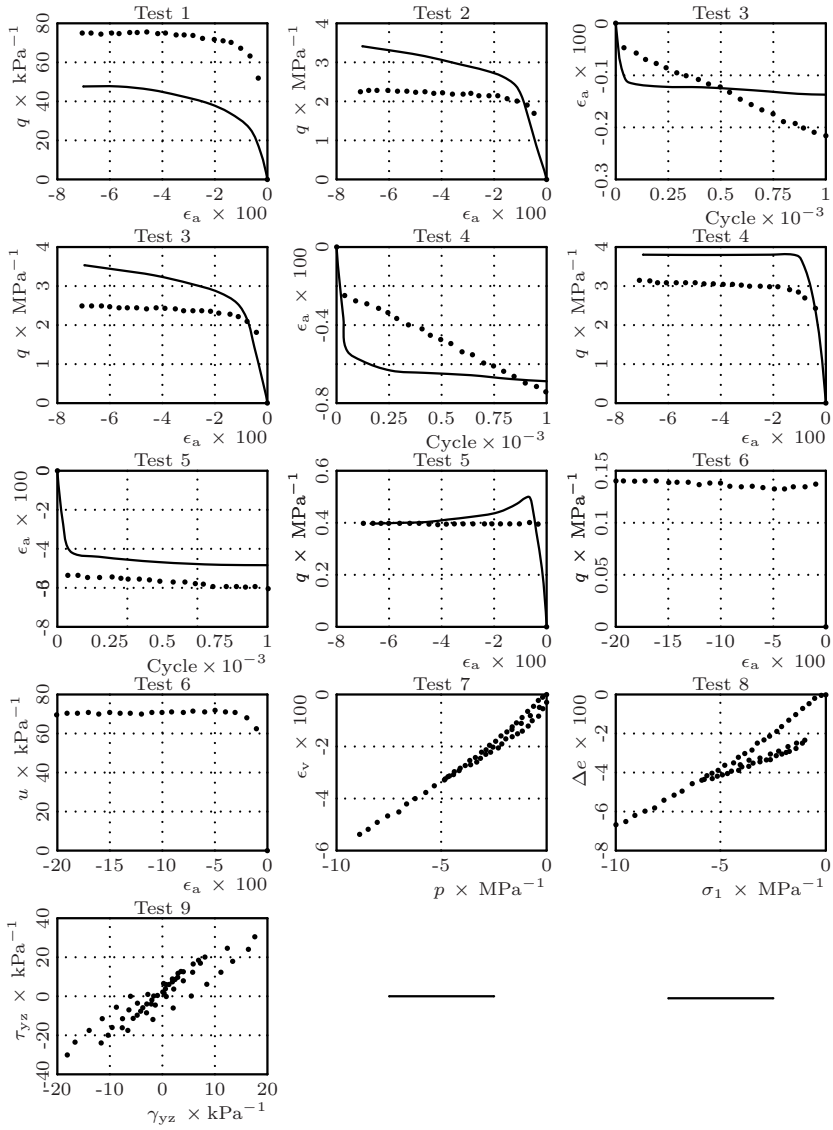
Test 1
Test 2
Test 3
Test 3
Test 4
Test 4
Test 5
Test 5
Test 6
Test 6
Test 7
Test 8
Test 9
$q \times \mathrm{kPa}^{-1}$
$q \times \mathrm{MPa}^{-1}$
$\epsilon_a \times 100$
$\epsilon_a \times 100$
$\epsilon_a \times 100

material and soil, given in page 117. Regarding friction angle ϕ, Figure 4.7 and 4.11 provide a $q\,p^{-1}$ failure surface slope of 1.88, which correspond to a friction angle of $\phi = 46\,^{\circ}$. For the simulation a value of $\phi = 44\,^{\circ}$ was used.

For subballast material, materialized by 'Maraicheres' gravel, a process identical to the one used in ballast material was used. In that way, Table 4.7, Figures 4.26 and 4.27 are present to summarize test conditions and to allow comparison between laboratory data and Hujeux law response. The responses presented in these two figures were obtained with the developed MATLAB® graphical script and the set of parameters present in Table 4.9 for 'Maraicheres' gravel. In this calibration, precise volumetric data was available which allowed the quantification of parameter β. The knowledge of the CSL had allowed an easier calibration process since the interpretation of both laboratory and numerical data could be performed in $e : \ln(p)$ space (Fig. 4.28).

Figures 4.26 and 4.27 are here presented to compare laboratory data with Hujeux law response. Triaxial tests, both monotonic and cyclic, were used and allowed a quality calibration of total permanent strain evolution, irreversible behavior during cyclic loading and void ratio evolution until critical state was achieved. From its analyzes one can verify that monotonic tests were reproduced with accuracy. Regarding the cyclic tests, reversible behavior was also well represented. However, total strain evolution during cyclic conditioning requires improvements, being the introduction of the auxiliary parameter N not enough to overcome this difficulty. Parameters N and ne were set equal to 50 and 0.12, respectively, so that a smooth reduction of total permanent rate exist. Notice that even with ne set to zero an excessive total deformation was detected in Hujeux law response. With respect to the 'artificial' tests, the mobilization of pore pressure induced by a contractant behavior of 'Maraicheres' gravel revels an initial state above the CSL. The CLS was analyzed in Figure 4.28, which perform the comparison between laboratory and Hujeux law results in $e : \ln(p)$ space. This figure illustrates the high capacity of the Hujeux law to simulate volumetric strains along triaxial tests, despite the dilatant behavior of the material that may induce a non homogeneous state in the specimen. From the laboratory data one deduces parameters $\beta = 120$, $\phi = 49\,^{\circ}$ and $\psi = 46\,^{\circ}$ which after an adjustment result in $\beta = 120$, $\phi = 43\,^{\circ}$ and $\psi = 43\,^{\circ}$. Table 4.9 summarize the set of parameters that best describe the 'Maraicheres' gravel, the soil to be used in the following Chapter as subballast material.

Regarding the capping layer materialized by 'Évora' sand (Tab. 4.8 and Fig. 4.29), no cyclic data was available and for that reason calibration rested on monotonic triaxial and oedometric tests results. Due to that fact, parameters N and ne could not be adjusted and were defined as equal to zero. Besides this fact, it was detected that oedometric and triaxial test data were not easily reproduced simultaneously by the Hujeux law. To increase the slope on oedometric simulation, a worst adjustment on the triaxial test was introduced, which required an error compromise to be found. Since the calibration of the geomateriais provide good matches between parameters β, ϕ and ψ and the values used in the simulation, for 'Évora' sand they assumed equal to $\beta = 95$, $\phi = 40\,^{\circ}$ and $\psi = 17\,^{\circ}$, similar to those found from the interpretation of the laboratory data ($\beta = 85$ and $\phi = 39\,^{\circ}$). The reduced value of ψ was used to improve the adjustment in the oedometric response. The use of this low ψ value induces higher volumetric deformations as one can see in Figure 4.30. Nevertheless, global tendencies were well captured.

Table 4.7: Laboratory data used in MATLAB® software for manual calibration of 'Maraicheres' gravel and presented in Figures 4.26 and 4.27

Figure position	**Test number**	**Initial stress** $(\sigma_3\,,q)$	**Trajectory**	**Test type**	**Drain condition**	**Restrain strains**	**Space**
(1,1)§	1	(-300 kPa,0 kPa)	$q\,p^{-1}=3$	Monotonic	Drained	None	$q:\epsilon_{\mathrm{a}}$
(1,2)§	1	(-300 kPa,0 kPa)	$q\,p^{-1}=3$	Monotonic	Drained	None	$\epsilon_{\mathrm{v}}:\epsilon_{\mathrm{a}}$
(1,3)§	2	(-150 kPa,0 kPa)	$q\,p^{-1}=3$	Monotonic	Drained	None	$q:\epsilon_{\mathrm{a}}$
(2,1)§	2	(-150 kPa,0 kPa)	$q\,p^{-1}=3$	Monotonic	Drained	None	$\epsilon_{\mathrm{v}}:\epsilon_{\mathrm{a}}$
(2,2)§	3	(-50 kPa,0 kPa)	$q\,p^{-1}=3$	Monotonic	Drained	None	$q:\epsilon_{\mathrm{a}}$
(2,3)§	3	(-50 kPa,0 kPa)	$q\,p^{-1}=3$	Monotonic	Drained	None	$\epsilon_{\mathrm{v}}:\epsilon_{\mathrm{a}}$
(4,1)§	4	(-40 kPa,0 kPa)	$q\,p^{-1}=3$	1 cycle ($\delta q=240$ kPa)	Drained	None	$q:\epsilon_{\mathrm{a}}$
(4,2)§	4	(-40 kPa,0 kPa)	$q\,p^{-1}=3$	1998 cycles ($\delta q=240$ kPa)	Drained	None	$\epsilon_{\mathrm{a}}:N_{\mathrm{c}}N$
(4,3)§	4	(-40 kPa,0 kPa)	$q\,p^{-1}=3$	1998 cycles ($\delta q=240$ kPa)	Drained	None	$\epsilon_{\mathrm{v}}:N_{\mathrm{c}}$
(5,1)§	4	(-40 kPa,0 kPa)	$q\,p^{-1}=3$	1 cycle ($\delta q=240$ kPa)	Drained	None	$q:\epsilon_{\mathrm{a}}$
(5,2)§	4	(-30 kPa,10 kPa)	$q\,p^{-1}=3$	10 cycles ($\delta q=40$ kPa)†	Drained	None	$q:\epsilon_{\mathrm{a}}$
(5,3)§	4	(-30 kPa,10 kPa)	$q\,p^{-1}=3$	10 cycles ($\delta q=40$ kPa)†	Drained	None	$q:\epsilon_{\mathrm{v}}$
(6,1)§	4	(-30 kPa,10 kPa)	$q\,p^{-1}=3$	10 cycles ($\delta q=120$ kPa)†	Drained	None	$q:\epsilon_{\mathrm{a}}$
(6,2)§	4	(-30 kPa,10 kPa)	$q\,p^{-1}=3$	10 cycles ($\delta q=120$ kPa)†	Drained	None	$q:\epsilon_{\mathrm{v}}$
(6,3)§	4	(-30 kPa,10 kPa)	$q\,p^{-1}=3$	10 cycles ($\delta q=200$ kPa)†	Drained	None	$q:\epsilon_{\mathrm{a}}$
(1,1)‡	4	(-30 kPa,10 kPa)	$q\,p^{-1}=3$	10 cycles ($\delta q=200$ kPa)†	Drained	None	$q:\epsilon_{\mathrm{v}}$
(1,2)‡¶	6	(-100 kPa,0 kPa)	$q\,p^{-1}=3$	Monotonic	Undrained	None	$q:\epsilon_{\mathrm{a}}$
(1,3)‡¶	6	(-100 kPa,0 kPa)	$q\,p^{-1}=3$	Monotonic	Undrained	None	$u:\epsilon_{\mathrm{a}}$
(2,1)‡¶	7	(-100 kPa,0 kPa)	$q=0$	Monotonic	Drained	None	$\epsilon_{\mathrm{v}}:p$
(2,2)‡¶	8	(0 kPa,0 kPa)	$q=kp^{*}$	Monotonic	Drained	ϵ_{r}	$e:\epsilon_{\mathrm{a}}$

Continued on next page...

Table 4.7 – *Continued*

Figure position	**Test number**	**Initial stress** $(\sigma_3\,,q)$	**Trajectory**	**Test type**	**Drain condition**	**Restrain strains**	**Space**
(2,3)[‡¶]	9	(-100 kPa,0 kPa)	$\sigma = 0$	1 cycle each ($\delta\tau_{\mathrm{xy}} = \{10, 20, 30\}$ kPa)	Drained	None	$\tau_{\mathrm{xy}} : \gamma_{\mathrm{xy}}$

[*] With k the natural impulse coefficient
[§] In Figure 4.26
[‡] In Figure 4.27
[†] Only last cycle ploted
[¶] No laboratorial data available

Since the set of parameters presented in Table 4.9 (for 'Évora' sand) reproduces its global behavior but it lacks a better response for the oedometric test, the soil was used within an optimization technique (see page 119) in order to fulfil two objectives: check if another distinct set of parameters could overcome the limitation found and analyze the potentiality of such an optimization technique to be used with such a complex constitutive model.

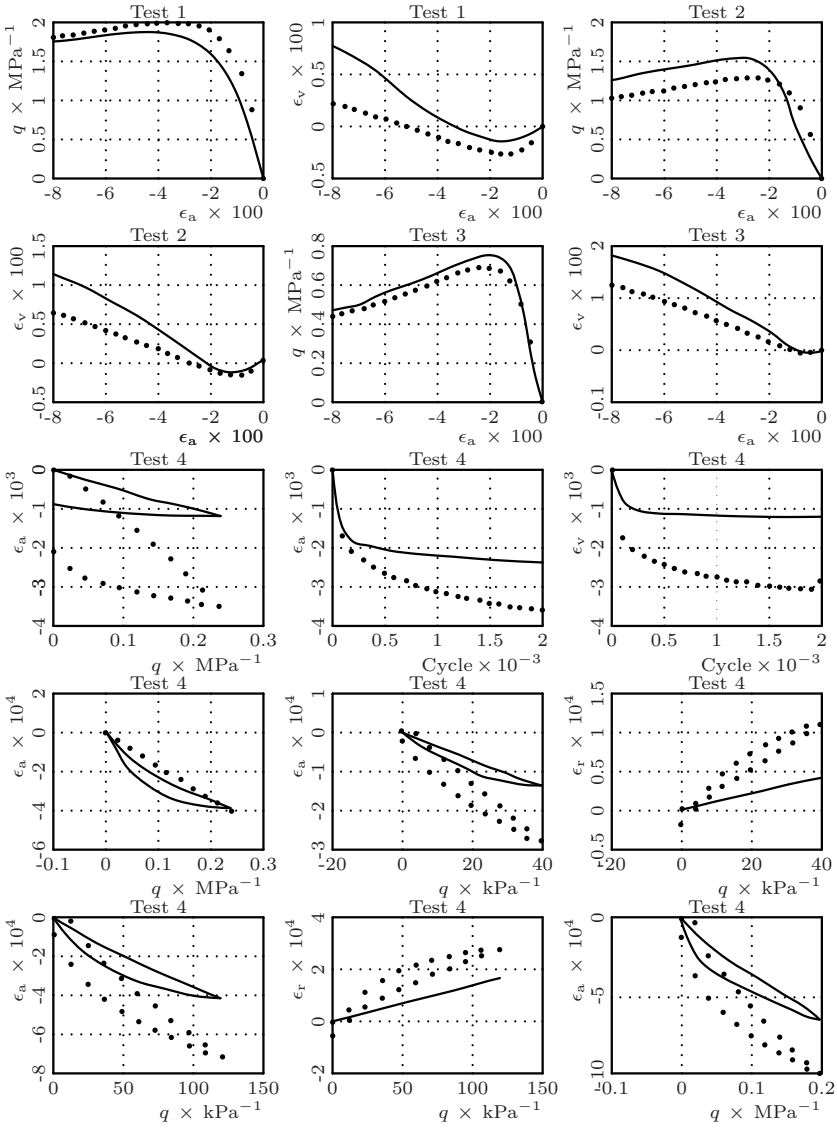

Figure 4.26: Hujeux law obtained response (dotted points) with 'Maraicheres' gravel parameters and comparison with laboratory results (continuous line) (part. 1)(signs according to Applied Mechanics convention)

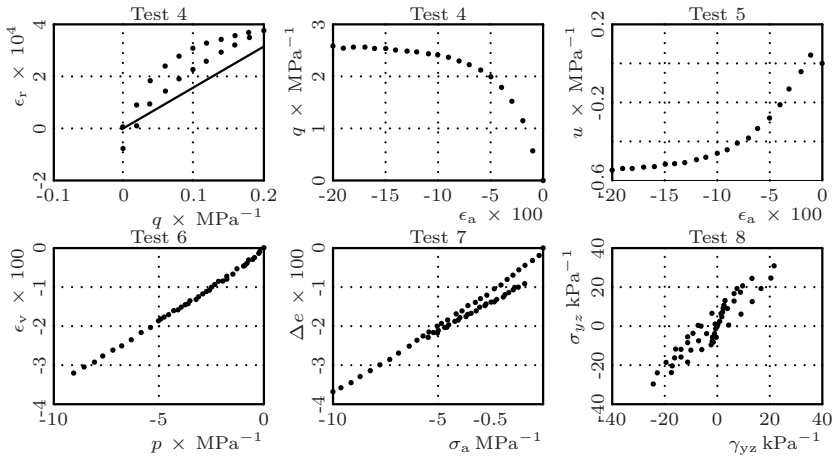

Figure 4.27: Hujeux law obtained response (dotted points) with 'Maraicheres' gravel parameters and comparison with laboratory results (continuous line) (part. 2)(signs according to Applied Mechanics convention)

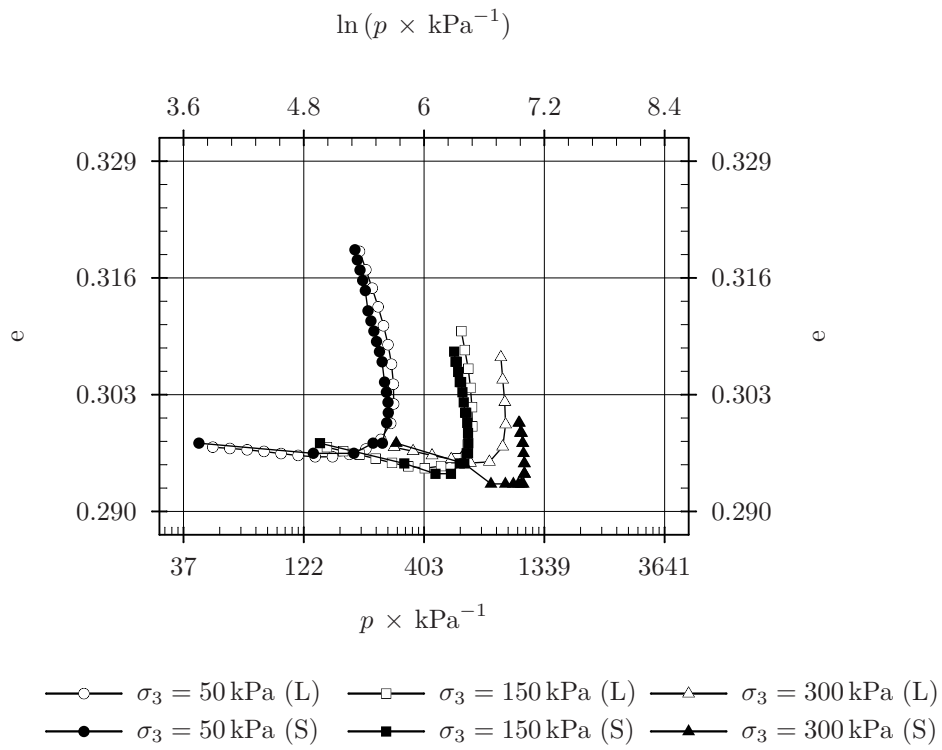

Figure 4.28: Comparison, in $e : \ln(p)$ space, between laboratory data obtained from the drained monotonic triaxial test (L) performed over the 'Maraicheres' gravel by Coronado (2005) and the numerical simulation (S)

Table 4.8: Laboratory data used in MATLAB® software for manual calibration of 'Évora' sand and presented in Figure 4.29

Figure position	**Test number**	**Initial stress** $(\sigma_3\,, q)$	**Trajectory**	**Test type**	**Drain condition**	**Restrain strains**	**Space**
(1,1)	1	(-300 kPa,0 kPa)	$q\,p^{-1} = 3$	Monotonic	Drained	None	$q : \epsilon_{\mathrm{a}}$
(1,2)	1	(-300 kPa,0 kPa)	$q\,p^{-1} = 3$	Monotonic	Drained	None	$\epsilon_{\mathrm{v}} : \epsilon_{\mathrm{a}}$
(1,3)	2	(-200 kPa,0 kPa)	$q\,p^{-1} = 3$	Monotonic	Drained	None	$q : \epsilon_{\mathrm{a}}$
(2,1)	2	(-200 kPa,0 kPa)	$q\,p^{-1} = 3$	Monotonic	Drained	None	$\epsilon_{\mathrm{v}} : \epsilon_{\mathrm{a}}$
(2,2)	3	(-100 kPa,0 kPa)	$q\,p^{-1} = 3$	Monotonic	Drained	None	$q : \epsilon_{\mathrm{a}}$
(2,3)	3	(-100 kPa,0 kPa)	$q\,p^{-1} = 3$	Monotonic	Drained	None	$\epsilon_{\mathrm{v}} : \epsilon_{\mathrm{a}}$
(3,1)	4	(0 kPa,0 kPa)	$q = kp^{*}$	Monotonic	Drained	ϵ_{r}	$e : \epsilon_{\mathrm{a}}$
(3,2)¶	5	(-100 kPa,0 kPa)	$q\,p^{-1} = 3$	Monotonic	Undrained	None	$q : \epsilon_{\mathrm{a}}$
(3,3)¶	5	(-100 kPa,0 kPa)	$q\,p^{-1} = 3$	Monotonic	Undrained	None	$u : \epsilon_{\mathrm{a}}$
(4,1)¶	6	(-100 kPa,0 kPa)	$q = 0$	Monotonic	Drained	None	$\epsilon_{\mathrm{v}} : p$
(4,2)¶	7	(-100 kPa,0 kPa)	$\sigma = 0$	1 cycle each ($\delta\tau_{\mathrm{xy}} = \{10, 20, 30\}$ kPa)	Drained	None	$\tau_{\mathrm{xy}} : \gamma_{\mathrm{xy}}$

* With k the natural impulse coefficient
¶ No laboratorial data available

From the analyze of Table 4.9, which summarizes the found set of parameters to be used in an 3D model developed in Chapter 5, one can verify that parameter β was used in the ballast material, the only one without a defined CSL (of great importance for the calibration of the model), presents the higher value of all materials, an expected situation since it is the stiffest of them all. Another important fact rests on the variation of parameter p_{co}, from -0.1 MPa (ballast material) to -37 MPa ('Maraicheres' gravel). This explains why pore pressure in undrained triaxial test is positive in the ballast material and negative in the subballast.

Regarding the calibration adjustment error E_{a}, the manual calibration process induced adjustments always smaller than 1. However, since these values do not have a physical meaning, and in order to compare results obtained in distinct materials, one should start by computing E_{a} according to Equation 4.40 (only with the relation with laboratory data available) and divide it by the number of know relation, i.e., 8, 16 and 7 respectively for ballast material, 'Maraicheres' gravel and 'Évora' sand. Following this procedure one obtained a normalized

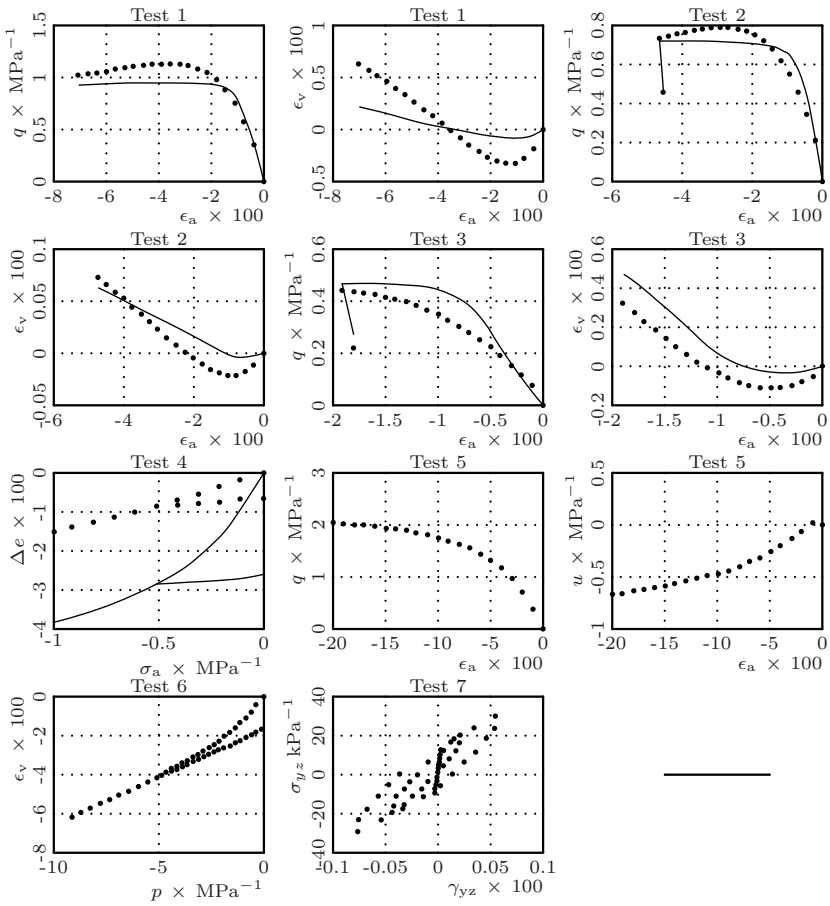

Figure 4.29: Hujeux law obtained response (dotted points) with 'Évora' sand parameters and comparison with laboratory results (continuous line)(signs according to Applied Mechanics convention)

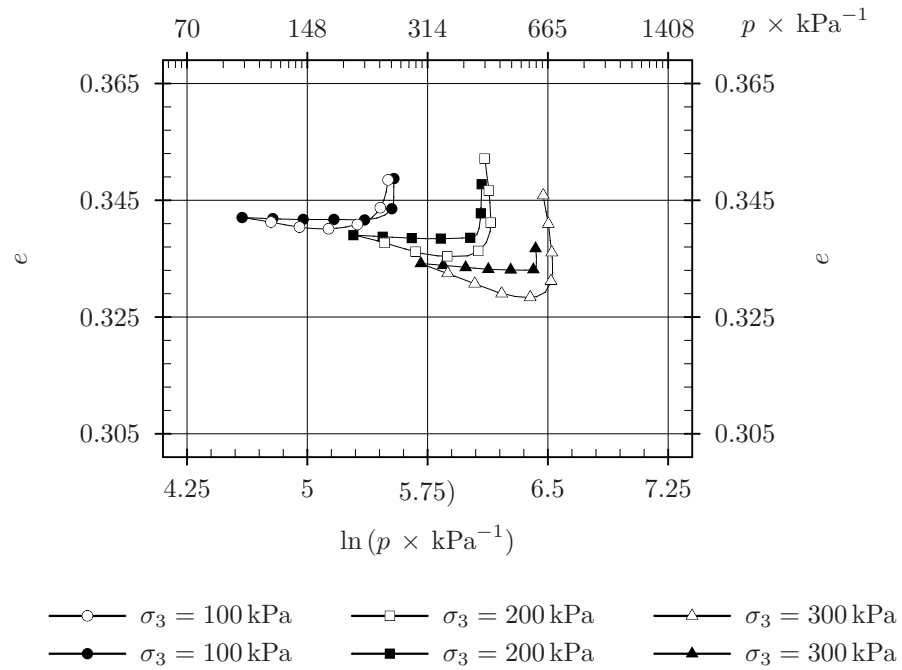

Figure 4.30: Comparison, in $e : \ln(p)$ space, between the laboratory data obtained from drained monotonic triaxial test performed over 'Évora' sand and Hujeux law response

error E_{nor} of: 28.2×10^{-3} for the ballast material, 14.1×10^{-3} for 'Maraicheres' gravel and 58.3×10^{-3} for 'Évora' sand. These normalized errors clearly revel that the worst set is the one used for 'Évora' sand, reason why this material was used in the optimization process described above.

Table 4.9: Hujeux parameters obtained for ballast material, 'Maraicheres' gravel and 'Évora' sand as result of the manual calibration process

Parameters	**Ballast**	**'Maraicheres' gravel**	**'Évora' sand**
$K_{\mathrm{ref}} \times \mathrm{Pa}^{-1}$	238×10^6	285×10^6	277×10^6
$G_{\mathrm{ref}} \times \mathrm{Pa}^{-1}$	217×10^6	260×10^6	208×10^6
ne	0.0	0.12	0.0
$p_{\mathrm{ref}} \times \mathrm{Pa}^{-1}$	-1×10^6	-1×10^6	-1×10^6
ϕ'_{pp}	44.0	43.0	40.0
β	150.0	120.0	95.0
b	0.2	0.2	0.2
d	9.0	10.0	1.5
a_1	8×10^{-4}	2×10^{-3}	5×10^{-3}
a_2	16×10^{-5}	4×10^{-4}	25×10^{-4}
ψ	44.0	43.0	17.0
α_ψ	0.05	0.5	0.8
m	1.1	0.5	0.348
c_1	0.01	0.005	0.03

Continued on next page...

Table 4.9 – *Continued*

Parameters	*Ballast*	*Subballast*	*Capping layers*
c_2	5×10^{-3}	25×10^{-4}	129×10^{-5}
r^{ela}	19×10^{-5}	19×10^{-5}	32×10^{-3}
r^{hys}	95×10^{-5}	95×10^{-5}	0.16
r^{mob}	0.95	0.95	0.8
$r^{\text{ela}}_{\text{iso}}$	0.003	0.003	1×10^{-4}
$p_{c0} \times \text{Pa}^{-1}$	-1×10^5	-37×10^5	-20×10^5

4.8. Optimization technique study

From obstacles encountered in the previous section and also as a general point of view, problems with numerical calibration are regularly encountered in situations where refined constitutive laws are used. The constitutive laws lean to include a high number of parameters which are generally assessed on the basis of laboratory test results. This is the case for the Hujeux law, in which the quantification of a large number of parameters is difficult and requires user experience. In order to perform a numerical calibration, a minimum amount of experimental data is required, in function of the complexity of the phenomena to be modeled. Besides the definition of the objective function, an optimization technique able to avoid local minimums must be chosen. In this context, the mathematical procedure for optimization can be divided in two main parts (Mattsson *et al.*, 2001):

1. formulation of an objective function which measures the difference between the theoretical and experimental results;

2. selection of an optimization technique enabling the search for the minimum of the objective function.

Cekerevac *et al.* (2006) used a gradient-stochastic method to calibrate the multimechanism elastoplastic constitutive Hujeux law developed at ECP by Aubry *et al.* (1982) and Hujeux (1985). In this author's opinion, this method is appropriate for problems where the number of parameters is high. This author also referred that, according to the definition of the objective function, the algorithms can be divided in two groups: a) direct search methods in which the search strategy is based only on values of the objective function and b) gradient methods, which also require computations of the derivatives of the objective functions. In general, the gradient methods are expected to be more powerful than those using only the values of the objective function. On the other hand, the gradient methods are more complex to implement because of the requirements of having an objective function which is always differentiable and which possesses continuous derivatives over the considered domain.

Costa and Oliveira (2001) referred that the gradient optimization techniques were only able to attempt special formulations, where continuity or convexity was imposed, or by exploiting special mathematical structures. Approaches based on stochastic algorithms, such as the one used by Cekerevac *et al.* (2006),

have been used successfully to tackle mixed integer non-linear programming problems. In the last years several studies were published on applications of evolutionary algorithms such as Genetic Algorithms (GAs), Evolution Strategies (ESs) and Simulated Annealing for the resolution of mixed integer non-linear programming problems. For instance, Miranda (2007) successfully uses an ESs algorithm to adjust model simulation on underground structures. These algorithms are distinct from conventional algorithms since usually only information regarding the objective function is required. Moreover, they start from a pool of points that evolves over the time, in the direction of the optimum solution (Costa and Oliveira, 2001).

Taking into consideration the available optimization techniques and, also, the high quantity of model parameters, the selection of an evolutionary algorithm was consider the most adequate. This option based on the studies performed by Miranda (2007), in which several minimization algorithms were simulated. In this author judgment, GAs algorithms are more indicated for discrete problems, being ESs algorithms more suitable for continues problems. UM by Professor Lino Costa. As all ESs algorithms, it mimics the natural evolution of the species in the natural systems. It works directly with a real representation of a parameter set, searching from an initial population (a set of points) normally generated randomly, requiring only data based on the objective function and constrains, and not based on derivatives or other auxiliary knowledge (Miranda, 2007). The transition rules are deterministic and the constrains are normally handled by eliminating the points outside its range.

For definition proposes, nomenclature meaning for distinguishing types of evolutive strategies will be presented. According to Miranda (2007), the nomenclature is based on the parents μ and offspring λ number and a selection type designated as "+", ",". The most simple form of evolutive strategy is the so-called two-membered (1+1)-ESs (Schwefel, 1965). In this strategy, at a given generation, there is only one parent ($\mu = 1$) and one offspring ($\lambda = 1$) generated by mutation adding a random quantity to the parent. Selection takes place between the two in relation to an error function value provided that it satisfies all the constraints. The selected one becomes then the parent of the next generation and the process is repeated until the stop criteria in met (Costa and Oliveira, 2001). Following the appearance of (1+1)-ESs, developments have been carried out and nowadays two main distinct types of ESs, differing basically on the selection procedures, which are: the $(\mu + \lambda)$-ES and the (μ, λ)-ES. In the $(\mu+\lambda)$-ESs, at a given generation, there are μ parents, and λ offspring are generated by mutation. Then, the $\mu + \lambda$ members become the parents of the next generation (i.e. the selection takes place between the $\mu + \lambda$ members). The (μ, λ)-ES differs from the previous one in terms of the selection that selection takes place only between the λ members. In case a mutation is performed after recombination the nomenclature for the ESs is usually referred as $(\mu/\rho + \lambda)$-ES or $(\mu/\rho, \lambda)$-ES.

One can now clarify that the chosen algorithm is classified as $\mu/\rho + \lambda$-ES (see Fig. 4.31 for evolution stages definition). In each generation, a set of 10 potential solutions were generated. The algorithm stopped its search when one of the following conditions was reached:

1. the maximum number of generations (100) was reached;
2. the difference between the two extreme values of the error function consi-

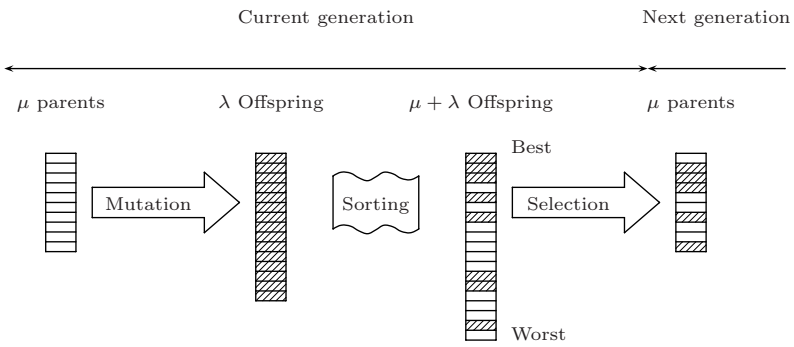

Figure 4.31: Evaluation stages of the $(\mu/\rho + \lambda)$-ES (Costa and Oliveira, 2001)

dering a given generation was lower than 10^{-6};

3. the ratio between the previous difference and the mean value of the error function within the generation lower than 10^{-6}.

After the definition of the optimization technique and its implementation on the developed MATLAB® graphic scrip (see Appendix for more details), one focuses on the definition of the objective function, computed in this study in function of 14 parameters, respectively: ϕ, ψ, β, p_{c0}, b, c, d, ACYCA, CCYCC, α_ψ, ELAHYS, HYSMBL, $r_{\text{iso}}^{\text{ela}}$ and a_1. Notice that parameters ACYCA, CCYCC, ELAHYS and HYSMBL were introduced to allow the use of the optimization technique, being its meaning presented in page 183. In fact, it is important to refer that all variables were introduced normalized, i.e. transformed into a value bettween 0 to 1, so that the efficiency of the algorithm could be improved.

To perform an efficiency analysis of the optimization technique, 7 computations (here described as **runs**) were performed. The first 3 were performed with relatively short intervals, all of them including the set of parameters manually defined for 'Évora' sand. When the solution presented a parameter near its extremes (0 or 1), the interval was shifted so that a better solution could be found. Regarding the 4th run, large intervals were used for all parameters, in order to see if the algorithm was able to find the same solution of the three first runs (or an even better one). For the remaining runs, parameter intervals were always identical to those used on the 3rd run. This repetition was performed to see if the algorithm converged to the same set of parameters. Results are given in Tables 4.10, 4.11 and in Figure 4.32, containing the chosen parameter intervals for each run, the three best solution for each run and adjustment error evolution along the optimization process.

From the interpretation of Tables 4.10 and 4.11, the optimization process reveals its capacity to find a set of parameters at least as good as the one obtained manually. From the three first performed runs, one found a set of parameters with $E = 0.114$, which after normalization provides $E_{\text{nor}} = 16.3 \times 10^{-3}$ (quite smaller than the $E_{\text{nor}} = 58.3 \times 10^{-3}$ found in the manual process). Nevertheless, focusing on results presented in the 4th run, if the parameter intervals are large the algorithm converge to an undesirable local minimum.

Table 4.10: Hujeux law parameters and respective interval used on the optimization process studies

Parameter	1st run	2nd run	3rd run	4th run	5th to 7th run
ϕ	[-45,-35]	[-55,-40]*	[-55,-40]	[-60,0]	[-55,-40]
ψ	[-20,-10]	[-10,0]*	[-10,0]	[-60,0]	[-10,0]
β	[-120,-70]	[-120,-70]	[-120,-70]	[-300,-50]	[-120,-70]
$p_{c0} \times 10^{-5}$	[-100,-1]	[-100,-1]	[-50,-0.1]*	[-100,-0.1]	[-50,-0.1]
b	[0.05,0.3]	[0.05,0.3]	[0.05,0.3]	[0.01,0.5]	[0.05,0.3]
c_1	[0.001,0.1]	[0.001,0.1]	[0.01,1]*	[0.001,1]	[0.01,1]
d	[1,3]	[1,3]	[1,3]	[1,5]	[1,3]
ACYCA	[0.001,0.99]	[0.001,1]*	[0.001,1]	[0.001,1]	[0.001,1]
CCYCC	[0.001,0.99]	[0.001,0.99]	[0.001,0.99]	[0.001,1]	[0.001,0.99]
α_ψ	[0.5,1.2]	[0.5,1.2]	[1,4]*	[0.01,4]	[1,4]
ELAHYS $\times 10^3$	[0.1,5]	[0.1,10]*	[0.1,100]*	[0.001,100]	[0.1,100]
HYSMBL $\times 10^3$	[10,500]	[0.1,10]*	[0.1,10]	[0.001,100] $\times 10^{-3}$	[0.1,10]
$r_{\text{iso}}^{\text{ela}} \times 10^3$	[0.001,1]	[0.1,100]*	[0.1,100]	[0.001,100]	[0.1,100]
$a_1 \times 10^2$	[0.01,1]	[0.01,1]	[0.005,0.5]*	[0.005,0.5]	[0.005,0.5]

* Interval changed from previous study

Table 4.11: Results of the optimization process studies

Normalized parameter (from 0 to 1000)	1st run	2nd run	3rd run	4th run	5th to 7th run
ϕ	(0,0,0)†	(262,265,264)	(296,326,295)	(410,429,410)	(296,326,295)
ψ	(1000,1000,1000)†	(999,999,996)*	(308,282,296)	(680,577,588)	(308,282,296)
β	(590,590,590)	(437,437,437)	(257,255,266)	(669,674,661)	(257,255,265)
p_{c0}	(913,913,913)	(925,925,925)†	(687,691,269)	(998,998,998)	(687,691,686)
b	(478,477,478)	(616,607,608)	(975,993,991)	(87,87,87)	(975,993,991)
c_1	(219,219,219)	(925,925,925)†	(47,47,47)	(0,0,0)	(47,47,47)
d	(122,122,121)	(417,417,417)	(0,6,0)	(386,364,388)	(0,6,0)
ACYCA	(1000,1000,1000)†	(993,952,942)*	(181,203,180)	(941,943,943)	(181,203,180)
CCYCC	(10,10,10)	(40,40,39)	(364,374,367)	(0,0,0)	(364,374,367)
α_ψ	(613,613,613)	(909,913,917)†	(278,277,283)	(0,251,294)	(278,277,283)
ELAHYS	(5,0,3)†	(914,882,923)†	(331,334,248)	(848,839,849)	(331,334,248)
HYSMBL	(0,0,0)†	(604,483,663)	(647,631,649)	(919,197,1000)	(647,631,649)
$r_{\text{iso}}^{\text{ela}}$	(928,909,746)†	(370,364,370)	(288,329,329)	(356,356,308)	(288,329,329)
a_1	(599,599,599)	(1000,999,999)†	(34,34,33)	(585,614,614)	(34,34,33)
Error	(0.120,0.120,0.120)	(0.114,0.114,1.114)	(0.116,0.117,0.117)	(0.432,0.432,0.432)	(0.116,0.117,0.117)

* Interval increment not allowed

† Parameter interval changed in the following iteration

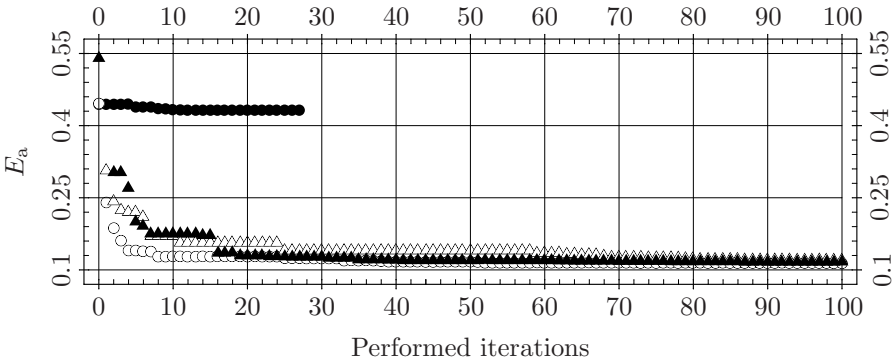

Figure 4.32: Adjustment error evolution for: 1st run (△), 2nd run (○), 3rd and 5th to 7th (▲), and 4th run (●)

Regarding the reproducibility of the convergency process, results presented in the last three runs show that solution matched the one found in third run. The same reproducibility was found when analyzing the best solutions found on each run, since there were relatively similar sets of parameters found. This can reveal that laboratory data, even if it could be more complete, is enough for the optimization process. To conclude, from the analyzes of Figure 4.32 it is possible to detect that all minimums were found after around 30 iterations, except for the case of run 4, in each one the algorithm converged to a local minimum after few iterations.

To summarize, this technique is able to quickly find a quality solution. Figure 4.33 compares the laboratory results with the best solution found by means of the manual and optimized process, clearly revealing the potentiality of this technique. Regarding the optimize solution, the best solution was found on the 2nd run: $\phi = 51.064°$, $\psi = 0.013°$, $\beta = 98.131$, $p_{c0} = -8.427 \times 10^5$ Pa, $b = 0.204$, $c_1 = 0.093$, $d = 1.834$, ACYCA $= 0.963$, CCYCC $= 0.041$, $\alpha_\psi = 1.136$, ELAHYS $= 9.14 \times 10^{-3}$, HYSMBL $= 6.078 \times 10^{-3}$, $r_{\text{iso}}^{\text{ela}} = 37.046 \times 10^{-3}$ and $a_1 = 0.01$. One of the limitations detected that can be pointed out is that the local minimum cannot be found if large parameter intervals are chosen and impossible set of parameters must be avoided since the computation of the objective function becomes impossible. To overcome this limitation, a new version of the minimization algorithm software should be developed (as a first step) and impossible set of parameters (for which Hujeux law is not able to compute the objective function) should be attended.

4.9. Summary

To overcome the limitation identified due to the linear elastic assumption of the railways structure components, this Chapter focused on the calibration of a complex constitutive model law, able to consider irreversible cyclic soil behavior. For this purpose laboratorial data from 3 different geomaterials was gathered for simulation. For each one a manual calibration process leading to a set of parameters able to reproduce its behavior was done. Along this process it was found that the stabilization of the total strain during a large

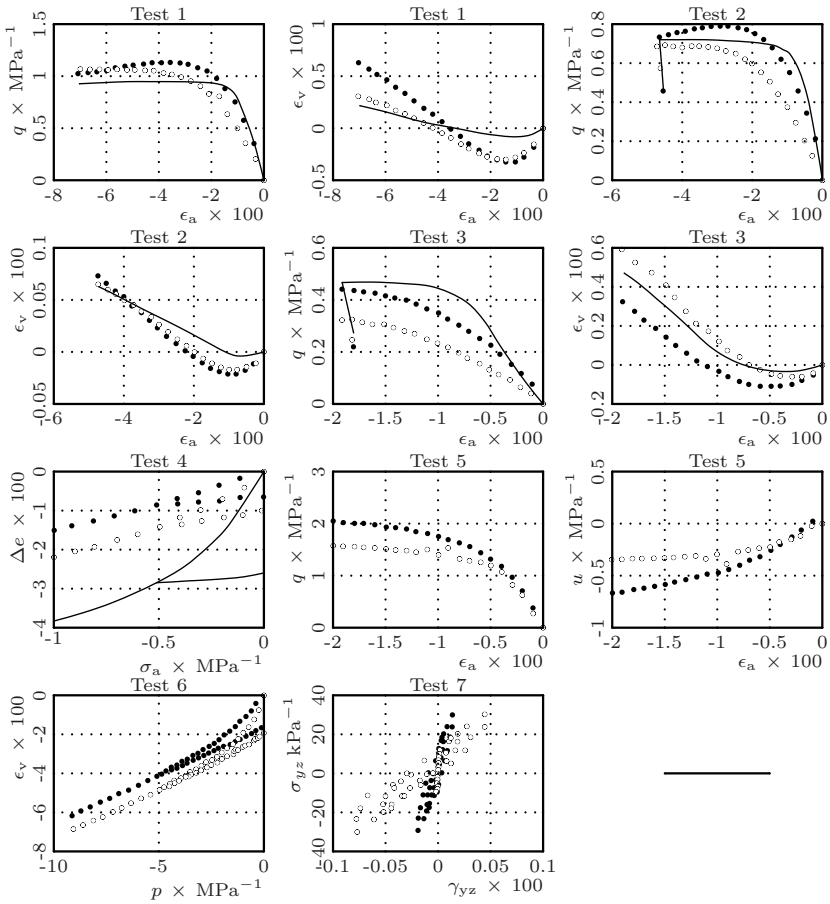

Figure 4.33: Comparison between Hujeux law manual calibration (closed dotted points), optimization calibration (open dotted points) and laboratory results (continuous line) of 'Évora' sand (signs according to Applied Mechanics convention)

number of cycles was not easy, even with the incorporation of a new parameter in the model. This new parameter was found to be useful to produce a smooth variation on the relation of the total permanent strain versus the performed number of cycles. However it was not sufficient to limit the maximum total permanent strain, excessive in all the study cases. To overcome this limitation, adjustments should be performed, being this aspect an important factor of the development.

Also, a preliminary study with the use of an optimization technique, developed at UM by Professor Lino Costa, was done to assist on the calibration process. To validate its efficiency it was used to calibrate a soil representative of the capping layer, since it was the one with the worst adjustment in the manual process. From its use it was possible to conclude that the technique is able to quickly define a set of parameters, at least as good as those obtained with the manual procedure. Nevertheless, it was also found that the algorithm could fall

into the local minimum if search intervals were excessively large, reason why an improved version of the algorithm is desirable.

Summing up, the study here performed allowed the definition of a set of parameters for each material that globally captures its geotechnical behavior. With it, the development of an 3D model able to consider the non-linear irreversible behavior of the soil can be performed in order to validate the conclusions presented in Chapter 3.

Stress-path evaluation: elastoplastic behavior

5.1. Introduction

The main purpose of this Chapter is to investigate the characteristic stress-path induced by HST in its near fields. The field measurements of train-induced ground vibrations were obtained, by Degrande (2000), in the railway line between Brussels and Paris during the passage of a Thalys HST at speeds varying between $160\,\mathrm{km\,h^{-1}}$ and $330\,\mathrm{km\,h^{-1}}$. The case study is the same as the one used in Chapter 3 so that the previous assumptions and conclusions could here be validated. Taking this fact into account, the site geometry, load characteristics and soil mechanical properties will not be provided here (see Chapter 3). Also, the Hujeux law calibration of the layers composing the railway structure, performed in the previous Chapter, is utilized used.

In order to investigate the characteristic stress-path, one must start by the definition of a finite element mesh. To do so, the choice between a 2D/3D simulation and train simulation (by means of moving concentrated loads or equivalent distributed loads) had to be done. Studies performed by several authors using FEM techniques in 2D (Gutowski and Dym, 1976; Kok, 2000; Hall, 2003; Wang and Zeng, 2004) and 3D model (Hall, 2003; Banimahd and Woodward, 2007) were analyzed to allow a better mesh definition, with minimum simplification. For example, Gutowski and Dym (1976) referred that vibration propagation can be studied by means of 2D models if the observation of the deformations is performed for distances inferior to $\frac{l_\mathrm{T}}{\pi}$. In the case study of this work, since the maximum train axle distance l_T (for a Thalys train) is equal to 192.9 m, results obtained with 2D model would only be valid for distances up to 61 m. It was also mentioned that it was necessary to pay attention to the train speed which, in 2D models, should be inferior to critical speed. This is due to the fact that wave propagation is only taken into consideration in 3D models. The biggest reported concern was the fact that a high number of small elements is required to allow the correct simulation of the wave propagation. Also, since a FEM numerical model has to be defined with boundary conditions, and bearing in mind that moving loads generate wave propagation from the rail to far neighborhoods, damping boundary conditions must be taken into consideration. Regarding the longitudinal maximum element size, previous studies performed by Kuhlemeyer and Lysmer (1973) suggested that the maximum element size

should be inferior to $1/8 \sim 1/5$ of the minimum shear wave length l_s^{min}. Regarding the time step Δt, and attending to the Nyquist theorem, the minimum wave length should be at least 10 times higher the product $\Delta t \times C_s^{max}$. The desirable frequency range should reach, in this case study, up to 29 Hz (the boogie frequency).

5.2. Mesh

5.2.1. Published cases

From the analyzes of the FEM meshes available in the literature a three-dimensional mesh similar to that used by Hall (2003) was built. This choice rests on the fact that dynamic effects are not well captured in bi-dimensional models and also because linear elastic assumption was made by the author. Hall (2003) referred that advanced constitutive models such as Drucker-Prager and Cam-Clay were available but were not used since the linear elastic material model was much less demanding on computer resources than a non-linear material model. This assumption bumps with the large shear strains computed (by the author) in the embankment and in the soft layers just beneath the railway embankment. This fact was taken into consideration by the author by means of an iterative reduction [sic] of the shear modulus of the materials where large shear strains were calculated.

Focusing on the geometry of the three-dimensional model developed by Hall (2003), it was referred that it measured 23 m large, 65 m long and 50 m deep and consisted of 98919 elements and 94010 nodes. The average element size in the upper part of the model is about 0.65 m in both width and height. The general elements consist in eight-node linear brick elements. However, inside the embankment, six-node linear brick elements were used in order to model sleepers and the complex geometry of the embankment. Euler-Bernoulli beam elements were used to simulate the rail, with geometry and properties of regular railway rails (UIC60). Hall (2003) used sharing nodes between the surface of the sleepers and the rails (no pad element was considered). At a depth of 9 m below the embankment surface, the height of the elements was gradually increased from 0.65 m to 8 m at the bottom. The average element size in the model was calculated to be 1.10 m. As previously referred, the model length was estimated to 65 m since only the response close to the track was considered. The center of the model (the symmetry line) was locked in the horizontal direction perpendicular to the rail. The nodes on the remaining vertical boundaries were connected to vertical and horizontal dashpots in order to absorb shear and compression waves. The nodes at the bottom boundary were fixed in every direction to simulate the bedrock. Vertical and horizontal springs were applied at both ends of the rail in order to keep the rail in place at the ends of the finite element model. The properties of the springs were given according to soil pressure. Marcelino (2007), in a 2D model of a HST railway line, also used the symmetry axle to reduce computational effort. The analyzes were performed with a fixed time step of 1 ms.

Hall (2003) also performed studies in 3D models without sleepers. To do so, the load distribution induced by the rail was calculated from the static solution of a beam resting on a Winkler foundation model. This strategy was also

used by Marcelino (2007), Alaoui and Naciri (1995) and Shaer *et al.* (2008). Marcelino (2007) points out that for a train speed inferior to critical speed, the deformation due to each axle is similar to the one obtained in a beam resting on an elastic medium (i.e., the Winkler's foundation beam). This author also referred that the shape of the loading curve depends on the speed of the load, the response of the railway structure and the foundation. For high load speed values, the loading curve becomes more localized and, if this speed becomes too near to the critical speed, the loading curve loses its symmetry and maximum loading is achieved after the passage of the train axle. Marcelino (2007) took advantage of an approximated procedure to define the load distribution presented in Japanese standards. According to those standards, 40 % to 60 % of the axle load is transferred to neighborhood sleepers. Regarding the shape of the load distribution, Marcelino (2007) used a simple model of a beam resting on a Winkler foundation submitted to a static axle load. The solution of this simplified model is given by:

$$W(y) = \frac{P}{2k_{\mathrm{s}}L}\mathrm{e}^{-|\frac{y}{L}|\left(\cos|\frac{y}{L}|+\sin|\frac{y}{L}|\right)} \tag{5.1}$$

in which $W(y)$ represents the vertical displacement of the beam, L the characteristic length, P the value of the axle load, k_{s} soil stiffness and y the cartesian coordinate of the load moving referential. This author points out that it is reasonable to assume that for train speeds inferior to critical speed, the load distribution should be similar. For this reason, the author proposes Equation 5.2, in which $P(y)$ represents load distribution (applied by the axle), P_{p} the axle load value and $\tilde{L}$ the length that implies a certain load distribution at $y = 0$.

$$P\left(y\right) = \frac{P_{\mathrm{p}}}{2\tilde{L}}\mathrm{e}^{-|\frac{y}{L}|}\left(\cos\mid\frac{y}{\tilde{L}}\mid+\sin\mid\frac{y}{\tilde{L}}\mid\right) \tag{5.2}$$

However, this approach is limited since the influence of each stiffness layer of the structure, sleeper spacing and train speed is only controlled by a direct load distribution consideration. An improved procedure was proposed by Alaoui and Naciri (1995) and used by Ricci *et al.* (2005), Shaer (2005) and Shaer *et al.* (2008). Alaoui and Naciri (1995), following calculations performed by Sauvage (1993), proposed Equation 5.3 to obtain the quasi-static component of the load induced by the passage of a wheel:

$$P(t, P_{\mathrm{p}}, C) = \frac{P_{\mathrm{p}}Y}{2}\left[X^{\left(\frac{Ct-5d}{d}\right)^2} + X^{\left(\frac{Ct-5d-L}{d}\right)^2}\right] \tag{5.3}$$

where P_{p} is the load per axle, C is the speed of the train, t is time, d is the distance between two consecutive sleepers, l is the distance between two axles of a boogie, and X and Y are non-dimensional variables ranging between 0 and 1. The values of X and Y depend on the elasticity modulus E of the soil and are given in Table 5.1.

Despite these considerations, Hall (2003) referred that since the beam elements were not included in the FEM model, a slight loss in accuracy is detected. Due to this fact, sleepers and rails should be defined in the mesh if more computational resources are required. To do so, the train load has to be applied as triangular pulses distributed between nodes, and moved from node to node by a time step equal to the node spacing of the loading nodes, Δx, divided by the speed C of the moving loads as $\Delta t = \Delta x \times C$.

Table 5.1: Values of X and Y in function of soil elasticity modulus for the evaluation of load distribution

E_s/MPa	10	30	60	80	100
X	0.820	0.715	0.640	0.625	0.610
Y	0.230	0.320	0.380	0.410	0.430

Other authors use distinct FEM models for simulating moving loads to analyze the assumptions made by Hall (2003). For instance, Ju and Lin (2004) used an extremely large FEM model with 941.2 m long, 242.7 m wide and 105 m deep with the maximum element size of 3 m. The top foundation layer was modeled by 8-node 3D solid element, the rail and pad with 2-node 3D beam element, the train by moving wheel element and the foundation layers, except the top one, modeled by damping boundaries. The FEM mesh of the model contains 1277824 (13 times the number of elements used by Hall (2003)) 8-node brick elements, 4225 3D beam elements, 48 wheel elements and 207159 damping boundaries. The time step length was set to 4.4 ms for the train speed below 500 km h^{-1} and 2.5 ms for train speed over it, and 2048 time steps were simulated. On the other hand, Wang *et al.* (2005) used a 3D finite element symmetric model quite similar to the one defined by Hall (2003). It consists of a 50 m long portion of an idealized high-speed railway structure resting on a block of soil 50 m long, 100 m wide, and 100 m deep. The symmetry plan was used by this author to split the rail structure and the soil foundation in half; points on the symmetry plan were freely assumed in the y and z direction but not in the x direction. The bottom of the foundation was fixed in all translational directions, while the sides of the foundation were fixed in the x and y direction. The model was meshed using three-dimensional, 20 node quadratic continuum elements analyzed with reduced integration. Fifty meters of the soil foundation was extended on both ends of the rail to allow for vibration dissipation through the surrounding soil. Materials composing the rail structure were assumed linear elastic while foundation soils were assumed elastoplastic with Mohr-Coulomb plasticity. Train passage was modeled with discrete pressure loads moving along each segment of the rail. The pressure load progressed over the rail, resting on each 5 m long segment of the rail for 66.67 ms before proceeding to the next segment (corresponding to a velocity of 270 km h^{-1})

5.2.2. New mesh

Based on previous models (e.g. the model defined by Hall (2003)), a new mesh was defined, using GEFDYN software, for the quantification of the characteristic stress-paths. It consists of a three-dimensional symmetric mesh (Fig. 5.1) with 48.9 m long, 22.6 m wide, 8.1 m deep and 33864 nodes. These dimensions do not take into account the elements in contact with the damping boundaries which were defined (on the direction perpendicular to the paraxial elements) with 10 m length so that low frequencies could be absorbed (since

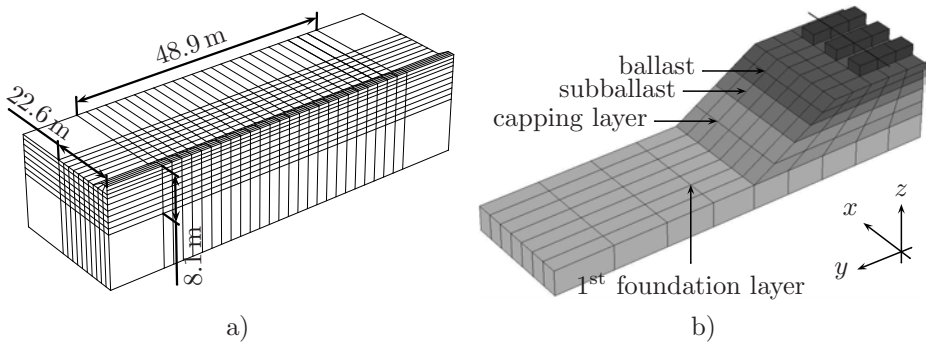

Figure 5.1: a) Global view of the FEM mesh and b) detail of the railway structure

$C_s^{\text{min.}} = 100\,\text{m}\,\text{s}^{-1}$, frequencies are filtered if they are higher than 1.25 Hz). The FEM mesh contains 26474 8-node isoparametric brick elements, 249 3D square mechanical interface elements with 8 nodes for controlling frictions and shear between tri-dimensional volumetric elements, 161 tri-dimensional linear elastic Wilson beams and 4290 tri-dimensional linear elastic paraxial elements (of zero degree) without incident fields. The mesh was built without pad elements since Hall (2003) obtained good results in a similar model without these elements and, consequently, achieved a computational effort reduction. Regarding the isoparametric brick elements, 249 were used to simulate sleepers, 1650 used to simulate ballast layer, 825 the subballast layers, 1650 the capping layer, 6930 the top layer of the foundation, 6930 the middle layer of the foundation and 8240 the bottom layer. Assuming a wavelength 8 times higher than the minimum longitudinal dimension of the elements (0.3 m), the minimum wavelength must be higher than 2.4 m. In this way, and attending to the fact that the minimum shear velocity in this study is 100 m s$^-$1, the maximum frequency studied in the model is 42 Hz. Regarding the maximum time step, since maximum compression wave velocity is $423\,\text{m}\,\text{s}^{-1}$, it is limited by 0.6 ms. This time step is significantly lower than the ones given in literature. That way and since train speed is $87\,\text{m}\,s^{-1}$ and the longitudinal discretization is 0.3 m, a time step of 1.7 ms was defined. With this time step, three points are computed for each period of the maximum compression wave, a value assumed reasonable to avoid heavy computations and able to simulate foundation behavior.

Boundary conditions were defined taking advantage of the symmetry surface that was locked in the horizontal direction perpendicular to the rail. The nodes on the remaining horizontal boundaries were connected to paraxial elements able to produce energy dissipation. The nodes at the bottom boundary also belonged to paraxial elements since no information exists regarding the position of the bedrock, therefore an infinite medium is considered. The paraxial elements were assumed with linear elastic behavior and defined by 3 mechanical parameters: unit mass ρ, Young modulus E and Poisson ratio ν. Regarding the trains excitation, one must refer that only the first boogie (one of the heaviest) was simulated. The load was applied instantly and kept constant during a period of 340 ms to allow energy propagation. After this period the load was applied as triangular pulses distributed between 5 nodes (Fig. 5.2), and moved from node

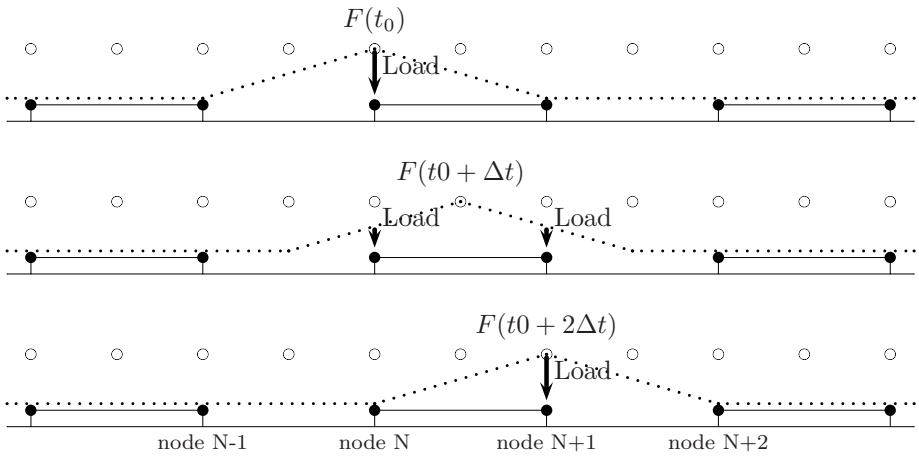

Figure 5.2: Loading scheme for a generic time step t

to node in intervals of one time step of 1.7 ms along a time interval of 312.8 ms (corresponding to a boogie movement of 27 m). Boogie initial position was 19 m away from model limit (the closest axle) in order to reduce disturbance.

Attending to the load distribution of load in the lateral (yy) and vertical (zz) directions, elements dimension grow from the railway structure to the limit of the model. Elements were divided in sections {0, 0.7, 1.39, 2.09, 2.79, 3.48, 4.28, 5.17, 6.17, 7.27, 8.46, 9.76, 11.15, 12.65}, along yy direction (in the foundation layers), and in zz direction 0.2, 0, -0.15, -0.3, -0.5, -0.75, -1, -1.47, -1.93, -2.4, -3.1, -3.9, -4.8, -5.8, -6.9, -8.1} m. These variations of element dimension, in these 2 directions, allow a significant reduction in the number of volumetric elements.

To conclude the description of the developed FEM mesh one must clarify the chosen constitutive laws. As previously referred the boundary paraxial elements were only available with linear elastic formulation. In addition to these elements, sleepers and rails were always computed assuming linear elastic behavior. Regarding the mechanical interface elements, they were introduced to allow sleeper uplift (in order to avoid unrealistic tractions in the soil) and also a certain slippage between the ballast and the sleeper. These elements (with 1 cm thickness) were assumed not deformable in the direction of loading (by means of a high value of E_{n}) and with a shear modulus (on the base surface of the sleeper) of 500 MPa. Foundation layers were always assumed with elastic behavior (see Chapter 3 for a description of the mechanical properties) and railway layers presenting three distinct constitutive behaviors:

1. Simulations assuming linear elastic behavior were performed to allow validation of the results presented in Chapter 3. This situation was studied in 2 cases, respectively with and without the application of a constant pressure of 20 kPa over the ballast layer. This introduction was required in the 2 following cases to allow convergence and was made by means of nodal forces applied only on the nodes on the top surface of the ballast layer. Damping was artificially introduced by means of the Newmark integration scheme (α=0.6 and β=0.303).

2. A simulation was performed assuming Mohr-Coulomb constitutive law for ballast, subballast and capping layer. This computation, performed with the application of the constant pressure of 20 kPa, was made since this law is widely used in the geotechnical projects, it is not demanding in terms of computational efforts and significantly improves the capacity of the model (when compared with the linear elastic case). Regarding the used values, they were defined in Chapter 4 during the calibration of the Hujeux law. This consideration was made since the Mohr-Coulomb law can be written as a simplification of Hujeux law. This law was defined in terms of E, ν, ϕ, ψ (equal to the values defined for Hujeux law) and a small artificial cohesion $c = 10\,\text{kPa}$.

3. The last study case used an elastoplastic cyclic multimechanism constitutive law. With the calibration performed in the previous Chapter it was possible to simulate the precise behavior of the ballast, subballast and capping layers. Foundation was assumed with linear elastic behavior.

5.3. Models validation

The mesh previously described was subject of validation for 4 distinct case studies, each one defined with a different constitutive law or excitation (only in terms of constant pressure load). This validation was performed in time domain in terms of the initial vertical stress (model initialization), sleeper vertical acceleration and sleeper vertical velocity. Attention was also paid to the fact that the load starts from a static configuration (at $t = 0$) and changes to a dynamic one, requiring the study of three points of the structure placed at distinct xx position: 20.1, 24.9 and 30.0 meters, respectively.

Regarding stress initialization, results were compared with the expected theoretical ones. Figure 5.3 presents the evolution of vertical stresses depending on depth and compares them with the theoretical ones, obtained from $\sigma_{\text{zz}} = z \times \gamma$. The points used in this validation are those presented in Figure 5.4.

From its analysis it was detected that numerical results are slightly inferior to those given by the theoretical ones. This is due to the fact that the railway structure presents infinite development only in the xx direction. More precise methods to obtain the theoretical results were not used (namely using Bousinesq elastic solutions) since they would not contribute significantly to an improvement of the validation.

Regarding the validation in terms of the sleeper acceleration and velocity, numerical results were compared with *in situ* measurements performed by Degrande (2000). These results were also used for the validation of the numerical model presented in Chapter 3. To perform this validation, three points of the linear elastic models were compared with the *in situ* data, respectively in sections xx at 20.1 m, 24.9 m and 30.0 m. Since similar results were obtained in all cases (Figs. 5.5 and 5.6) the non-linear models were compared just for one point of the sleeper, placed under the rail and at $xx = 30\,\text{m}$. Figures 5.5 to 5.8 summarize all validation performed in terms of the dynamic analyzes.

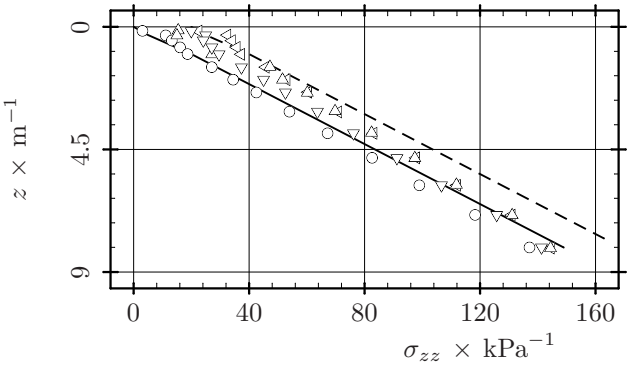

Figure 5.3: Vertical stress initialization for the points given in Figure 5.4 assuming: (○) elastic constitutive law without a vertical pressure over the top of the ballast, (◁) elastic constitutive load assuming a vertical pressure of 20 kPa over the top of the ballast, (△) Mohr-Coulomb constitutive law assuming a vertical pressure of 20 kPa over the top of the ballast, (▽) Hujeux constitutive law assuming a vertical pressure of 20 kPa over the top of the ballast, (**solid line**) theoretical vertical stress without a vertical pressure over the top of the ballast and (**dashed line**) theoretical vertical stress assuming a vertical pressure of 20 kPa over the top of the ballast.

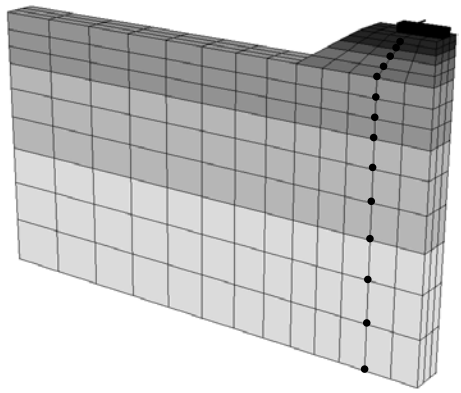

Figure 5.4: Study points depending on depth with $(y \times \mathrm{m}^{-1}, z \times \mathrm{m}^{-1})$ coordinates of: (0.85,-0.15), (0.94,-0.30), (1.07,-0.50), (1.23,-0.75), (1.39,-1.00), (1.39,-1.47), (1.39,-1.93), (1.39,-2.40), (1.39,-3.10), (1.39,-3.90), (1.39,-4.80), (1.39,-5.80), (1.39,-6.90) and (1.39,-8.10)

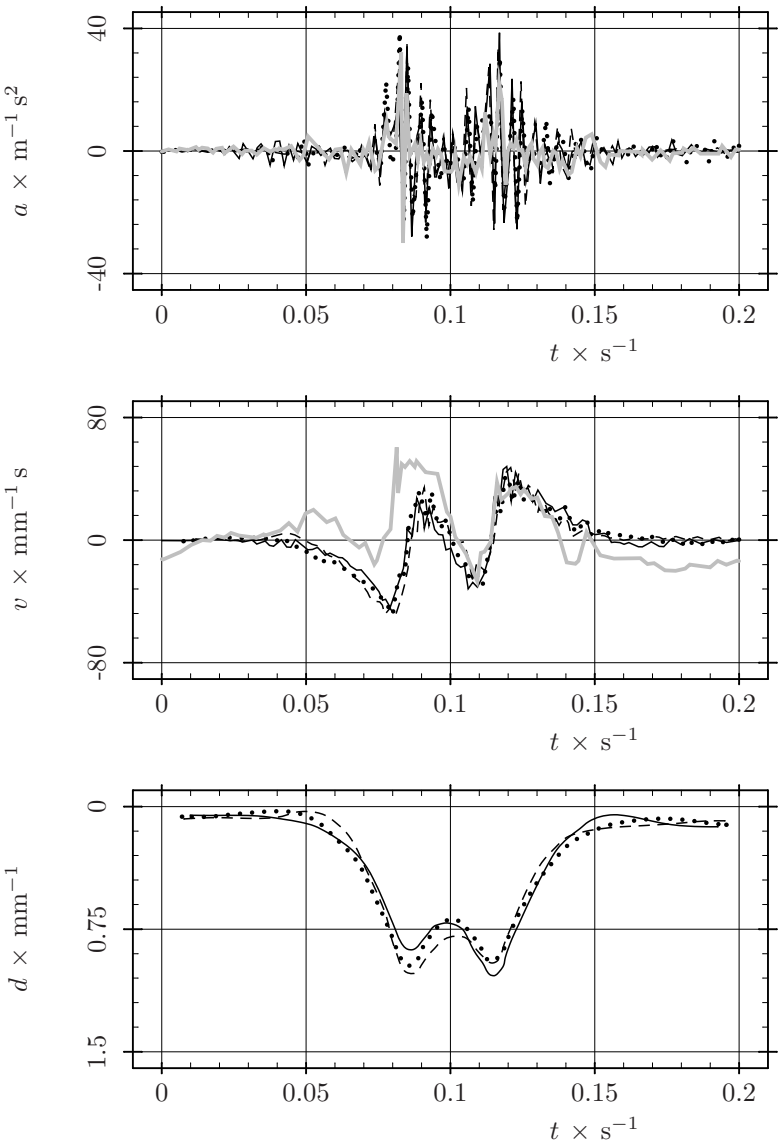

Figure 5.5: Comparison (assuming linear elastic constitutive law and no vertical pressure over the ballast layer) between *in situ* measurements (gray line) and numerical results obtained in 3 distinct sleepers: (dashed line) $x = 20.1\,\mathrm{m}$, (dotted line) $x = 24.9\,\mathrm{m}$ and (continuous line) $x = 29.7\,\mathrm{m}$

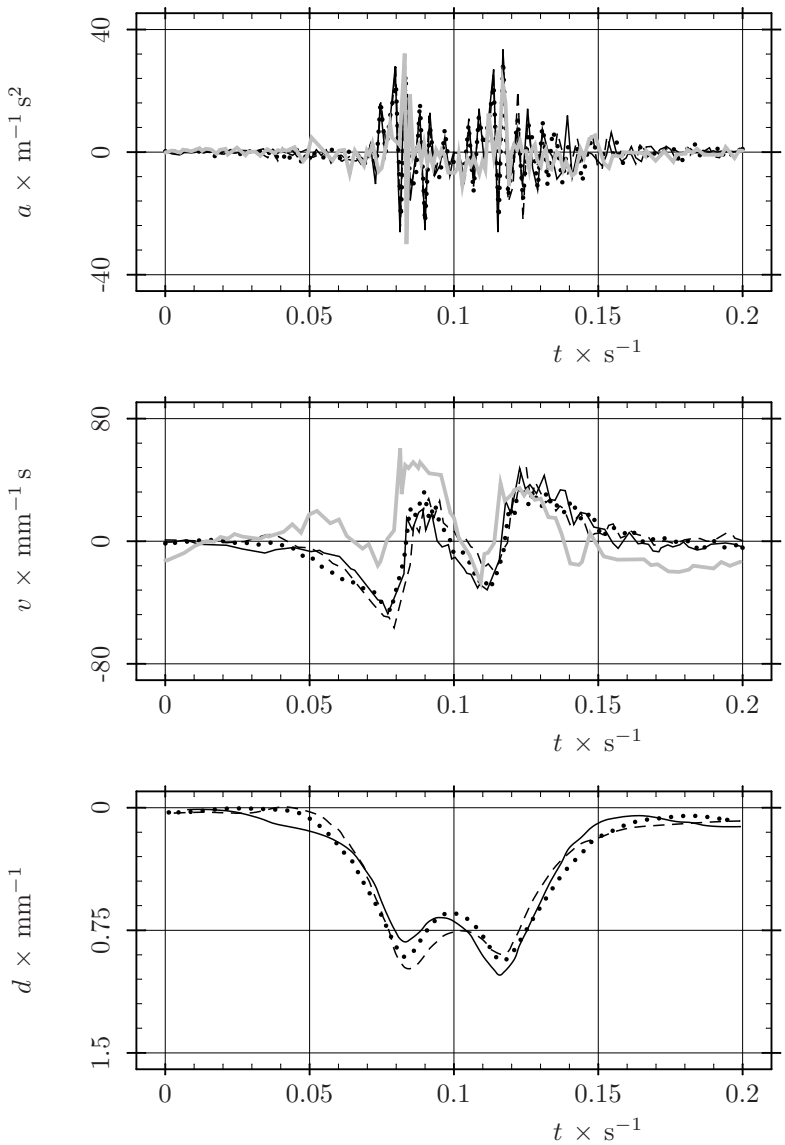

Figure 5.6: Comparison (assuming linear elastic constitutive law and a vertical pressure over the ballast layer of 20 kPa) between *in situ* measurements (gray line) and numerical results obtained in 3 distinct sleepers: (dashed line) $x = 20.1\,\mathrm{m}$, (dotted line) $x = 24.9\,\mathrm{m}$ and (continuous line) $x = 29.7\,\mathrm{m}$

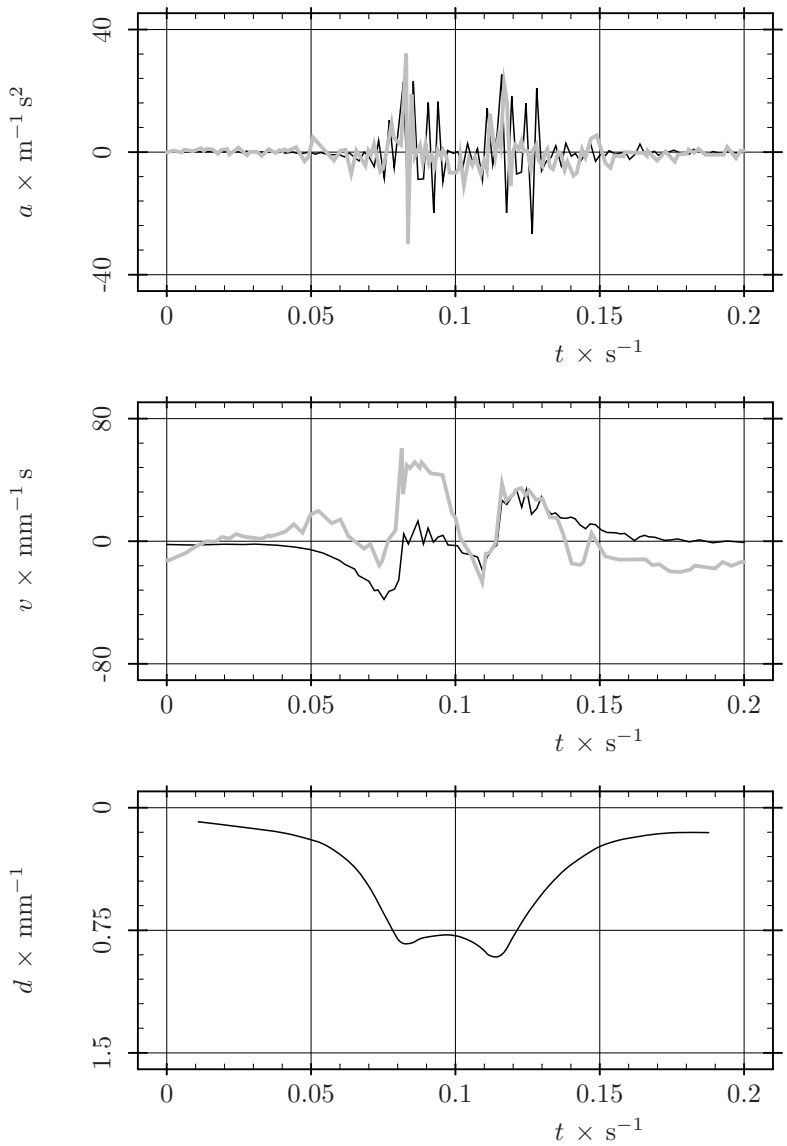

Figure 5.7: Comparison (assuming Mohr-Coulomb constitutive law and a vertical pressure over the ballast layer of 20 kPa) between *in situ* measurements (gray line) and numerical results (continuous line) obtained in a sleeper placed at $x = 29.7\,\mathrm{m}$

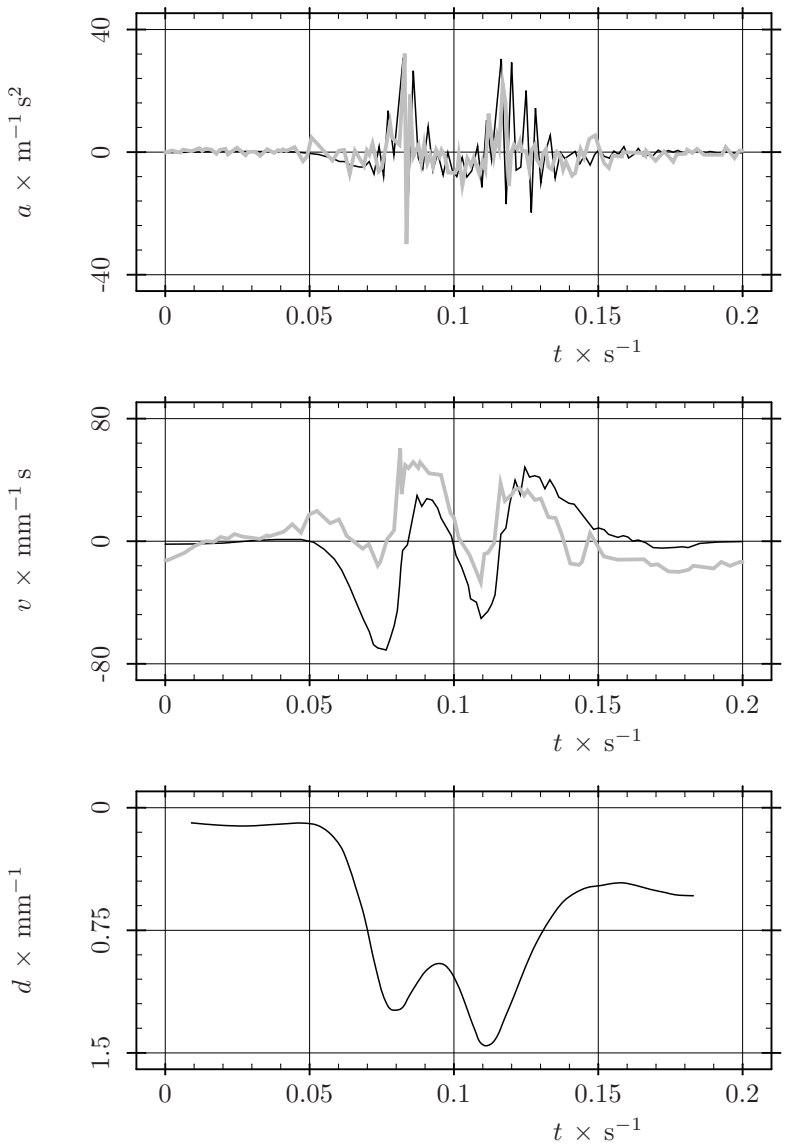

Figure 5.8: Comparison (assuming Hujeux constitutive law and a vertical pressure over the ballast layer of 20 kPa) between *in situ* measurements (gray line) and numerical results (continuous line) obtained in a sleeper placed at $x = 29.7\,\mathrm{m}$

After interpreting these results, it is acceptable to state that the introduction of the constant pressure over the ballast layer did not introduce a perceptible modification between the two elastic simulations. With this confirmation the use of this load in the non-elastic studies, required to avoid convergence problems due to the dynamic uplift of the element in the top boundary of the railway structure, was considered valid. Having accepted this assumption, the comparison in terms of acceleration, velocity and displacement can be performed between all models.

In terms of acceleration response, in all simulations, it presents a maximum value around $30\,\mathrm{m\,s^{-2}}$. This value is quite similar to that recorded by Degrande (2000). The difference between the highest positive and the lowest negative acceleration is also perceptible. In terms of velocity, it is important to remember that it was obtained from the integration of the acceleration response. This fact introduces, due to the low frequency content, a higher adjustment to zero position of the 'measured' response. This is confirmed when the comparison is made between 'measured' and any of the numerical results. Nevertheless, the adjustment is quite small and the integration response can be considered valid. It is also possible to refer that all models present similar response, with the exception of the last one (which uses Hujeux constitutive law). The remaining cases presented a maximum velocity around $40\,\mathrm{mm\,s^{-1}}$, a value quite similar to that provided by Degrande (2000). In Hujeux law case this value increases to nearly the double. This increase in velocity is due to the existence of irreversible deformations which increase vertical displacement. Finally, in terms of displacement, the linear elastic and Mohr-Coulomb cases simulations present a maximum reversible settlement near 1 mm. This value was, however, higher for the Hujeux law simulation which presents a total settlement of 1.5 mm. This value can, however, be decomposed in a reversible component of 1 mm and in an irreversible one of 0.5 mm. This value cannot be compared with *in situ* measurements since no data was collected at the time. Nonetheless, in Mohr-Coulomb simulation the irreversible component is negligible because the model presents perfect elasticity before plasticity is reached. In Hujeux law case, however, a quite small linear elastic domain is assumed to introduce, in the first loading of the structure, a strong irreversible component.

In sum, all models provide accurate response in all domains (i.e., acceleration and velocity) and will be used to validate results obtained in Chapter 3, which was able to reproduce velocity but not acceleration field. From the application of the hybrid FEM-BEM model it was assumed that stresses induced in the railway structure were correct. In this Chapter this hypothesis is validated since the same level of displacement is provided (around 1 mm). The high global displacement presented in Chapter 3 is assumed due to the filtering of the low frequency components of the signal, responsible for the large wavelength deformation. The amplitude of the large wave deformation are significantly smaller if the foundation is stiffer and its removal is, consequently, less noticed.

5.4. Characteristic stress-path

Once clarified the definition of the new FEM mesh and performed the validation for all case studies, the quantification of the induced stress field was possible. To do so, the evolution in depth of the 6 components of the stress

tensor are given in Figures 5.9 to 5.12. These Figures represent the stress evolution during the passage of a boogie for the points given in Figure 5.4 and for a section at $x = 24.9\,\mathrm{m}$.

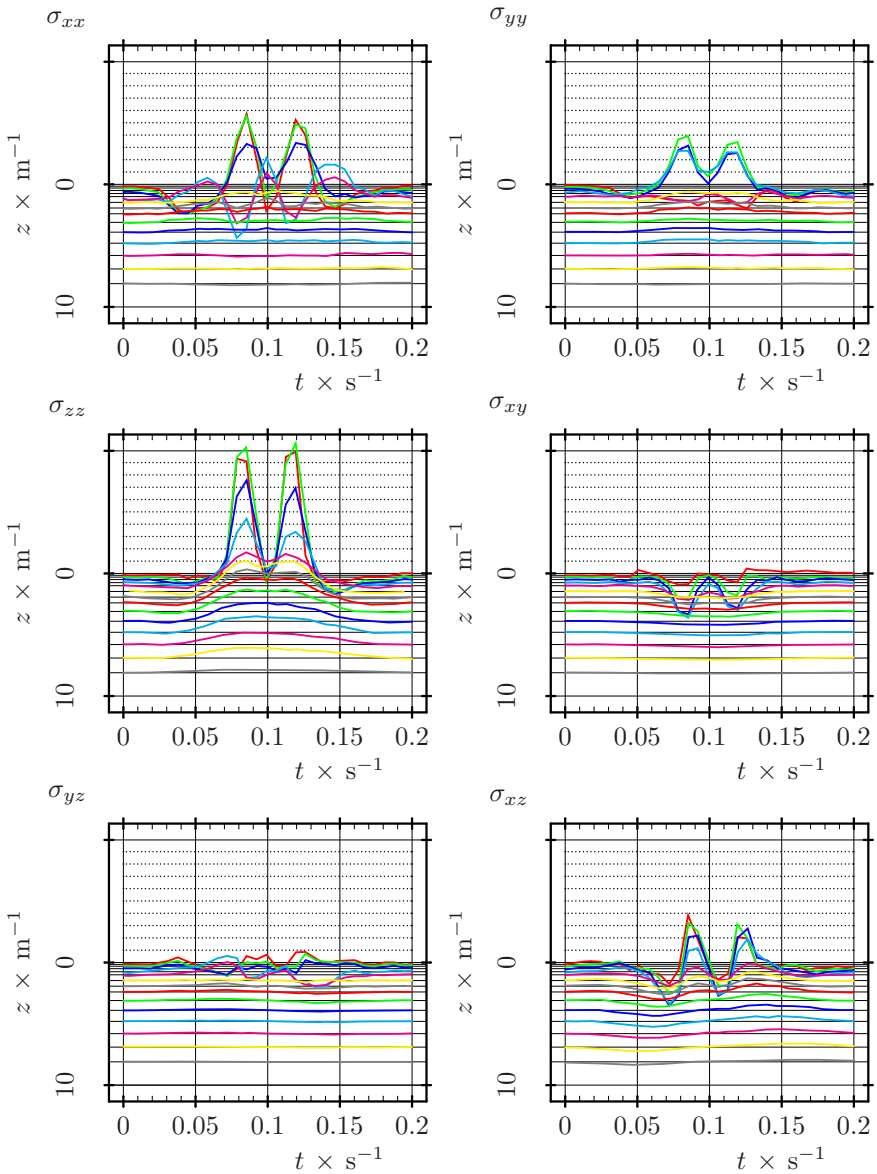

Figure 5.9: Stresses (in the nodes defined in Figure 5.4) induced by the passage of a boogie and assuming elastic constitutive law without a vertical superficial load applied on the ballast (dotted grid represents increments of 5 kPa)

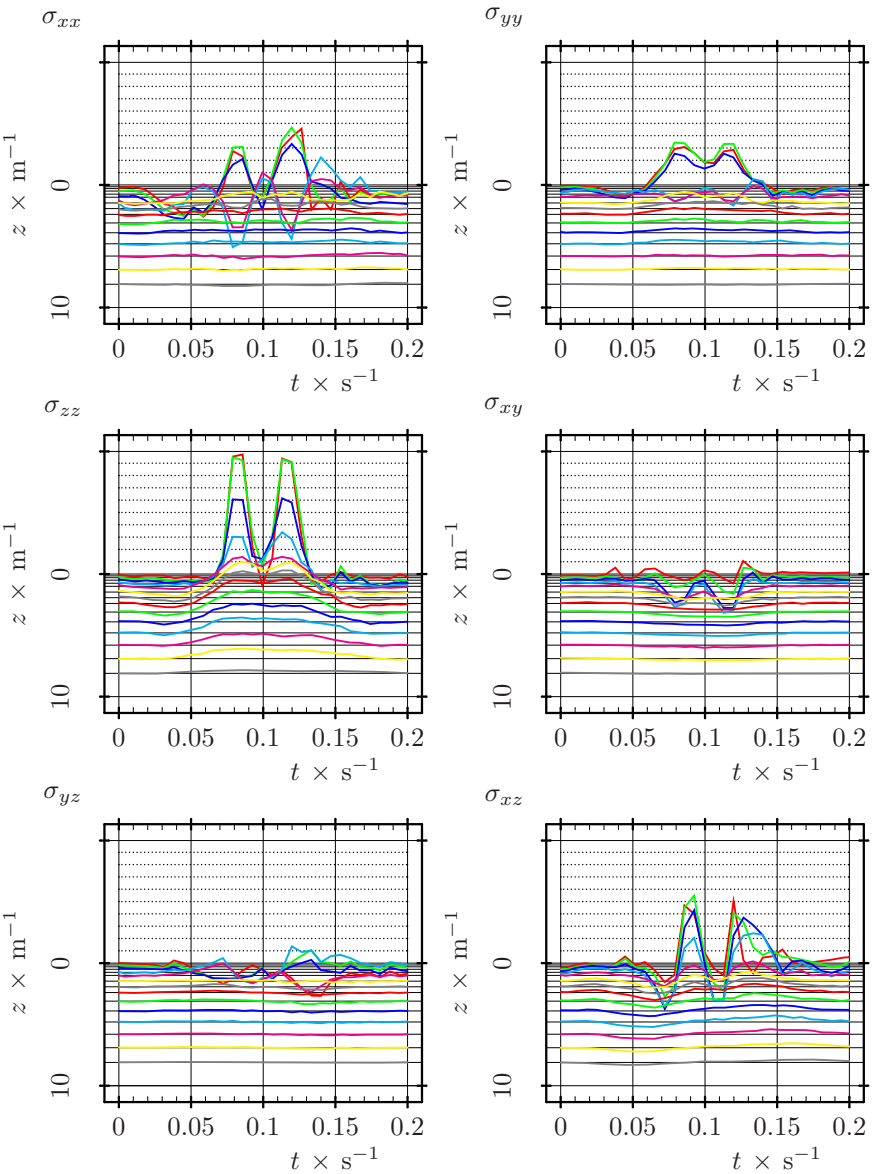

Figure 5.10: Stresses (in the nodes defined in Figure 5.4) induced by the passage of a boogie and assuming elastic constitutive law with a vertical superficial load applied on the ballast (dotted grid represents increments of 5 kPa)

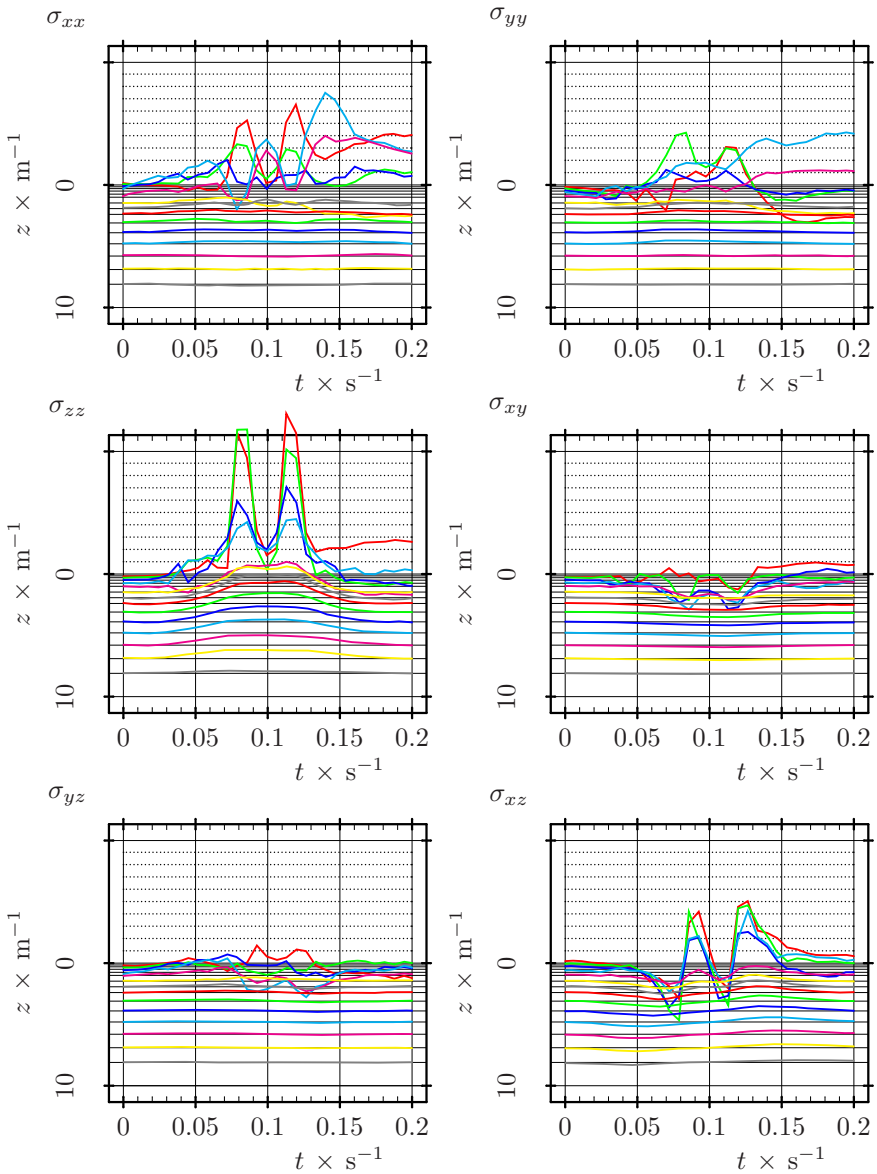

Figure 5.11: Stresses (in the nodes defined in Figure 5.4) induced by the passage of a boogie and assuming Mohr-Coulomb constitutive law (dotted grid represents increments of 5 kPa)

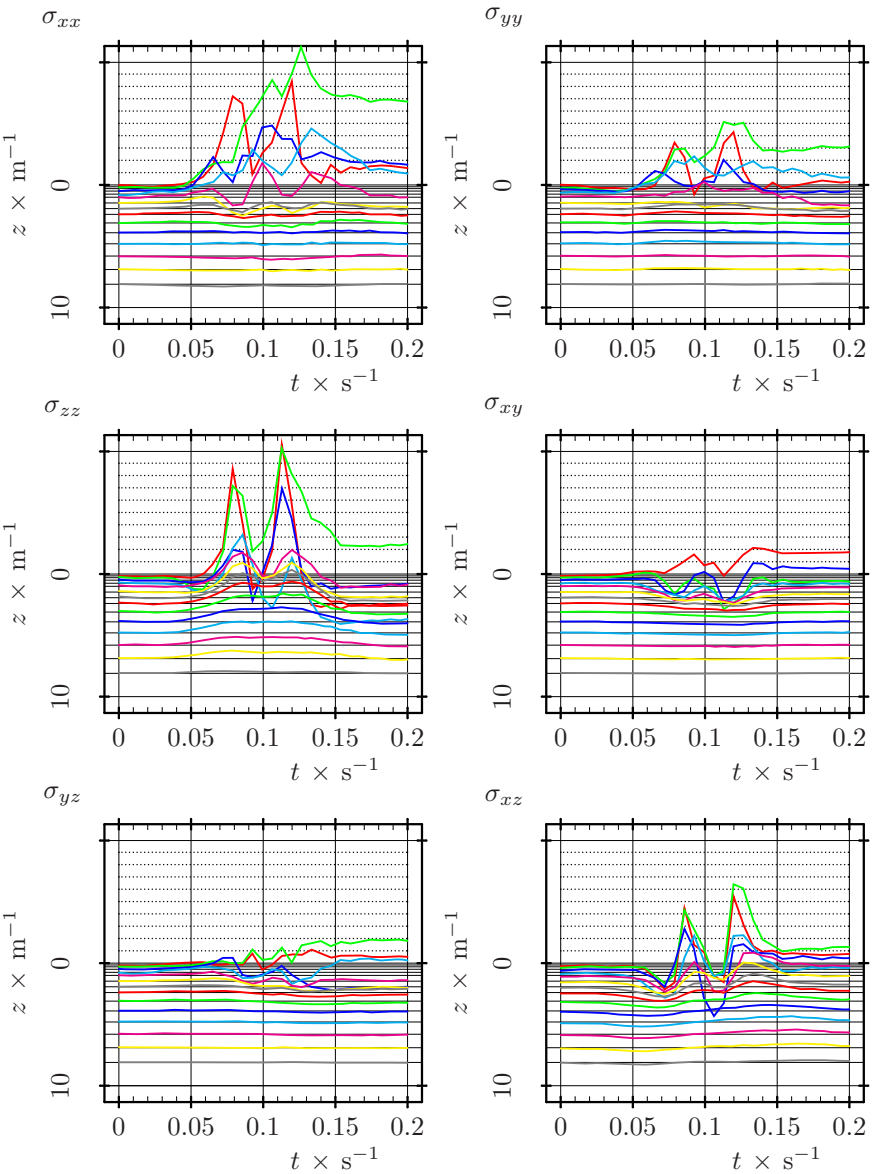

Figure 5.12: Stresses (in the nodes defined in Figure 5.4) induced by the passage of a boogie and assuming Hujeux constitutive law (dotted grid represents increments of 5 kPa)

Note that Figures 5.9 to 5.12 were built using the following concept: the computed stress value is shifted according to the position of the study node. For example, if no stress exists for all time instants, the graphical representation would be a horizontal line that intersects yy axis on the value that represents the depth of the study's point. Also, the value of the stress is added according to the distance between two grid lines (which represents intervals of 5 kPa). They allow the comparison between different material behavior assumptions (elastic or not) in terms of stress evolution. For instant, it is visible in all cases that computed σ_{xy} and σ_{yz} are significantly smaller than those obtained for σ_{xz}. The value of σ_{xy} and σ_{yz} is around $5 \sim 10$ kPa , while σ_{xz} is around $25 \sim 30$ kPa. This fact is due to sleeper distribution and low shear excitation in the horizontal surface. Excitation occurs only along the direction x and z. Regarding normal stresses, it is confirmed that vertical stress is the dominant component. This characteristic is also found in the case of Hujeux law, in which the normal longitudinal stress (σ_{xx}) reaches a similar value. The value of σ_{yy} is around $15 \sim 20$ kPa, while the value of σ_{zz} is around $45 \sim 55$ kPa. The value of σ_{xx} was around $20 \sim 25$ kPa, except for the Hujeux law case in which it reaches a maximum value around 50 kPa. Using Hujeux law (without a large elastic domain), plastic longitudinal movements were highly magnified with the movement of the load. From the analysis of the first phase of the dynamic computation, i.e., the instantaneous application of the boogie, no significant horizontal movements are detected. However, with the introduction of load movement, induced waves produce permanent deformation. This exaggerated permanent deformation does not, however, invalidate model validation. Both acceleration and velocity match *in situ* measurements. Regarding structures vertical deformation, it corroborates the high plastic value found in the simulation (around 0.5 mm).

These analyzes (comparison with *in situ* measurements and stress evolution) were performed to validate the model's general behavior and allow a valid stress-path analyzes. Stress-path study, the aim of this Chapter, is performed through interpretation of Figures 5.13 to 5.16. In these Figures the evolution of the vertical strain is also presented in order to validate the assumption of the elastic foundation. This validation is here done assuming that the elastic domain found in Chapter 2 is valid for the material representative of the top layer of the foundation. Since no information exists about the elastic domain of the foundation soils, data obtained with Perafita sand was used.

Regarding the evolution of the stress-path, for the four points of the railway structure and for all numerical models, tendencies are similar to those found in Chapter 3. However, results present a higher level of dispersion than those found with the frequency domain model. For this reason, and to facilitate interpretation, a stress-path obtained from a linear adjustment of the results was plotted for each study point. Based on their evolution, model tendencies are compared with those found in Chapter 3 (for the unload elastic model) and also between models (to study the influence of the introduction of more realistic constitutive laws). On this context it is possible to refer that the evolution of the stress along structure depth, for the elastic unload case, is identical to that found in Chapter 3. The characteristic stress-path of the ballast is practically identical to NSL slope. This direction, however, increases in depth and assumes, for a point in the base of the capping layer, a stress-path with a small variation on the mean stress. This evolution is again assumed to be introduced by the elastic assumption that, due to the bending effect of the structure, induces

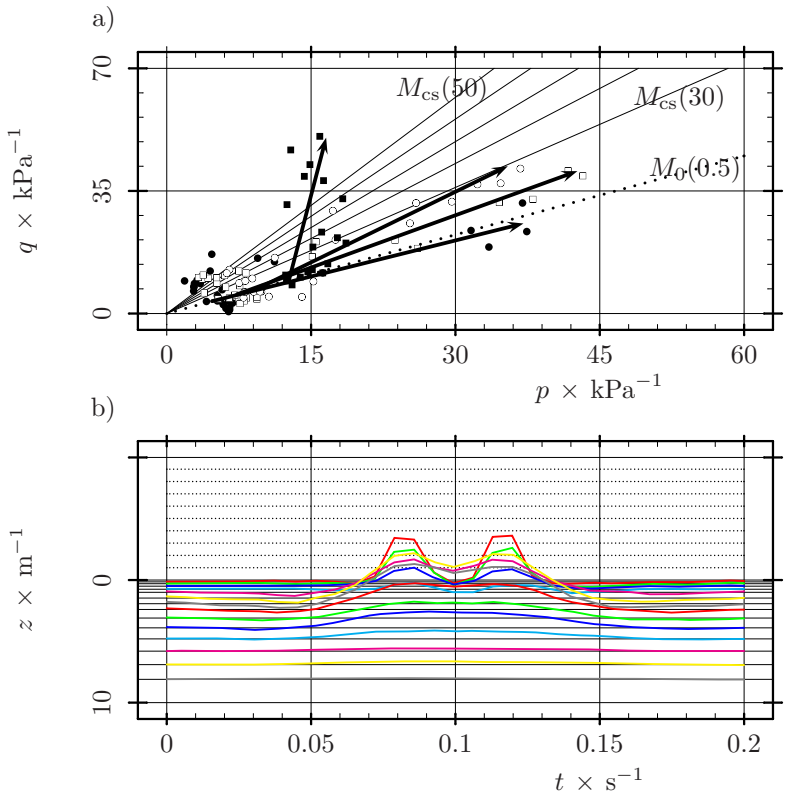

Figure 5.13: a) Characteristic stress-path assuming linear elastic constitutive law without a vertical pressure applied on top of the ballast, for a point placed at: (●) middle of the ballast layer $(x, y, z) = (24.9\,\mathrm{m}, 0.85\,\mathrm{m}, -0.15\,\mathrm{m})$, (□) interface ballast/subballast $(x, y, z) = (24.9\,\mathrm{m}, 0.94\,\mathrm{m}, -0.30\,\mathrm{m})$, (○) interface subballast/capping layer $(x, y, z) = (24.9\,\mathrm{m}, 1.07\,\mathrm{m}, -0.5\,\mathrm{m})$ and (■) middle of the capping layer $(x, y, z) = (24.9\,\mathrm{m}, 1.23\,\mathrm{m}, -0.75\,\mathrm{m})$. b) Vertical strain (dotted grid represents increments of 5×10^{-5})

a stress reduction. With such a stress-path, the structure would reach failure envelope even for a friction angle ϕ of 50°. Nevertheless, despite this non realistic behavior, this result confirms those obtained in Chapter 3, the reason why non-linear constitutive models are studied in this Chapter. Since the reference model (unload linear elastic case) validates the results obtained with the frequency domain model, analyzes are made with the remaining cases. For both Mohr-Coulomb and Hujeux constitutive law, rupture is not detected. Regarding Mohr-Coulomb case, even if a small dispersion of the characteristic stress-path slope is present, it can be assumed as parallel to the failure envelope obtained with $\phi = 40°$. This dispersion is smaller with Hujeux law assumption, a case that can be assumed with a constant slope parallel to the failure envelope obtained with $\phi = 30°$. There is still one last topic that requires analyzes, which is the assumption of the elastic domain for all foundation layers. To do so, it was assumed that the elastic domain quantified in Chapter 2 was valid for the superficial foundation layer (the one subjected to the highest strain levels). In

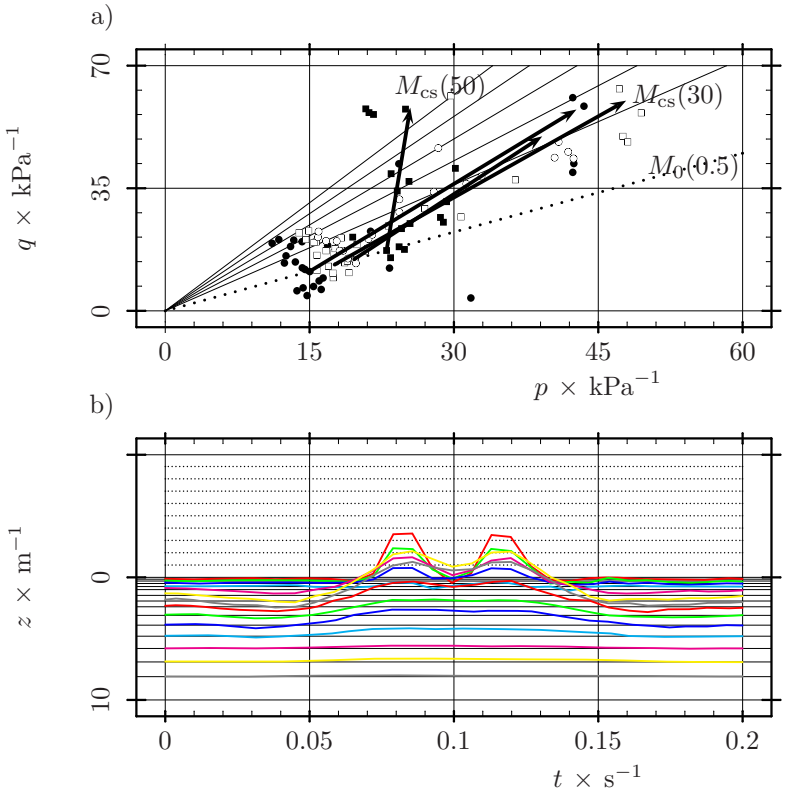

Figure 5.14: a) Characteristic stress-path assuming linear elastic constitutive law with a vertical pressure on top of the ballast of 20 kPa, for a point placed at: (●) middle of the ballast layer $(x, y, z) = (24.9\,\mathrm{m}, 0.85\,\mathrm{m}, -0.15\,\mathrm{m})$, (□) interface ballast/subballast $(x, y, z) = (24.9\,\mathrm{m}, 0.94\,\mathrm{m}, -0.30\,\mathrm{m})$, (○) interface subballast/capping layer $(x, y, z) = (24.9\,\mathrm{m}, 1.07\,\mathrm{m}, -0.5\,\mathrm{m})$ and (■) middle of the capping layer $(x, y, z) = (24.9\,\mathrm{m}, 1.23\,\mathrm{m}, -0.75\,\mathrm{m})$. b) Vertical strain (dotted grid represents increments of 5×10^{-5})

order to perform the validation it is required the level of deformation to be within the linear elastic domain. Observing Figures 5.13 to 5.16, the maximum value of ϵ_{zz} was equal to 2×10^{-4} when assuming Hujeux constitutive law, and 1.5×10^{-4} in the remaining cases. This value is significantly higher than those found when defining the elastic limit in Chapter 2, showing that the elastic assumption may be invalid. To perform a quantitative analyzes the induced stress-path is required, in this case for a point at the top of the foundation and under the rail. A slope $\Delta q/\Delta p$ of 0.56 was computed and presented; an initial state (p_0, q_0) of $(32\,\mathrm{kPa}, 24\,\mathrm{kPa})$; an mean stress amplitude Δp of 30 kPa and a deviatoric stress amplitude Δq of 17 kPa. With these values, it is possible to obtain $\alpha = 30°$and a r value of 1.08, the later being higher than the limit ratio given by Equation 2.4 ($r = 0.13$). This confirms that the assumption of the elastic foundation, at least for the top layer, is not realistic. It would be interesting, in future developments, to use of non-linear elastic constitutive law for the superficial layer foundation. This will allow irreversible deformation of foundation surface, a phenomenon observed in real structures.

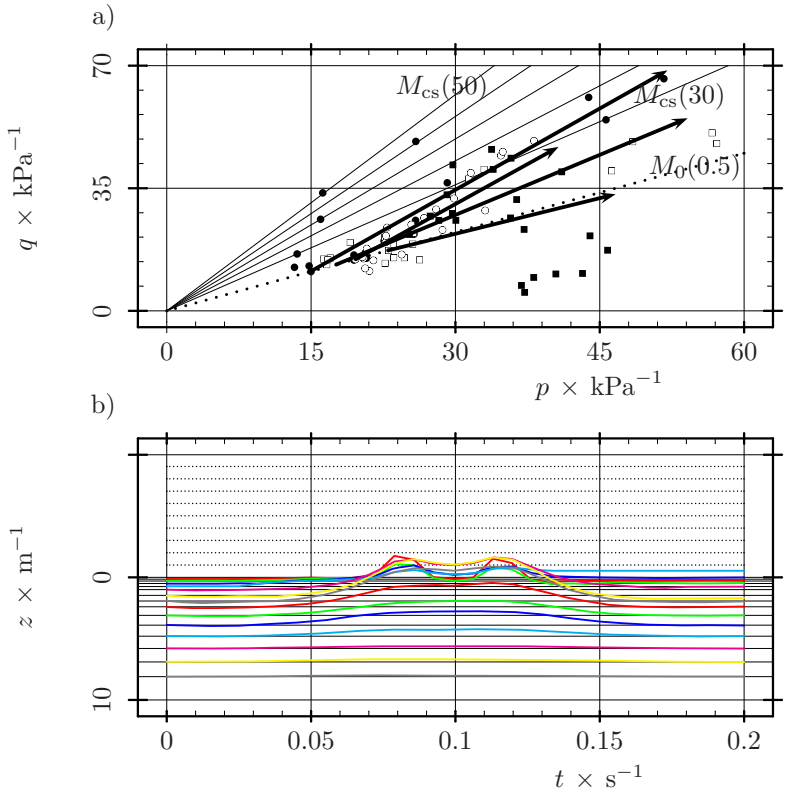

Figure 5.15: a) Characteristic stress-path assuming Mohr-Coulomb law with a vertical pressure on top of the ballast of 20 kPa, for a point placed at: (●) middle of the ballast layer $(x, y, z) = (24.9\,\mathrm{m}, 0.85\,\mathrm{m}, -0.15\,\mathrm{m})$, (□) interface ballast/subballast $(x, y, z) = (24.9\,\mathrm{m}, 0.94\,\mathrm{m}, -0.30\,\mathrm{m})$, (○) interface subballast/capping layer $(x, y, z) = (24.9\,\mathrm{m}, 1.07\,\mathrm{m}, -0.5\,\mathrm{m})$ and (■) middle of the capping layer $(x, y, z) = (24.9\,\mathrm{m}, 1.23\,\mathrm{m}, -0.75\,\mathrm{m})$. b) Vertical strain in the nodes defined in Figure 5.4 (dotted grid represents increments of 5×10^{-5})

5.5. Summary

After a successful calibration of a complex constitutive model, a new simulation of the case study described in Chapter 3 was performed but using a time domain model and 3 distinct constitutive laws (linear, Mohr-Coulomb and Hujeux law). Since no laboratorial data was available for the material that composes the railway structure, equivalent materials were used, i.e, materials that could be part of a railway structure and that were assumed to have equivalent response when submitted to train loading. All numerical simulations used a FEM model able to take into account dynamic effects, such as the propagation of compression and shear waves. Since 3 constitutive laws were used, 4 case studies were implemented: 2 models with linear elastic laws (with and without a vertical constant pressure over the ballast) and 2 models with laws capable of introducing plastic deformations (Mohr-Coulomb and Hujeux law).

Regarding results, it was detected that with the linear elastic models, charac-

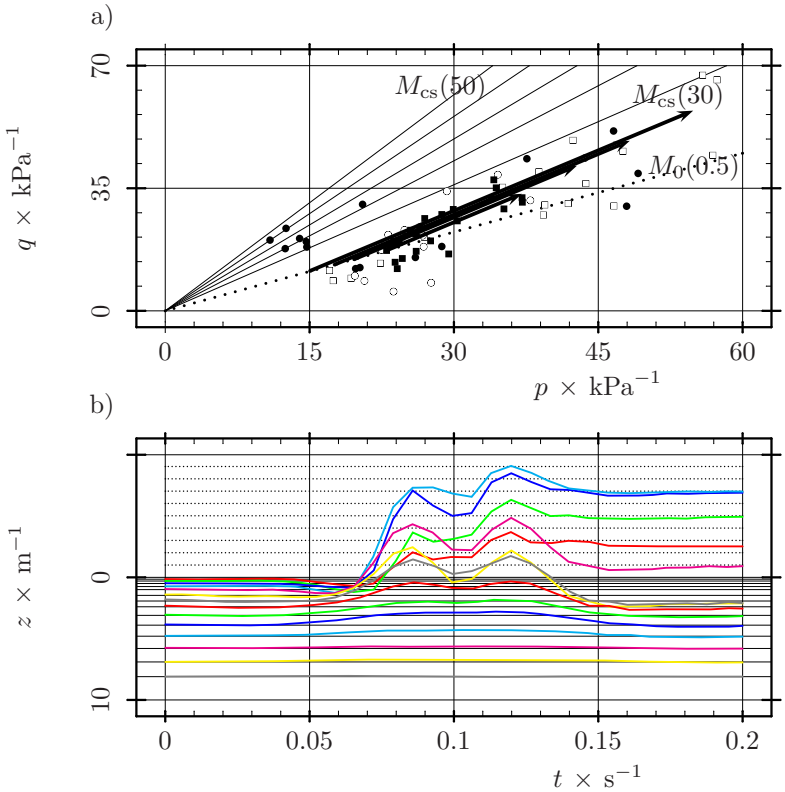

Figure 5.16: a) Characteristic stress-path assuming Hujeux constitutive law with an impose vertical pressure on top of the ballast of 20 kPa, for a point placed at: (●) middle of the ballast layer $(x, y, z) = (24.9\,\mathrm{m}, 0.85\,\mathrm{m}, -0.15\,\mathrm{m})$, (□) interface ballast/subballast $(x, y, z) = (24.9\,\mathrm{m}, 0.94\,\mathrm{m}, -0.30\,\mathrm{m})$, (○) interface subballast/capping layer $(x, y, z) = (24.9\,\mathrm{m}, 1.07\,\mathrm{m}, -0.5\,\mathrm{m})$ and (■) middle of the capping layer $(x, y, z) = (24.9\,\mathrm{m}, 1.23\,\mathrm{m}, -0.75\,\mathrm{m})$. b) Vertical strain (dotted grid represent increments of 5×10^{-5})

teristic stress-path range from a slope parallel to the NSL (on the ballast layer) to a practically vertical one (on the capping layer). This effect is due to the bending effect of the structure that reduces horizontal stress. This effect is not present in the models with more realistic constitutive laws. In those cases the slope remains almost constant and far from the failure envelope. Note that this constant slope should be understood as an narrow zone including the scattered on stress zone. This is expected to occur since structure reaches rupture by a mechanics distinct from a direct loading condition (rupture is accompanied by a permanent deformation of the structure). The slope $\Delta q/\Delta p$ of the non-linear cases was estimated between 1.21 and 1.43 with an average amplitude of the stress-path of 45 kPa. Even if values provided by the Hujeux law case induce an expected reduction of this amplitude with depth, since no confirmation is found in the Mohr-Coulomb case, only the average value is given here.

In terms of prospective work, it would be desirable to introduce non-linearity behavior in the top layer of the soil foundation, since in this layer it was detected

that the induced stresses overcome the assumed elastic domain. This improvement would allow a more realist simulation of the permanent deflection of the track structure, with the simulation of the permanent deflection of the track structure including foundation. Also, the application of the found stress-path in a large cyclic triaxial apparatus developed in the Civil Engineering Department at UM by Gomes Correia *et al.* (2010), would be interesting. With this apparatus and the stress-path found, the irreversible behavior of several railway materials can be studied and structural design improved.

This page was intentionally left blank.

Main summary

R.1. Conclusions

This thesis studied the effect of a moving load (materialized by a High-Speed Train - HST) over the distinct layers of a railway structure. To do so, a summary of the main characteristics of the structural system was reported and several numerical models developed assuming linear and/or non-linear constitutive laws were described. In addition, a laboratory work was performed to quantify the elastic domain envelope surface of a Portuguese soil. From the numerical simulations, a characteristic stress-path induced by a Thalys train was successfully quantified. The reciprocal use of linear/non-linear elastoplastic constitutive laws allowed the interpretation of constitutive law assumption, i.e., the consequence of this assumption on stress and displacement fields. With the quantification of the elastic domain, also successfully performed, the hypothesis of a foundation simulated with a linear elastic constitutive law was commented.

Describing in detail the main achievements found in each Chapter, the following conclusions can be pointed out.

Along Chapter 1, the description of the contribution of each track component, expected design behavior, moving load dynamic concepts, laboratorial testing and consequence of simplifications in numerical models were presented. With this task, it was detected that railway structures should allow an efficient stress distribution to reduce to admissible levels the stresses applied to the foundation. Moreover, the influence of wave propagation should be taken into account when modeling and, of great importance, it becomes unquestionable that maintenance costs are a crucial aspect to consider and require better design techniques to allow maximum cost reduction. To do so, numerical models must rely on accurate laboratory procedures. Also, since simulations are mainly performed assuming elastic behavior of the entire railway structure, the implication of this simplification in the induced fields stresses can be questioned. Although for noise and vibration generation (far field response) the assumption of linear elastic analyzes allows precise results, stresses and strains mobilized in the structure (near field response) may be unrealistic. Due to this, the evolution of induced stresses on the ballast, subballast and capping layer for linear elastic and non-linear plastic cases was considered one of the main developments of this research work. Since the stress degradation occurs through the structural layers of the track, a first attempt was done assuming elastic foundation behavior in the numerical model.

To check this assumption a laboratory test equipment was developed in

Chapter 2, which allowed the definition of the elastic domain of a national foundation soil (Perafita sand). For this purpose, it was necessary to develop a strain measurement system and a fully automated stress-path triaxial system. The strain measurement instrument was the LDT due to its low cost and high precision. Regarding the stress-path system, it was fully automated by means of proportional closed-loop valves controlled by means of LabVIEW® software. Based on experimental results with this laboratory facility, it was found that the elastic domain envelope depended on the initial stress state and on the applied stress-path. The influence of the initial mean stress p_0 presented higher influence than the initial deviatoric stress q_0. In addition, increments on the applied stress induced larger elastic domain envelopes in all paths applied in this study. A standardized envelope surface was defined using normalized values with the initial mean stress p_0. Taking into account the evolution of the domain radius r, the elastic domain of Perafita sand was written as Equation R.1, with r the radius of the elastic domain surface in $q\,p_0^{-1} : p\,p_0^{-1}$ space and α (in radians) the angular position.

$$r(\alpha) = 0.13 + 0.02\cos(\alpha) - \sin^2(\alpha)\frac{3\alpha + 55}{10^3} \;\; \forall\,\alpha \in [0, 2\pi] \tag{R.1}$$

Using a 3D frequency domain model with the objective of evaluating the stress-path and of validating the assumption of elastic behavior of materials (Chapter 3) it was possible to identify several limitations of the model to reproduce the response of a case study. The principal limitations were the following: the low range of the simulated acceleration due to the inability of the model to simulate high frequency modes and the unrealistic slopes, such as the one present in the capping layer, for the case of a low stiffness foundation due to the bending of the railway structure. Nevertheless, it was possible to identify, despite the observed limitations, that the velocity results accurately matched those obtained from the integration of the acceleration response. Since only the near field (with a main response defined by low frequencies) is here in subject of study and since velocity simulation presented high accuracy, the model was considered valid for stress evaluation. From this, the importance of the study of the behavior beyond the elastic domain is highlighted since bending on the structure occurs, which induces a decrease of the mean stress. This effect was not found when the foundation was assumed rigid (i.e. bedrock), but it was pronounced when the stiffness of the foundation was considered low. This was an expected behavior, although it may be amplified due to the elastic assumption. The increase in path slope can induce unrealistic slopes such as the one present in the capping layer for the case of a low stiffness foundation, where the stress-path overcomes an assumed failure envelope ($\phi = 45°$).

In order to surpass these constraints, a more robust material model was used in the time domain. To overcome the limitation identified due to the linear elastic assumption of the railways structure components, Chapter 4 focused on the calibration of a complex constitutive model law, capable of considering irreversible cyclic soil behavior. For this purpose, laboratorial data from 3 different geomaterials was used by a manual calibration process leading to a set of parameters able to reproduce its behavior, as well as in a preliminary study with an optimization technique. The results obtained showed that the optimization technique was able to provide a quality set of parameters if suitable and valid intervals were defined. This should not be considered as a limitation

since these can be attributed according to experimental test results for each type of material (e.g., clay, sand or gravel). Along the manual calibration process, it was detected that the model presented high capability of reproducing monotonic behavior with respect to all test results, e.g., variation of the deviatoric stress and volumetric strain. Regarding cyclic testing, reversible behavior was well represented. However, total strain evolution during cyclic conditioning requires improvements, namely since the introduction of the auxiliary Hujeux parameter N, implemented to reduce ne (power scalar to correlate the modulus with the mean stress p by means of a power law) according to the number of cycles previously performed, was not enough to overcome this difficulty. Nevertheless, this new parameter was useful to produce a smooth variation on the relation of cumulative strain versus performed number of cycles. Summing up, the performed calibration allowed for the definition of a set of parameters for each geomaterial, capable of globally capturing its geotechnical behavior.

After a successful calibration of a complex constitutive model, Chapter 5 proceeded to the simulation of the same case study described in Chapter 3, but using a time domain model. Since no laboratorial data was available for the material that composed the railway structure of the case study, synthetic materials were used, i.e., materials that could be used to compose a railway structure and that were assumed to have equivalent response when submitted to train loading. The numerical simulation used a FEM model which enabled to take into account dynamic effects, such as the propagation of compression and shear waves. Since 3 constitutive laws were used, 4 case studies were implemented: 2 linear elastic models (with and without a vertical constant pressure over the ballast) and 2 models with the capacity of introducing plastic deformations (Mohr-Coulomb and Hujeux law). The analyzes of the results showed that the elastic assumption induced characteristic stress-paths ranging from a slope $\Delta q/\Delta p$ equal to the consolidation line to a practically vertical one, corroborating the results presented in Chapter 3. However, more realistic constitutive laws produced stress-path slopes which remained almost constant and far from the failure envelopes. This constant slope should be understood as a narrow zone including the scatter on stress zone. The slope $\Delta q/\Delta p$ was estimated (with the non-linear models) between 1.21 and 1.43, and an average amplitude of the stress path circa 45 kPa. In conclusion, these obtained results show that a linear elastic model is able to reproduce the vertical displacement and velocity induced by the passage of a HST but it seems questionable to be capable of quantifying the stress evolution, particularly in the capping layer of the railway structure.

R.2. Prospective work

As future work, and regarding the definition of the elastic domain, it would be desirable to perform tests at higher confining pressures to confirm that the detected trends remain. Difficulties were detected on their application, due to limitations of the supply network (limited to 600 kPa) and the use of only half course of the proportional valves (they require an analog input from 0 to 10 V instead of the 0 to 5 V analog output provided by the AD converter). A device to measure suction should also be introduced on the equipment since the performed tests featured samples with water content around 12.8 %. Alternatively,

future testing should be performed on dry or saturated specimens. Regarding hardware improvements, it would be advantageous to change specimen geometry from cylindrical to prismatic (if LDTs are used to measure horizontal deformation). Finally, testing using the most recently developed software (see Appendix) should be performed to verify the efficiency of the simultaneous use of two proportional servo-valves (mainly in terms of testing speed).

Results obtained along this study are intended for application in the laboratory on a large cyclic triaxial apparatus developed in the Civil Engineering Department at UM. Through the use of this facility it is intended, mainly to experimentally quantify the irreversible behavior of the subballast layer (or other materials), record quality laboratory data and improve design.

Regarding the calibration of the Hujeux model (performed in Chapter 4), even if global behavior during consolidation and reversible cyclic testing is well represented, studies with imposed variation of β (plastic compressibility modulus that introduce the influence of the densification of the material in the final resistance) and r^{elas} (elastic ratio that determines the size of the elastic deviatoric domain), similar to those performed with ne, may improve cumulative prediction. With this improvement and the use of a new version of the minimization algorithm (capable of avoiding local minimum if the search interval of the parameters is excessively large) a more accurate set of parameters may be found.

The FEM Model developed in Chapter 5 can be improved extending elastoplastic constitutive law to the top layer of the soil foundation, since in this layer it was detected that the induced stresses overcome the assumed elastic domain. This improvement would allow a more realist simulation of the permanent deflection of track structure, with the simulation of the permanent deflection of the track structure including foundation.

Bibliography

Abdelkrim, M., Bonnet, G. and Buhan, P. "A computational procedure for predicting the long term residual settlement of a platform induced by repeated traffic loading." *Computers and Geotechnics*, 30: 463–476 (2003).

AFNOR. "Measurement of the capacity to adsorption methylene blue in soils or rock materials *'Mesure de la capacité d'adsorption de bleu de méthylène d'un sol ou d'un matériau rocheux'*." (1993). Association française de normalisation, ref. P94-068.

AFNOR. "Pavement base : non treated gravels : definitions, composition, classification *'Assises de chaussées : graves non traitées : définitions, composition, classification'*." (1994). Association française de normalisation, ref. P98-129.

Alaoui, A. and Naciri, T. "Ballasted railway lines *'Les voies ballastées'*." Technical report, Ecole Nationale des Ponts et Chaussées (1995). Paris (in French).

Andersen, L. and Nielsen, S. "Reduction of ground vibration by means of barriers or soil improvement along a railway track." *Soil Dynamics and Earthquake Engineering*, 25: 701–716 (2005).

Araújo, N. "Development of a precision triaxial apparatus for the evaluation of the elastic domain of geomaterials *'Desenvolvimento de equipamento triaxial de precisão para obtenção do limite elástico de geomateriais'*." Technical report, Universidade do Minho (2007). Guimarães (in Portuguese).

ASTM. "Standard practice for classification of soils for engineering purposes (unified soil classification system)." (1975). American Society for testing of Materials, ref. D-2487.

Aubry, D. "An integrated approach for the soil-structure interaction *'Sur une approche intégrée de l'interaction sismique sol-structure'*." *Revue Française de Géotechnique*, 38: 5–24 (1986). In French.

Aubry, D., Hujeux, J., Lassoudire, F. and Meimon, Y. "A double memory model with multiple mechanisms for cyclic soil behaviour." In "International Symposium on Numerical Models in Geomechanics," (1982). Zurich, 13–17 September.

Balay, J., Gomes Correia, A., Jouve, P., Hornych, P. and Paute, J. "Mechanical behaviour of soils and unbound granular materials, modelling of flexible pavements: recent advances." In "8th International Conference on Asphalt Pavements," (1997). Washington, 10–14 August.

Banimahd, M. and Woodward, P. "3-dimensional finite element modelling of railway transitions." In "9th International Conference on Railway Engineering," (2007). London, 20–21 June.

Banister, D. and Hall, P. "The second railway age." *Built Environment*, 19: 157–162 (1994).

Brandl, H. "Geotechnics of rail track structures." In "Geotechnics for Roads, Rail Tracks and Earth Structures," (2001).

Brandl, H. "Geotechnical aspects for high-speed railways." In "International Seminar on Geotechnics in Pavement and Railway Design and Construction," (2004). Athens, 16–17 December.

Brown, S., Kwan, J. and Thom, N. "Identifying the key parameters that influence geogrid reinforcement of railway ballast." *Geotextiles and Geomembranes*, 25: 326–335 (2007).

Burland, J. "Small is beautiful - the stiffness of soils at small strains." *Canadian Geotechnical Journal*, 26: 499–516 (1989).

Burland, J. and Symes, M. "A simple axial displacement gauge for use in the triaxial apparatus." *Géotechnique*, 32: 62–65 (1982).

Burrow, M. and Ghataora, G. "Analytical track substructure design." In "International Seminar on Geotechnics in Pavement and Railway Design and Construction," (2004). Athens, 16–17 December.

Cekerevac, C., Girardin, S., Klubertanz, G. and Laloui, L. "Calibration of an elasto-plastic constitutive model by a constrained optimisation procedure." *Computers and Geotechnics*, 33: 432–443 (2006).

Chang, C. and Hicher, P.-Y. "An elasto-plastic model for granular materials with microstructural consideration." *International Journal of Solids and Structures*, 42: 4258–4277 (2005).

Chebli, H., Othman, R. and Clouteau, D. "Response of periodic structures due to moving loads." *Comptes Rendus Mecanique*, 334: 347–352 (2006).

Chebli, H., Othman, R., Clouteau, D., Arnst, M. and Chatterjee, P. "3D periodic model for soil-structure dynamic interaction: common physical features and numerical rules." In "11th International Conference on Soil Dynamics & Earthquake Engineering - 3rd International Conference on Earthquake Geotechnical Engineering," (2004). California, 7–9 January.

Clayton, C., Khatrush, S., Bica, A. and Siddique, A. "The use of Hall effect semiconductor in geotechnical instrumentation." *Geotechnical Testing Journal*, 12: 69–76 (1989).

Clough, R. and Penzien, J. *Dynamics of structures*. McGraw-Hill International Editions in Civil Engineering Series (1993).

Clouteau, D. *Wave propagation in a heterogeneous medium: application in the field of seismic construction* 'Propagation d'ondes dans des milieux hétérogènes: aplication à la tenue d'ouvrages sous séismes'. Ph.D. thesis, Ecole Centrale Paris (1990). Paris (in French).

Clouteau, D. "ProMiss 0.2." Technical report, Ecole Centrale Paris (2000). Paris (in French).

Clouteau, D., Aubry, D. and Elhabre, M. "Periodic BEM and FEM-BEM coupling: applications to seismic behaviour of very long structures." *Computational Mechanics*, 25: 567–577 (2000).

Clouteau, D., Chebli, H., Hamadi, K., Lopez-Caballero, F., Modaressi, A. and Yeregui, A. "Numerical modelling of short-term and long-term track response." Technical report, Ecole Centrale Paris (2005). Paris.

Clouteau, D., Degrande, G. and Lombaert, G. "Numerical modelling of traffic induced vibrations." *Meccanica*, 36: 401–420 (2001).

Coronado, O. *Study of the mechanical behaviour of compacted granular materials unsaturated under cyclic loading* 'Étude du comportement mécanique de matériaux granulaires compactés non saturés sous chargement cycliques'. Ph.D. thesis, Ecole Centrale Paris (2005). Paris (in French).

Costa, L. and Oliveira, P. "Evolutionary algorithms approach to the solution of mixed integer non-linear programming problems." *Computers and Chemical Engineering*, 25: 257–266 (2001).

Costa D'Aguiar, S. *Numerical modelling of soil-pile load transfermechanisms.* Ph.D. thesis, Ecole Centrale de Paris (2008). Paris.

Cundall, P. and Strack, O. "A discrete numerical model for granular assemblies." *Géotechnique*, 29: 47–65 (1979).

Dafalias, Y. and Herrmann, L. *Bounding surface formulation of soil plasticity*, chapter 10, 253–282. John Wiley and Sons Ltd (1982).

Dahlberg, T. "Railway track dynamics - a survey." Technical report, Linköping University (2003). Linköping.

Dan, L. *Study of small strain behaviour and time effects on deformation characteristics of dense gravel by triaxial and true triaxial tests.* Ph.D. thesis, Civil Engineering Department of Tokyo University (2001). Tokyo.

Degrande, D. "Free field vibrations measurements during the passage of a Thalys high-speed train." Technical report, Katholiere Universiteit Leuven (2000). Leuven.

Degrande, G. and Lombaert. "High-speed train induced free field vibrations: in situ measurements and numerical modelling." In "International Workshop Wave," (2000). Rotterdam, 29–41 December.

Dewulf, W., Degrande, G. and G., D. R. "Special analysis of surface waves: an automated inversion technique based on a Gauss-Newton inversion algorithm." In "Inverse Problems of Wave Propagation and Diffraction," (1996). Aix-les-Bains, 23–27 September.

Duncan-Williams, E. and Attoh-Okine, N. "Effect of geogrid in granular base strength: an experimental investigation." *Construction and Building Materials*, 22: 2180–2184. (2008).

Elhabre, M. *Modelling the interaction soil-fluid-diaphragm walls by means of a periodic approach* 'Modélisation de l'interation sol-fluide-parois moulées suivant une approche périodique'. Ph.D. thesis, Ecole Centrale de Paris (2000). Paris (in French).

Esveld, C. *Modern railway track*. MRT-Productions (2001).

Fleureau, J., Hadiwardoyo, S., Dufour-Laridan, E., Gomes Correia, A. and Langlois, V. "Influence of suction on the dynamic properties of a silty sand." In "8th Congresso Nacional de Geotecnia," (2002). Lisbon, 15–18 April.

Gomes Correia, A. *Contribution for the mechanical study of soils submitted to cyclic loading* 'Contribution a l'etude m'ecanique des sols soumis a des chargements cyclique'. Ph.D. thesis, Ecole National des Ponts et Chaussées (1985). Paris (in French).

Gomes Correia, A. "Deformability characteristic of soils that interest to structures functionality *'Características de deformabilidade dos solos que interessam à funcionalidade das estruturas'*." *Revista da Sociedade Portuguesa de Geotecnia*, 100: 103–122 (2004a). In Portuguese.

Gomes Correia, A. "Evaluation of mechanical properties of unbound granular materials for pavements and rail tracks." In "International Seminar on Geotechnics in Pavement and Railway Design and Construction," (2004b). Athens, 16–17 December.

Gomes Correia, A., Araújo, N. and Reis Ferreira, S. "A large precision triaxial apparatus for study geomaterials under cyclic loading *'Triaxial cíclico de grandes dimensões para o estudo de geomateriais sob carregamento cíclico'*." In "12th Congresso Nacional de Geotecnia," (2010). Guimarães, 26–29 April (in Portuguese).

Gomes Correia, A. and Biarez, J. "Stiffness properties of materials to use in pavements and rail track design." In "12th European Conference on Soil Mechanics and Geotechnical Engineering - Geotechnical Engineering for Transportation Infrastructure.", (1999). Amsterdam, 7–12 June.

Gomes Correia, A. and Gillet, S. "A large triaxial test apparatus for study of granular materials under repeated loading used at LNEC." In "European Symposium of Flexible Pavements Design EUROFLEX93," (1993). Lisbon, 20–22 September.

Gomes Correia, A., Reis Ferreira, S. and Araújo, N. "Precision triaxial tests to evaluated deformability characteristics *'Triaxiais de precisão para determinação das características de deformabilidade'*." In "10th Congresso Nacional de Geotecnia," (2006). Lisbon, 22–25 May (in Portuguese).

Goto, S., Tatsuoka, F., Shibuya, S., Kim, Y.-S. and Sato, T. "A simple gauge for local small strain measurements in the laboratory." *Soils and Foundations*, 31: 169–180 (1991).

Graham, J., Tanaka, N., Crilly, T. and Alfaro, M. "Modified Cam-Clay modelling of temperature effects in clays." *Canadian Geotechnical Journal*, 38: 608–621 (2001).

Gutowski, T. and Dym, C. "Propagation of ground vibration: a review." *Journal of Sound and Vibration*, 42: 179–193 (1976).

Hadiwardoyo, S. *Characterization of granular materials from very small to large strain.* Ph.D. thesis, Ecole Centrale de Paris (2002). Paris.

Hall, L. "Simulations and analyses of train-induced ground vibrations in finite element models." *Soil Dynamics and Earthquake Engineering*, 23: 403–413 (2003).

Hardin, B. and Richard, F. "Elastic wave velocity in granular soils." *Journal of the Soil Mechanics and Foundations Division*, 89: 33–65 (1963).

Heelis, M., Collop, A., Chapman, D. and Krylov, V. "Predicting and measuring vertical track displacements on soft subgrades." In "2nd International Conference on Railway Engineering," (1999a). London, 25–26 May.

Heelis, M., Collop, A., Dawson, A., Chapman, D. and Krylov, V. "The 'Bow-wave' effect in soft subgrade beneath high speed rail lines." *Geotechnical Special Publication*, 94: 338–349 (2000).

Heelis, M., Dawson, A., Collop, A., Chapman, D. and Krylov, V. "Resilient modulus of soft soil beneath high speed rail lines." *Transportation Research Record*, 1687: 39–46 (1999b).

Hildebrand, R. "Vertical vibration attenuation in railway track: a wave approach." *Journal of Sound and Vibration*, 247: 857–874 (2001).

Hoque, E., Sato, T. and Tatsuoka, F. "Performance evaluation of LDTs for use in triaxial tests." *Geotechnical Testing Journal*, 20: 149–167 (1997).

Hujeux, J. "A constitutive law for the cyclic loading of soils *'Une loi de comportement pour le chargement cyclique des sols'*." *Genie Parasismique*, 1: 287–302 (1985). In French.

Ilias, H. "The influence of railpad stiffness on wheelset/track interaction and corrugation growth." *Journal of Sound and Vibration*, 227: 935–948 (1999).

Indraratna, B., Lackenby, J. and Christie, D. "Effect of confining pressure on the degradation of ballast under cyclic loading." *Géotechnique*, 55: 235–328 (2005).

Iwnicki, S. *Handbook of railway vehicle dynamics.* Taylor & Francis (2006).

Jamiolkowski, M., Lancellotta, R. and Lo Presti, D. "Stress distribution in railway formation: a simulated study." In "2nd International Symposium on Pre-failure Deformation Characteristics of Geomaterials," (1999). Torino, 28–30 September.

Jardine, R. "Some observations on the kinematic nature of soil stiffness." *Soils and Foundations*, 32: 111–124 (1992).

Jardine, R., John, H., Hight, D. and Potts, D. "Some practical applications of a non-linear ground model." In "10th European Conference on Soil Mechanics and Foundation Engineering," (1991). Florence, 27–30 May.

Jardine, R., Symes, M. and Burland, J. "The measurements of soil stiffness in the triaxial apparatus." *Géotechnique*, 34: 323–240 (1984).

Ju, S.-H. and Lin, H.-T. "Analysis of train-induced vibrations and vibration reduction schemes above and below critical Rayleigh speeds by finite element method." *Soil Dynamics and Earthquake Engineering*, 24: 993–1002 (2004).

Kaynia, A. and Clouteau, D. *Improved performance ob ballasted tracks*, chapter 1, 17–30. Taylor & Francis (2007).

Knothe, K. and Wu, Y. "The influence of elasticity in order to fallow stress/load evolution *'Einflußder Elastizitätsanordnung im Gleis auf die Beanspruchung durch Radunrundheiten'*." *Eisenbahntechnishe Rundschau*, 49: 150–158 (2000). In German.

Kok, A. "Finite element models for the steady state analysis of moving loads." *HERON*, 45: 53–61 (2000).

Kramer, S. *Geotechnical earthquake engineering*. Prentice-Hall International Series in Civil Engineering and Engineering Mechanics (1996).

Kruyt, N. and Rothenburg, L. "Micromechanical bounds for the effective elastic moduli of granular materials." *International Journal of Solids and Structures*, 39: 311–324 (2002).

Krylov, V., Dawson, A., Heelis, M. and Collop, A. "Rail movement and ground waves caused by high-speed trains approaching track-soil critical velocities." *Journal of Rail and Rapid Transit*, 214: 107–116 (2000).

Kuhlemeyer, R. and Lysmer, J. "Finite element method accuracy for wave propagation problems." *Journal of Soil Mechanics and Foundations Division*, 99: 421–427 (1973).

Lade, P. "Elasto-plastic stress strain theory for cohesionless soils with curved yield surfaces." *International Journal of Solids and Structures*, 13: 1019–1035 (1977).

Liao, C., Chan, T., Suiker, A. and Chang, C. "Pressure-dependent elastic moduli of granular assemblies." *International Journal for Numerical and Analytical Methods in Geomechanics*, 24: 265–279 (2000).

Lim, W. *Mechanics of railway ballast behaviour*. Ph.D. thesis, University of Nottingham (2004). Nottingham.

LNEC. "Compaction test *'Ensaio de compactação'*." (1966). Laboratório Nacional de Engenharia Civil, ref. E 197.

LNEC. "Equivalent sand test *'Ensaio de equivalente de areia'*." (1967). Laboratório Nacional de Engenharia Civil, ref. E 199.

Lopez-Caballero, F. *The influence of the nonlinear behaviour of soils in the seismic movements of geo-structures* 'Influence du comportement non linéaire du sol sur les mouvements sismiques induits dans des géo-structures'. Ph.D. thesis, Ecole Centrale de Paris (2003). Paris (in French).

Lopez-Caballero, F., Modaressi, A. and Modaressi, H. "Nonlinear numerical method for earthquake site response analysis I - elastoplastic cyclic model and parameter identification strategy." *Bulletin of Earthquake Engineering*, 5: 303–323 (2007).

Lu, M. and McDowell, G. "Discrete element modelling of railway ballast under triaxial conditions." *Geomechanics and Geoengineering*, 3: 257–270 (2008).

Marcelino, J. "Bi-dimensional model for the study of vibrations induced by high-speed trains *'Modelo bi-dimensional para o estudo das vibrações devidas a comboios de alta velocidade'*." Technical report, LNEC (2007). Lisbon (in Portuguese).

Martins, J. *Compaction and its influence on structural behaviour of high-speed railways*. Ph.D. thesis, University of Minho (2011). Guimarães.

Martins, J., Gomes Correia, A., Caldeira, L., Maranha das Neves, E. and Delgado, J. "Comparison of static plate loading tests results following AFNOR NF P94-117-1 and DIN 18134 standards *'Comparação de resultados de ensaios de carga segundo as normas AFNOR NF P94-117-1 e DIN 18134'*." In "XI Congresso Nacional de Geotecnia," (2008). Coimbra, 7–11 April (in Portuguese).

Mattsson, H., Klisinski, M. and Axelsson, K. "Optimisation routine for identification of model parameters in soil plasticity." *International Journal for Numerical and Analytical Methods in Geomechanics*, 25: 435–772 (2001).

McDowell, G. and Amon, A. "The applicability of weibull statistics to the fracture of soil particles." *Soils and Foundations*, 40: 133–141 (2000).

McDowell, G., Harireche, O., Konietzky, H., Brown, S. and Thom, N. "Discrete element modelling of geogrid-reinforced aggregates." *Geotechnical Engineering*, 159: 35–48 (2006).

McElvaney, J. and Snaith, M. *Analytical design of flexible pavements*, chapter 15, 395–423. Elsevier (2002).

Miranda, T. *Geomechanical parameters evaluation in underground structures. Artificial intelligence, Bayesin probabilities and inverse methods*. Ph.D. thesis, University of Minho (2007). Guimarães.

Miura, S., Takai, H., Uchida, M. and Fukada, Y. "The mechanism of railway tracks." *Japan Railway & Transport Review*, 3: 38–45 (1998).

Modaressi, A. and Lopez-Caballero, F. "Global methodology for soil behaviour identification and its application to the study of cite effects." In "4th International Conference on Recent Advances in Geotechnical Earthquake Engineering and Soil Dynamics," (2001). California, 26–31 March.

Montanelli, F. and Recalcati, P. "Geogrid reinforced railway embankment: design concepts and experimental test results." In "IABSE Symposium for Structures for High-Speed Railway Transportation," (2003). Antwerp, 27–29 August.

Mroz, Z. and Pietruszczak, S. "A constitutive model for sand with anisotropic hardening rule." *International Journal for Numerical and Analytical Methods in Geomechanics*, 7: 305–320 (1983).

Newson, T. "Validation of a non-associated critical state model." *Computers and Geotechnics*, 23: 277–287 (1998).

NP. "Specific density determination *'Determinação da densidade das particulas'*." (1965). Norma Portuguesa, ref. 83.

NP. "Atterberg limits determination *'Determinação dos limites de consistência'*." (1969). Norma Portuguesa, ref. 143.

Ortiz, M. and Pandolfi, A. "A variational Cam-Clay theory of plasticity." *Computer Methods in Applied Mechanics and Engineering*, 193: 2645–2666 (2004).

Powrie, W., Yang, L. and Clayton, C. "Stress changes in the ground below ballasted railway track during train passage." *Journal of Rail and Rapid Transit*, 221: 247–261 (2007).

Rampelo, S. and Viggiani, G. "The pre-failure behaviour of soils as construction materials." In "2nd International Symposium on Pre-failure Deformation Characteristics of Geomaterials," (1999). Torino, 27–29 September.

Raymond, G. "Track and support rehabilitation for a mine company railroad." *Canadian Geotechnical Journal*, 37: 318–332 (2000).

Reis Ferreira, S. *The influence of unsaturation and grain size curve in the deformability characteristics of a granite aggregate* 'Influência da não saturação e da granulometria nas características de deformabilidade de um agregado granítico'. Master's thesis, Instituto Superior Técnico (2003). Lisbon (in Portuguese).

Ricci, L., Nguyen, V., Sab, K., Duhamel, D. and Schmitt, L. "Dynamic behaviour of ballasted railway tracks: a discrete/continuous approach." *Computers and Structures*, 83: 2282–2292 (2005).

Roscoe, K., Schofield, A. and Wroth, C. "On the yielding of soils." *Géotechnique*, 8: 22–52 (1958).

Saïm, R. *The behaviour of uncohesive grains identifiable in a example of a real soil* 'Dés comportements repéres des grains sans colle à un exemple de sol réel'. Ph.D. thesis, Ecole Centrale Paris (1997). Paris (in French).

Santos, J., Gomes Correia, A., Modaressi, H., Lopez-Caballero, F. and Gomes, R. "Validation of an elastoplastic model to predict secant shear modulus of natural soils by experimental results." In "3rd International Symposium on Deformation Characteristics of Geomaterials," (2003). Lyon, 21–25 September.

Sauvage, J. ., G. INRETS / LTN. "Railway track vertical static behaviour." Technical report, Institute National de Recherche sur les Transportes et leur Scurit - Laboratoire des Technologies Nouvelles (1993). Paris (in French).

Schmitt, L. "Track measurements in Beugnâtre." Technical report, Société Nationale des Chemins de fer fran cais (2005). Paris.

Schwefel, H. *Cybernetic evolution as an experimental strategy. Research in current technology* 'Kybernetische Evolution als Strategie der exprimentellen. Forschung in der Stromungstechnik'. Master's thesis, Technical University of Berlin (1965). Berlin (in German).

Seed, H. and I.M. "Soil moduli and damping factors for dynamic response analyses." Technical report, University of California - Earthquake Engineering Research Center (1970). Berkeley.

Selig, E. and Boucher, D. "Abrasion tests for railroad ballast." *Geotechnical Testing Journal*, 13: 301–311 (1990).

Selig, E. and Waters, J. *Track geotechnology and substructure management.* Thomas Telford (1994).

Selig, E. T., Yoo, T. S., Adegoke, C. W. and Stewart, H. E. "Status report-Ballast experiments, Intermediate (175 mgt), substructure stress and strain data." Technical report, University of Massachusetts (1981). Cambridge.

Shaer, A. *Study of the permanent deformation of ballasted railway lines - dynamic approach* 'Analyse des deformations permanentes des voies ferrées ballastées - aproche dynamique'. Ph.D. thesis, Ecole Nationale des Ponts et Chauss'ees (2005). Paris (in French).

Shaer, A., Duhamel, D., Sab, K., Foret, G. and Schmitt, L. "Experimental settlement and dynamic behaviour of a portion of ballasted railway track under high speed trains." *Journal of Sound and Vibration*, 316: 211–233 (2008).

Shin, E., Kim, D. and Das, B. "Geogrid-reinforced railroad bed settlement due to cyclic load." *Geotechnical and Geological Engineering*, 20: 261–271 (2002).

Suiker, A., Selig, E. and Frenkel, R. "Static and cyclic triaxial testing of ballast and subballast." *Journal of Geotechnical and Geoenvironmental Engineering*, 131: 771–782 (2005).

Thompson, A. and Taylor, B. *Guide for the Use of the International System of Units (SI).* National Institute od Standards and Technology (2008).

Valanis, K. and Peters, J. "An endochronic plasticity theory with shear-volumetric coupling." *International Journal for Numerical and Analytical Methods in Geomechanics*, 15: 77–102 (1991).

Vinale, F., Onofrio, A., Mancuso, C., Magistris, F. and Tatsuoka, F. "The pre-failure behavior of soils as construction material." In "2nd International Symposium on Pre-failure Deformation Characteristics of Geomaterials," (1999). Torino, 27–29 September.

Voyiadjis, G. and Song, C. "Finite strain, anisotropic modified Cam-Clay model with plastic spin. i: theory." *Journal of Engineering Mechanics*, 126: 1012–1019 (2000).

Wan, R. and Guo, P. "A simple constitutive model for granular soils: modified stress-dilatancy approach." *Computers and Geotechnics*, 22: 109–133 (1998).

Wang, J. and Zeng, X. "Numerical simulations of vibrations attenuation of high-speed train foundations with varied trackbed underlayment materials." *Journal of Vibrations and Control*, 10: 1123–1136 (2004).

Wang, J., Zeng, X. and Mullen, R. "Three-dimensional finite element simulations of ground vibrations generated by high-speed trains and engineering countermeasures." *Journal of Vibration and Control*, 11: 1437–1453 (2005).

Wu, L. *Design and performance analysis of geosynthetics applications in railroad track mitigation*. Ph.D. thesis, National Cheng-kung University (2003). Taiwan.

Wu, W., Bauer, E. and Kolymbas, D. "Hypoplastic constitutive model with critical state for granular materials." *Mechanics of Materials*, 23: 45–69 (1996).

Yao, Y., Sun, D. and Matsuoka, H. "A unified constitutive model for both clay and sand with hardening parameter independent on stress path." *Computers and Geotechnics*, 35: 210–222 (2008).

Zhu, H., Mehrabadi, M. and Massoudi, M. "Three-dimensional constitutive relations for granular materials based on the dilatant double shearing mechanism and the concept of fabric." *International Journal of Plasticity*, 22: 826–857 (2006).

Appendix

A.1. Frequency domain model

For the sake of clarity, the following Sub-Sections describe the mathematical formulation of a frequency domain model developed at 'Ecole Centrale de Paris' by Professor Didier Clouteau and Doctor Hamid Chebly, along the European Project SUPERTRACK. Their work was used along Chapter 3 in order to quantify stress-path evolution induced by the passage of a High-Speed Train.

A.1.1. Floquet transform

Recalling the formulation developed by Chebli *et al.* (2006), lets assume Ω to be an unbounded open domain. The position vector of any point of this domain is given by $x = x_1x + x_2y + x_3z$ with (x, y, z) a Cartesian reference system. The domain Ω is assumed to be periodic in the y direction with a period T, so invariant through any translation of vector nTy, where n is signed integer. The Floquet transform of any function f defined in Ω is a function $\tilde{f}$ defined in $\widetilde{\Omega} \times \left[-\frac{\pi}{T}, \frac{\pi}{T}\right]$, with $\widetilde{\Omega} = \{x \in \Omega | 0 < x \cdot y < T\}$, and such that:

$$\tilde{f}\left(\tilde{x}, \kappa\right) = \sum_{n=-\infty}^{+\infty} f\left(\tilde{x} + nTy\right) \mathrm{e}^{in\kappa T} \tag{A.1}$$

in which the wavenumber $\kappa \in \left[-\frac{\pi}{T}, \frac{\pi}{T}\right]$, and where $\tilde{x}$ is the position vector in the reference cell $\widetilde{\Omega}$ defined by $\tilde{x} = \tilde{x}_1x + \tilde{x}_2y + \tilde{x}_3z$ with $\tilde{x}_1 = x_1$, $\tilde{x}_2 = x_2 - nT$, $\tilde{x}_3 = x_3$. It should be noted that the Floquet transform $\tilde{f}$ is periodic of the second kind, that is:

$$\tilde{f}(\tilde{x} + Ty, \kappa) = \mathrm{e}^{-i\kappa T} \tilde{f}(\tilde{x}, k) \tag{A.2}$$

Finally, for any $x = \tilde{x} + nTy$ with $x \in \Omega$ and $\tilde{x} \in \widetilde{\Omega}$, f may be recovered from its Floquet transform (Chebli *et al.*, 2006) by:

$$f(x) = \frac{T}{2\pi} \int_0^{\frac{2\pi}{T}} \tilde{f}(\tilde{x}, \kappa) \mathrm{e}^{-in\kappa T} \, \mathrm{d}\kappa \tag{A.3}$$

A.1.2. Floquet relation with Fourier transform

Let $F(x)$ be a function (defined on $\Re$ for the sake of accuracy). It is recalled that its Fourier transform $\widehat{F}$ can be defined:

$$\widehat{F}(k) = \int_{-\infty}^{+\infty} \mathrm{e}^{-ikx} F(x)\,\mathrm{d}x, \forall k \in \Re \tag{A.4}$$

The function F can be recovered from its Fourier transform as follows:

$$F(x) = \frac{1}{2\pi} \int_{-\infty}^{+\infty} \mathrm{e}^{-ikx} \widetilde{F}(k)\,\mathrm{d}k \tag{A.5}$$

Using these conventional formula, the Fourier transform of the function f_{x_1,x_3} defined as $f_{x_1,x_3}(x_2) = f(x)$ can be calculated from the Floquet transform of f (Clouteau *et al.*, 2000) as:

$$\tilde{f}_{x_1,x_3}(k_{x_2}) = \int_0^T \mathrm{e}^{ik_{x_2}\tilde{x}_2} \tilde{f}(x_1 x + \tilde{x}_2 y + x_3 z, \kappa)\,\mathrm{d}\tilde{x}_2 \tag{A.6}$$

where $\kappa \in \left[-\frac{\pi}{T}, \frac{\pi}{T}\right]$ and $k_{x_2} = \kappa + \frac{2n\pi}{T}$. Moreover, the Floquet transform of f is recovered from $\tilde{f}_{x_1,x_3}$ (Chebli *et al.*, 2006) by:

$$\tilde{f}(\tilde{x}, \kappa) = \frac{1}{2\pi} \sum_{n=-\infty}^{+\infty} \mathrm{e}^{-i(\kappa + \frac{2n\pi}{T})\tilde{x}_2} \hat{f}_{x_1,x_3}(\kappa + \frac{2n\pi}{T}) \tag{A.7}$$

A.1.3. Problem associated to a periodic domain

In an one-dimensional case (assumed for the sake of accuracy), let A be a differential operator with periodic coefficients (T being the period) such as:

$$A(x+T)u = A(x)u \tag{A.8}$$

for any real value x and for any function u belonging to its domain of definition $D(A)$. Moreover, let us introduce the family of operators $\widetilde{A}_k$ as the restriction of A on a reference cell $0 < x < T$. Then, as shown by Clouteau *et al.* (2000); Elhabre (2000), if $Au = f$ has an unique solution $u \in D(A)$, with f as a function belonging to the image of A, and if $\widetilde{A}_k \tilde{u} = \tilde{f}$ has an unique solution $\tilde{u} \in D(\widetilde{A}_k)$ such as:

$$\tilde{u}(T) = \mathrm{e}^{-i\kappa T} \tilde{u}(0) \quad \forall \kappa \in]-\frac{\pi}{T}, \frac{\pi}{T}[\tag{A.9}$$

then $\tilde{u}$ is to the Floquet transform of u defined by (Clouteau *et al.*, 2005):

$$\tilde{u}(\tilde{x}, \kappa) = \sum_{N_y=-\infty}^{+\infty} u(\tilde{x} + N_y T) \mathrm{e}^{i\kappa N_y T} \tag{A.10}$$

for any $\tilde{x} \in]0, T[$ and for any wavenumber $\kappa \in]-\frac{\pi}{T}, \frac{\pi}{T}[$. It should be noted that $Au = f$ can represent the usual Equation for a system subjected to an external

force f, being u the displacement field. Consequently, instead of solving $Au = f$, one can solve $\widetilde{A}_k \tilde{u} = \tilde{f}$ on the generic periodic cell (Fig. A.1) and built the solution u using the inverse Floquet transform.

These results have been extended by Clouteau *et al.* (2000); Elhabre (2000) to the three-dimensional soil-structure dynamic interaction problem with periodicity T along one direction.

A.1.4. Soil-track interaction model

Since for very long structures partially embedded in the soil (such as railway tracks) the dynamic soil-track interaction is of great importance (Clouteau *et al.*, 2005), the computer code MISS (Clouteau, 2000) developed in ECP and based on a domain decomposition method was used. Thus, the three-dimensional domain considered (the generic periodic cell) was decomposed into two subdomains (the track-structure and the soil), independently modeled and coupled on a given interface (Fig. A.2). The BEM technique with special Green's functions was used for the soil while the track-structure is modeled using FEM and its periodic modes. The use of SDTools, developed at ECP by Etienne Balmès, was required to perform mesh and eigenvectors generation. The overall process is controlled through MATLAB® scripts.

Briefly recalling some results presented by Aubry (1986), Clouteau (1990) and Clouteau *et al.* (2005), let $\tilde{u}_{\mathrm{st}}$ be the displacement field in the bounded generic structure cell, able to be decomposed on a given basis $\{\tilde{\phi}_k\}_{k=1,\ldots,N}$ of periodic modes which satisfy Equation A.9. Then, the displacement field $\tilde{u}_{\mathrm{st}}$ is

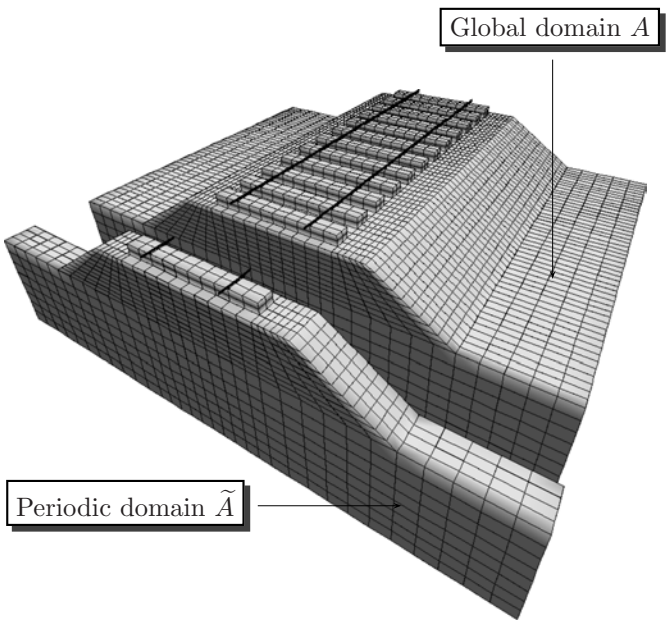

Figure A.1: Periodic domain selection

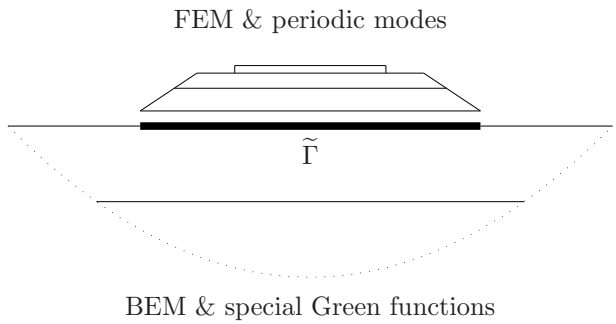

Figure A.2: Generic cell decomposed in track and soil domain (Chebli *et al.*, 2006)

written as:

$$\tilde{u}_{\mathrm{st}}(\tilde{x}) = \sum_{k=1}^{N} \tilde{\phi}_k(\tilde{x}) c_k = \phi(\tilde{x}) c \tag{A.11}$$

in which $\tilde{x} \in]0, T[$. Moreover, the soil displacement in the generic cell is defined by $\tilde{u}_s = \tilde{u}_i + \tilde{u}_{do} + \tilde{u}_{\mathrm{sc}}$ with $\tilde{u}_{\mathrm{i}}$ being the incident wave field, $\tilde{u}_{\mathrm{do}}$ being the locally diffracted wave field and $\tilde{u}_{\mathrm{sc}}$ the scattered wave field. The soil displacement can be further decomposed as:

$$\tilde{u}_{\mathrm{s}}(\tilde{x}) = \tilde{u}_{\mathrm{i}}(\tilde{x}) + \tilde{u}_{\mathrm{do}}(\tilde{x}) + \sum_{k=1}^{N} \tilde{u}_{\mathrm{dk}}(\tilde{x}) c_{\mathrm{k}} \tag{A.12}$$

where $u_{\mathrm{dk}k=1,\ldots,N}$ are elastodynamics fields. On the interface $\tilde{\Gamma}$ kinematic conditions read:

$$\begin{aligned} \tilde{u}_{\mathrm{i}} + \tilde{u}_{\mathrm{do}} &= 0 \\ \tilde{u}_{\mathrm{dk}} &= \tilde{\phi}_k \end{aligned} \tag{A.13}$$

The use of a standard Galerkin approximation procedure to write the equilibrium of the generic structure cell in a weak sense (for any $\tilde{\phi}_k$ in the basis) produces the linear system:

$$[K_{\mathrm{st}}(\kappa) - \omega^2 M_{\mathrm{st}}(\kappa) + K_{\mathrm{s}}(\kappa, \omega)] c(\kappa, \omega) = F_{\mathrm{st}}(\kappa, \omega) + F_s(\kappa, \omega) \tag{A.14}$$

for all angular frequency ω and wavenumber $\kappa \in]-\frac{\pi}{T}, \frac{\pi}{T}[$. K_{st} and M_{st} matrices correspond respectively to the stiffness and mass matrices of the structure, K_{s} is the soil impedance; F_{st} is the generalized force vector applied on the structure and F_s is the generalized force vector due to the incident wave field.

A.1.5. Moving load response

Recalling results presented by Chebli *et al.* (2006), lets assume a general pinpoint load moving along the y axis at a constant velocity C and:

$$
\begin{aligned}
Z(y,t) &= g(y_2 - V)\cdot\delta(y_1 - U)\cdot\delta(y_2 - V - C_{\mathrm{t}}t)\cdot\delta(y_3 - W)\cdot z \\
&= Z(y_2,t)\cdot\delta(y_1 - U)\cdot\delta(y_3 - W)\cdot z
\end{aligned}
\tag{A.15}
$$

with $y = y_1x + y_2y + y_3z$, $X = (U, V, W)$ as the position of the moving force at the time $t = 0$, $Z(y_2, t) = g(y_2 - V)\cdot\delta(y_2 - V - C_{\mathrm{t}}t)$ and $g(y_2 - V)$ as the variation of the moving force range.

Assuming, without any loss of generality, that the point x is in the generic cell, so $x = \tilde{x}$, and $\hat{u}(x, X, \omega)$ the displacement in x due to a moving load acting on X at $t = 0$. This field is given by:

$$
\hat{u}(x, X, \omega) = \int_{-\infty}^{+\infty} \widehat{Z}(y_2, \omega)\hat{h}(x, y = Xx + y_2y + Wz, \omega)\,\mathrm{d}y_2 \tag{A.16}
$$

where $\hat{h}(x, y, \omega)$ is the displacement in the frequency domain of a point x due to an impulse force at a point y. Moreover, $\widehat{Z}$ is the Fourier transform of Z and is given by:

$$
\widehat{Z}(y_2, \omega) = \mathrm{e}^{iC_{\mathrm{t}}^{\omega}(y_2 - V)}g(y_2 - V) \tag{A.17}
$$

For the sake of clarity, arguments x, X and ω will be often omitted in the following. Then, replacing Equation A.17 in Equation A.16 and expressing with its Fourier transform $g(y_2 - V)$, defines:

$$
\hat{u} = \frac{1}{2\pi}\int_{-\infty}^{+\infty}\int_{-\infty}^{+\infty} \mathrm{e}^{-i\breve{k}(y_2 - V)}\hat{g}(k_{y_2})\hat{h}(y_2)\,\mathrm{d}y_2\,\mathrm{d}k_{y_2} \tag{A.18}
$$

with $\breve{k} = (k_{y_2} - \frac{\omega}{C_{\mathrm{t}}})$. Equation A.18 is also equivalent to:

$$
\tilde{u} = \frac{1}{2\pi}\int_{-\infty}^{+\infty} \hat{g}(k_{y_2}) \sum_{n=-\infty}^{+\infty} \int_{nT}^{(n+1)T} \mathrm{e}^{-i\breve{k}(y_2 - V)}\hat{h}(y_2)\,\mathrm{d}y_2\,\mathrm{d}k_{y_2} \tag{A.19}
$$

Taking $\tilde{y}_2 = y_2 - nT$ leads to:

$$
\tilde{u} = \frac{1}{2\pi}\int_{-\infty}^{+\infty} \hat{g}(k_{y_2}) \int_{0}^{T} \sum_{n=-\infty}^{+\infty} \mathrm{e}^{-i\breve{k}(\tilde{y}_2 + nT - V)}\hat{h}(\tilde{y}_2 + nT)\,\mathrm{d}\tilde{y}_2\,\mathrm{d}k_{y_2} \tag{A.20}
$$

Due to the geometric periodicity:

$$
\hat{h}(x, \tilde{y}_2) + nT = \hat{h}(x - nTy, \tilde{y}_2) \tag{A.21}
$$

Moreover, the Floquet transform of the function $\tilde{h}(x, \tilde{y}_2)$, with respect to the variable x, is the function $\tilde{\hat{h}}_x(x, \tilde{y}_2, \kappa)$ defined by:

$$
\tilde{\hat{h}}_x(x, \tilde{y}_2, \kappa) = \sum_{n=-\infty}^{+\infty} \hat{h}(x + nTy, \tilde{y}_2)\mathrm{e}^{in\kappa T} \tag{A.22}
$$

From equations A.20 to A.22 Chebli *et al.* (2006) presents:

$$\hat{u}(x) = \frac{1}{2\pi} \int_{-\infty}^{+\infty} \hat{g}(k_{y_2}) \mathrm{e}^{i\breve{k}V} \int_{0}^{T} \mathrm{e}^{-i\breve{k}\tilde{y}_2} \tilde{\hat{h}}_x(x, \tilde{y}_2, \kappa_0) \, \mathrm{d}\tilde{y}_2 \, \mathrm{d}k_{y_2} \tag{A.23}$$

where $\kappa_0 = \breve{k} - \frac{2m\pi}{T}$, m being the signed integer such as $\kappa_0 \in]-\frac{\pi}{T}, \frac{\pi}{T}[$.

When using Equation A.23, only the response of the generic cell is necessary instead of the response of the domain as required in Equation A.16. The displacement due to a moving load in the frequency domain is also directly derived from the transfer function $\tilde{\hat{h}}$ in the $\omega : \kappa$ domain. Then, no inverse Floquet transform is needed.

In the case of a constant moving load, with $Z(y_2, t)$ equals to:

$$Z(y_2, t) = Z_0 \cdots \delta(y_2 - V - C_\mathrm{t} t) \tag{A.24}$$

with Z_0 being a real constant, Equation A.23 is equivalent to:

$$\hat{u} = \frac{Z_0}{2\pi} \mathrm{e}^{-iC_\mathrm{t}^\omega V} \int_{0}^{T} \mathrm{e}^{iC_\mathrm{t}^\omega \tilde{y}_2} \tilde{\hat{h}}_x(\tilde{y}_2, \kappa_0) \, \mathrm{d}\tilde{y}_2 \tag{A.25}$$

A.2. Stress-path software

A.2.1. Purpose

In order to improve test accuracy and to allow a stand alone apparatus, a laboratory software was developed using LabVIEW® and MATLAB®. Previous versions of this software were used to obtain the laboratory data presented in Chapter 2 and are in the genesis of this version. This software is here described to allow future application on the Geotechnical Laboratory at UM.

In general terms, it is intended for use with triaxial tests in which prismatic specimens are instrumented by means of 4 LDTs (2 for the axial deformations and 2 for the radial deformation). It allows the automatic control of 2 proportional servo-valves, one step motor and automatically performs data treatment, i.e, data is recorded into a file as strains, average stress and deviatoric stress. Note that cylinder specimens may be studied but they require code modification regarding the calculus of specimen area.

In order to simplify future use and improvements, the description of the developed LabVIEW® front panel and block diagram, the MATLAB® scripts and all test variables, is here presented. A testing procedure resume is presented to allow an easier starting for new users.

A.2.2. Software front panel

Regarding the software's front panel (Fig. A.3), it was developed using LabVIEW® boolean, graphic controls, numeric controls and indicators, leds, file path control and fill slides. In order to allow the application of any desirable stress-path (by means of 2 proportional servo-valves and/or 1 step motor) over a prismatic specimen, 66 control elements were used. These elements allow the complete control of the software and are described in the following topics. Readers should attend that since the text of some push buttons labels can assume 2 distinct values, the action performed by the software is presented together with the definition of button text label, in this document given in `Typewriter` style.

Controls description topics:

1. It corresponds to an '2D' graphics mainly useful for the evaluation of the elastic domain (stress-strain relation) and the visualization of the applied stress-path ($q : p$ space). Nevertheless, to allow other types of visualization, channels represented in axes xx and yy can be chosen by means of the numeric controls described on topics 5 and 6.

2. This topic is related with an '1D' graphic (since axle xx is always CPU time) for the evaluation of control efficiency. In it 2 channels are always represented simultaneously. Any channel can be represented as yy variable by means of the numeric controls described in topics 52 and 53. This graphic is useful to visualize the efficiency of the automatic control and, that way, to adjust the proportional gains described in topics 31 and 38.

3. It consists of a push button that allows 2 distinct representations over the graphic described on topic 1. When `One point` label is visible on the push button, only the last acquired data is plotted and visible. The

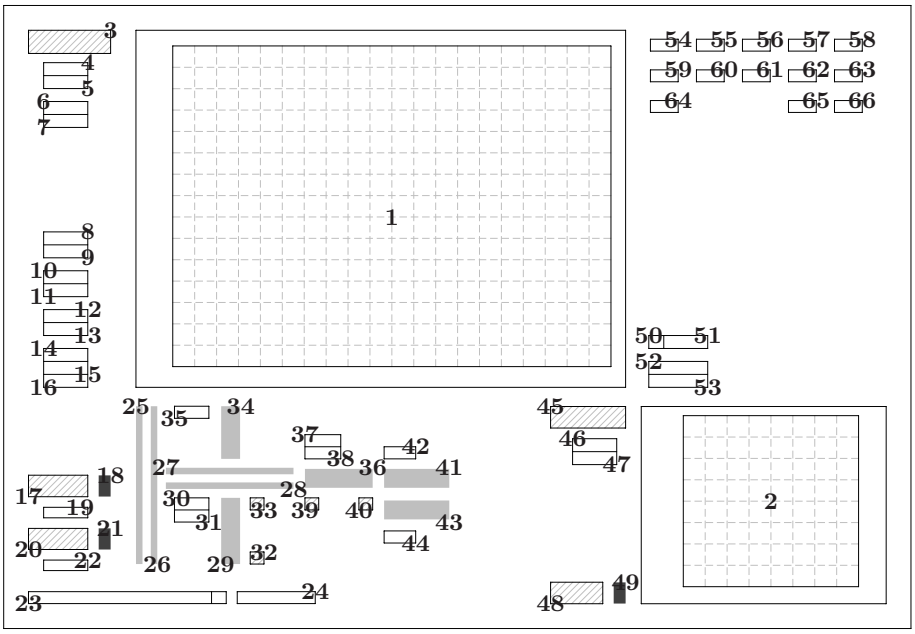

Figure A.3: LabVIEW® front panel of the software developed for stress-path control

second choice is activated when *Multiple plot* label is visible, which starts by clear the graphic and then plot all data acquired after the instant of definition of the push button label as *Multiple plot*.

4. In this numeric control one must define the channel to be represented in xx axes of the graphic described on topic 1. The meaning of each channel is given in table A.1 (page 178).

5. The function of this numeric control is identical to the one described on topic 4. The difference is that on this case the defined channel is represented in axle yy of the graphic described on topic 1.

6. This numeric indicator shows the numeric value of the last acquired data plotted in axle xx of the graphic described on topic 1.

7. It shows the last acquired value plotted in axle yy of the graphic described on topic 1.

8. This numeric control is of great importance for the definition of the initial dimension of the specimen. On it one must enter the length (mm) of the first axial LDT at the same time instant of the value given in topic 13.

9. As in topic 8, but for the second axial LDT.

10. The length (mm) of the first radial LDT, read at the same time instant of the value given in topic 12, should be written on this numeric control.

11. As in topic 10, but for the second radial LDT.

12. On this topic one should enter the specimen height h (mm). This height should be entered after placing the specimen in the chamber. It is recommended that specimen is submitted to a small vacuum (around $5 \sim 10\,\mathrm{kPa}$) so that errors due to adjustments of LDTs pseudo-articulations can be reduced.

13. Same as topic 12, but on this case regarding specimen width l (note that this software is developed for prismatic specimens).

14. Since it may be necessary to change the initial reading of the pressure transducer that records σ_3, this numeric control is given so that a new initial value can be defined. Note that signal increments will not be affected. If a zero value is intended, the reading of the transducer should be entered in this numeric indicator.

15. As in topic 14, but for the load cell that captures N_{a}.

16. As in topic 14, but for the equipment that captures u.

17. This push button allows to record data into a file. If ***Not saving*** label is visible, the obtained data is not being recorded. If ***Saving*** label is visible, data is recorded into a file according to the information provided in topics 23 and 24. It should be noticed that when the software is executed and the push button label is set to ***Saving***, the data file will overwrite any existing file with the same name. However, if during the execution of the software the push button label changed from ***Not saving*** to ***Saving***, a numeric index is added to the file name so that no overwriting occurs. This also allows user to control data file size.

18. It consists of a led indicator that light up each time data is saved into a file.

19. Before clearing the meaning of this variable, one should note that acquisition with fix specimens rate may produce system crashes. Due to that, this software was developed with acquisition on demand, i.e., the software runs on an eternal loop and during each loop one average specimens is recorded for each transducer. With this technique system crashes cannot occur. However, since time interval between loops is variable, it was necessary to find a way to correctly define the time when the data was recorded. This was solved using a MATLAB® command that provides CPU time. Having exposed this particularity, it is possible to say that the variable defined in this topic does not refers to time, but to the number of loops between recorded data. For example, if one enters 10 to this numeric control, only the data collected in the loops multiple of 10 will be recorded (0, 10, 20, 30, ...). Depending on the computer performance, the number of cycles per second may change. In the standard computer used for the laboratory work, each loop took about 0.15 seconds.

20. This push button allows user to define a constant loop record procedure (if ***Constant dt*** label is visible) as defined in topic 19 or a variable loop record procedure (if ***Variable dt*** label is visible). Considering that some

tests demand a high number of information during the initial phase of the test and only a few in the end (e.g., oedometric and consolidation on triaxial tests), a MATLAB® script was introduced in the block diagram (see page 176 for more details). This script allows user to define the loops (i.e., the data) that should be recorded into a file.

21. This led indicator light up when the push button described on topic 20 presents is label text as *Variable dt*.

22. This numeric indicator shows the number of recorded time instants.

23. The folder where the record file is to be saved can be defined in this file path control.

24. This numeric control allows user to define the name of the data file.

25. This fill slide with range $[145.5, 150]$ graphically displays the reading of the first axial LDT.

26. As in topic 25, but for the second axial LDT.

27. As in topic 25, but for a range $[71.8, 74]$ and for the first radial LDT.

28. As in topic 27, but for the second radial LDT.

29. This fill slide with range $[0, 10]$ graphically displays the applied analogic output of the proportional servo-valve that controls the axial actuator.

30. The numeric value of the analogic output applied to the proportional servo-valve that controls the axial actuator is shown in this numeric indicator.

31. This numeric indicator allows user to define a constant value to allow for a better control of the axial actuator. If during test the actuator is not able to follow it's numeric reference, a higher value should be used. On the other hand, if overshoot occurs, a smaller value should be used.

32. This push button allows user to reduce the analogic input provided to the proportional servo-valve that controls the axial actuator. Its interference is always present, even when automatic control (topic 49) is activated. It should be used to define the initial stress state.

33. As in topic 32, but to increase the analogic input.

34. This fill slide with range $[0, 3]$ graphically displays the reading N_{a} of the load cell.

35. The actual value of N_{a} is shown in this numeric indicator.

36. As in topic 29, but for the proportional valves that controls σ_3.

37. As in topic 30, but for the proportional valves that controls σ_3.

38. As in topic 31, but for the proportional valves that controls σ_3.

39. As in topic 32, but for the proportional valves that controls σ_3.

40. As in topic 33, but for the proportional valves that controls σ_3.

41. This fill slides with range $[0, 400]$ graphically displays the reading of the pressure transducer that obtains σ_3.

42. As in topic 35, but for σ_3.

43. As in topic 41, but for u.

44. As in topic 42, but for u.

45. In order to avoid damaging the LDTs transducers, this push button was introduced. When *Security OFF* label is visible, no protection against excessive deformation is considered. When *Security ON* label is visible and the lower limits of any LDT is reached (see topics 46 and 47), the analogic signal provided to the proportional servo-valves is set to zero so that no damage occurs in the transducer. Also, software execution is aborted.

46. This numeric control is used to define the minimal length l, in millimeters, of the axial LDTs.

47. As in topic 46, but for the radial LDTs.

48. The automatic control of the proportional servo-valve is turned on using this push button.

49. When the push button label described in topic 48 is set to *Control ON*, the led lights up to indicate that automatic control is in progress.

50. This numeric control allows user to define the channel to be displayed in topic 51. It is useful to check channels values during test without using graphics described in topics 1 and 2.

51. The value of the channel defined on topic 50 is displayed in this numeric indicator.

52. Graphic 2 is used to display, over time t, the variation of 2 channels. In this numeric control the user may choose the channel to be represented as a red line.

53. As in topic 52, but for a green line representation.

54. This software was developed to allow the application of any trajectories in $q : p$ space. To do so, a MATLAB® script (see page 177 for more details) was used to allow user to easily define the mathematical relations that the proportional servo-valves should follow during automatic control. Since a sine variation $A + B\sin(\alpha + t/T)$ was intended during the laboratory testing of this thesis, the script presented in the block diagram and in the front panel should be used for that purpose. In this situation, this numeric indicator allows user to define the value of C for the proportional servo-valve that controls the axial actuator.

55. As in topic 54, but to define the value of α.

56. As in topic 54, but to define the value of A.

57. As in topic 54, but to define the value of T.

58. This numeric control is used to define the channel to compare with the mathematical signal of the proportional servo-valve that controls the axial actuator. It allows user to freely control the test in terms of force, displacement,...

59. As in topic 54, but for the proportional servo-valve that controls σ_3.

60. As in topic 55, but for the proportional servo-valve that controls σ_3.

61. As in topic 56, but for the proportional servo-valve that controls σ_3.

62. As in topic 57, but for the proportional servo-valve that controls σ_3.

63. As in topic 58, but for the proportional servo-valve that controls σ_3.

64. The step motor control is here introduced so that a certain channel variable can remains constant, being the constant value defined in this numeric control.

65. This numeric control allows user to define the loops in which the step motor should apply corrections. If this numeric control is set to 300, corrections will be performed on loops multiple of 300 (i.e. 0, 300, 600, 900, ...). The correction consists on a pulse that induces a rotation on the motor equal to 1.8°.

66. As in topic 58, but for the step motor.

A.2.3. Software block diagram

In order to take full advantage of this software, simple modifications are required inside LabVIEW® block diagram. Six regions will be displayed inside this graphical code and 3 of them may require adjustments.

The first region (marked as 1 in Fig. A.4), allows the configuration of the analogic conversers. In order to perform testing monitoring, the acquisition of 7 transducers and 2 system proprieties must be defined. These transducers are: 2 axial LDTs, 2 radial LDTs, 1 load cell, 1 pressure transducer and 1 device to record interstitial pressure (not defined during this work and here set as 0). Regarding system proprieties, they are the diameter of the load piston (here defined equal to 0.02 m) and the membrane correction. In this work, membrane correction was not applied (set as 0 kPa) since low deformation was involved. If a higher value was expected, it should be considered. The second one (region 2) is used to execute signal output for the proportional servo-valves. They should be configured for the converser used and, if any signal amplification is introduced, the factor should be entered in the correction factors of the fill slide described in topics 29 and 36. In topic 20 (see front panel - Fig. A.3) it was mentioned that variable loop recording was possible and defined by means of a MATLAB® script. This script is found on the block diagram in the region marked as 3. On this script, one should consider that **T** refers to testing time and **aux** to a

variable that replaces the value defined on topic 19. User should only modify the conditions on the **if** structure to define distinct values of **aux** for certain time intervals. For the definition of the math signals, a MATLAB® script is also used and is located in region 4 of the block diagram. In this block diagram, the user can define any mathematical relation for the transducers considering that **Time** is the control time, **average** is the signal used to control the pressure chamber and **deviatoric** is the signal used to control the axial actuator. Region 5 is used to configure the converser that provides the digital outputs that controls the step motor. Finally, region 6 is used to define transducers calibrations. This task was not performed inside National Instruments Measurement & Automation software, since the use of the calibrations inside the code was considered to be more reliable. Since laboratory computers can be used by several users and in testing apparatus, undesirable calibration modification is avoided.

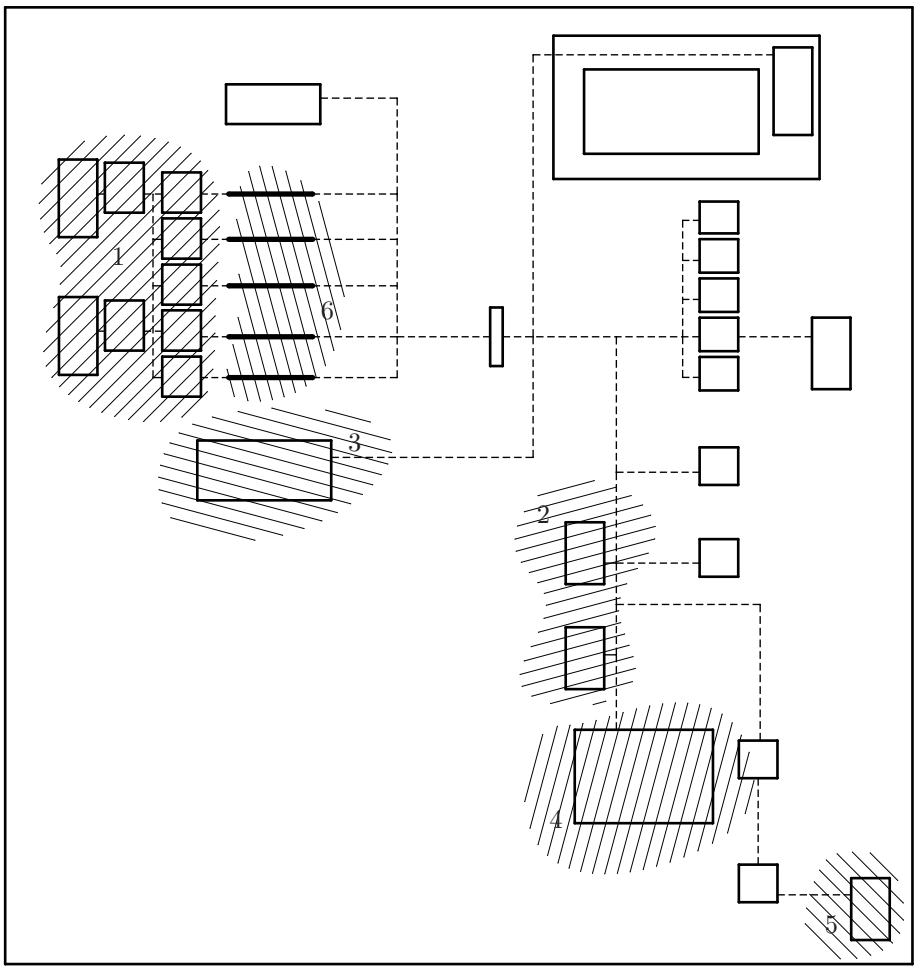

Figure A.4: Schema of LabVIEW® block diagram and regions that require adjustment

Table A.1: Available variables and channel reference

Channel reference	Description
0	testing time t (s)
1	length of the first axial LDT (mm)
2	length of the second axial LDT (mm)
3	length of the first radial LDT (mm)
4	length of the second radial LDT (mm)
5	confining pressure σ_3 (kPa)
6	axial force N (kN)
7	axial extension $\epsilon_{\mathrm{a}} \times 10^5$
8	radial extension $\epsilon_{\mathrm{r}} \times 10^5$
9	volumetric extension $\epsilon_{\mathrm{v}} \times 10^5$
10	specimen height h (mm)
11	specimen width l (mm)
12	specimen area A (m^2)
13	deviatoric stress q (kPa)
14	average total stress p (kPa)
15	average effective stress p' (kPa)
16	interstitial pressure u (kPa)
17	membrane extra confining pressure (kPa)
18	math signal for control of the axial actuator
19	math signal for control of chamber pressure

A.2.4. Channels and data file

After exposing all variables and scrips of the front panel and block diagram, one may focus on the available variables and recorded files for control and test analyzes. The software was developed so that all variables are updated on each loop and are available to control. Variables may also be recorded into a data file so that no post-treatment is required. This is useful since it eliminated post-treatment errors.

Even if previously mentioned (see page 172) it was important to refer again that valid data is only obtained if the initial dimensions of the specimen (topic 12 and 13) and the initial lengths of LDT transducers (topics 8 to 11) are registered at the same instant. This allows the correct control of the specimen volume by means of LDTs' monitoring. After clearing this import test detail, Table A.1 is provided with all available variables:

Regarding the data file (to be opened in EXCEL), all relevant information is automatically recorded and easily understood. The lines above show an example of a data file that corroborate this statement.

UMinho - DEC: Geotechnics (by Nuno Araújo)

date: 11-11-2009 11:42:17

Extensions were obtained with parameters from the end of compactation...
ldt.v1i/mm = 150
ldt.v2i/mm = 150
ldt.h1i/mm = 74
ldt.h2i/mm = 74
hi/mm = 200
li/mm = 100

Records: final values
Column B: t/s
Column C: v1/mm
Column D: v2/mm
Column E: h1/mm
Column F: h2/mm
Column G: s3/kPa
Column H: f/kN
Column I: ea/1e-5
Column J: er/1e-5
Column K: ev/1e-5
Column L: h/mm
Column M: l/mm
Column N: a/m2
Column O: q/kPa
Column P: p/kPa
Column Q: p/kPa
Column R: u/kPa
Column S: m/kPa
42137 150 150 74 74 0 0 0 0 0 200 100 0.01 0 0 0 0 0
...

A.2.5. Recommended test procedure

Since all important details regarding this software configuration and variable meaning (see software front panel for topics description) were exposed, new users can now exploit it and perform all desirable modifications. Nevertheless, this last topic will describe how triaxial test procedure should be performed so that new users adaptation is less time consuming.

As referred above, this software was mainly developed to be used in a triaxial chambers featuring an axial actuator (for application of a deviatoric force) and 2 proportional servo-valves. All tests start by a specimen construction and placement in the triaxial chamber inside a suitable latex membrane and reliable LDT pseudo articulation (it is assumed that new users knows how to do so). At this point, software should be launched (control (topic 48), saving (topic 17) and protections (topic 45) should be set to **off** before start running the software) transducers working for at least 15 minutes (to allow system stabilization). After this period, specimen should be submitted to a vacuum pressure (about $5 \sim 10\,\text{kPa}$) and its dimensions (height h and width l) measured. Since latex membrane is placed, measure values should reduce 2 times its thickness. Besides this dimensions, the lengths of all 4 LDTs should also be registered. This 6 values must be entered in the front panel (topic 8 to 13) since they are used to compute test variables. They will also be saved in the data files. After this step, the top of the chamber must be placed and chamber pressure slowly increased at the same time vacuum pressure decreases. Once all vacuum removed, σ_3 must be set to the desirable value (to do this refer to topics 32 and 33 of the front panel). The introduction of the deviatoric stress q must always follow the input of σ_3. Otherwise, specimen is destroyed. For the input of q, note that since no contact exists between the specimen and the top of the triaxial chamber, the signal of the proportional servo-valve that controls the axial actuator must be increased very slowly until axial piston starts to move. When movement begins, user should wait for the contact to occur. This detail is essential to avoid damaging the specimen. After that, the axial load can be increased to the desirable deviatoric test value. Note that step motor is not included in this test procedure. Once the initial stress state is applied ($q_0 : p_0$), the configuration of the parameters related with the math control signal (see front panel - topics 54 to 66), the minimum values of the LDTs (topics 46 and 47), the folder and name of the record file (topics 23 and 24) is required. Wait for strain stabilization and, when it has been reached, turn LDT protections (topic 45) **on**, start recording (topic 17) and start testing by setting topic 45 to `Control ON`. To conclude, only test ending need exposition. In order to do so, disactivate the automatic control, remove LDT protections and remove the axial force before reducing chamber pressure σ_3. This procedure allows the safe removal of the applied stress state without damaging LDT transducers. Stop test software and remove specimen from the triaxial test apparatus.

A.3. Hujeux law calibration software

A.3.1. Purpose

Since the calibration of the elasto-plastic multimechanism Hujeux law requires an interactive process, so that numeric results represent laboratory data, a MATLAB® graphical script was developed to assist on this task. Through it, errors induced by repetitive task are removed and several distinct sets of parameters can be easily tested, even by users without experience in working with MATLAB®. The software was developed to read laboratory data from a text file and, for a certain defined set of parameters, compute Hujeux law response and compare it with the laboratory one. This comparison is performed by means of a square power error equation and all necessary results are plotted into a multi-graphic figure. Along with the development of the manual calibration tool, an optimization algorithm was introduced. It means that the software here presented is capable of performing a stand alone adjustment once defined the laboratory data and variables of the objective function.

Summing up, this software and these short descriptions about its use are here given to allow future users to apply their own laboratory data and determine the respective set of Hujeux law parameters. Along the following pages all important details regarding its use will be exposed, as well as an example of a valid text file containing laboratory data which can be used as model for new data files.

A.3.2. Software description

This software consists of a simplified interface (Fig. A.5) which can be divided into 8 groups. Each of this groups is relative to a specific control part of the process, namely:

1. ***Auxiliar variable***: This group of variables is not directly used by the Hujeux law. However, since elasticity parameters are interconnected and are usually given as E and ν, respectively the Young modulus and the Poisson coefficient, they were here introduced. Other useful variables were introduced to allow the implementation of optimization strategies. These variables were ELAHYS, HYSMBL, ACYCA and CCYCC. Their meaning is detailed in Equations A.26 to A.29. A last parameter is defined on this group, which is parameter N. This was introduced to allow the variation of ne along cyclic testing and is explained in detail in Chapter 4.

2. ***Gefdyn variable***: the Hujeux law parameters presented in this group are to be used in the numeric computating. For detailed information regarding the meaning of each parameter, users can access ECP website `www.mssmat.ecp.fr/gefdyn/notice/node319.html`. Nevertheless, it is important to present the relationship between these parameters and those given on Chapter 4. For that purpose Table A.2 was introduced which contains the correspondence between the terms used along this thesis and those given in the website. Some notes regarding parameters units and signals were also provided. User should also notice that from the 32 parameters defined in this group, 8 cannot be directly defined, namely: RAYELA, RAYHYS, XKI, XGI, CCYC, ACYC, XKAUX and XGAUX.

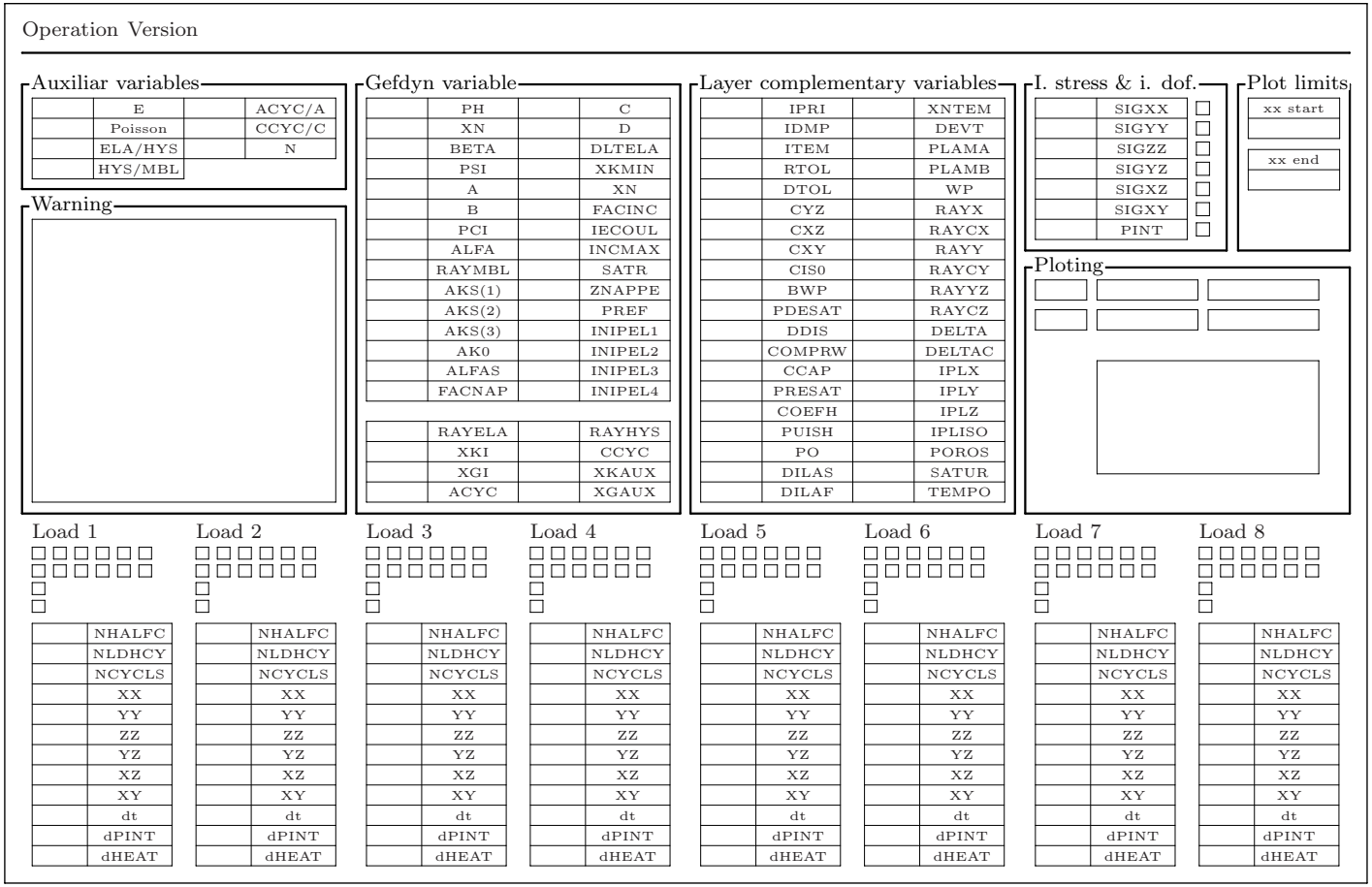

Figure A.5: Developed MATLAB® graphical script to assist on Hujeux law calibration process

These parameters are computed from the parameters defined in the ***Auxiliary variable*** group and the remaining parameters defined of ***Gefdyn variable*** group.

3. ***Lawyer complementary variables***: this group of parameters is used to control the software (Lawyer.exe) that computes the Hujeux law response (a manual is available on `www.mssmat.ecp.fr/-Lawyer,724-`). Regarding this group, it is important for the user to pay attention to parameter POROS, which is the initial soil porosity n. This value does not affect Hujeux law, being just used to set the initial void ratio by means of Equation A.30.

4. ***Initial stress and imposed dof***: this group was created to allow the definition of the initial stress state. The value of the 6 components of the stress tensor can be defined here as well as the initial pore pressure. Furthermore, user can define if the associate degree of freedom should be free (check box **off**) or not (check box **on**). User should note that if the degree of freedom associated to the pore pressure if not free, then an undrained test configuration will be performed.

5. ***Plot limits***: this group is used to limit results (start and ending lines of the variable saved in **res.mat**) to be plotted.

6. ***Warnings***: on this space the status of the simulations is printed, as well as the reported errors if computing is not possible.

7. ***Plot***: this group is useful to study the influence of Hujeux law parameters. It is possible to multiply Hujeux law response by constants (useful to remove negative values or to change units), to define which variable to plot on each axis (see Table A.3 for possible values) or even the type of axis (linear or logarithmic).

8. The last group consists of 8 load configurations. User start by defining the applied stresses (first line of the check boxes), applied deformation (second line), applied pore pressure (third line) or applied temperature (fourth line). Applied pore pressure and heat can be applied independently of the status of the check box described on topic *`Initial stress and imposed dof`*. Regarding applied stresses and deformation, they cannot be marked simultaneously and must be restrained in *`Initial stress and imposed dof`* group. If any of this 8 possible configurations is defined without any marked check box, it won't be considered in the simulation. For more details about the remaining parameters, see Lawyer manual.

$$\text{ELAHYS} = \frac{r^{\text{elas}}}{r^{\text{hys}}} \tag{A.26}$$

$$\text{HYSMBL} = \frac{r^{\text{hys}}}{r^{\text{mob}}} \tag{A.27}$$

$$\text{ACYCA} = \frac{a_2}{a_1} \tag{A.28}$$

Table A.2: Parameters name relations between those defined in ECP website and Chapter 4

Website	Chapter 4	Note
PHI	ϕ	Always negative
XN	ne	-
BETA	β	Always negative
PSI	ψ	Always negative
A	a_1	-
ACYC	a_2	-
B	b	Between 0 and 1
PCI	p_{c0}	Always negative and defined in Pascal (Pa)
ALFA	α_ψ	-
DLTELA	$r_{\mathrm{iso}}^{\mathrm{ela}}$	-
RAYELA	r^{elas}	-
RAYHYS	r^{hys}	-
RAYMBL	r^{mob}	-
C	c_1	-
CCYC	c_2	-
D	d	-
XM	m	-
PREF	p_{ref}	Always -10^6 Pa
XKI	K_{ref}	-
XGI	G_{ref}	-

$$\mathrm{CCYCC} = \frac{c_2}{c_1} \tag{A.29}$$

$$e = \frac{n}{1+n} \tag{A.30}$$

Table A.3: Relation between row file (on **RES.mat** file) and Hujeux law variable

Row of **RES.mat**	Variable	Meaning
1	KSTEP	Simulation step
2	SIGXX	Normal stress
3	SIGYY	Normal stress
4	SIGZZ	Normal stress
5	SIGYZ	Shear stress
6	SIGXZ	Shear stress
7	SIGXY	Shear stress
8	PINT	Pore pressure

Continued on next page...

Table A.3 – *Continued*

Row of **RES.mat**	Variable	Meaning
9	SIGC	-
10	PLIM	-
11	EPSXX	Normal strain
12	EPSYY	Normal strain
13	EPSZZ	Normal strain
14	EPSYZ	Shear strain
15	EPSXZ	Shear strain
16	EPSXY	Shear strain
17	TIME	-
18	SATURATION	-
19	HEAT	-
20	PCI	Critical mean effective stress
21	WP	-
22	FWP	-
23	DEPXX	-
24	DEPYY	-
25	DEPZZ	-
26	DEPYZ	-
27	DEPXZ	-
28	DEPXY	-
29	EVP	-
30	DDEPXX	-
31	DDEPYY	-
32	DDEPZZ	-
33	DDEPYZ	-
34	DDEPXZ	-
35	DDEPXY	-
36	DEVP	-
37	RAYyzM	-
38	RAYxzM	-
39	RAYxyM	-
40	RAYisoM	-
41	RAYyzC	-
42	RAYxzC	-
43	RAYxyC	-
44	RAYisoC	-
45	ALFAKyz	-
46	Ayz	-
47	ALFAKxz	-
48	Axz	-
49	ALFAKxy	-
50	Axy	-
51	skemp	-
52	compwa	-

Continued on next page...

Table A.3 – *Continued*

Row of **RES.mat**	Variable	Meaning
53	sfi	-
54	vide	Void ratio
55	poros	Porosity
56	satur	-
57	Seuilyz	-
58	Seuilxz	-
59	Seuilxy	-
60	Seuiliso	-
61	IpelYZ	-
62	IpelXZ	-
63	IpelXY	-
64	IpelISO	-
65	p	Average stress
66	q	Deviatoric stress
67	EPSV	Volumetric strain

To conclude the exposition of this graphical MATLAB® script, the meaning of the function available on menu 'Operation' is exposed. This menu contains 9 sub-menus which allow user to load saved configurations, save actual configuration or even compute Hujeux law response in 3 possible scenarios (manual single-result, manual multi-results and optimized multi-results).

This sub-menus are:

- ***Clear warning window***: clear the warning window.
- ***Update automatized variables***: computes the 8 parameters present on group ***Gefdyn variables***, defined in function of the parameters of group ***Auxiliar variables***.
- ***Plot graphic***: plot Hujeux law response saved in file **RES.mat** for the chosen set of axis. Useful for acquiring experience with the software.
- ***Run lawyer***: computes Hujeux law response for the actual configuration and save the result in a file named **RES.mat**. Useful for acquiring experience with the software.
- ***Run manual strategy***: this sub-menu exists so that the calibration of any soil can be performed manually. In order to do so, the user must write a text file named **evolutionary.nn**. This file should contain all laboratory data available for the soil subject to study so that all responses can be computed and presented on a multi-graphic picture. This sub-menu also computes the adjustment error, which assists user on the calibration process. Regarding the text file, data is assigned as a text line afterwards divided in sub-arrays with a length of 10 symbols. Some text is introduced on the file to make it user-friendly. However, users should note that, when defining new files, these text lines (even the empty ones) are required. For the sake of clarity, parameter names presented along the

example file **evolutionary.nn** (see Subsection A.3.3.) are equal to those defined on Figure A.5, with the exception of 4 new parameters, respectively: NVAR, NTEST, NREL and NRES. NTEST indicates the number of distinct tests used on the simulation; NREL indicates the number of loading configuration (limited to 8); and NTEST the number of laboratory available relationships. NVAR does not affect the manual calibration and is described in the following topic. Regarding the data defined bellow NTEST, the user must enter the exact names defined in Table A.3 in order to allow the software to extract the correct row of results on the result file **RES.mat**.

- ***Run evolutionary strategy***: this sub-menu also requires the definition of a file **evolutionary.nn**. In this case, instead of being the user to change the values of the Hujeux law parameters, an optimization algorithm developed by Professor Lino Costa (UM) performs this task. For that, file **evolutionary.nn** starts with the definition of NVAR (number of parameters to be used on the optimization process) and is followed by the definition of EPAR, MIN and MAX, the parameter name, lower limit and upper limit respectively. Regarding possible names for variables to be used on the optimization process, 20 can be enumerated: E, ELAHYS, HYSMBL, POISSON, ACYCA, CCYCC, PHI, XN, BBETA, PPSI, A, B, PCI, ALFA, RAYMBL, C, D, DLTELA, XM, and ALFAS.

- ***Save values as default***: save the actual parameter configuration in a file named **data.mat**.

- ***Restore default values***: read the configuration saved in **data.mat**.

- ***Write parameters***: create a text file (designed **gdfile.nn**) containing Hujeux law parameters in a format valid to be used in GEFDYN software.

A.3.3. Example of an evolutionary.nn file

NVAR
14

EPAR	MIN	MAX
PHI	-55	-40
PPSI	-10	0
BBETA	-120	-70
PCI	-5e6	-1e4
B	0.05	0.3
C	0.01	1
D	1	3
ACYCA	0.001	1
CCYCC	0.001	0.99
ALFA	1	4
ELAHYS	1e-4	1e-1
HYSMBL	1e-4	1e-2
DLTELA	1e-4	1e-1
A	0.005	0.5

NTEST
2

TITLE
triaxial test (s3=300kPa)

POROS

Continued on next page...

Continued

0.2407											
SIGXX	SIGYY	SIGZZ	SIGYZ	SIGZX	SIGXY	PINT					
-300e3	-300e3	-300e3	0	0	0	-1					
XX	YY	ZZ	YZ	XZ	XY	PINT2					
1	1	1	0	0	0	0					
NREL											
8											
S1	S2	S3	S4	S5	S6						
1	1	0	0	0	0						
D1	D2	D3	D4	D5	D6						
0	0	1	0	0	0						
P1											
0											
H1											
0											
NHALFC	NLDHCY	NCYCLS	XX	YY	ZZ	YZ	XY	XY	dt	dPINT	dHEAT
1	20	1	0	0	-0.07	0	0	0	1	0	0
S1	S2	S3	S4	S5	S6						
0	0	0	0	0	0						
D1	D2	D3	D4	D5	D6						
0	0	0	0	0	0						
P1											
0											
H1											

Continued on next page...

Continued

0											
NHALFC	NLDHCY	NCYCLS	XX	YY	ZZ	YZ	XY	XY	dt	dPINT	dHEAT
1	20	1	0	0	-0.07	0	0	0	1	0	0
S1	S2	S3	S4	S5	S6						
0	0	0	0	0	0						
D1	D2	D3	D4	D5	D6						
0	0	0	0	0	0						
P1											
0											
H1											
0											
NHALFC	NLDHCY	NCYCLS	XX	YY	ZZ	YZ	XY	XY	dt	dPINT	dHEAT
1	20	1	0	0	-0.07	0	0	0	1	0	0
S1	S2	S3	S4	S5	S6						
0	0	0	0	0	0						
D1	D2	D3	D4	D5	D6						
0	0	0	0	0	0						
P1											
0											
H1											
0											
NHALFC	NLDHCY	NCYCLS	XX	YY	ZZ	YZ	XY	XY	dt	dPINT	dHEAT
1	20	1	0	0	-0.07	0	0	0	1	0	0
S1	S2	S3	S4	S5	S6						
0	0	0	0	0	0						

Continued on next page...

Continued

D1	D2	D3	D4	D5	D6						
0	0	0	0	0	0						
P1											
0											
H1											
0											
NHALFC	NLDHCY	NCYCLS	XX	YY	ZZ	YZ	XY	XY	dt	dPINT	dHEAT
1	20	1	0	0	-0.07	0	0	0	1	0	0
S1	S2	S3	S4	S5	S6						
0	0	0	0	0	0						
D1	D2	D3	D4	D5	D6						
0	0	0	0	0	0						
P1											
0											
H1											
0											
NHALFC	NLDHCY	NCYCLS	XX	YY	ZZ	YZ	XY	XY	dt	dPINT	dHEAT
1	20	1	0	0	-0.07	0	0	0	1	0	0
S1	S2	S3	S4	S5	S6						
0	0	0	0	0	0						
D1	D2	D3	D4	D5	D6						
0	0	0	0	0	0						
P1											
0											
H1											
0											

Continued on next page...

Continued

NHALFC	NLDHCY	NCYCLS	XX	YY	ZZ	YZ	XY	XY	dt	dPINT	dHEAT
1	20	1	0	0	-0.07	0	0	0	1	0	0
S1	S2	S3	S4	S5	S6						
0	0	0	0	0	0						
D1	D2	D3	D4	D5	D6						
0	0	0	0	0	0						
P1											
0											
H1											
0											
NHALFC	NLDHCY	NCYCLS	XX	YY	ZZ	YZ	XY	XY	dt	dPINT	dHEAT
1	20	1	0	0	-0.07	0	0	0	1	0	0
NRES											
2											
PLX											
EPSZZ											
PLY											
q											
NPOINT											
12											
XL											
0	-0.0035	-0.0070	-0.0105	-0.0140	-0.0175	-0.0210	-0.0245	-0.0280	-0.0315	-0.0350	-0.0385
YL											
0	369.0e3	643.7e3	831.3e3	895.8e3	918.1e3	928.6e3	934.9e3	938.3e3	940.2e3	941.5e3	942.7e3
NODES											

Continued on next page...

Continued

1	2	3	4	5	6	7	8	9	10	11	12
PLX											
EPSZZ											
PLY											
EPSV											
NPOINT											
12											
XL											
0	-0.0035	-0.0070	-0.0105	-0.0140	-0.0175	-0.0210	-0.0245	-0.0280	-0.0315	-0.0350	-0.0385
YL											
0	-6689e-7	-9002e-7	-9485e-7	-9004e-7	-7885e-7	-6424e-7	-4892e-7	-3352e-7	-1779e-7	-147e-7	1570e-7
NODES											
1	2	3	4	5	6	7	8	9	10	11	12
TITLE											
triaxial test (s3=200kPa)											
POROS											
0.2453											
SIGXX	SIGYY	SIGZZ	SIGYZ	SIGZX	SIGXY	PINT					
-200e3	-200e3	-200e3	0	0	0	-1					
XX	YY	ZZ	YZ	XZ	XY	PINT2					
1	1	1	0	0	0	0					
NREL											
2											

Continued on next page...

Continued

S1	S2	S3	S4	S5	S6						
1	1	0	0	0	0						
D1	D2	D3	D4	D5	D6						
0	0	1	0	0	0						
P1											
0											
H1											
0											
NHALFC	NLDHCY	NCYCLS	XX	YY	ZZ	YZ	XY	XY	dt	dPINT	dHEAT
1	19	1	0	0	-0.047	0	0	0	1	0	0
S1	S2	S3	S4	S5	S6						
1	1	0	0	0	0						
D1	D2	D3	D4	D5	D6						
0	0	1	0	0	0						
P1											
0											
H1											
0											
NHALFC	NLDHCY	NCYCLS	XX	YY	ZZ	YZ	XY	XY	dt	dPINT	dHEAT
1	1	1	0	0	0.001	0	0	0	1	0	0
NRES											
2											
PLX											
EPSZZ											
PLY											

Continued on next page...

Continued

q											
NPOINT											
12											
XL											
0	-0.0025	-0.0049	-0.0074	-0.0099	-0.0124	-0.0148	-0.0173	-0.0198	-0.0223	-0.0247	-0.0272
YL											
0	239.2e3	444.4e3	588.3e3	653.6e3	677.2e3	689.8e3	698.8e3	705.2e3	709.6e3	713.0e3	715.5e3
NODES											
1	2	3	4	5	6	7	8	9	10	11	12

PLX											
EPSZZ											
PLY											
EPSV											
NPOINT											
12											
XL											
0	-0.0025	-0.0049	-0.0074	-0.0099	-0.0124	-0.0148	-0.0173	-0.0198	-0.0223	-0.0247	-0.0272
YL											
0	-4239e-7	-5571e-7	-5006e-7	-2513e-7	1519e-7	5924e-7	10349e-7	14784e-7	19214e-7	23628e-7	28012e-7
NODES											
1	2	3	4	5	6	7	8	9	10	11	12

This page was intentionally left blank.